University of Salford
MANCHESTER

Role of Connate Water Salinity in Gas Dispersion during Enhanced Gas Recovery by Carbon dioxide Injection and Sequestration

Muhammad Kabir Abba

(B.Eng., M.Sc.)

Ph.D. Thesis   **2018**

Role of Connate Water Salinity in Gas Dispersion during Enhanced
Gas Recovery by Carbon dioxide Injection and Sequestration

Muhammad Kabir ABBA

School of Computing, Science, and Engineering

College of Science and Technology,

University of Salford, Manchester, UK

Submitted in Partial Fulfilment of the Requirements for the Degree of
Doctor of Philosophy, December 2018

Abstract

A better understanding of the factors that influence mixing between CO_2 and CH_4 in natural gas reservoirs can provide an avenue to minimise the gas dispersion during Enhanced Gas Recovery (EGR). This highlights EGR's field scale adoption as a potential method for simultaneously reducing CO_2 emissions through sequestration and enhancing natural gas recovery and, thus, showcases it economic viability. An important aspect of the reservoir is connate water. So, what is the role of its connate water salinity on mixing during EGR?

In this investigation, three (3) different sandstone core samples (*Grey Berea, Buff Berea,* and *Bandera Grey*) with different petrophysical properties were used in this research. Phase I of this study entailed the cleaning and the characterisation of the core samples using experimental core analyses to determine the petrophysical properties. A novel practical approach to grain diameter determination of the core samples using image analysis was developed. The measurement showed that *Buff Berea* had the largest average grain size of 165.70 μm amongst the core samples used, followed by *Grey Berea* with 94.66 μm, and lastly *Bandera Grey* with 57.15 μm. This facilitated the determination the *Peclet number* during the displacement which helped develop a robust injection strategy for displacement of the CH_4 with minimum contamination by providing an optimum injection rate ranges for this application.

Phase II involved core flooding process to simulate the displacement of CH_4 by CO_2 that was carried out at 1300 psig and 50°C with varying injection rates of 0.2, 0.3, 0.4, and 0.5 ml/min. This was performed on dry core samples at different injection orientations –horizontal and vertical - to ascertain the effects of these variations on the displacement efficiency. The optimum injection rate was determined based on the dispersion coefficient and the CH_4 recovery efficiency obtained from testing individual core samples. *Grey Berea* at 0.3 ml/min in the vertical orientation gave the best results based on the criteria adopted and provided the benchmark for subsequent sensitivity analyses.

The Phase III of the study focused on the impact of connate water salinity of the mixing and dispersion of CO_2 into CH_4 during the displacement at the simulated reservoir conditions during EGR with different brine salinities (0, 5, 10 wt% NaCl) using the optimum conditions determined in Phase II for consistent results. The results from the core flooding process indicated that the dispersion coefficient decreases with increasing salinity, hence the higher the density of the immobile phase (connate water) the lower the dispersion of CO_2 into CH_4. This is the first investigation into the relationship between the connate water salinity and the dispersion coefficient in EGR. Consequently, feasibility of the solubility trapping as a secondary mechanism for CO_2 storage during EGR was experimentally investigated through core flooding process. Solubility trapping was found to increase the CO_2 storage capacity of natural gas reservoir by about 60% during EGR and the higher the connate water salinity the higher the sequestration potential of CO_2 but lower the CH_4 recovery was realised.

With this new information, the effect of connate water salinity on EGR is substantial and its inclusion in simulations studies will be helpful for field scale applications of EGR technique.

Acknowledgement

Declaration

I, Muhammad Kabir Abba, declare that this thesis is my original work, and has not been submitted elsewhere for any award. Any section, part or phrasing that has been used or copied from other literature or documents copied has been clearly referenced at the point of use as well as in the reference section of the thesis work.

………………………   …………………………….

Signature   Date

List of Symbols

μ	gas viscosity, cP
K_L	longitudinal dispersion coefficient, cm^2/s
K_t	transverse dispersion coefficient, cm^2/s
u	interstitial velocity, cm/s
t	time, s
c	solute concentration, 1
Pe	*Peclet* number, 1
P_{ex}	medium Peclet number, 1
Q	Darcy flow rate, cm^3/s
v	superficial velocity, cm/s
τ	tortuosity, 1
α	dispersivity, 1
t_D	dimensionless time
x_D	dimensionless distance
u_m	mean interstitial velocity
dP	differential pressure, psig
D	diffusion coefficient, cm^2/s
$OGIP$	original gas in place
RF	recovery factor
ADE	advection dispersion equation
ds	diameter of bubble from apex, m
de	equatorial diameter, m
H	Bond number, 1
B_g	gas formation volume factor, cm3/scm3
S	solubility
γ	interfacial tension, mN/m
ϕ	porosity, 1
S_w	water saturation, %
σ	linear attenuation coefficient, 1
ρ	density, g/cm^3

Table of Contents

List of Tables

List of Figures

List of Publications

A list of publications arising from this study and contributed to its development is highlighted below:

1. Abba, M.K., Al-Othaibi, A., Abbas, A.J., Nasr, G.G., Mukhtar, A., 2018. Experimental investigation on the impact of connate water salinity on dispersion coefficient in consolidated rocks cores during Enhanced Gas Recovery by CO_2 injection. J. Nat. Gas Sci. Eng.

2. Abba, M. K., Al-Othaibi, A., Abbas, A. J., & Nasr, G. G. (2018). Solubility Trapping as a Potential Mechanism for CO_2 Sequestration during Enhanced Gas Recovery by CO_2 Injection. Journal of Natural Gas Science and Engineering (Accepted).

3. Abba, M. K., Abbas, A. J., & Nasr, G. G. (2017). Rock Grain Diameter measurement using SEM as an imput paramter for rock dispersivity determination. In Salford Postgraduate Annual Research Conference (SPARC 2017) Manchester, UK.

4. Abba, M. K., Abbas, A. J., & Nasr, G. G. (2017). Enhanced Gas Recovery by CO_2 Injection and Sequestration: Effect of Connate Water Salinity on Displacement Efficiency. In SPE Abu Dhabi International Petroleum Exhibition & Conference. Abu Dhabi, UAE.

5. Abba, M. K., Abbas, A. J., Al-Othaibi, A., & Nasr, G. G. (2018). Enhanced Gas Recovery by CO_2 Injection and Sequestration: Effects of Temperature, Vertical and Horizontal Orientations on Dispersion Coefficient. In SPE Abu Dhabi International Petroleum Exhibition & Conference. Abu Dhabi, UAE.

6. Abba, M. K., Al-Othaibi, A., Abbas, A. J., & Nasr, G. G. (2018). Effects of gravity on flow behaviour of supercritical CO_2 during enhanced gas recovery and sequestration. In Fifth CO_2 Geological Storage Workshop. Utrecht, Netherlands.

CHAPTER 1

1   INTRODUCTION

1.1   Overview

This chapter aims to highlight the importance, need, and prospects of Enhanced Gas Recovery (EGR) as a method of additional gas recovery and anthropogenic carbon dioxide (CO_2) emission storage in brief. Additionally, the chapter is divided into sections: Section 1.2 presents the enhanced gas recovery background. Section 1.3 presents the problem statement. The research contribution is presented in Section 1.4. Justification, aim and objectives are discussed in section 1.5. Research methodology is highlighted in Section 1.6.

1.2   Background

The growing energy demand to cater for the growing world population has forced the exploitation of alternate sources of energy, using newer or otherwise unexploited technologies. Natural gas is considered as one of the most abundant, cleanest, and cheapest sources of fossil fuels and it is gaining more attention globally (Amin et. al, 2012; Benson et al., 2005). These features of natural gas have placed it at the forefront in the race to obtain not only an efficient source of energy but also an environmentally friendly one. As time progresses, production of this natural gas from the reservoirs can be interrupted and the reservoir abandoned. These reservoirs are termed depleted reservoirs. Depleted reservoirs are abandoned for a variety of reasons; common amongst which is the non-economic production rate, other reasons could be as a result of water invasion and also formation subsidence (Kalra & Wu, 2014). These depleted reservoirs, however, are not devoid of residual hydrocarbons in-situ and the need for further production and recovery to cater for the growing energy demand merits employment of enhanced recovery techniques, especially when CH_4 is displaced and CO_2 is stored.

The services of these depleted gas reservoirs may be "re-enlisted" for anthropogenic CO_2 geological storage. The concept of enhanced gas recovery by CO_2 injection utilises the availability of residual CH_4 in the reservoir and the storage volume of the depleted gas reservoirs to produce CH_4, and at the same time to store the injected CO_2. This technique serves as a simultaneous process as large volume of CO_2 will be sequestered along with substantial recovery of CH_4 from the depleted reservoirs. This concept is gaining attention globally due to the growing concern about climate change and greenhouse gas emissions

(Honari, Bijeljic, Johns, & May, 2015). It has the potential to minimise the anthropogenic CO_2 emissions in the atmosphere whilst recovering marketable CH_4 from natural gas reservoirs. Kalra & Wu (2014) enumerated four reasons for the choice of natural gas reservoirs as good candidates for CO_2 storage sites as follows:

i. The gas reservoir is a container for gases with proven integrity for it has stored gases for thousands of years. Incidentally, one of the problems with CO_2 subsurface storage in oil reservoirs, however, is the possibility of leaks (Zatsepina & Pooladi-Darvish, 2012) into adjacent aquifers and to the surface as a result of enhanced oil recovery techniques which changes the morphology of the oil reservoirs. Hence the preference of gas reservoirs over the oil reservoirs or CO_2 sequestration.

ii. Due to the density and viscosity differences of CO_2 and the in-situ CH_4, density and viscosity gradients play an important role in the displacement of CH_4 by CO_2 during the injection process. In that, CO_2 with higher density and viscosity than CH_4 will provide a favourable viscosity ratio to be able to efficiently displace the CH_4 from the reservoir.

iii. The cost of CO_2 sequestration process can be offset by additional income from the recovered natural gas owing to its market value and demand.

iv. The existing infrastructure (wells; either producers or injectors) potentially makes the process more economical as there will be no cost for drilling new wells.

Oil reservoirs have the potential to become possible storage site as well (Honari et al., 2015; Koide et al., 1993). But a potential problem may be attributed to the stimulation techniques employed during tertiary recovery processes or production optimisation as aforementioned. Hydraulic fracturing, for instance, may be a deterrent in the use of depleted oil reservoirs as CO_2 storage front as fractures may provide channels through which CO_2 may leak into adjacent aquifers or find its way to the surface.

CO_2 emissions from fossil fuel have strong impact on the environment and these effects cannot be overstressed. Being a greenhouse gas, it contributes to the global warming problem plaguing the environment. There is a rising global attention to reduce the carbon footprint emanating from the fossil fuels use. The use of CO_2 injection as a method for both Enhanced Gas Recovery (EGR) and Enhanced Oil Recovery (EOR) could be an approach to deal with the world growing energy demand and also, as means of reducing the amount of CO_2 present

in the atmosphere. These concepts are promising as methods of hydrocarbon recovery and CO_2 sequestration (Khan, Amin, & Madden, 2013).

At the onset of natural gas production, a natural gas field has reservoir pressures of up to 6,000 psi, depending on the local pressure gradient and depth of the reservoir (Blok, Williams, Katofsky, & Hendriks, 1997). A gas reservoir is said to be depleted when the reservoir pressure has dropped to about 300-700 psi, even though a fair amount of the original natural gas still remains in the reservoir (Blok et al., 1997). Any injection of whatever type of fluid into the reservoir for the purpose of incremental or additional recovery of the remaining gas is termed Enhanced Gas Recovery (EGR).

The type of lithology also plays a very important role in the simultaneous concept of EGR with CO_2 injection and sequestration. Sandstones formations provide the most preferred type of lithology for natural gas recovery and CO_2 storage, owing to their favourable petrophysical properties which aid different trapping mechanisms and assist in the recovery of residual hydrocarbons (Michael et al., 2010; Riaz & Cinar, 2014).

1.3   Problem Statement

Carbon dioxide (CO_2) is a greenhouse gas that is detrimental to the environment as a whole and reduction of its footprint has become very important. CO_2 sequestration technique is one of the sure-fire ways of isolating the CO_2 emitted into the atmosphere by our industries and storing it safely underground. Effective use of this technique requires a thorough understanding of the mechanics involved during the storage process. Exploring the mechanisms of this process will provide means of efficiently adopting this method of CO_2 injection for enhanced gas recovery and its isolation in depleted gas fields with subsequent cost reduction in the carbon emission tax imposed on industrialised nations.

The adoption of EGR generally has not been generally well received as a result of the excessive mixing of the injected CO_2 and in-situ CH_4 during the displacement process as a result of their thermodynamic and physical properties (Al-Abri et. al., 2009; Honari et al., 2015; Honari, Hughes et. al., 2013; Honari et al., 2016; Hughes et al., 2012; Khan et al., 2013; Oldenburg & Benson, 2002; Patel et. al., 2016; Shtepani, 2006; H. Sidiq, Amin et. al., 2011a; Sim et al., 2008; Turta et. al., 2009a; 2007; Yi Zhang et al., 2014). The mixing in situ grossly contaminates the recovered CH_4 and reduces its calorific value and thus reducing its

pipeline quality, and invariably incurs additional cost during the sweetening processes. (Oldenburg & Benson, 2002; Sim et. al., 2008; Turta et. al., 2009b)

The problem with EGR by CO_2 injection is in the nature of the gas-gas displacement mechanism in-situ. The efficiency of this displacement process is affected by the mixing of the displacing fluid (CO_2) and the displaced fluid (CH_4), given the complete miscibility of these two gases at conditions relevant to EGR process (Hughes et al., 2012) albeit their density and viscosity contrasts at those conditions. This major challenge has not only limited the EGR project to a few field trials (Honari et al., 2015; Pooladi-Darvish et al., 2008), but has also made the process largely unprofitable because the mixing phenomenon which is poorly understood (Patel et al., 2016). This warrants further investigation of the physics of mixing in relation to the porous media. One of the reasons, as earlier stated, for the choice of natural gas reservoirs as a good candidate for the sequestration is that the recovered natural gas should offset the cost of the sequestration process (Kalra & Wu, 2014). With this reason, the adoption and feasibility of EGR by CO_2 injection and sequestration rests greatly on minimising the contamination of the recovered CH_4.

Hence, the need for further research to minimise this mixing in-situ has become paramount. Some authors (Nogueira & Mamora, 2005; Turta et al., 2007) used N_2 and flue gas to displace CH_4 in order to determine the displacement efficiency. They reported poor displacement due to the low density of N_2 and the flue gas which is almost the same as that of the in situ CH_4. This unfavourable displacement condition gave rise to rapid N_2 gas breakthrough. With this, N_2 and flue gas may not be suitable for efficient CH_4 displacement. Several authors, also, like (Al-abri, Sidiq, & Amin, 2009; Honari et al., 2015, 2013, 2016; Hughes et al., 2012; H. Sidiq & Amin, 2009; H. Sidiq et al., 2011a) have carried out extensive researches on the sensitivity of overburden pressure, temperature, gas compositions on dispersion of CO_2 in CH_4 to ascertain the influence of these parameters on the gas-gas mixing during EGR but did not take into account the salinity of the formation water which has potential impact on the efficiency of EGR. Investigating the effect of salinity variation of the connate water will help reservoir engineers better characterise gas systems for an efficient adoption of EGR by CO_2 and subsequent sequestration in natural gas reservoirs.

1.4   Research Contributions

a. Highlight the influence of connate water salinity on displacement efficiency during CO_2 injection in terms of enhance gas recovery and also present solubility trapping as a potential secondary trapping mechanism when EGR is employed as a method of CO_2 storage.

b. Establish an alternative depiction of characteristic length scale of mixing in the medium *Péclet* number determination by measuring the mean grain diameter experimentally to give a more practical representation for consolidated porous media.

c. Account for effects of injection orientation of CO_2 on the mixing/dispersion during enhanced gas recovery and storage/sequestration.

1.5   Aims and Objectives

In this study, a comprehensive and robust approach will be used to understand and assess the mechanisms and factors that affect the gas-gas displacement efficiency in enhanced gas recovery process by CO_2 injection. The described mechanisms arising from these factors and their significance in the flooding process will be analysed in terms of design and operational applications.

Research aims:

i. To investigate the influence of injection orientation and connate water salinity on the displacement efficiency during enhanced gas recovery by CO_2 injection and sequestration.

ii. To evaluate the feasibility of solubility trapping as a secondary mechanism of CO_2 storage during enhanced gas recovery by CO_2 injection through laboratory experiments.

The key objectives are:

- To determine experimentally petrophysical properties (porosity, permeability) of the core samples using different characterisation techniques and also measure the grain diameter of the core samples using SEM and image analysis.

- To investigate the effect of vertical and horizontal injection orientations on the displacement efficiency during EGR so as to appraise the extent of mixing between CO_2 and CH_4 through laboratory core flooding experimentation.

- To assess the effect of connate water salinity variations on recovery efficiency during enhanced gas recovery and their influence on dispersion coefficient;
- To evaluate the effectiveness of the mechanism of solubility trapping as a secondary storage mechanism for CO_2 in sandstones by measuring IFT between brines of different concentrations and the gases (CO_2, CH_4) and their mutual solubility.
- To develop a numerical simulation for comparison and sensitivity of the experimental results using COMSOL Multiphysics®.

1.6 Thesis Structure

The thesis is structured into chapters and each chapter highlights and presents the details contained therein. A summary of each chapter is presented as follows:

Chapter 1: Introduction

The chapter introduces the technique of enhanced gas recovery by CO_2 injection and its importance in the realm of greenhouse gas emissions mitigation. The drawback of the technique was also thumbed, and the possible solution postulated. The research contribution of the thesis, the aims and objectives were also stated.

Chapter 2: Concept of enhanced gas recovery

This chapter covers the concept and theory of gas flow in porous media as applicable in EGR. It provides the insight into geological storage of CO_2 and how EGR can play a role and even maximise the storage capacity when natural gas reservoirs are used as sequestration sites. Concepts of IFT as a measure of CO_2 and CH_4 solubility were highlighted. Also, relevant literature on the miscible flooding and effects of physics of mixing between CO_2 and CH_4 were thumbed.

Chapter 3: Materials and methods

The chapter highlights the experimental methodology and materials required to carry out the experiments in this thesis. The detailed design of the steps of the work is discussed and presented here.

Chapter 4: Experimental setup and design

Detailed setup of individual equipment and their components are presented in this chapter. Various working principles and description of the apparatus were highlighted and also the procedure and precautions of operation were discussed.

Chapter 5: Results and discussions

The results obtained using the methodology in Chapter 3 and the experimental setup and procedures in Chapter 4 are presented and the observation tabled. All assertions made with respect to the results are discussed and analysed according to each experimental phase as designed in Chapter 3.

Chapter 6: EGR flow physics modelling using COMSOL Multiphysics

The comparison of the experimental results was carried out using COMSOL Multiphysics® simulation software. Furthermore, a comparison is made between the experimental results and the numerical simulation.

Chapter 7: Conclusion and Future approach to enhanced gas recovery by CO_2 injection

Here, the conclusions from the outcomes of the experimental work were drawn and the future approach to the technique was highlighted.

CHAPTER 2

2 LITERATURE REVIEW

2.1 Overview

This chapter highlights the concept of gas transport in porous media and principles of enhanced gas recovery. It also presents a summary of the concept of CO_2 geological storage and trapping mechanisms. Furthermore, relevant literatures are reviewed in support of the conceptual framework for this study.

2.2 Gas transport in porous media

Gas transport in porous media occurs extensively in various applications which include carbon sequestration, oil and gas exploitation, and food processing industry to mention a few. The significance of understanding the mechanisms of gas transport in porous media lies in designing and optimising the processes which embody the transport of gases. This gas transport is based on several models employed to optimise and evaluate the design and performance of the processes aforementioned. This work will focus on gas transport solely and not vapour transport unless otherwise stated therein. A good distinction between a vapour and a gas was made by (Ho & Webb, 2006) who differentiated them in terms of their states at standard temperature and pressure (293.15K, 14.7 psi). That is, if the gas constituents can exist, at standard temperature and pressure, as a liquid then it is considered as a vapour. Invariably, if the gas constituents remain gaseous i.e. not condensable at standard temperature and pressure, then it is considered a gas. This distinction is fundamental in that there are different processes affecting the behaviour and transport of gases and vapours through porous media. In addition, focus was made on the dominant porous media transport/displacement mechanisms in this study.

Furthermore, a brief description of the general displacement mechanisms and their concepts will be done to provide an overview of the concept of gas transport in porous media.

2.3 Theory of gas diffusion and dispersion

The components of dispersion are diffusive and mechanical mixing. Gas diffusion is usually portrayed to be dominated by molecular diffusion i.e. the random and haphazard spreading of solute specie along the concentration gradient with time. It is described by the Fick's second law which is one dimensional:

$$\frac{\partial C}{\partial t} = D_b \frac{\partial^2 C}{\partial x^2}$$ (2.1)

Here, C is the gas concentration, t is time, and D_b is molecular diffusion coefficient, and x is the position/point along the longitudinal axis of flow. Molecule to molecule collision is the only type of collision present in molecular diffusion implying that the system is without walls. Several complex diffusion processes may occur in some cases which include non-equimolar collision (which occur due to the presence of porous media walls and a gas mixture), Knudsen, and viscous diffusion (which occur due to presence of gas molecule and wall collision and presence of pore walls) as reported by Ho & Webb (2006). These conditions may lead to departure from Fick's law.

As a result of the relationships between the average kinetic energies, molecular masses, and velocities, diffusion as a component of dispersion is *solute dependent* Ho & Webb (2006). Diffusion is the dominant transport mechanism in low permeability porous media because of the low mobility/molecular velocity of the gas through the narrow pathways of the porous medium.

2.3.1 Concept of advection (Mechanical Mixing)

A *solute independent* component of dispersion, mechanical mixing, is governed by the velocity of the gas being transported and the physical properties of the porous medium. This velocity variation is a result of many phenomena as shown in Figure 2.1.
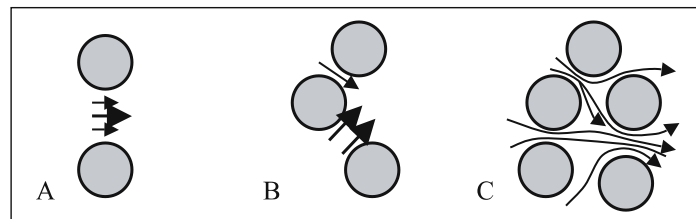
Figure 2.1 Flow through different arrangement of pore structures

From Figure 2.1, A shows a non-uniform velocity profiles within the pore throats of a set of rock grains, i.e., the velocity is higher at the centre of the pore throat where there is less resistance to flow compared with the lower velocities at the walls of the porous medium. B shows a non-uniform distribution of the pore sizes of the porous medium giving rise to different velocity profiles. C presents the tortuous flow paths.

Dispersion can be described as the irreversible mixing that occurs during miscible displacements (Adepoju, Lake, Johns, & Energy, 2013). This phenomenon is a resultant of two simultaneous mechanisms namely: molecular diffusion and mechanical dispersion (advection) (Perkins & Johnston, 1963). When two fluids come in contact with each other during a miscible displacement, and one displaces the other in a porous medium, the displaced fluid tends to mix with the displacing fluid. The efficiency of local displacement in miscible flooding is substantially affected by the mixing taking place within the rock spaces of the porous medium. A transition or mixing zone develops which is termed the displacement front where the concentration of the displaced fluid decreases from one to zero (Figure 2.2). It has been reported by Ekwere (2007) that several experiments show that the mixing zone propagates as displacement process progresses to a point where the concentration of the displacing fluid becomes ample in relation to the displaced fluid. The macroscopic dispersion observed in the porous media is used to quantify the mixing taking place (Jha et. al., 2013). This can be, to an extent, analysed by measuring the concentration of the displacing fluid relative to the displaced fluid in the produced effluent stream.
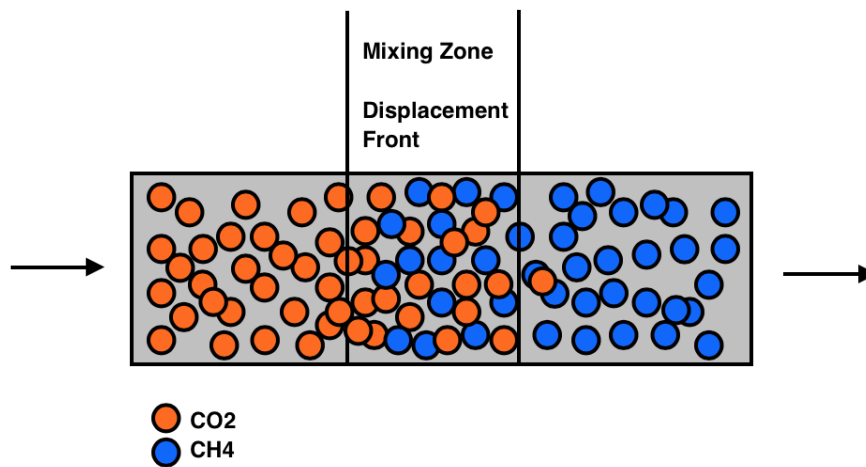
Figure 2.2 A *schematic of a miscible displacement of CH_4 by CO_2*

In the case where CO_2 is used to displace CH_4 in a miscible displacement technique, the progress of the process hinges on the purity of the recovered CH_4. In order to minimise the cost of producing CH_4 and maximise potential return during displacement process, the degree to which injected CO_2 gas mixes with CH_4 in situ has to be well evaluated and assessed. Newberg & Foh (1988) reported that mixing has been found to be controlled by several factors including pore geometry, turbulence, stagnant fraction of pore space, presence of an immobile fluid, viscous fingering, adsorption/desorption, and gravity segregation. These

factors are important in order to assess the extent of mixing during miscible displacements and thus, evaluating their effects will provide insight into the physics of mixing during any miscible displacement process. Fluid flow physics and behaviour are functions of the fluid viscosity; this provides an advantage in the case where supercritical CO_2 is used to displace CH_4 because the viscosity ratio is favourable when supercritical CO_2 displaces CH_4 as CO_2 is more viscous than CH_4 at reservoir conditions, i.e.: $\frac{\mu CH_4}{\mu CO_2} < 1$

2.4   Advection-Dispersion model

Advection-Dispersion equation (ADE) is often used to describe the gas transport in porous media. The effects of dispersion in one-dimensional ADE are showcased by the longitudinal dispersion coefficient which is defined in its simplest form as follows:

$$K_L = D_b \tau + \alpha v \tag{2.2}$$

where K_l is the dispersion coefficient (m^2/s), D_b is the molecular diffusion coefficient (m^2/s) τ is the tortuosity factor (dimensionless), α is the longitudinal dispersivity of the gas phase (m), v is the average gas velocity (m/s).

2.4.1   Dispersion and diffusion coefficients

The term *Péclet* number, P_e, is a dimensionless measure of the level of dispersion of a solute which is defined as the ratio of advective to dispersive processes (Rose, 1973) as reported by Ho & Webb (2006). This variable is usually obtained through curve fitting of a solute concentration profile with a A-D transport model (Eq. 2.2). The degree or level of dispersion is inversely proportional to the magnitude of the *Péclet* Number. At low *Péclet* numbers, the degree of dispersion is large. It is expressed as follows:

$$P_e = \frac{vL}{K} \tag{2.3}$$

where v is the interstitial velocity, K is the dispersion coefficient, and L is termed the characteristic length of the system.

Perkins & Johnston (1963) presented another definition of *Péclet* number termed medium Péclet number, denoted by P_{ex}, which describes the dominant displacement regime during a dispersion process and expressed as:

$$P_{ex} = \frac{u_m d}{D} \tag{2.4}$$

Where P_{ex} is medium *Péclet* number, u_m is the mean interstitial velocity (m/s), D is the diffusion coefficient (m^2/s), and d is the characteristic length scale of the porous medium, which is defined as the medium grain diameter of the sandpack but it is poorly defined in consolidated medium. Hughes et al., (2012) presented an exemplar to represent the characteristic length scale of the consolidated core sample as the mean pore throat diameter obtained from Porosimetry or the ratio of permeability to porosity of the rock given as $\sqrt{\frac{k}{\phi}}$. Coats et. at., (2009) correlated dispersion coefficient with diffusion as follows:

$$\frac{K_l}{D} = \frac{1}{\tau} + \alpha \frac{u_m^n}{D} \tag{2.5}$$

Where α is in (m) the dispersivity of the porous medium, n is an exponent. Which is $1 \leq n \leq 1.5$ and τ can range from $\sqrt{2}$ for packed beds and can be as large as 13 for consolidated media as reported by Honari et al. (2013) and literatures therein. The parameter τ can be obtained empirically through several methods, but α and n can only be determined experimentally through core flooding. Generally, at $P_{ex} < 0.1$, diffusion dominates the dispersion process and the ratio, $\frac{K_l}{D}$ is constant and equates to $\frac{1}{\tau}$ and conversely, at $P_{ex} > 10$ advective mixing dominates the dispersion process and the ratio $\frac{K_l}{D}$ linearly proportional to P_{ex}. A transition region exists for values of P_{ex} between 0.1 and 10 where both advection and diffusion are significant. Additionally, if $n=1$, from (Eq. 2.5) $\alpha \frac{u_m^n}{D} = P_{ex}$ with α analogous to the characteristic length scale for mixing in (Eq. 2.4).

Takahashi and Iwasaki (1970), reported by Hughes et al. (2012) and Liu et al., (2015), established a correlation between the diffusion coefficient, temperature and pressure and measured the diffusion coefficient for CO_2 in CH_4 at 298 to 348K and pressures of 5-15 MPa in a porous medium. This correlation was used by the authors to obtain accurate diffusivity using Eq. 2.5 at conditions relevant to enhanced gas recovery by CO_2 injection. The correlation is as follows:

$$D = \frac{(-4.3844 \times 10^{-13} p + 8.55440 \times 10^{-11}) T^{1.75}}{p} \tag{2.6}$$

where D (m^2/s) is the molecular diffusion coefficient of CO_2 in CH_4 at temperature T (K) and pressure p (MPa).

2.4.2 Dispersivity

Dispersivity is, generally, not a function of fluid velocity, making it a property of the porous medium. Coats et al. (2009) expressed that the magnitude of dispersion is quantified by the rock property dispersivity (α) which is of the order of 0.01 ft (3.048×10^{-3} m) in consolidated rock and many times lower in sand packs, from laboratory measurements.

(Coats & Whitson, 2004) defined dispersivity as:

$$\alpha = \frac{K_l}{u} \tag{2.7}$$

Where K_l is the longitudinal dispersion and u is interstitial velocity. Comparing Eq. 2.7 to Péclet number, P_e, expression, we have;

$$\alpha = \frac{1}{P_e} L \tag{2.8}$$

Eq. 2.8 shows the significance of *Péclet* number during a miscible flooding process, as it shows that it scale-dependent and a function of dispersivity.

Accurate determination of the dispersivity is vital when it comes to modelling the miscible fluids displacement process in porous medium as in the case of EGR (Hughes et al., 2012).

Ekwere (2007) reiterated that molecular diffusion is more important to transverse dispersion than to longitudinal dispersion. This is because the regime dominated by molecular diffusion occurs over a larger range of Péclet numbers for transverse dispersion than to longitudinal dispersion as seen from (Figure 2.3 and Figure 2.4) as adapted from (Perkins & Johnston, 1963) below.
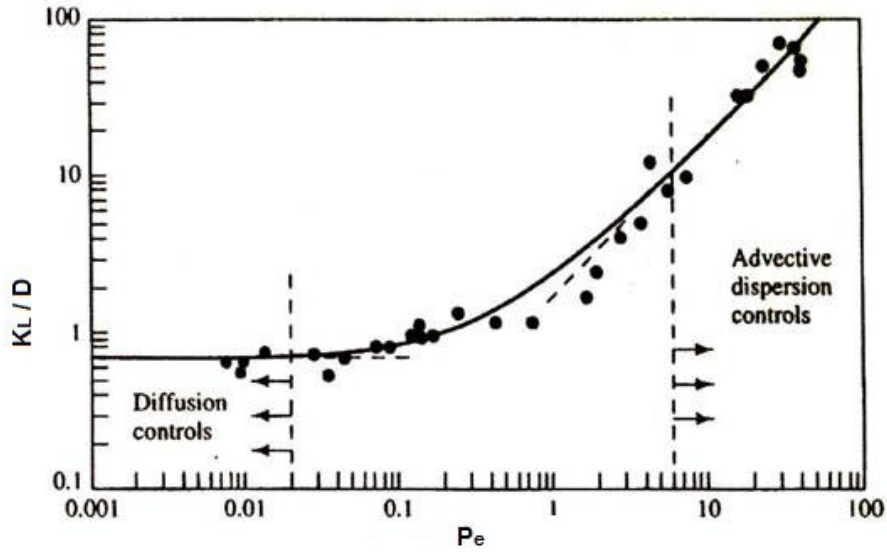
Figure 2.3 Longitudinal dispersion coefficients in porous media adapted from Perkins (1963)

The figure shows K_L/D plotted against the *Péclet number* of the porous medium, P_{ex}, where D is the diffusion coefficient. At low values of P_{ex}, molecular diffusion dominates over advective dispersion. Invariably, at high Péclet numbers, the longitudinal dispersion coefficient is higher than the transverse dispersion coefficient. At typical reservoir velocities, the Péclet number is normally greater than 6 (Ekwere, 2007), and as such molecular diffusion can be neglected. The transverse dispersion coefficient also shows a higher range of Peclet number which shows wider ranges of the dominant displacement mechanisms compared to the longitudinal.
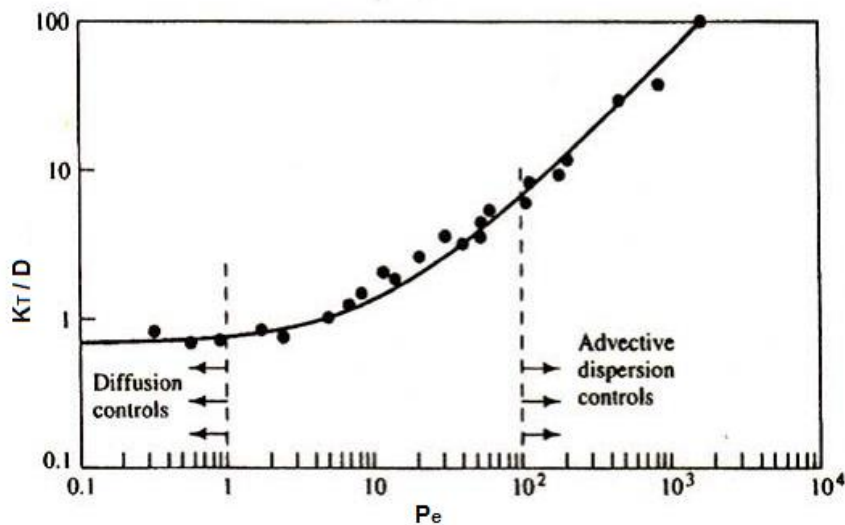
Figure 2.4 Transverse dispersion coefficient in porous media adapted from Perkins (1963)

14

2.5 Application of gas transport in porous medium in enhanced gas recovery (EGR)

The gas mixing process which takes place in porous media is a diffusion-like process due to velocity and concentration gradients created as a result of different species of gases present during the process. The dispersion coefficient represents the rate of mixing when two miscible fluids come in contact with each other during displacement at the displacement front of a flooding process. It is dependent on the direction of the dispersive flux with respect to the main convective flux. The smallest value of the dispersion coefficient occurs perpendicular to the main convective path/flux often called transverse dispersion, and the largest occurs for dispersion in the main convective flux called longitudinal dispersion which is in the same direction of flux direction. Transverse dispersion coefficient, K_t, is more difficult to obtain experimentally and as result, very few data is available in literature besides those of Perkins & Johnston (1963).

Newberg & Foh (1988) used a single parameter diffusion-type equation (Eq. 2.1) to correlate the numerical dispersivities with experimental results.

$$K_l \frac{\partial^2 C}{\partial x^2} - u \frac{\partial C}{\partial x} = \frac{\partial C}{\partial t} \qquad (2.9)$$

Where, C is the CO_2 concentration at location x at time t, K_l is the coefficient of longitudinal dispersion, and u is the interstitial velocity.

This model was used to evaluate the longitudinal dispersion coefficients and "scale of dispersion" (dispersion coefficient divided by velocity) which thus describes the dispersion occurring during the displacement process in EGR.

Invariably, (Eq. 2.9) may be written in dimensionless form as follows (Mamora & Seo, 2002);

$$\frac{1}{P_e} \frac{\partial^2 C}{\partial x_D^2} - \frac{\partial C}{\partial x_D} = \frac{\partial C}{\partial t_D} \qquad (2.10)$$

Where;

$P_e = \dfrac{uL}{K_l}$, Peclet number (ratio of convection to dispersion), L is length of core

$$t_D = \frac{tu}{L}, dimensionless\ time$$

$$x_D = \frac{x}{L}, dimensionless\ distance, and$$

$$u, interstitial\ velociy, = \frac{Q}{\pi r^2 \phi}\ , Q\ is\ superficial\ velocity, \phi\ is\ porosity$$

$K_l, Longitudinal\ dispersion$

Since the carbon dioxide injection inlet is at $x = 0$,

then initial condition: $C = 0\ at\ t_D = 0$,

boundary conditions: $C = 1\ at\ x_D = 0, C \to 0\ as\ x_D \to \infty$

The solution to (Eq. 2.10) maybe shown as follows:

$$C = \frac{1}{2}\left\{ erfc\left(\frac{x_D - t_D}{2\sqrt{t_D/P_e}}\right) + e^{P_e x_D} erfc\left(\frac{x_D + t_D}{2\sqrt{t_D/P_e}}\right)\right\} \tag{2.11}$$

CO_2 concentrations profiles from EGR core flooding experimentation can be compared against those based on analytic solutions from (Eq. 2.11) for several values of *Péclet* number, P_e from which the corresponding dispersion coefficient can be evaluated. The correct dispersion coefficient is that which gives the best agreement between experimental data and the analytical solution.

Hydrocarbon reservoirs are often used for seasonal natural gas storage (Benson et al., 2005; Zhang & Song, 2013). This presented the idea of using these depleted fields for anthropogenic CO_2 storage and disposal. Koide et al. (1993) investigated the underground storage of CO_2 in both natural gas reservoirs and also "useless" aquifers. They concluded that depleted natural gas reservoirs can be excellent storage sites for CO_2 and also deep saline aquifers have the ability to host larger volumes of CO_2 than depleted natural gas reservoirs. But their preliminary economical and technical survey on the storage system showed that the process may incur substantial cost, hence the need for an augmented kick back is needed to strike a balance between cost and storage. As earlier mentioned, one of the reasons for the choice of natural gas reservoirs as possible sequestration sites is that the recovered natural gas has the potential to offset the cost of the sequestration process. Therefore, further research on

the feasibility of CO_2 injection into a depleted reservoir to recover additional CH_4 is needed to make the process widely profitable.

Blok et al. (1997) inferred that, as at the time of their report, there was only one publication (Vanderburgt, Cantle, & Boutkan, 1992) in literature in which the injection of CO_2 into depleted gas reservoirs for EGR is described. This was a report prepared and presented by Shell. In that report, simulations were carried out to see the feasibility of displacing residual natural gas from a depleted gas reservoir using CO_2 miscible injection technique.

Consequently, more authors (Mamora & Seo, 2002; Nogueira & Mamora, 2005; Oldenburg, 2003; Oldenburg & Benson, 2002) have carried out simulation and experimental studies to investigate the feasibility of adopting EGR phenomenon for simultaneous CO_2 storage and recovery of CH_4. They concluded that in situ mixing of the injected CO_2 and the nascent CH_4 poses a challenge in the economic viability of the EGR process/technique.

More investigations on the parametric sensitivity analysis of factors that influence the mixing in situ were carried out by several authors (Al-Abri et al., 2009; Mehranfar & Ghazanfari, 2014; Sidiq et al., 2011a; Sim et al., 2008; Sim et al., 2009a, 2009b; Turta et al., 2007). They accentuated that the mechanisms of the displacement are responsible for pore scale mixing of the displacing and displaced gases in the porous medium. These mechanisms are molecular diffusion and mechanical dispersion as Coats et al. (1964); Perkins (1963) have rightly defined these mechanisms in fluid flow in porous media. The dominant mechanism has to be properly defined to better understand the mixing phenomenon and just then can this unfavourable phenomenon be minimised. Mixing in situ occurs due to either diffusion or dispersion depending on the flow conditions. In the case of EGR, the gas behaviour is what the technique banks on given that the gases are in their supercritical states during the process. So, the inevitable mixing is also a factor of the gas properties at the conditions relevant to EGR. This is discussed in the next section.

2.6 Supercritical CO_2 (SCO_2) and methane phase behaviour

CO_2 reaches its critical condition at a temperature of 31^oC (88^oF) and a pressure of 7.38 MPa (1,070 psia, 73.8 bara) as shown in a simulation carried out using PVTSim v8 in Figure 2.6 and CH_4 reaches its critical condition at a temperature of -82^oC (-117^oF) and at a pressure of 4.64 MPa (673 psia, 46.4 bara) as shown in Figure 2.5. This means that these gases will remain in supercritical state, at temperature and pressures typically encountered in the field, and in gaseous states regardless of operational conditions (Patel et al., 2016). However, at

low temperatures well below the critical temperature of CO_2, researchers focus on hydrates formation from a CH_4-CO_2 binary system (Sidiq & Amin, 2010). The density of the CO_2 at its supercritical state is close to that of a liquid whilst still maintaining a gas viscosity. This property helps create a density gradient which is responsible for the displacement of the in situ CH_4 to an extent. Furthermore, CO_2 sinks to the bottom of the reservoir and create an avenue also for not only the additional CH_4 recovery but also provide a site for the geological storage of CO_2.
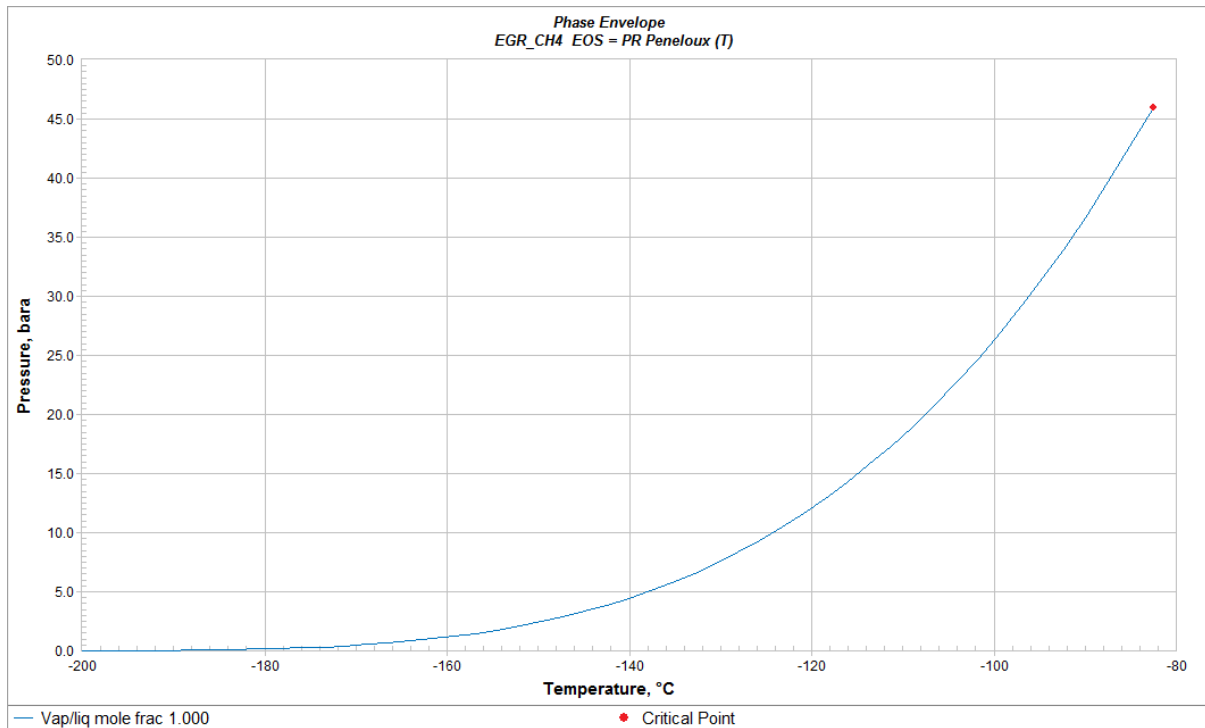
Figure 2.5 Phase envelope for CH_4 showing critical points (PVTsim v.8)
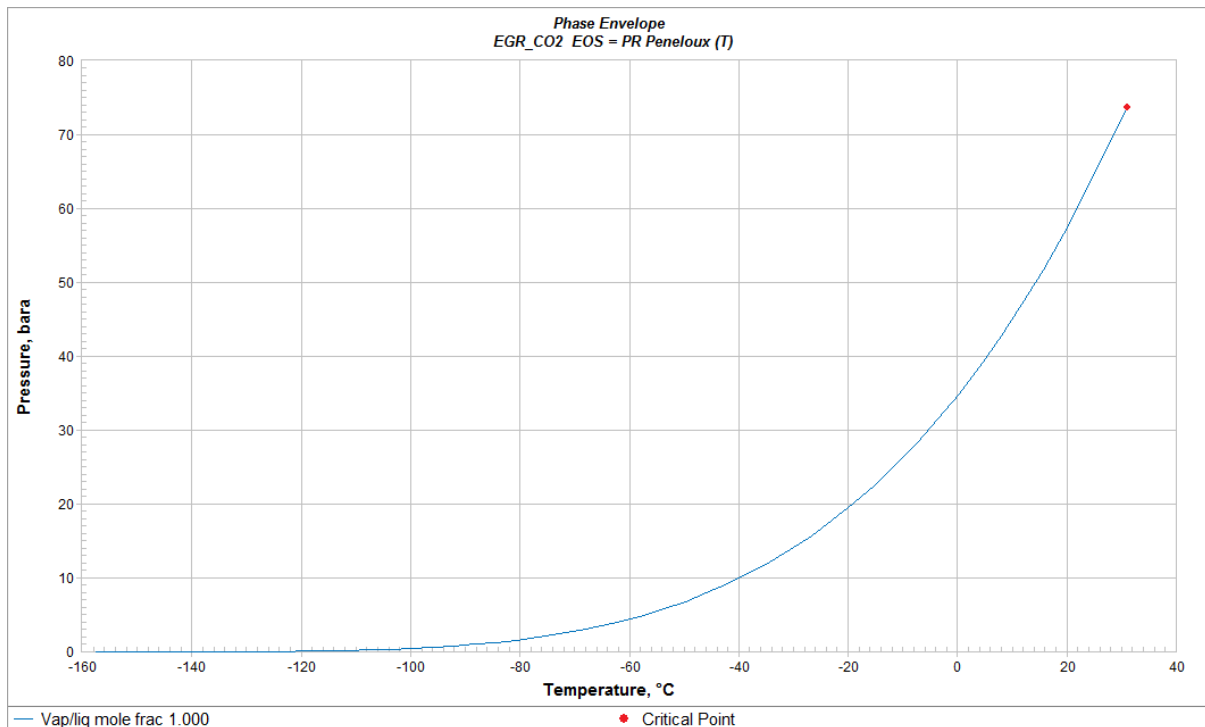
Figure 2.6 Phase envelope for CO_2 showing critical points (PVTsim v.8)

2.7 CO_2 Geological Storage

Possible CO_2 geological sequestration sites include: salt domes, unmineable coal seams, oil and gas depleted reservoirs, deep saline aquifers, and deep ocean floors as shown in the schematics (Figure 2.7). These possible sequestration sites must be assessed and evaluated for economic and environmental suitability. Cost effectiveness is one of the key elements to assess when embarking on a geological storage process. Environmental concerns precede with its growing global awareness. In this study, the option of depleted gas reservoir will be analysed as it shows semblance of balance of the environmental concerns and the safety with the cost effectiveness therein as aforementioned in the literature.
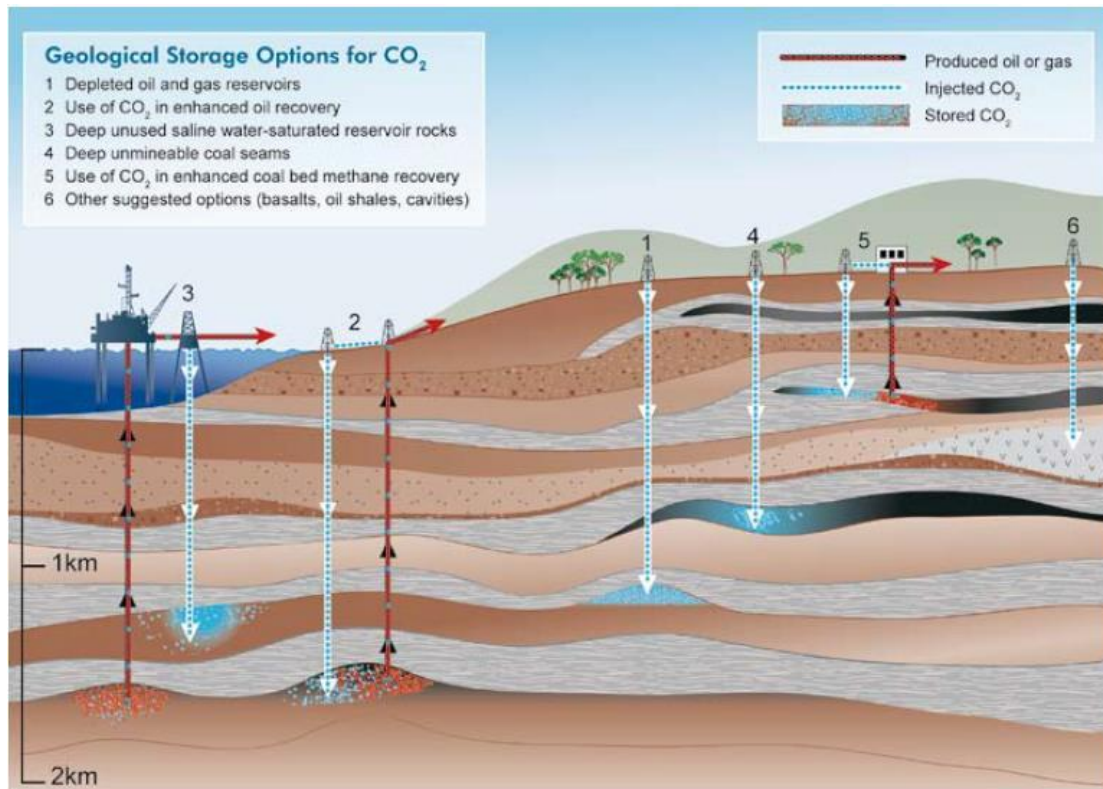
Figure 2.7 Options for storing CO_2 in deep underground geological formations (Benson et al., 2005)

2.7.1 CO_2 storage trapping mechanisms

The mechanisms for long-term immobilisation stabilisation of CO_2 are:

- Mineral trapping by geochemical fluid/mineral reactions and precipitation of minerals.
- Structural and stratigraphic trapping,
- Dissolution in the brine (convection induced dissolution enhancement), and
- Residual (capillary) trapping.

The overall contribution of each of these trapping mechanisms will depend on the geological make-up, injection strategy, site location, and migration pattern at later stages of stabilisation and will determine their efficiency in immobilising parts of the CO_2 trail. (CO2 Care, 2011).

These trapping mechanisms can be alluded to a time-wise process, in that the injection and invocation of the trapping mechanism can be time dependent as shown in Figure 2.8.
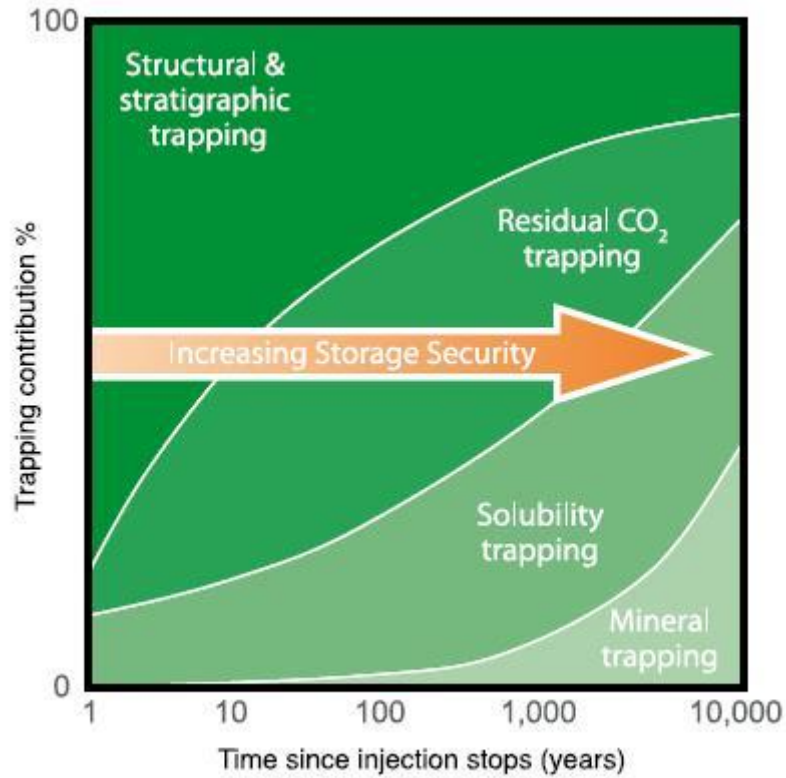
Figure 2.8 Contribution from the different trapping mechanisms (Benson et al., 2005)

The type of trapping mechanism concerned in this work is the solubility trapping. This mechanism will be exploited during EGR process by CO_2 injection. The idea is to dissolve the CO_2 in the formation brine and as a result retarding the breakthrough time of the injected CO_2 thereby enhancing recovery efficiency of the process and also increase the storage capacity of the gas reservoirs.

2.7.2 CO_2 solubility/dissolution trapping mechanism in natural gas reservoirs

In actual storage projects, large volumes of CO_2 are injected deep underground. The largest injection time of CO_2 storage is the Sleipner Project in Norway which started in 1996, where 1 Mt CO_2 per annum is injected into the Utsira sandstone formation in the Norwegian part of the North Sea (Iglauer, 2011).

When CO_2 dissolves in formation water (brine), a process universally called solubility trapping follows. CO_2 will migrate upwards after its injection to the interface between reservoir and cap rock and then spreads laterally under caprock as an independent phase. This CO_2 then contacts the ambient formation brine where mass transfer occurs with CO_2 dissolving in the formation brine until an equilibrium is attained (Zhang & Song, 2013). At this interface, the CO_2 dissolves in water by molecular diffusion/convection. The CO_2 will

then saturate the formation brine and a concentration gradient will be established spatially. The dissolution of CO_2 in brine will slightly increase the density of the saturated brine by about 1% compared with the original brine as reported by Zhang et al (2016). The heavier brine on the upper part of the reservoir will flow downwards by convection due to gravity segregation in a cyclic manner by pushing the lower lighter brine upwards. This process enhances the mixing of the brine and CO_2 gas by diffusion that invariably promotes more CO_2 dissolution.

The principal advantage of solubility trapping is that once CO_2 is dissolved, it does not exist as a separate phase any longer, thus eliminating the buoyant forces that tends drive it upwards. The CO_2 solubility in formation water decreases as salinity and temperature increase (Zhang et al., 2016).

Dissolution of CO_2 in formation water can be denoted by the chemical reaction:
$$CO_2 \text{ (g)} + H_2O \leftrightarrow H_2CO_3 \leftrightarrow HCO_3^- + H^+ \leftrightarrow CO_3^{2-} + 2H^+ \tag{2.12}$$
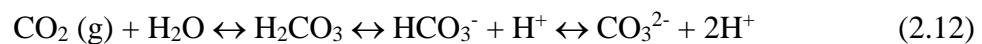
Iglauer (2011) concluded that dissolution trapping is a potential solution for large anthropogenic CO_2 storage.

By virtue of the presence of the cap rock in the gas reservoir, the structural trapping mechanism is the primary trapping mechanism for EGR. The presence of the formation water also paves a way for solubility trapping which will increase the CO_2 storage capacity of the gas reservoirs. The storage capacity limitation of oil and gas reservoirs as potential storage sites undermines the potential of these reservoirs when it comes to CO_2 storage compared to deep saline aquifers as noted by (Allen et. al., 2017; Bennaceur, 2013; Riis & Halland, 2014; Sanguinito et. al., 2018; Gupta et. al., 2017). This limitation was mostly based on the size of the deep saline aquifers which of course is substantially larger than oil and gas reservoirs. But oil and gas reservoirs provide additional recovery of the hydrocarbon resource thereby increasing the economic viability/incentives derivable when used as sites for CO_2 storage as aforementioned in Section 1.1 which is one of the reasons for the choice of natural gas reservoirs as potential sequestration sites. This research will showcase the feasibility of using natural gas reservoirs as potential sequestration sites by demonstrating solubility trapping in addition to structural and capillary trapping mechanisms. Solubility trapping in the formation water (brine) increases the storage capacity of the natural gas reservoir by accommodating more injected CO_2 through its dissolution in the brine.

2.8   CO₂ Solubility in Brine and interfacial tension IFT

The relationships between these two parameters will be presented here. First, the parameters will be discussed and explicated individually and then their relation will be showcased.

2.8.1   Interfacial Tension (IFT) measurement between CO₂ and Brine

A thin layer between two immiscible fluids (in this case CO_2 and brine) when they come in contact with each other is termed the interface between these two fluids. This is as a result of the imbalance between the interfacial interactive forces exhibited by the two fluids in contact. Interfacial tension is defined as the force exerted at the interface of the fluids in contact per unit length. The unit is dyne/cm or mN/m (Werth et. al., 2013).

The most common method of the IFT measurements at high working conditions of temperature and pressures is the pendant drop method. This is based on the idea of generating a droplet of a fluid (usually denser phase) in a lighter phase at a condition where the phases are in equilibrium. The droplet profile can be employed to evaluate the interfacial tension between the phases. An exemplar is shown in Figure 2.9 where the dimensions of the droplet depicted are used in a mathematical equation to measure the IFT based on the difference in density of the phases under investigation.
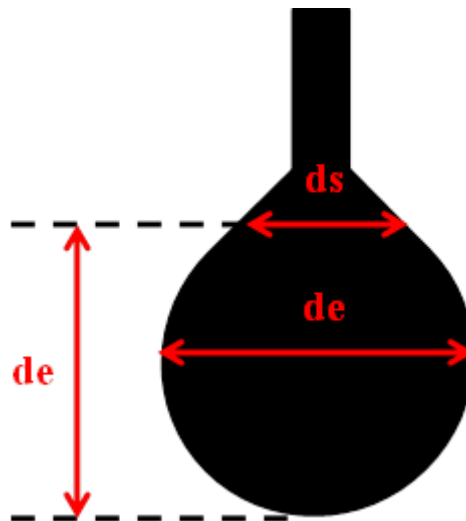
Figure 2.9 Dimensions of droplet used for IFT measurement

The equation for calculating the IFT is shown below in Eq. 2.17

$$\gamma = \frac{\Delta \rho g d_e^2}{H} \qquad\qquad (2.13)$$

Where γ is the interfacial tension in mN/m, g is acceleration parameter in cm/s^2, $\Delta\rho$ is the density different between the two phases (liquid and gas), *de* is the diameter of the droplet at the equator in cm, *ds* is the diameter of the droplet from the tip of the droplet to the equivalent length of *de*, *H* is the droplet shape factor which is a function of the ratio of *ds* and *de* as shown in in Eq. (2.18)

$$H = f\left(\frac{d_s}{d_e}\right) \qquad\qquad (2.14)$$

Rising bubble method is similar to pendant drop method which is a better for gas-liquid IFT measurement (Kashefi et. al, 2016) with the only difference being the configuration of injecting the lighter phase. In the pendant drop method (depicted in Figure 2.9) the injection of the denser phase is from the top of the measurement cell but in the rising bubble, as the name implies, the lighter phase is injected into the denser phase from the bottom where the gas bubble is aided by the buoyancy within the denser phase to form.

The importance of IFT measurement between CO_2 and brine, in this study, is to relate the parameter with the solubility of CO_2 in brine.

2.8.2 Relationship between CO_2 solubility and interfacial tension in brine

Abundant literature data for CO_2 solubility exist which shows the behaviour of CO_2 at sub and supercritical states in the presence of brines at different conditions of temperatures and pressures (Ahmadi & Chapoy, 2018; Chen et. al., 2018; Liu et. al., 2018; Jin et al., 2018; Benson et. al., 2013; Pooladi-Darvish et al., 2008; Rashid et. al., 2017; Shabani & Vilcáez, 2017; Sun et al., 2016; Yan et. al., 2011; Yuan et. al., 2017). These investigations were carried out using both experimental and numerical modelling approaches.

Solubility is a property of the gas to dissolve in a brine to form an aqueous and homogeneous solution. This property of CO_2 is desirable in miscible flooding for EOR applications and most recently, EGR and deep saline aquifer storage of CO_2 gas. Its ability to dissolve and reduce in volume is ideal for CO_2 sequestration in formation water during EGR. Therefore, importance is given to assessing the CO_2 solubility during EGR to evaluate the storage capacity of the natural reservoir and also the effect of this solubility in terms of CH_4 recovery.

However, there exists a strong relationship in IFT between two the water and CO_2 systems and their solubility (Ayirala & Rao, 2006; Bennion & Bachu, 2008). A number of literatures

(Chalbaud et al., 2009; Zhang et. al., 2018a; Partovi et al., 2017; Tohidi et. al., 2017; Martínez et. al., 2018) have shown the relationship between IFT and the solubility of CO_2 in different brines which can be used to analyse the dissolution of the gas in an external phase.

 Bennion & Bachu (2008) used exhaustive data from literature to come up with a correlation between the solubility of CO_2 in different brines and also the CO_2/brine IFT. The relationship can generally be shown graphically in Figure 2.10 below.
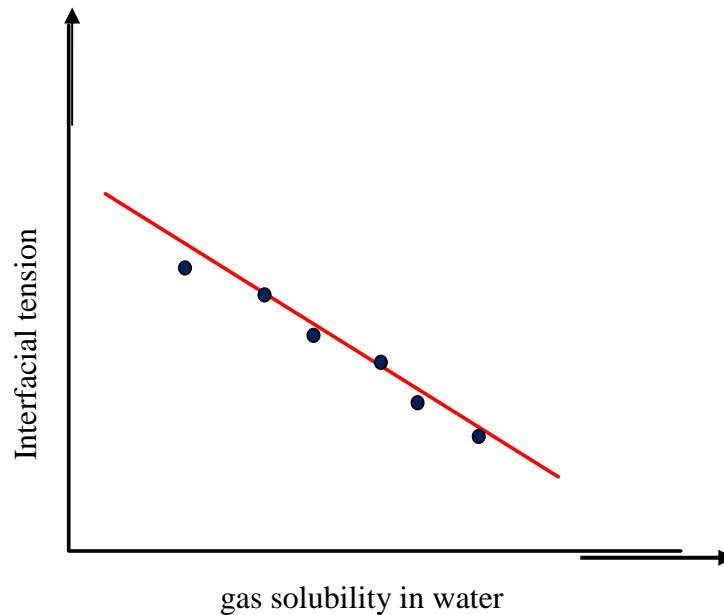
Figure 2.10 Relationship between IFT and Gas solubility in water

From the literatures examined by Bennion & Bachu (2008), they inferred that the solubility increases:

- ✓ with decrease in brine salinity
- ✓ with temperature increase
- ✓ and with pressure decrease in the brine

This relationship shows that solubility is strongly dependent on all these primary variables and from IFT data also obtained in literature, they pointed the same dependence of the IFT on these same variables of temperature, pressure, and salinity. They came up with a correlation between the variables for a temperature range of 41 -120°C and pressures between 2-27 MPa and brine salinity of fresh water to about 350,000 ppm TDS). This is shown in Eq. 2.19 below:

$$\gamma = -0.0004\,(S)^4 + 0.0241(S)^3 - 0.3836(s)^2 - 0.7305(S) + 73.264 \quad (2.15)$$

Where γ is the IFT in mN/m and S is the CO_2 solubility in aqueous phase in m^3 CO_2 per m^3 aqueous solution.

Thus, an experimental approach to evaluating the solubility of CO_2 in brine can be achieved through its relationship between interfacial tension measurements (IFT) and will be adopted in this study. This relationship between CO_2 and brine IFT is based on the mass transfer between the gas phase and the brine phase.

2.9   Gas reservoirs

There are two classes of gas reservoirs based on drive mechanisms: depletion gas reservoirs and water drive gas reservoirs.

Depletion gas reservoirs, often referred to as volumetric gas reservoirs, are those gas reservoirs whose pressure declines due to production and there is an insignificant water influx from the adjoining aquifer into the gas reservoir. Thus, the reservoir volume occupied by hydrocarbons will not decrease during depletion (Dake, 1978). This reserve type can be estimated using the volumetric method to establish the Original gas in Place (OGIP). The gas formation volume factor is usually used to relate the volume of gas at reservoir conditions to the volume at standard conditions. It is defined as the ratio of the actual volume occupied by the amount of gas at a given temperature and pressure (usually reservoir conditions) to the volume occupied by the same amount of gas at standard temperature and pressures (Ahmed, 2010). It is expressed mathematically as:

$$B_g = \frac{V_{p,T}}{V_{sc}}$$ (2.16)

Where B_g is gas formation volume factor, v/v, $V_{p,T}$ is the gas volume at pressure p and temperature T, v, V_{sc} is the volume of the gas at standard conditions.

This can be expressed in terms of real gas equation of state and will be simplified to present;

$$B_g = \frac{p_{sc}}{T_{sc}} \frac{zT}{p}$$ (2.17)

26

Where z is gas compressibility factor, p_{sc} and T_{sc} are pressure and temperature at standard conditions; P and T are pressure and temperatures at desired conditions. Taking p_{sc} and T_{sc} to be 14.7 psia and 18°C (291.15K), equation 2.18 becomes;

$$B_g = \frac{zT}{20p} \tag{2.138}$$

This property is important in the volumetric estimation of the OGIP (G) and is related as follows:

$$G = \frac{V_b \phi (1 - S_w)}{B_g} \tag{2.19}$$

V_b is the bulk volume of the reservoir ft^3, ϕ is reservoir porosity, S_w is formation water saturation, and B_g is gas formation volume factor, ft^3/scf.

When the reduction in reservoir pressure leads to the expansion of the adjacent aquifer, there will be a consequent influx of water into the gas reservoir. Such reservoirs are termed water drive reservoirs or reservoirs under active water drive. For depletion gas reservoirs, the pore volume containing gas remains unchanged over the exploitation duration. Gas recovery is usually accompanied by a decline in static reservoir pressure, and the ultimate recovery depends on the pressure of abandonment. Recovery could be within the range of 70-85% G which is very high, with little or no water production (Turta et al., 2007).

Conversely, for many water drive reservoirs, the reservoir pressure may still be high at abandonment. For these reservoirs, as reservoir pressure drops below a certain point, water encroaches into the reservoir. The water influx in many circumstances is almost equal to gas production at reservoir conditions, which leads to pressure stabilisation and in this case the abandonment pressure is the stabilised pressure. The water drive can be a bottom water drive or an edge water drive. In both cases, the water influx into production wells is usually in the lower parts of the pay zone. In addition, the ultimate gas recovery is often low (50%-60% OGIP) and volumetric sweep efficiency is low due to both relatively low sweep and the trapped gas in the water-invaded zone. A very high value of the abandonment pressure

(stabilised pressure) leads to trapping of a large volume of gas in the water invaded zone, resulting, at abandonment, a lower recovery factor.

From the brief insight into these classes of gas reservoirs, the water drive reservoir will have lower hydrocarbon pore volume (HCPV) for storage due to the influx of water into the reservoir which occupies a significant pore volume from sequestration point of view. However, this can be exploited from the multifaceted point of EGR in that the low ultimate recovery (in the range of 50%-60%) of the water drive reservoirs will provide economic incentives for EGR as more gas will be recovered and, exploiting the solubility trapping mechanism for CO_2 storage, more CO_2 can be sequestered.

2.10 CO_2-CH_4 miscible core flooding experiments

In recent times, several core flooding experiments have been reported in literature (Al-Abri et. al., 2009; Honari et al., 2015; Honari, Hughes et. al., 2013; Honari et al., 2016; Hughes et al., 2012; Khan et al., 2013; Oldenburg & Benson, 2002; Patel et. al., 2016; Shtepani, 2006; H. Sidiq, Amin et. al., 2011a; Sim et al., 2008; Turta et. al., 2009a; 2007; Yi Zhang et al., 2014) using CO_2 at supercritical and subcritical conditions to evaluate the efficiency of CO_2 injection for enhance gas recovery in sand packs and consolidated porous media. Some also have investigated the concept of using flue gas (Marmora et. al. 2005) of different compositions as the injection fluid during enhanced gas recovery in place of CO_2 alone. However, there is limited investigation on some important factors that could potentially affect the efficiency of the displacement process. Lack of data available that will quantify the effects of these factors on the displacement process will present a challenge in accurately defining the displacement efficiency of CO_2 injection as a method of enhanced gas recovery and sequestration. The importance of investigating the factors that affect the displacement process and recovery efficiency is that it will provide good and accurate accounts of those influencing factors as input variables in evaluating field applications of laboratory findings and the feasibility of projects through reservoir simulations. Some of these factors that received no attention are connate water salinity and its saturation and how they affect dispersion during EGR by CO_2 injection. Connate water saturation, in particular, has received only a limited recognition during core flood experimentation for enhanced gas recovery. It is usually attributed to reduction of pore volume available for CO_2 storage which will inherently lead to early CO_2 breakthrough during the displacement process as highlighted in the work of Nogueira & Mamora (2005) and not inherent effects on the overall recovery efficiency. Consequently, salinity of the connate water has not been investigated as a factor that could

affect the displacement efficiency in enhanced gas recovery nor has its variation in the connate water received a wide spread recognition. Literatures only include salinity as a factor when it comes to CO_2 injectivity investigations during geological sequestration/storage in deep saline aquifers where salting-out and precipitation are usually eminent. Highlighting these effects has become paramount when an adequate evaluation of all potential factors that affect recovery and displacement efficiencies during CO_2 injection for enhanced gas recovery purposes.

2.10.1 Effect of connate water saturation on CO_2 displacement efficiency and dispersion

Limited numbers of technical literatures are available on the effects of the inclusion of connate water saturation and salinity in the porous medium on CO_2-CH_4 system displacements experiments. Sidiq & Amin (2009) were the only authors before Honari et al. (2016) to consider the inclusion of connate water saturation when determining the dispersion coefficient of CO_2 in CH_4 in a carbon dioxide-methane system only. Sidiq & Amin (2009) determined the dispersion coefficient using a new model developed in their work. They, however, did not present any comparative analysis of the dispersion coefficient obtained from their experiments between saturated core samples and core samples that are without any form of saturation (dry) to establish the impact of connate water saturation on the displacement process.

Numerous literatures, as reported by Honari et al. (2016), are available which considered the dispersion phenomenon in a multicomponent systems comprising of different gases (N_2, O_2, H_2O) in the presence of immobile water in the porous medium. In this study, emphasis was made on the experimental works carried out by researchers to investigate this phenomenon in CO_2-CH_4 systems only.

Although not solely in a CO_2-CH_4 system, Turta et al. (2007) carried out a series of displacement tests comprising of gases on Berea cores at a temperature of 70°C and a pressure of 6.2 MPa using N_2 and CO_2 as injection fluids to displace CH_4. The tests were conducted both in the presence of connate water saturation and also without connate water saturation to evaluate the effects of connate water on the recovery efficiency of EGR. The tests on test cores revealed that for pure N_2 and pure CO_2, used as the displacing fluids, the recovery efficiency was comparably close. Furthermore, in the case where a mixture of CO_2 and N_2 was used to displace the CH_4, it was noted that there was an apparent delay in CO_2 breakthrough during the displacement test, which was associated with a period when only a

mixture of CH_4 and N_2 was produced. This can be credited to the solubility of CO_2 in connate water which is extensively higher than that of N_2. This conversely leads to a higher CH_4 recovery due to a longer resident period, given the fact that a 20% N_2 contamination in marketable CH_4 tolerable in the produced stream, as opposed to only 2% contamination level for the case of CO_2 in sales gas. They concluded that when using CO_2 as a displacing fluid, it was found that the recovery was higher in the presence of irreducible water saturation than in its absence invariably due to the dissolution of CO_2 in the formation brine.

In addition, the first measurement of dispersion as function of water saturation for supercritical gases in a CH_4-CO_2 system was carried out by Honari et al. (2016). They systematically measured fluid dispersion in various rock cores of different types and compositions, for both dry and at connate water saturation, at reservoir conditions. They found out that irreducible water increases dispersivity by a factor of about 7.3. The irreducible water present in the pore matrix of the core samples occupied smaller pores thereby creating narrower pores and with more tortuous flow paths giving rise to a higher degree of dispersion/mixing between the injected CO_2 and the nascent CH_4. Sim et al. (2009) conversely, inferred that the presence of the connate water saturation in the reservoir pore spaces tends to minimise its heterogeneity and as such minimises excessive mixing as shown in their work where they used a sand pack with various degrees of permeability distributions and also a N_2, CH_4, CO_2 multicomponent system.

These works, however limited, have touched on the impacts of connate water saturation on the displacement efficiency in enhanced gas recovery by CO_2 injection. They have attributed the presence of connate water to the recovery efficiency therein. They, conversely, did not account for effect of the salinity/concentration variance of the connate water on the recovery efficiency and or dispersion. The pulse injection technique employed in their work (Honari et al., 2015, 2013, 2016) to minimise the density and concentration gradient provide longer residence time for the displacing fluid during the displacement process as opposed to constant rate injection technique.

2.10.2 Effects of brine salinity on CO_2 and CH_4 solubility at reservoir conditions

Numerous literatures are available which investigated the interplay between aqueous solutions of brine of different ionic strengths and pure water and their effects on CO_2 and CH_4 solubility. It is well established, that the presence of salts in the aqueous phase raises the interfacial tension (IFT) of a water-gas system as in the case of water under the same

temperature and pressure conditions. Conversely, from the works of Kashefi et. al. (2016) and Pereira et al. (2016), it is pertinent that at the same temperature, pressure, and brine salinity, CH_4 exhibits higher IFT than CO_2. This shows that more CO_2 will dissolve in brine compared to CH_4 at those conditions. In an enhanced gas recovery perspective, during the displacement process in the presence of brine saturation, there will be a significant yield of recovered natural gas and a delay in CO_2 breakthrough due to the differences in gas solubility in brine. This can be seen in the work of Sim et al. (2009) who conducted a series of gas-gas displacement tests to ascertain the effects of temperature, pressure, and injection velocity on displacement process at low pressures between 0.7-3.5 MPa and room temperature in the presence of connate water. They conducted methane displacement with pure gases, CO_2 and N_2, and found out that CO_2 provided better breakthrough than N_2 in terms of CH_4 production and went on to attribute this trend to the higher solubility of CO_2 in water (connate) compared to CH_4 as discussed earlier. However, the effect of salinity variation on the dissolution of CO_2 is yet another important investigation as it may also affect the efficiency of gas-gas displacement during enhanced gas recovery process. Rochelle & Moore (2002) conducted an experimental study to ascertain the effect of brine salinity on the dissolution of CO_2, where a range of solubility measurements were made using both synthetic Utsira formation water and distilled de-ionised water at 37°C and 10 MPa (100 bar) simulating in-situ conditions. Measured CO_2 solubility values in distilled de-ionised water were in the order of 5.1 g of CO_2 per 100 g of water. However, measured CO_2 solubility values in synthetic Utsira formation water were lower than those obtained for distilled de-ionised water at 37°C and 10 MPa. Sun et al. (2016) also conducted similar experiment to measure the solubility of CO_2 in brine in which they concluded that the solubility of CO_2 decreases with increase in brine salinity.

These experiments to determine the effects of brine salinity precluded another factor that may affect the dissolution of the gases in brine. The injection rate will play a significant role in the solubility of the gas in brine as in the case of enhanced gas recovery by CO_2 injection.

2.10.3 Effects of impurities on dispersion coefficient

Mamora & Seo (2002) conducted core flooding experiments on carbonate core samples at pressures up to 3000 psig with temperatures up to 140°F and at a constant injection rate of 0.25 ml/min. They conclude that CO_2 dispersion coefficient in a range of 0.01-0.12 cm^2/min in methane (CH_4) was low, implying less dispersion during the process hence, less

contamination of the recovered CH_4 and late breakthrough of the injected CO_2. Techniques to keep the values of the dispersion coefficient low require a thorough understanding of the factors that affect the displacement process.

Nogueira & Mamora (2005) investigated the effects of flue gas impurities on the injection and storage of CO_2 by measuring the dispersion coefficient and recovery efficiency in a carbonate core sample. Using different flue gas types (dehydrated flue gas 13.574 mole% CO_2 and a treated flue gas with 99.433 mole% CO_2) at 1,500 psig and 70°C injected into an Austin Chalk Core. The experimental value of dispersion coefficient increased with respect to increasing flue gas concentration with the dehydrated flue gas (~13% CO_2) exhibiting the largest dispersion coefficient. It can be concluded that since the flue gas was dehydrated, its density will be close to the density of the in-situ CH_4. Therefore, the flue gas will disperse more rapidly into the in-situ methane and excessive mixing will ensue. In addition, the CH_4 recovery showed that the treated flue gas (~99% CO_2) had the highest recovery compared to the dehydrated one.

2.10.4 Effects of permeability distribution on recovery efficiency

Using two parallel non-communicating sand-packs of differential permeability, S. Sim et al. (2009) conducted an experiment in a heterogeneous and homogeneous system to determine the effect of permeability distribution using flue gas as the injecting fluid. The recovery rate of CH_4 was found to be more efficient for the homogeneous system than the heterogeneous system, moreover, the highest output was from higher permeability sand-packs. Injection of water into the higher permeability sand-pack of the heterogeneous porous medium was found to improve methane recovery by mitigating the degree of heterogeneity. But this effectiveness was reduced when the water injection stopped. Gravity segregation was found to be significant between the displacing and displaced gas at 3.5 MPa and in their physical model, it was observed that the gravity segregation was however unfavourable to reservoirs with that are fining upwards but favourable when it is coarsening upwards. However, the effect of different variation of the volumes of nitrogen in the flue gas was not investigated. As their findings suggest that the gravity segregation due to differences in densities mitigates the effect of heterogeneity, the extent of this mitigation could be further investigated.

Many researchers have attributed excessive mixing in-situ with heterogeneity as reported by Honari et al. (2015). Honari et al. (2013) measured the supercritical dispersion coefficient data in sandstone cores, accounting for erroneous gravitational and entry exit effects contributions as levied in their earlier work (Hughes et. al., 2012) using the measured value

of dispersivity as the characteristic length scale of mixing. They found out that heterogeneity plays a very important role in the mixing of CH_4 and CO_2 gases as they have higher dispersivities than an earlier experiment they conducted using homogeneous samples. Kalra & Wu (2014) deduced also that recovery factors are affected by reservoir heterogeneity and anisotropy. Highly heterogeneous reservoirs will lead to lower natural gas recovery and also reduce the CO_2 pore volume injected due to excessive mixing in the formation. The minimum formation depth of 4000 ft, according to them, is most ideal for enhanced gas recovery and CO_2 storage.

2.10.5 Effects of a combination of intrinsic properties on dispersion coefficient

Pressure, injection speed, and gas composition play crucial roles in the displacement process in EGR in that they affect the dispersion coefficient and invariably the mixing between the injected fluid and the displaced fluid. An insight into their behaviour at conditions relevant to EGR is of utmost importance.

Sidiq & Amin (2009) came up with a straightforward method of calculating the dispersion coefficient of CO_2 displacing CH_4 in a linear porous reservoir. The dispersivity of CO_2 was found to be a function of injection pressure, injection rate, and in-situ gas composition. They found it to vary with injection rate and changes in purity of the displaced phase while varying inversely with injection pressure. This led them to believe that there exists an interfacial tension (IFT) between CH_4 and CO_2 during EGR displacement at higher pressures as researchers Tensiometer et al. (2006) have shown that there is evidence of interfacial tension between miscible fluids but they disclosed that their findings may not apply to all miscible systems. Amin et al. (2010) went further to conduct the first ever gas-gas interfacial tension measurement experiment. They observed an immiscible interface between the two gases (CO_2 & CH_4) at a temperature range of $95 - 160^oC$ and a pressure range of $6.9 - 41.37MPa$. They employed a modified pendant drop method of the experiment within the range of conditions analogous to reservoir conditions. They noted that IFT decreases linearly with both temperature and pressure. However, at 10MPa, it was noted to increase very sharply and was independent of temperature. It was found that the IFT of CO_2 and CH_4 was lower at higher temperatures. Hughes et al. (2012) conversely, attributed the findings of Amin et. al., (2010) to the existence of transient stresses in dynamic interfaces between miscible fluids induced by density gradients as proposed by Korteweg (1901) and reported by Morra & Yuen (2008). They further explained that thermodynamically stable interface can only exist between wholly immiscible fluids and CO_2 and CH_4 are fully miscible at EGR conditions and

ramifications. Hughes et al. (2012) reviewed existing literatures on EGR by CO_2 injection and reported new measurements of longitudinal dispersion of CO_2 and CH_4 at various conditions. They conducted core flooding experiments on sandstone cores of different permeability in different orientations to ascertain the effect of gravity on EGR and deduced that high permeability cores oriented horizontally showed significant gravitational effects during low velocity core flooding.
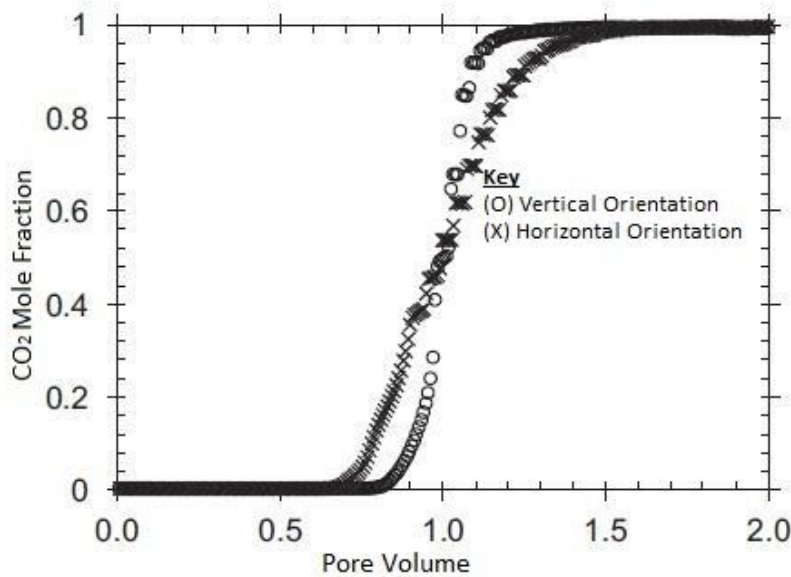
Figure 2.11 Displacement of CH_4 by CO_2 in vertical and horizontal orientations (Hughes et al., 2012)

As seen from (Figure 2.11) the vertical orientated profile is steeper than the horizontal orientation, meaning that the mixing zone length is shorter in the vertical than the horizontal profiles. They were able to reconcile the experimental data with literature data with less scatter in the dispersivity profile of supercritical fluids by catering for the entry/exit effects during the experiments. However, in terms of EGR by sequestration, horizontal displacement will give a better surface area for a better sweep efficiency of the process.

Al-Abri et al. (2012) investigated the mobility ratio, sweep efficiency, and relative permeability of CO_2 and CH_4 injection to enhance CH_4 and gas condensate recovery using core flooding experimentation on sandstone core samples at a temperature of 95^oC and a pressure of 5900 psia. They found out that CO_2 injection to enhance gas recovery is optimum when the in-situ gas composition has less CO_2 contamination. Also, injection of pure CO_2 yields a higher CH_4 recovery compared to a mixture of injection fluids (in this case CH_4 and

CO_2) at the same operating condition. The relative permeability of the fluids was calculated using the JBN method and it was deduced that it improved following the supercritical CO_2 injection as it provides better mobility conditions and a more stable displacement front. This is in line with the works of Zhang et al. (2014) and Liu et al. (2015) who carried out a laboratory displacement processes using sand packs samples of glass beads. They proved the existence of the mixing zone but no interface was observed. They deduced that dispersion coefficient increased exponentially with temperature in their temperature ranges and attributed this phenomenon to molecular kinetic theory. Dispersion coefficient increases with flowrate of CO_2 and decreases with pressure. Following the relative permeabilities of CH_4 and CO_2, Sidiq et al. (2011b) investigated the impact of different parameters on SCO_2-CH_4 relative permeability in reservoir porous media. The relative permeability of the injected phase was identified to vary proportionally with impurity of the displaced phase while inversely varying with injection speed, pressure, and heterogeneity of the porous media. The impact of injection rate and in-situ gas composition on multiphase gas flow is obvious compared to the influence of other parameters that affect gas-gas relative permeability. This accentuates the importance of injection rate during a gas flooding process. Too high a speed may bring about channelling and early breakthrough and conversely, too low a speed will eventually increase the retention time of the injected fluid to mix thoroughly with the in-situ fluid thereby leading to contamination and an early breakthrough of the injected phase. Hence, the injection rate, pressure, and gas compositions affect the dispersion of the injecting fluid, thus affecting the recovery efficiency.

Other researchers (Agarwal, & Zhang, 2016; Holdich, 2004; Khan et al., 2013; Narinesingh & Alexander, 2014, 2016; Oldenburg & Benson, 2002; Pooladi-Darvish et al., 2008) and many more used simulation to study the effects of different parameters on EGR process and to also optimise the flooding efficiency.

Accounting for the salinity of the connate water saturation is vital as different reservoirs have different salinities. It will also help to establish the solubility trapping mechanism during CO_2 geological storage. So, this can invariably be exploited; the density increment of the super critical CO_2 by injecting a compatible slug of brine in the stream at variable injection rates to humidify the stream with the aim of getting a better flooding efficiency and CH_4 recovery while simultaneously dissolving the injected CO_2 in the formation brine thereby exploiting the solubility trapping mechanism.

CHAPTER 3

3 MATERIALS AND METHODS

3.1 Overview

This chapter starts with a detailed analysis of the experimental setup and the order of design steps which were made to concisely depict the performance of the experimental apparatus. Then the materials used in all experiments and the methods for preparing them will be discussed therein.

3.2 Experimental Methodology

The flow chart below (Figure 3.1), presents the structure and summary of the sequence of the experimental procedure. The experimental method is divided into three phases. Each phase entails specific objectives as will be seen. Detailed description of the materials used and apparatus description in each phase will be presented in chapter 4 of which will provide in-depth depiction of the overall experiment.

After the repeatability and reproducibility tests, the main experiments were carried out using the experimental design blueprints. All core flooding experiments and IFT measurements were carried out at 1300 psig and 50°C. The choice of these conditions was on the basis of the average gas reservoir depth of 6000 ft using geothermal and pressure gradients (Jones & Lineweaver, 2010; Kargarpour, 2017) of 1.74°F/100ft and 0.45 psi/ft respectively. The summary of the methodology is discussed in the next section.
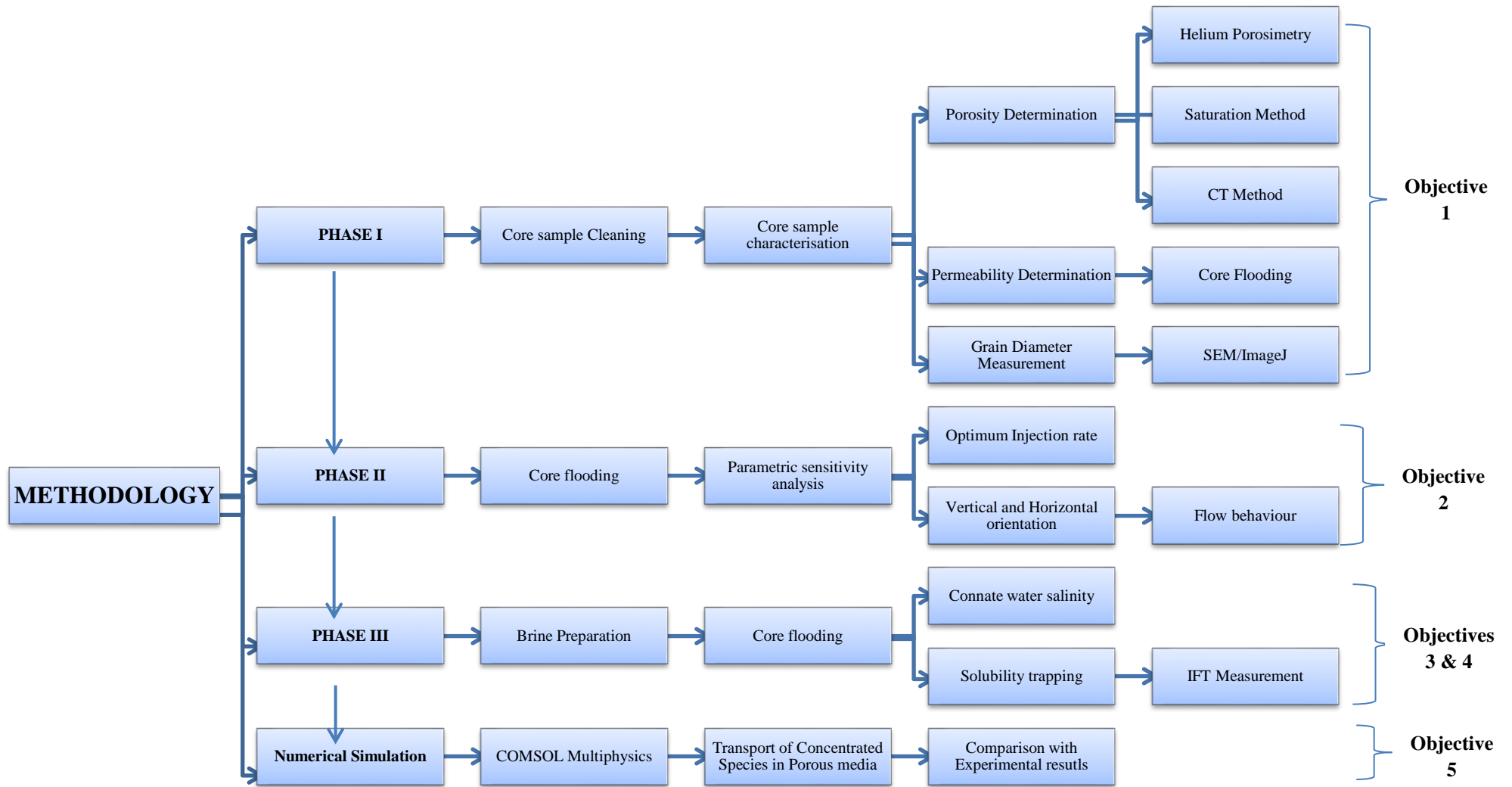
Figure 3.1 Experimental methodology design

3.2.1 Summary of Methodology

1. **Phase I**: **Core sample characterisation**: The first phase of the research is core sample acquisition which were obtained from Kocurek Industries INC. Soxhlet Extraction was used to clean the core samples to remove any potential contaminant within the pore spaces. The core samples characterisation – permeability, porosity - was carried out using various specialised characterisation techniques comprising of Gas Porosimetry, X-Ray CT, and core flooding to obtain actual petrophysical properties of the cores. SEM, in conjunction with an image processing software, was used to measure the mean grain diameter of the various types of sandstone samples. This forms the first objective of this research which provides the properties required for the next phase of the research involving setting up a core flooding benchmark for subsequent investigations.

2. **Phase II**: **Core flooding: injection rate and orientation variation**: This phase provided preliminary results and set up of the research and parametric sensitivity analyses using the properties obtained in Phase I. Core flooding was carried out to investigate the effects of the variation CO_2 injection rates and orientation to assess the effects of gravity on the displacement process during EGR. It also provided insight into the behaviour of the flooding process. Several dry ($S_w = 0$) runs of the simulated EGR core flooding experiments were carried out to establish the control experiments or benchmarks to determine the optimum flow conditions for the salinity sensitivity investigations in Phase III.

3. **Phase III**: **Parametric sensitivity analysis:** Methodical brine saturation of the core samples were carried out to saturate the samples with brine ($S_w = 10\%$) of different brine salinities to simulate connate water. Using the optimum displacement conditions evaluated in Phase II, the impact of the connate water salinity through core flooding process on the dispersion of CO_2 in CH_4 in different brine salinities was determined. Furthermore, the feasibility of the solubility trapping mechanism during EGR was investigated to explore the potential of subverting the limitations of natural gas reservoirs as CO_2 sequestration sites. And finally, a numerical simulation was used to compare the experimental results obtained in this research work with the simulation using COMSOL Multiphysics® software package and also explain the trends observed in the experiments.

3.3 Materials

In this study, sandstone cores samples (Figure 3.2) were used to conduct the core flooding experimentation whose dimensions are shown in Table 3.1. Details are discussed in Chapter 4.
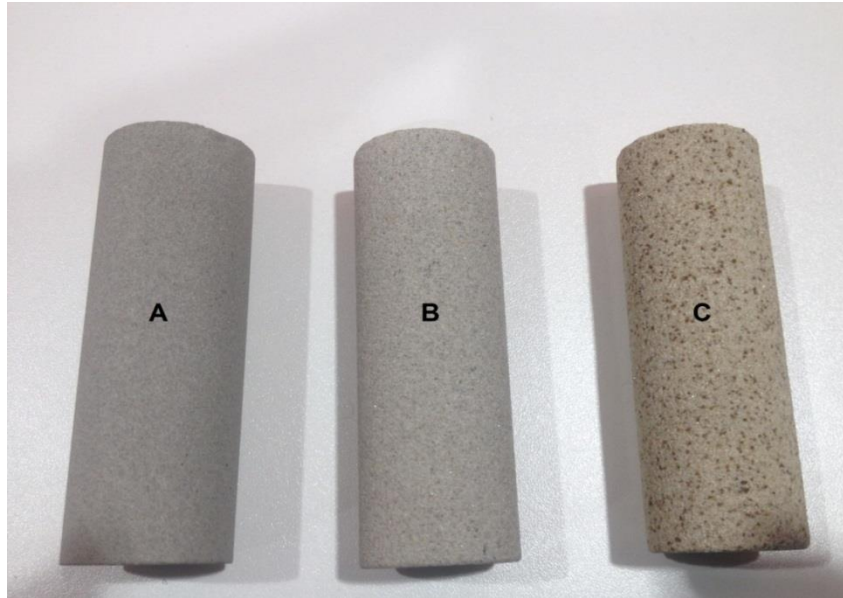
Figure 3.2 (A) Bandera Grey (B) Grey Berea (C) Buff Berea Core samples

Table 3.1 Dimensions and petrophysical properties of core samples used in this research

Core samples	Length (mm)	Diameter (mm)	*Porosity (%)	*Permeability (mD)
Grey Berea	76.27	25.22	19-20	200-315
Bandera Grey	76.00	25.47	21	30
Buff Berea	76.18	24.95	22	350-600

*Determined by Kocurek industries from where the samples were sourced

3.3.1 Gases

Carbon dioxide (CO_2), Nitrogen (N_2), Helium (He) and Methane (CH_4) stored in BOC gas cylinder under the pressure of 200 bar (2900 psia) and temperature 15^0C, were used for core flooding experiments and Gas Chromatograph operation. The purity of all the gases was 99.996%. The gases were supplied by BOC in Surrey UK.

3.3.2 Brine Preparation

Synthetic reservoir brine with varying salinity at 23 °C were prepared. Brine was prepared by dissolving a desired mass of NaCl (sodium chloride) salt into an appropriate volume of distilled water using a hot plate and a magnetic stirrer setup as shown in Figure 3.3. The salinity and concentration of salt in the fluid was determined using a refractometer shown at room temperature and pressure. The NaCl salts were purchased from Fisher Scientific and had a purity of 99.9% (Figure 3.4).

Figure 3.3 Brine preparation set up
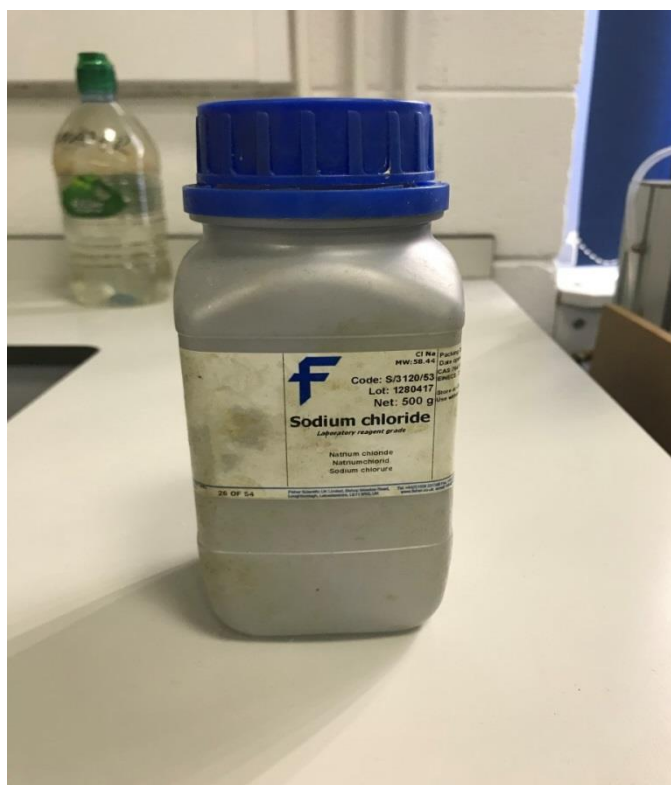
Figure 3.4 Sodium chloride salt

3.4 Core samples characterisation

Characterisation of the core samples is vital as to ascertain the actual petrophysical properties of the sample prior to the commencement of the experiments. This helps to obtain accurate results based on the specific core samples experimented upon.

3.4.1 Porosity and pore volume determination

Determination of porosity is vital in core flooding experimentation as it provides the pore volume or in generic terms; the void spaces or the fluid carrying capacity of the given core sample. There are several methods of porosity determination. In this work, however, the use of non-destructive and state-of-the-art methods of Gas Porosimetry and Computerised Tomography (CT) Scanner will be employed. Details of the methods employed and working principles are described in the subsequent sections.

3.4.2 Permeability determination

The absolute permeability for various core samples selected for this research was determined using a simple core flooding set up which are described in detail in the Chapter 4. The

principle of operation of the set-up is based on Darcy law. The following variables; the flow rate, constant differential pressure, sample dimensions and the fluid properties obtained from the set-up of the permeability experiment were used to compute the absolute gas permeability of the core samples.

3.4.3   Core grain diameter determination

A correct determination of the grain diameter of a porous media is vital in the dispersion investigation during enhanced gas recovery process. Being a property of the porous medium, it is depicted as the characteristic length of mixing during solute transport investigations. However, the dispersivity of the porous medium is often used for consolidated porous media or several analogies like the mean grain diameter are experimented on in unconsolidated porous media (pack beds, sand packs etc.) to determine the P_{ex} which details the dominant flow mechanism (molecular diffusion or mechanical dispersion) based on the relationship between the medium *Péclet* number and the characteristic length of mixing.

In this study, a combination of Scanning Electron Microscopy (SEM) integrated with an image processing tool (ImageJ) were used to determine the mean grain diameter of the core samples which will be used to determine the dominant flow mechanism during the core flooding experimentation.

3.5   Core flooding experimentation

This experimentation is central for simulating the EGR displacement process. The flooding process was carried out using a UFS-200 core flooding system from Core Lab Instruments Division of Core Laboratories LP, Tulsa, Oklahoma USA. It provided an avenue to carry out investigations in the laboratory at reservoir conditions relevant to the research using state of the art instrumentation and control systems. The core samples were first cleaned using Soxhlet extraction to get rid of any fluid that could potentially contaminate the experiment and results. In the absence of a heat shrink, the core samples were wrapped in cling film (Figure 3.4) and then in duct tape, as shown in figure 3.5 which acts as an anti-extrusion and also to minimise permeation of the gases into the Vitton sleeves housing the core samples when inserted into the core holder.

Figure 3.5 Process of core samples wrapping in cling film
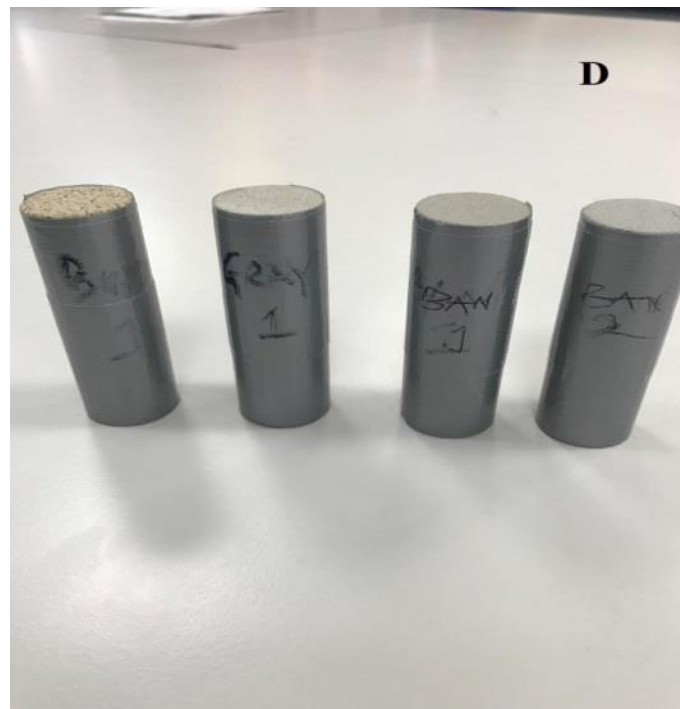
Figure 3.6 Conditioned samples ready for experimentation

3.5.1 Gas analysis

The effluent analysis is a vital step in this experiment as the concentration profile which the whole work centres on. In this work, an Agilent 7890A Gas chromatograph was used to evaluate and analyse the gas effluent from the core flooding apparatus. This uses a modified

Method and Sequence shown in Appendix B to obtain the concentrations of each gas at a specific time stamp.

3.6 IFT measurement

The IFT measurement was set up to measure the interfacial interaction between the test gases and the brines under investigation. The IFT was used to evaluate the solubility of the gases at reservoir conditions when they come in contact with the brine to simulate the extent of solubility trapping mechanism as a potential method for secondary sequestration of CO_2 during EGR. The IFT investigation utilises an IFT equipment supplied by CoreLab USA. Detail of the equipment will be discussed in Section 4.7.

3.7 Data analysis

For the data obtained from the pore volume determination using Helium Porosimetry, Microsoft Excel 2010 was used to compute the grain volume and to evaluate the pore volume of each of the test core samples. Conversely, the image reconstruction and analysis from the Computed Tomography technique was carried out using Volume Graphics Studio Pro version 2.2. Also, the microscale images obtained from Scanning Electron Microscopy (SEM) using the back-scatter electron detection (BSED) technique was processed using ImageJ version 1.5k software to measure the mean particle size and the statistical tool. The permeability results were plotted using IBM SPSS version 23 for scatter plots and fit regression and histogram.

For the core flooding evaluation, Origin Pro 2016 was employed for least squares regression for analytical fitting of solution of 1D ADE to experimental data for longitudinal dispersion coefficient determination. Also, PVTsim v.20 software was used to simulate the physical fluid properties of the water and gases at reservoir conditions.

DropImage software was used to evaluate the IFT between the test fluids and OriginPro v8 to plot the results to provide a statistical representation.

CHAPTER 4

4 EXPERIMENTAL SETUP AND DESIGN

4.1 Overview of equipment description

This chapter presents a detailed design and description of the equipment used in the research. It ranges from core cleaning procedures to the core flooding experimentation itself. The principles by which each equipment operates and the experimental procedures are, also presented in detail therein. The description will be done in two parts, the first part is the core sample characterisation and the second part are the core flooding and IFT measurements.

4.2 Core sample characterisation

The determination of the petrophysical properties of the core samples was carried out using the equipment that will be discussed next. A detailed step by step depiction for these analyses using individual equipment is presented to showcase the sequence the experiments carried out in this research followed.

4.2.1 Core sample cleaning using Soxhlet Extraction

This is the first step for any experiment for core sample preparation. Getting rid of any contaminant residing in the core sample is vital in acquiring concise and reliable results. Upon receipt of the core samples, they are subjected to cleaning using Soxhlet Extraction in which both organic and inorganic residues in the core sample are removed.

Soxhlet extraction equipment consists of a Pyrex flask (which is a long neck round-bottom flask), a thimble, a condenser - where cold water circulates, and, finally, an electrical heater to provide the necessary heat to evaporate the toluene solvent around the system.

4.2.1.1 Procedure

During the process, toluene is heated to about 70℃ so that it evaporates upwards into the condenser. The vapour thus condenses in the condenser, which has cold water circulating through it, and then drips into the Thimble which houses the core sample and also serves as a reciever of the fluid extracted from the sample. The core sample becomes saturated with the toluene vapour and the recondensed toluene fills up the Thimble till it reaches the liquid level within the Soxhlet tube to the top of siphon tube arrangement, the liquid within the Soxhlet tube automatically drains itself by siphon effect and flows into the Pyrex flask containing the boiling toluene. This process allows the toluene to clean any organic fluid within the core sample in a reflux state. The process was allowed to continue for 48 hours for a thorough

cleaning. A moderate temperature was permitted so that the toluene will not boil off. The set-up is shown in Figure 4.1.
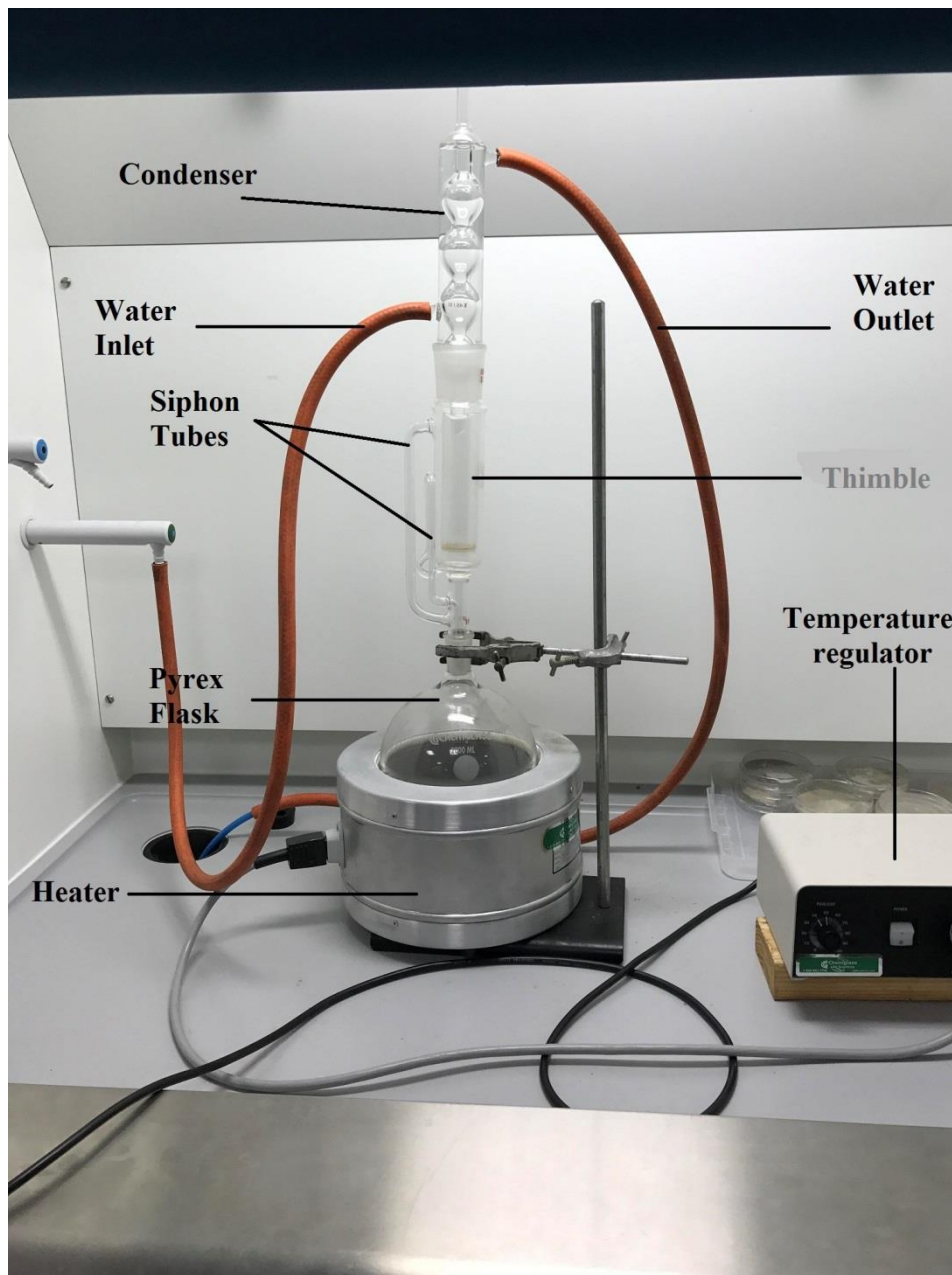
Figure 4.1 Soxhlet extraction set up

4.2.2 Porosity determination

Porosity determination is very important for any petroleum engineering application. It determines the capacity or void of a core sample which translates to how much hydrocarbon can stored within the pore spaces of the core sample. It is the regarded as the OGIP for efficiency determination during the core flooding experiments. Three methods are employed

here to evaluate this parameter for consistency. These are helium Porosimetry, CT scanning, and saturation method.

4.2.2.1 Helium Porosimetry (PORG-200TM)

This method enables the determination of the porosity of rock cores using the grain volume of the core sample which is the volume of the rock grains or solids alone without the voids enclosed therein. The pore volume is now determined from the difference between the grain volume obtained by this method and the bulk volume which is defined as the total physical volume the sample occupies in space. The core bulk volume is determined empirically through measuring the dimension of the core samples using a high accuracy Vernier caliper and thus evaluating the total volume from analytical measurements, in this case using the volume of a cylinder.

$$Pore\ Volume = Bulk\ Volume - Grain\ Volume \qquad (4.14)$$

Where, $Bulk\ Volume = \frac{\pi d^2}{4} \times L$, and d is the core sample diameter, and L is core sample length.

Helium is the expanding gas of choice in this experiment because it is an inert gas and therefore will not have any rock-fluid interactions that may alter the morphology of the sample being analysed. Also, helium has a high diffusivity and therefore will measure porosity very accurately.

4.2.2.2 Principle of Grain Volume Determination

In principle, the equipment (PORG-200TM) uses Boyle's law to determine grain volume from the expansion of a known volume of helium into a calibrated sample holder (Matrix Cup). Boyle's Law states that the volume of an ideal gas is inversely proportional to the pressure at a fixed temperature. Figure 4.1 shows the set-up gas Porosimeter. The equipment has two volume chamber or cells termed the reference cell and the sample chamber. The reference cell has a fixed volume V_1 at a regulated pressure between 90-95 psig and the sample chamber V_2 which is of an unknown volume at a normal atmospheric pressure. The helium gas was first introduced into the reference cell then expanded into the sample cell of unknown volume, and it was allowed to stabilise all through the chambers. Then P_1 and P_2

were recorded, and the unknown volume V_2 which is the grain volume was determined with the application of Boyle's law.

From ideal gas law:

$$\frac{P_1 V_1}{T_1} = \frac{P_2 V_2}{T_2}$$

(4.2)

Where:

$P_1 = \ Initial\ Absolute\ Pressure$

$V_2 = \ Initial\ Volume$

$T_1 = \ Initial\ Absolute\ Temperature$

$P_2 = \ Expanded\ Absolute\ Pressure$

$V_2 = \ Expanded\ volume$

$T_2 = \ Expanded\ Absolute\ Temperature$

The reference volume is always pressurised to about 90 psig and expanded into a Matrix Cup (sample holder) containing the sample to be analysed. The second pressure is read and used to compute the unknown volume. The equation below shows how the grain volume is determined.

$$V_g = \ V_c - \ V_r \left(\frac{P_1 - P_2}{P_2 - P_a} \right) + V_v \left(\frac{P_2}{P_2 - P_a} \right)$$

(4.3)

$V_g = Grain\ Volume$

$V_c = Sample\ Chamber\ Volume$

$V_r = Reference\ Chamber\ Volume$

$V_v = Valve\ Displacement\ Volume$

$P_1 = Absolute\ Initial\ Reference\ Volume\ Pressure$

$P_2 = Absolute\ Expanded\ Pressure$

$P_a = Absolute\ Atmospheric\ Pressure\ Initially\ in\ the\ sample\ Chanber$

The Experimental setup is shown in Figures 4.2 and 4.3
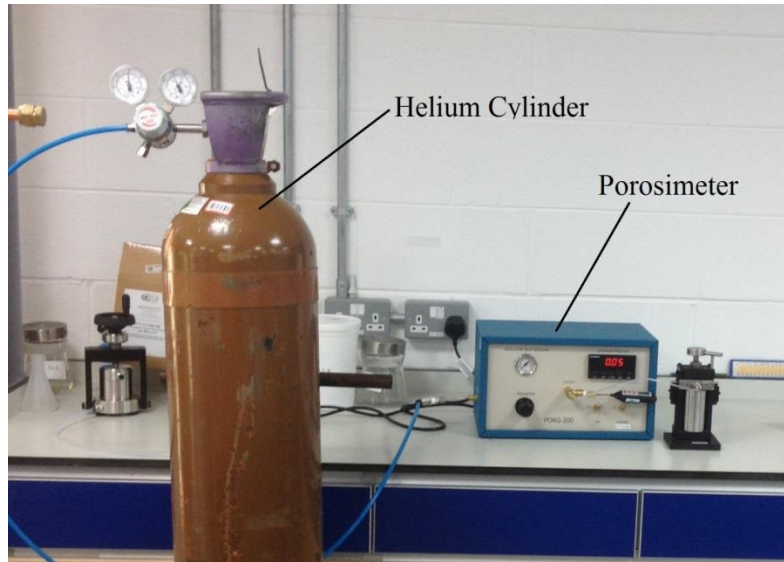
Figure 4.2 Helium Porosimeter Set-up showing all the components
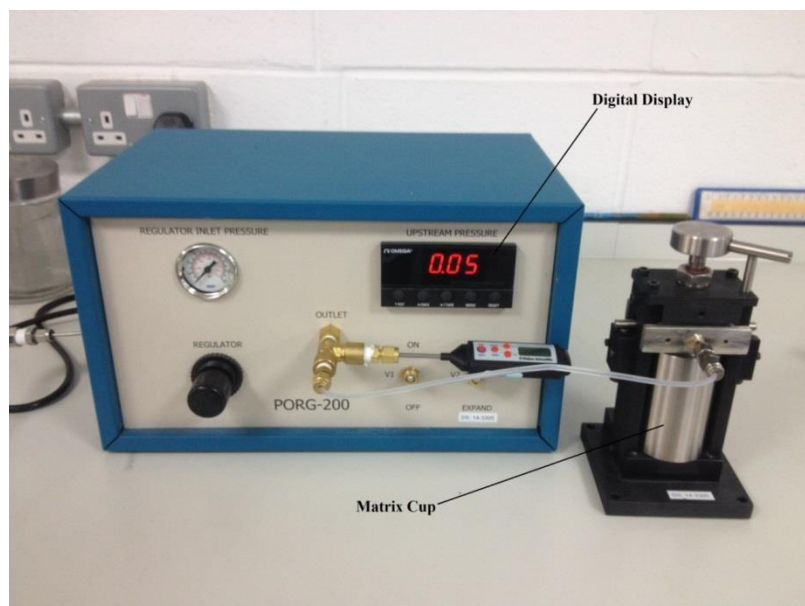
Figure 4.3 PORG-200 porosimeter
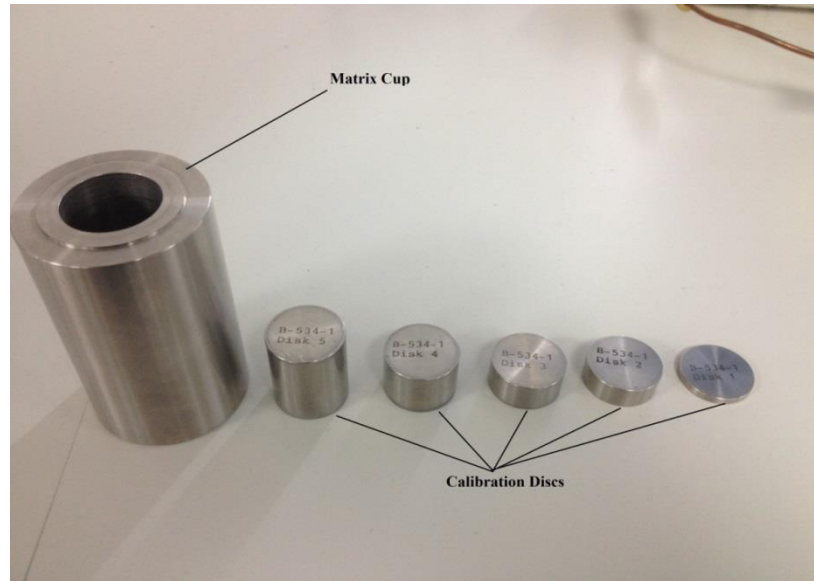
Figure 4.4 Matrix cup and calibration discs

4.2.2.3 Measurement Procedure

1. A pressure test was carried out to ensure a leak tight system before commencing the grain system volume calibration. To achieve this, the system was powered on for about thirty minutes to stabilise and ensure that the pressure transducer reached equilibrium. Then the helium gas supply was connected to the helium inlet port of the instrument and was set to 120 psig on the Helium gas bottle regulator.

2. After the leak test, the system grain volume calibration was performed on the Porosimeter. The matrix cup with reference discs was connected to the instrument. Valve V_2 was switched to vent and valve V_1 was switched to ON. Then the regulator was set to 90 psig as the reference pressure P_1; the valve V_1 was switched to OFF and valve V_2 to EXPAND position to equilibrate the pressure in the chamber till a pressure drop was stabilised and a reading was taken as expanded pressure P_2. This was done for all the calibration discs as shown in Figure 4.4.

3. Subsequently, the sample grain volume measurement was performed with the same procedure used for the system grain volume calibration. The obtained results for both calibrations were recorded in the provided application written in excel spreadsheet to calculate the grain volume of each sample.

4.2.3 Computed Tomography (CT) Technique

The CT technique is a non-destructive method used to analyse the external and internal geometries of an object by determining the variation in densities and atomic compositions of the object. In principle, CT scanning directs x–rays onto an object to produce its shadow image the object. The object absorbs part of the x-rays and there is an attenuation in the x-ray stream just around the object thus allowing a detailed analysis of its internal geometry. Also, the absorbed x-ray contains the picture element (pixel) which reflects the average value of the linear attenuation coefficient of the object materials with a certain thickness (Voxel). The basic parameter measured in each voxel of a CT image is the linear attenuation coefficient given by Beer's law as:

$$\frac{I}{I_0} = e^{-\sigma h} \tag{4.4}$$

Where *Io* is the x-ray incident intensity, *I* represent the intensity of the x-ray after is has passed through a thickness of *h*, and σ is the linear attenuation coefficient.

X-ray attenuation is essentially a function of the bulk density, thickness of the material, and atomic number of the elemental make-up of the material. It is also a function of the x-ray energy through the material. The x-ray passes through the object and the detector receives the signal attenuation as the sample rotates about its axis during the scanning process. The detectors register the x-rays signal attenuation that passes through the object as a picture in the process of creating the image. The image data received by the detector is sent to a computer to reconstruct all of the individual "pictures" into one or multiple cross-sectional images (slices) of the internal geometry of the object. This technique can be used to obtain the porosity of a core sample using the CT number relation.

4.2.3.1 Porosity determination using X-ray CT

After the image has been reconstructed, the values of the linear attenuation coefficients are deduced for each pixel. The linear attenuation coefficients are thus converted to into corresponding numerical values called the CT numbers by pitching the linear attenuation coefficients of the scan against that of pure water. The equation is shown below (Akin & Kovscek, 2003);

$$CT = 1000 \frac{(\mu - \mu_w)}{\mu_w} \tag{4.5}$$

CT number is in Hounsfield (H) units, μ is the linear attenuation coefficient of the material, μw is the linear attenuation coefficient of water.

Porosity can be obtained from images of core sample scanned using X-ray CT. this can be obtained from the correlation by Akin & Kovscek (2003) as reported by Liu et al. (2015) given as;

$$\phi = \frac{CT_{wet} - CT_{dry}}{CT_w - CT_{air}} \qquad (4.6)$$

Where, CT_{wet} and CT_{dry} are the image CT Numbers as scanned for the core sample fully saturated with distilled water and dry core sample respectively. CT_w and CT are also image CT numbers for water and air respectively using the same CT conditions.

4.3.4 Components of X-ray CT Scanner

For this technique, the GE Phoenix v|tome|x s Industrial High-Resolution CT & X-Ray System was employed. The basic components of the scanner are the x-ray tubes (x-ray source), the detector, and the rotational system. Details of which will be described as follows;
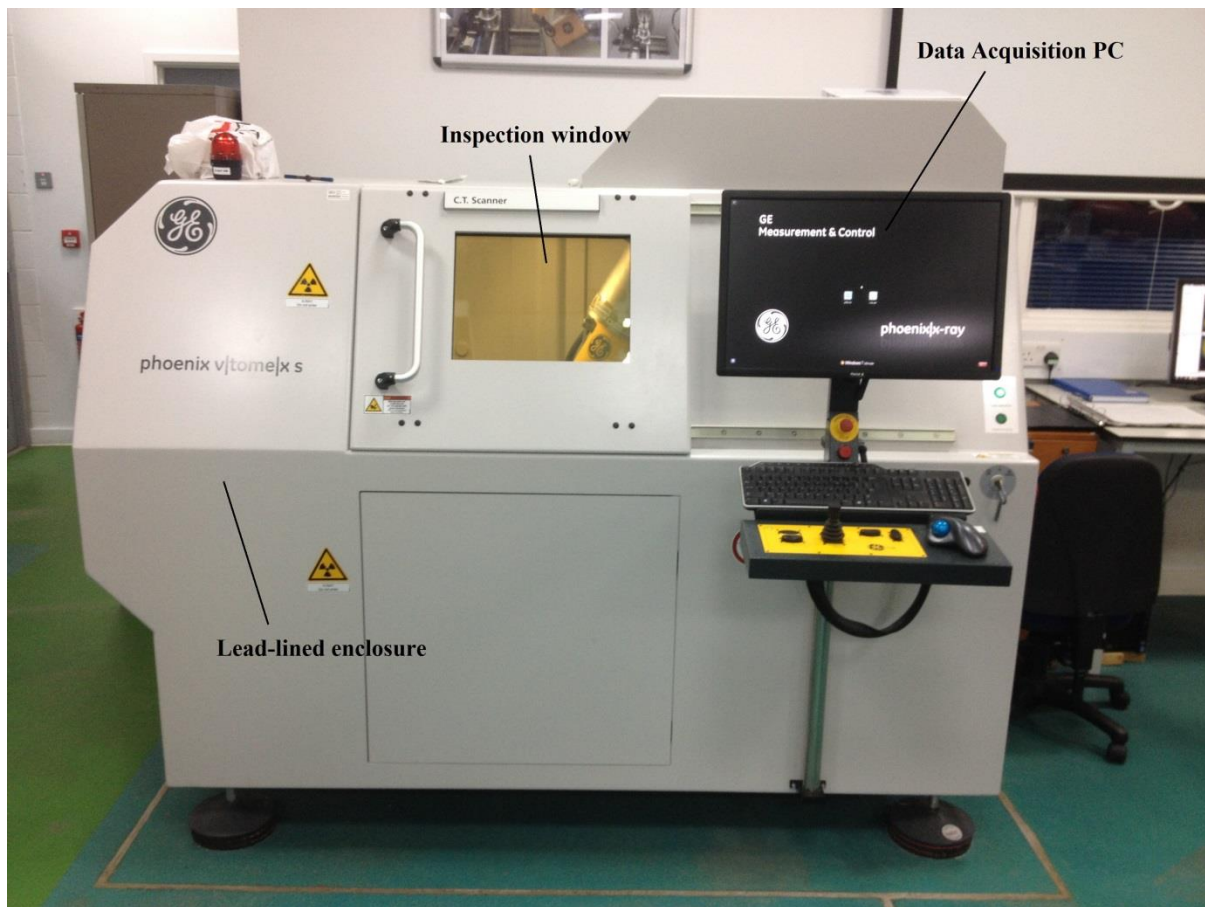
Figure 4.5 GE Phoenix v|tome|x s X-ray CT Scanner

4.2.3.2 X-Ray Tubes

There are two types of x-ray tubes in the equipment located inside the radiation protection cabinet; the transmission and directional X-ray tube as shown in Figure 4.6. Inside these tubes is the cathode which is the source of the X- rays. The x-ray streams pass through the tube target (beam exit window) and penetrate the sample to the detector which detects the attenuations in the x ray stream.

Figure 4.6 X-ray Tubes

4.2.3.3 The x-ray detector

The detector is in the radiation protection cabinet opposite the x-ray tubes. The x-ray penetrates the sample and is cast on the detector. The live image information is transmitted to the quality/ assurance diagnostic image software in real time.

4.2.3.4 Rotational System

The rotational system allows the object to rotate about the horizontal (x, z) and vertical (y) axis between the detector and the x-ray tubes using the object manipulator located on the control panel. The sample can also be rotated and tilted $\pm 45°$ in the x-ray stream path.
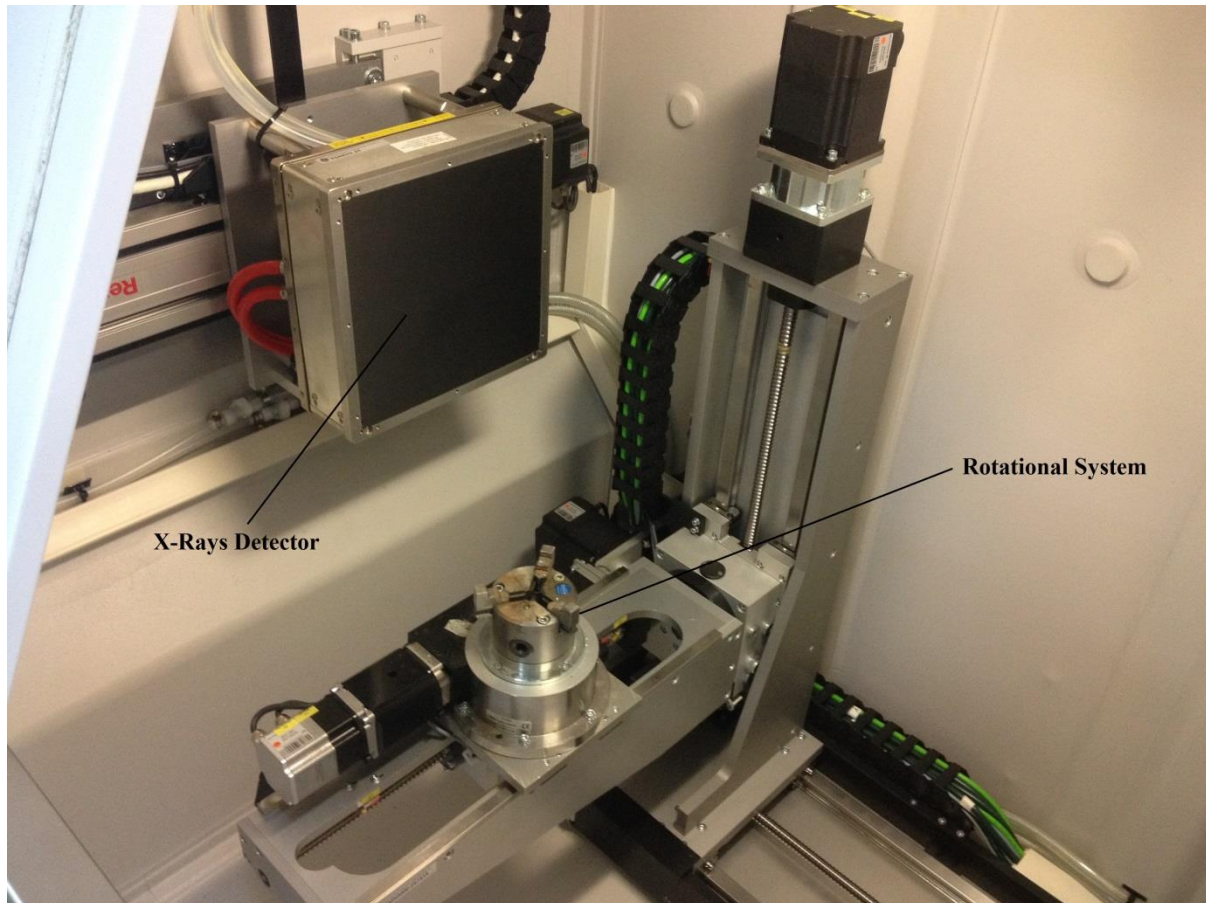
Figure 4.7 Rotational System of the CT scanner

4.2.3.5 Object manipulator

The object manipulator is located on the control panel and it is the control component of the rotational system which enables the user to manipulate the orientation of the object being scanned in any number of positions by tilting and rotating the object about any axis.

Figure 4.8 Object manipulator control panel of the CT scanner

4.2.3.6   Precautions during the Scanning Process

- Optimum operating parameters (voltage and current) were used to scan each sample to eliminate the effect of noise in the background of 3-D reconstructed image. To ensure this, low current and high voltage were used for high contrast sample (sandstone) since the lower the voltage, the higher the contrast. Therefore, the higher the power, the lower the resolution.

- During the scanning process, the samples were positioned closer to the X-ray source to obtain higher resolution, and for full penetration of the object at each angle of penetration. To obtain a high- quality result of the scanned object, the Region of Interest (ROI) was within the scanning window in a 360° rotation in its entirety. The farther away the object position from the x-ray source, the lesser the object is scan at a ROI/scan lesser than 360° resulting in a poorer resolution which results in artefacts effect in the 3-D reconstructed image such as ring artefact effect, geometry effect and beams hardening effect.

- Shading correction /offset was applied to the image, so that all pixels will be symmetrical towards X-ray, thereby eliminating intensifier image effect which produces a brighter image at the centre of the image.

- During the scanning process, the contrast in the image was increased by the aperture because a scattered, and irrelevant radiation (red) carries no information but decreases contrast and increase noise in an image.

4.2.3.7 CT Image Analysis Procedure

The CT Image analysis consists of the following procedures; the scanned image is first open with the 3-D editing software, once the image has been open, the image optimiser was applied to improve the quality of the image. An appropriate region of interest is selected, on a single cross-sectional image. The image in the selected region of interest is now saved in a suitable folder, which automatically restarts to generate a new datasheet for volume analysis. The reopen data set for volume analysis (volume of interest) refers to image segmentation, and it is the integration of all the ROIs across all the selected image which defines the segmented image or binarized image in the 3-D reconstructed image. Then, the automatic threshold value was applied during segmentation construction.

Grey value that is higher than selected threshold appears as white in the reconstructed image, and it considers as solid objects. Voxels with a grey value less than the chosen threshold appear as part of the background, and it shows as black. These grey values were then read off and recorded as it varies with the density of the scanned material. In order to apply equation 4.4, there is a need to scan the samples at different conditions of wetness. First, the samples were cleaned, dried and weighed. Then they are scanned and their grey values were recorded. Secondly, these samples are saturated, as demosbtrated in the next section, under vacuum with distilled water and they are subsequently scanned and grey values obtained. Air and water were also scanned to obtain their various grey values at the same power settings and positioning of the CT scanner as the samples; both dry and wet conditions. The oiptimum power settings used are 195V, 85 amp, timing of 333 seconds, with a 1x1 binning, using stabdard VFocus.

4.2.3.8   Core samples saturation for Porosity determination Using X-ray CT

The core samples were evacuated and saturated with distilled water under vacuum using the set up below which comprises of a vacuum pump and a desiccator.
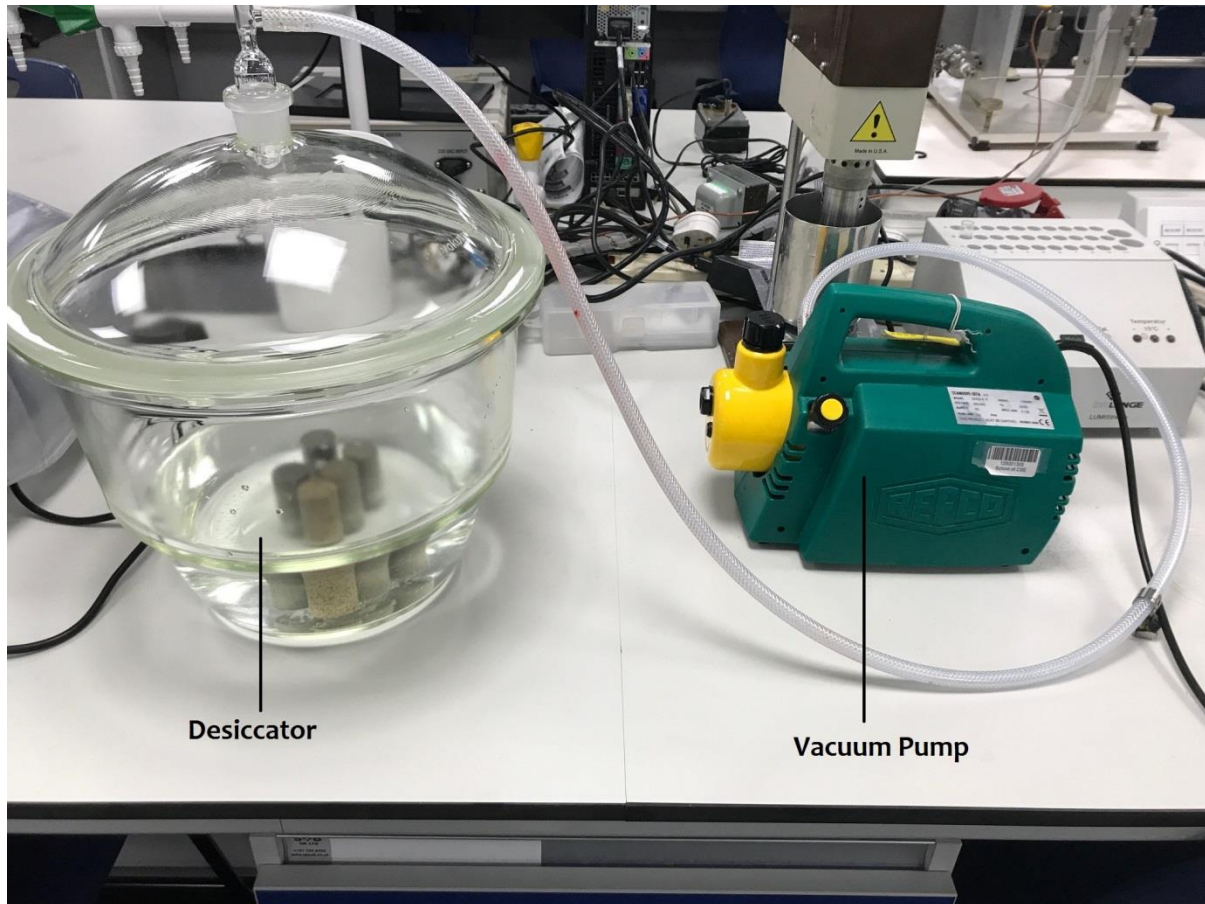
Figure 4.9 Simplified core saturation set-up

This process provides excellent saturation levels as it removes the entrained air within the pore spaces of the samples and replaces it with water.
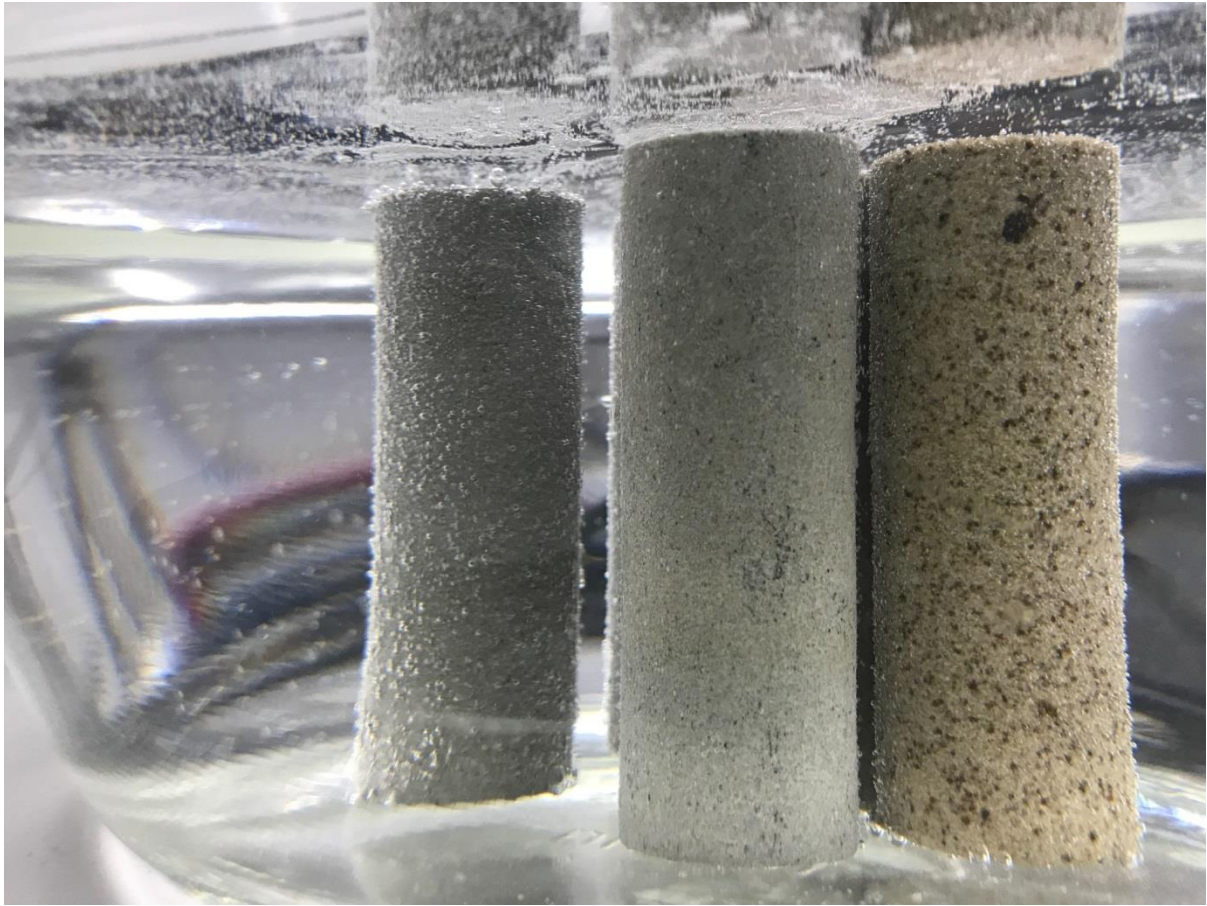
Figure 4.10 Air being extracted from core samples during saturation

4.2.4   Permeability determination

The permeability measurement set-up comprises of a Hassler-Type core holder ECH series, a pressure regulator, a static pressure gauge, and a rotameter. The compressed air is supplied from the humidifier from the UFS 200 core flooding apparatus. The pressure regulator applies the pressure in the required increments to evaluate the permeability at different pressures and flow rates. These are the required parameters for permeability evaluation. The regulator applies the upstream pressure and the pressure gauge records the downstream pressure. The rotameter measures the flowrates. The setup is shown in Figure 4.11.
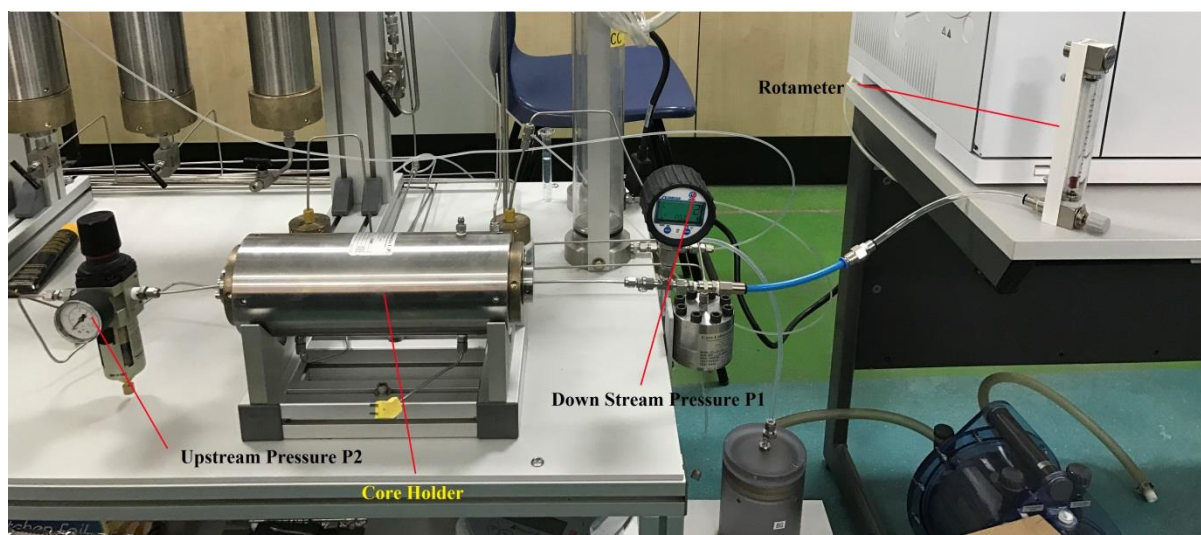
Figure 4.11 Permeability measurement set up

4.2.5   Grain diameter measurement using SEM Image analysis

This is a qualitative technique which is usually used for high magnification imaging and elemental analyses in mesopores. The morphology and texture of a catalyst is also observed with this technique. SEM is very expensive and is usually not available in characterisation laboratories. However, it is frequently employed in obtaining data on the shape, homogeneity, size, crystalline habit as well as presence of crystalline and amorphous compounds and their various distributions.

The SEM was done on the samples using a FEI Quanta 250 Field Emission Scanning Electron Microscope with EDAZ Genesis Energy dispersive X-ray analyses system attached. The images were obtained back scatter electron diffraction technique (BSED) which also, as the X-ray CT, depends on the densities of the penetrated material.

4.2.5.1   Procedure for Image analysis

The SEM images of different magnifications were obtained using the SEM equipment from different slices of the core sample. Being a non-destructive analysis, different angles of the core sample were scanned, and the images captured.

These images were analysed individually using the ImageJ software version 1.5K which is an open source software developed by Wayne Rasband of National Institute of Health USA. The version employed in this work has plug-ins for raw image processing for photography. The interface of the software is shown in Figure 4.13.
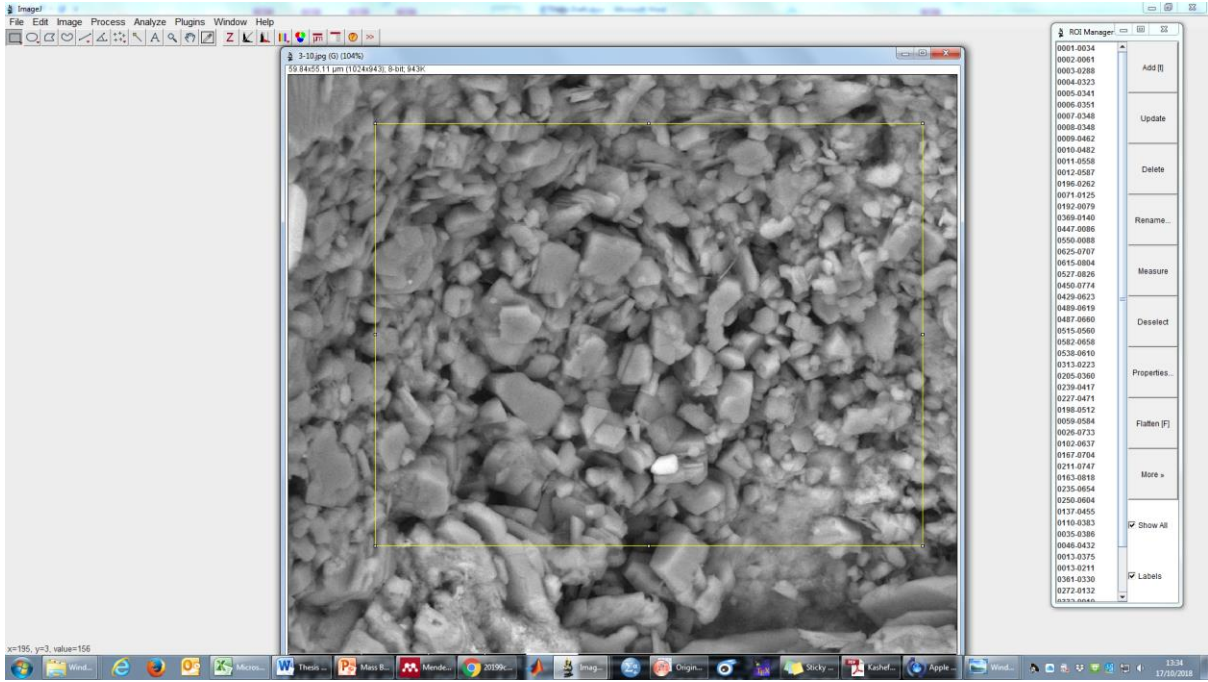
Figure 4.12 Interface of ImageJ with an imported SEM image of Buff Berea

First, the SEM image was imported into the software. Then a scale measurement and adoption were carried out to utilise the actual size of each grain by pixel length. Preparation of the image was further done by adjusting the threshold of the images to form a mask and overlay of each pixel to correspond to each cluster of grains in the image. After that is done, a band filter pass is applied to further isolate the clusters of each image and flatten the image. This distinction in masks will provide an outline of the clusters and makes it easier to define the edges for measurements. The area of each cluster is calculated by the software based on the pixel density of each cluster in the band of the grey values. These areas are obtained and using Feret's equivalent circle diameter (Olson, 2011) based on the circularity and shape factor of the grain. It is given by:

$$De = \sqrt{\frac{4A}{\pi}} \qquad (4.7)$$

And;

$$A = \sum a \qquad (4.8)$$

Where De is the equivalent circle diameter (µm), A is the area the grain (µm^2), *a* is the area of the particle of each individual pixel cluster.

60

4.3 Experimental design

To set up the experiments, two separate equipment were incorporated as a single unit to reify aims of the research. These are the core flooding system and the gas chromatograph (GC): The core flooding system, which comprises of a number of components, was used to simulate the displacement process in the core sample and the GC, which was set up at the downstream of the core flooding system, which measured the effluent (gases) composition for analysis. These systems were set up such that as the displacement process progressed with time, the products of the displacement process were measured in real time to create a concentration profile which helped facilitate the investigation. Being different systems of individual complexities, a modification of the set up and the modes of operation was necessary.

The core flooding system, which was initially designed for liquid system, was reconfigured to accommodate a gas flow system by re-introducing O-rings in the accumulators and core holders to create better pressure seals which were changed frequently given the acidic nature of CO_2. The pressure transducers were also calibrated to measure the incessant pressure fluctuations due to the compressibility and other physical properties of the gases at reference conditions. Compression fittings were fitted at vulnerable points, like core holder connection points, along the tubing of the equipment to withstand high pressure and fluctuations. Gas flow controllers were installed at the downstream of the core flooding system to measure the effluent flow rate to quantify the volume of the produced gases and stepping down the pressures before entry into the gas sampling valve of the GC which has a rating of not more than 1 bar pressure.

The GC equipment was originally configured to analyse natural gas with a wide range of compositions and even heavier natural gas liquids (NGL). The analysis time was in excess of 30 mins per sampling cycle. The volume analysed during that time was 250 μL of gas sample was injected into the sampling loop. However, the rate gas production from the core flooding system warrants frequent analysis as the measurements of the concentration of each individual species of the gas is vital to the research. Therefore, a method and the sequence of the feed injection to the GC was modified to reduce the analysis time by a 6th of the original time it took. This was challenging as there are 4 different columns in the oven of the GC of different type of material and functions. This called for the re-routing of the carrier gas and the analyte (gas sample) through loops to bypass some of the columns, which react unfavorably with the effluents injected, using the gas sampling valves. Increasing the carrier gas inflow rate and increasing the temperature of the oven and front inlet of the gas sampling

valve helped to reduce the elution time of the samples drastically. But before the temperature increase, an oxygen and moisture trap were installed after the mass flow controllers from the core holder to remove these gases so as to avoid condensation between the front inlet and the oven. Condensation affects the expensive detector which measures the thermal conductivity of the gas sample and identifies each gas by that property. The design of the setup is shown in Figure 4.13.
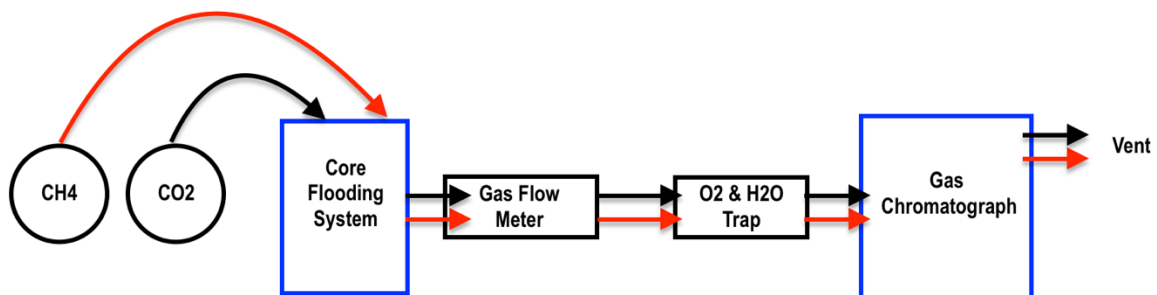
Figure 4.13 Experimental setup and design of core flooding equipment and GC

Prior to the main experiments, a thorough core characterisation was carried out for the purpose of determining the petrophysical properties of the core samples.

4.4   Core flooding apparatus and effluent analysis

The CoreLab UFS-200 is a core flooding system that is configured for two phase liquid displacements under unsteady state or steady-state conditions and single-phase gas steady-state experiments. The system is rated to 3,500 psig pore pressure, and 5,000 psig confining pressure at ambient temperature. The inlet pressure into the core sample and outlet pressures on the other side of each core are measured with gauge pressure transducers. The SmartFlood software forms an integral part of the system which interfaces the UFS system and the computer data-acquisition-and-control system hardware and provides on-screen display of all measured values (pressures, temperatures, volumes etc.), automatic logging of test data to a computer data file. The core sample is held within a rubber vitton sleeve inside a Hassler-type core holder by radial confining pressure, which simulates reservoir overburden pressures provided by a pump.

Inlet and outlet distribution plugs allow fluids and gases to be injected through the core sample. All flow lines and internal volumes are kept to a minimum, so that accurate flow data can be determined by reducing the dead volume in the system. The simulated pore pressure is applied through an ISCO model 500D, two-barrel metering pump system with a flow rate range adjustable from 0 to 200 ml/min and a maximum pressure rating of 3,750 psig.

The overburden (confining) pressure pump is a hydraulic pump Model S-216-JN-150 pump, with pressure output of up to 10,000 psig and will provide the desired overburden in the system. The back pressure is regulated with CoreLab dome-loaded type back-pressure regulator which controls the back pressure to whatever pressure is supplied to its dome. It is rated for a maximum working pressure of 5,000 psig. Floating-piston accumulators are provided as part of the system and are rated for 5,000 psig pressure and 350°F (177°C) temperature. The accumulators provide for injecting fluids without allowing the fluid to come in contact with the metering pump. 2.5-inch-dial pressure gauges are used to monitor the Overburden Pressure and the BPR Dome Pressure. The pressure range on these gauges is 15,000-psig full scale. A 160 psi gauge is provided to monitor the main inlet air going to the pump and air actuated valves. Rosemount transducer provided with the system measure differential pressure across the core holder. The effluent flowrate and produced volume are measured by Bronkhorst mass flow controllers/meters which is an integral part of the core flooding equipment and records the effluent rates on the logging worksheet of the SmartFlood software.
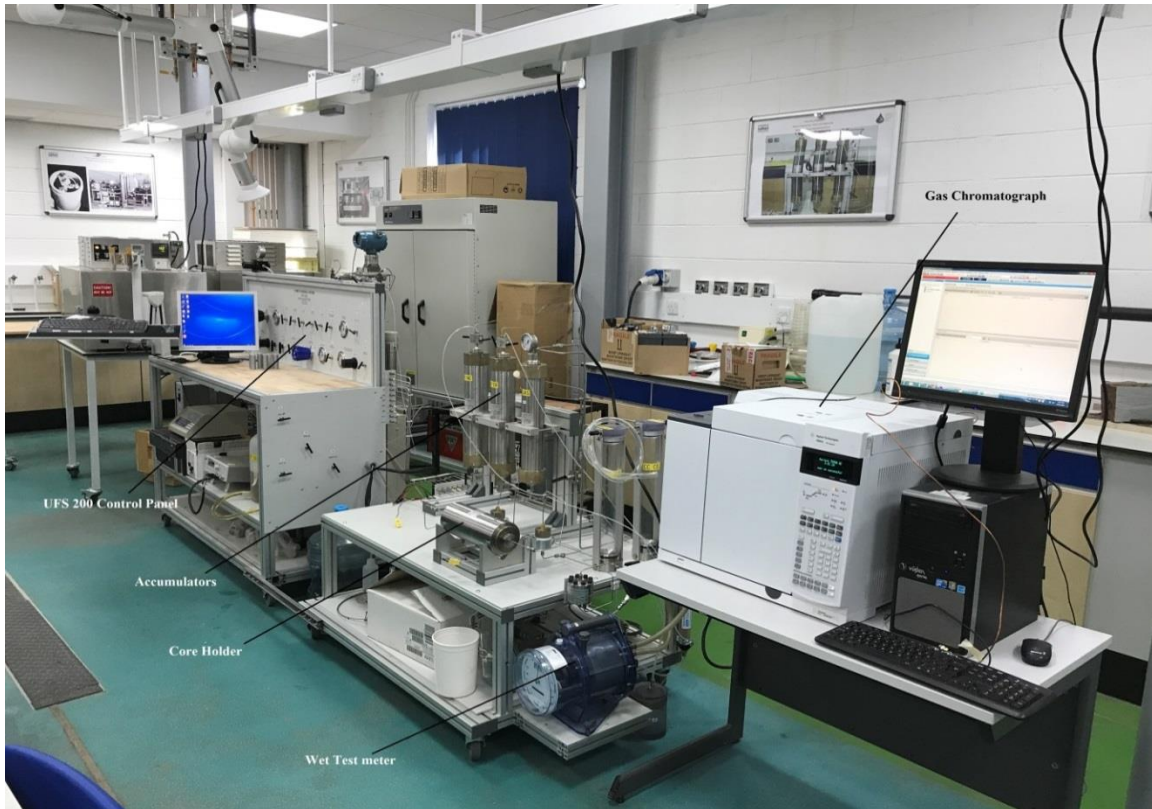
Figure 4.14 Core flooding set up integrated with gas chromatograph
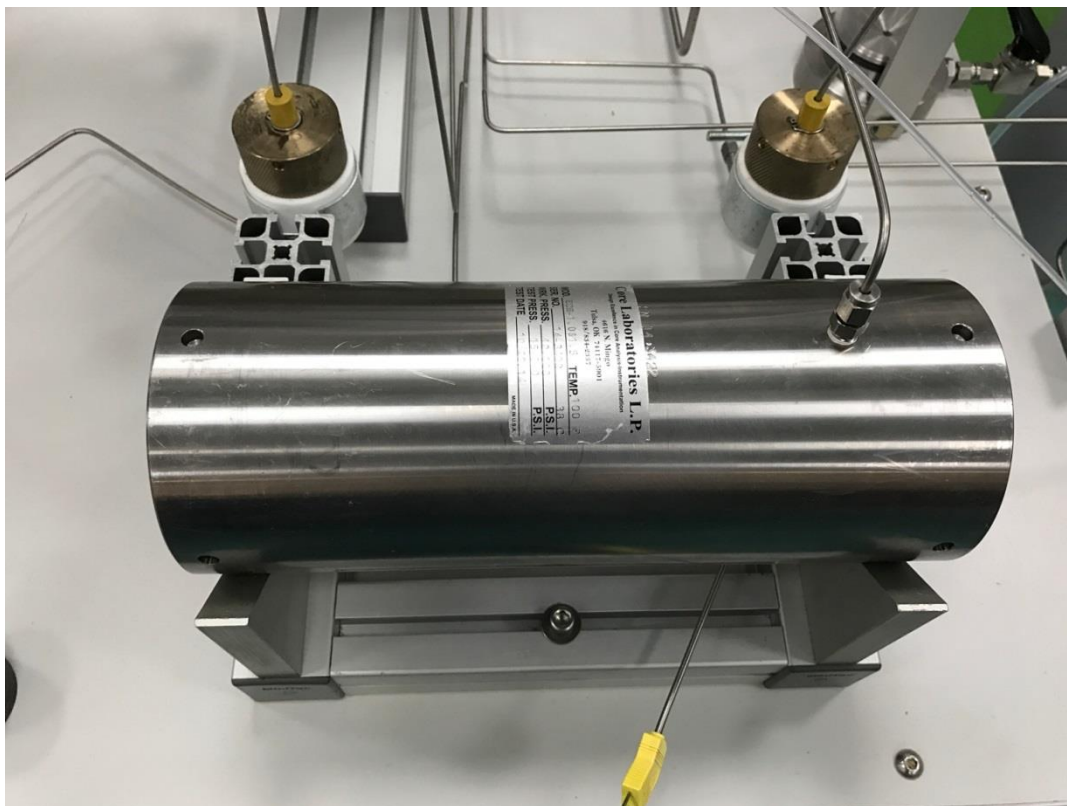
Figure 4.15 Hassler-type core holder ECH-1 series
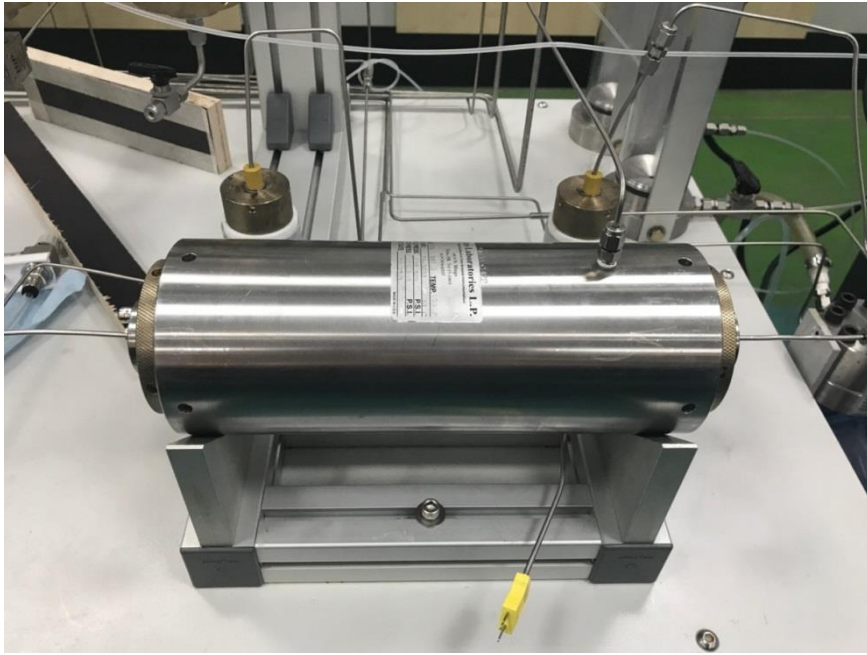
Figure 4.16 A coupled core holder with a core sample inside

Figure 4.17 Fixed end component of the core holder showing the distribution plug

Figure 4.18 Isco pump controller

Figure 4.19 Two-barrel metering pump system (pumps A-D)

Figure 4.20 Hydraulic pump Model S-216-JN-150 with hydraulic oil reservoir

Figure 4.21 Floating piston accumulators and a gas humidifier

Figure 4.22 Rosemount pressure transducer system

Figure 4.23 Bronkhorst mass flow meters and a pressure relief valve

4.4.1 Principle of operation

The UFS 200 core flooding systems works on the principle Darcy law. Henri Darcy empirically defined fluid flow in porous media in 1856 as being proportional to the differential pressure per unit length. The relationship was derived from data collected during a series of experiments on the vertical flow of water through gravel packs. Subsequent work has proved the validity of Darcy's Law for flow in all directions and confirmed the experimental observations by derivation from the basic laws of physics.

$$Q = \frac{kA(P_1 - P_2)}{\mu L} \tag{4.9}$$

where:

k Permeability (Darcies)

μ Viscosity (centipoise)

Q Flow Rate (cc / sec)

L Length of Flow (cm)

A	Cross-Sectional Area of Flow (cm^2)
P$_1$	Upstream Pressure, atmospheres
P$_2$	Downstream Pressure, atmospheres

Rearranging Darcy's Law, and changing the units of permeability to millidarcies and pressure to psig, the equation becomes:

$$K = \frac{14700 \ v\mu L}{\Delta p A t}$$

(4.10)

Where:

K	Permeability (millidarcies)
V	Flow Volume (milliliters)
L	Length of Flow (cm), i.e. length of test sample
μ	Viscosity (centipoises)
Δp	Differential Pressure (psig)
t	Time (seconds)
A	Cross-Sectional Area of Flow (cm^2), i.e. of core sample

4.4.2 Procedure

The core sample was wrapped in foil paper to avoid the permeation of the supercritical gases through the sleeve and into the annulus of the core holder. A layer of cling film was first placed between the core sample and the foil paper to prevent the foil paper from sticking to the core sample. The core sample was then placed inside the vitton sleeve and installed on the distribution plugs of the core holder and secured with clamps on both sides and inserted into the core holder. A heat jacket was placed around the core holder and the temperature ramping was set and the hydraulic pump was initiated to pump the hydraulic oil into the annulus of the core holder to provide the overburden pressure necessary for the experiment in lieu of the simulated depth pressure. A pressure of 2200 psig was set as the overburden pressure in accordance with the pressure gradient of 0.45 psi/ft. The simultaneous hydraulic oil pumping and heating was done to avoid high temperature ramping with uncontrolled pressure rise.

When the core holder temperature reached 50°C, the temperature ramping was stopped, and the temperature was kept constant. Hydraulic oil leaks were checked for on both sides of the core holder to ensure that the clamping of the core sample and set up integrities were not compromised.
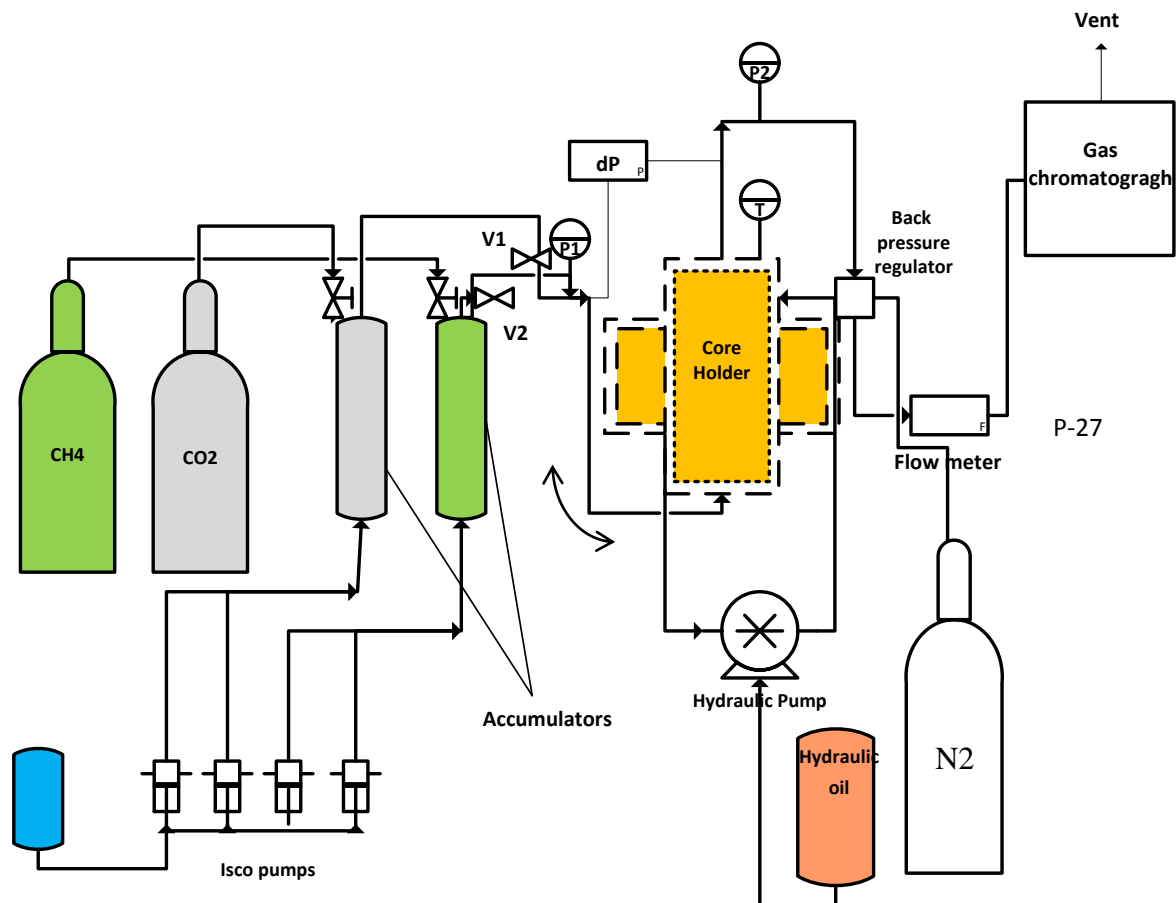
Figure 4.24 Schematics of the core flooding equipment with the operational components

The schematic of the setup is shown in Figure 4.24. As a safety precaution, all the valves are shut off. V1 was opened to provide access to the accumulator. D1, depicted in the schematics in Figure 4.24. When there was no increment in the level of the distilled water in the reservoir, D1 was shut off and then V1 was shut off too. The back-pressure reference pressure was set to 1300 psig using the N_2 gas bottle. The N_2 gas was used to set the dome pressure of the back-pressure regulator as opposed to the hydraulic oil because of the compressibility of the gas which provides a smoother flow of the gas and avoid pressure

build-up within the core flooding and the reference pressure be kept constant. V2 was then opened to saturate the system with CH_4. Pumps A&B were engaged to compress the gas in the system to provide the desired system pressure. V2 was then shut off.

The same filling procedure was carried out with accumulator b, ACC-B, and the flowrate was varied between 0.2- 0.5 ml/min (depending on the investigation). V4 was then opened and then the logging commenced and also the GC sequence as run. The items logged were differential pressure, dP, production rate, and each time stamp was recorded which corresponded with the injection times of the GC, whose method sequentially runs for five minutes to sample the effluent every five minutes. The flowrate was measured with the flow meters. The overburden pressure was carefully monitored and was kept more than 500 psig above the pore pressures to avoid the rupturing of the vitton sleeve, given that the pumps deliver a constant flowrate and the pressures rapidly build to maintain the desired flowrate.

Each experimental run came to an end when there were insignificant volumes of CH_4 in the effluents. These steps are repeated for all core flooding experiments.

4.4.3 Core holder orientation set up

The core flooding entailed a change in the injection orientation of the core holder to evaluate the effect of the injection orientation on displacement efficiency, dispersion coefficient, and the flow behaviour of the injected CO_2. As the system was designed to carry out core flooding in a horizontal orientation, a construction of a vertical stand to change the orientation to horizontal orientation was carried out to achieve the objective of the effect or sensitivity of this change/switch on the parameters as aforementioned.

First a measurement of the core holder was carried out to ascertain the length and width to fit into the contraption so that all the tubing leading to and away from the core holder sit right to accommodate the heat jacket. Schematics of the construction and assembly are shown in Figure 4.25 to 4.29 to highlight the transformation from horizontal to vertical orientations before the commencement of the experimentation.
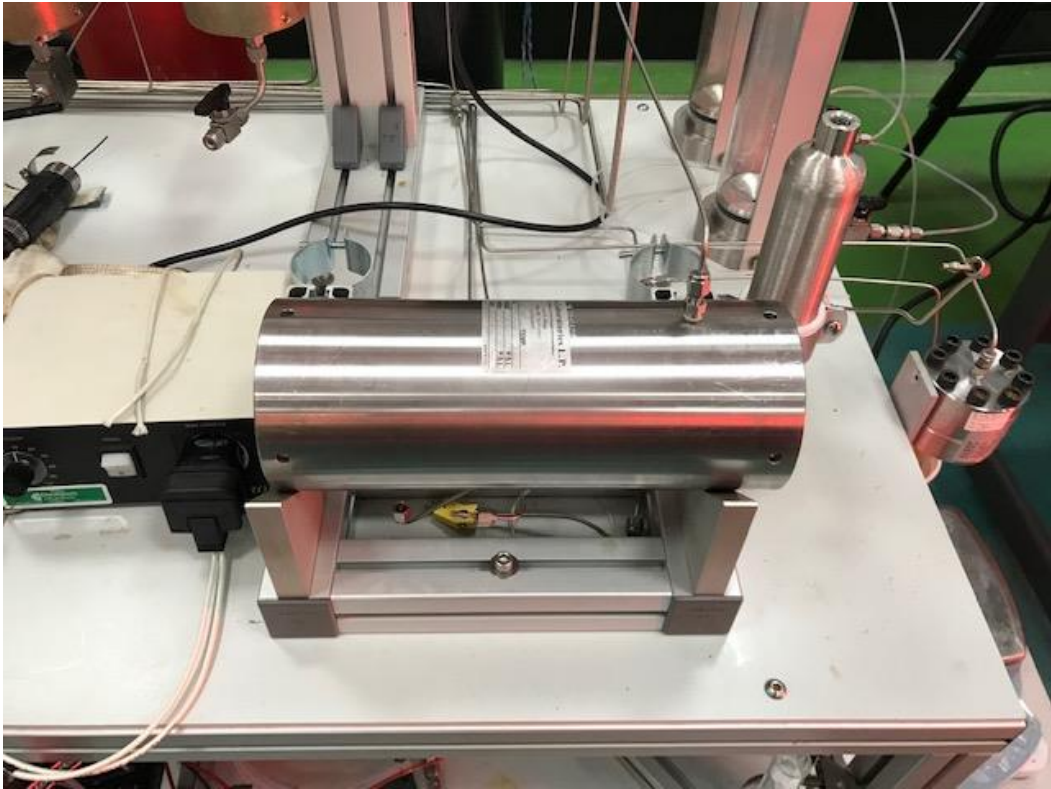
Figure 4.25 Core holder situated in a horizontal orientation

Core holder
brackets

Figure 4.26 Constructed stand for the core holder to be situated vertically
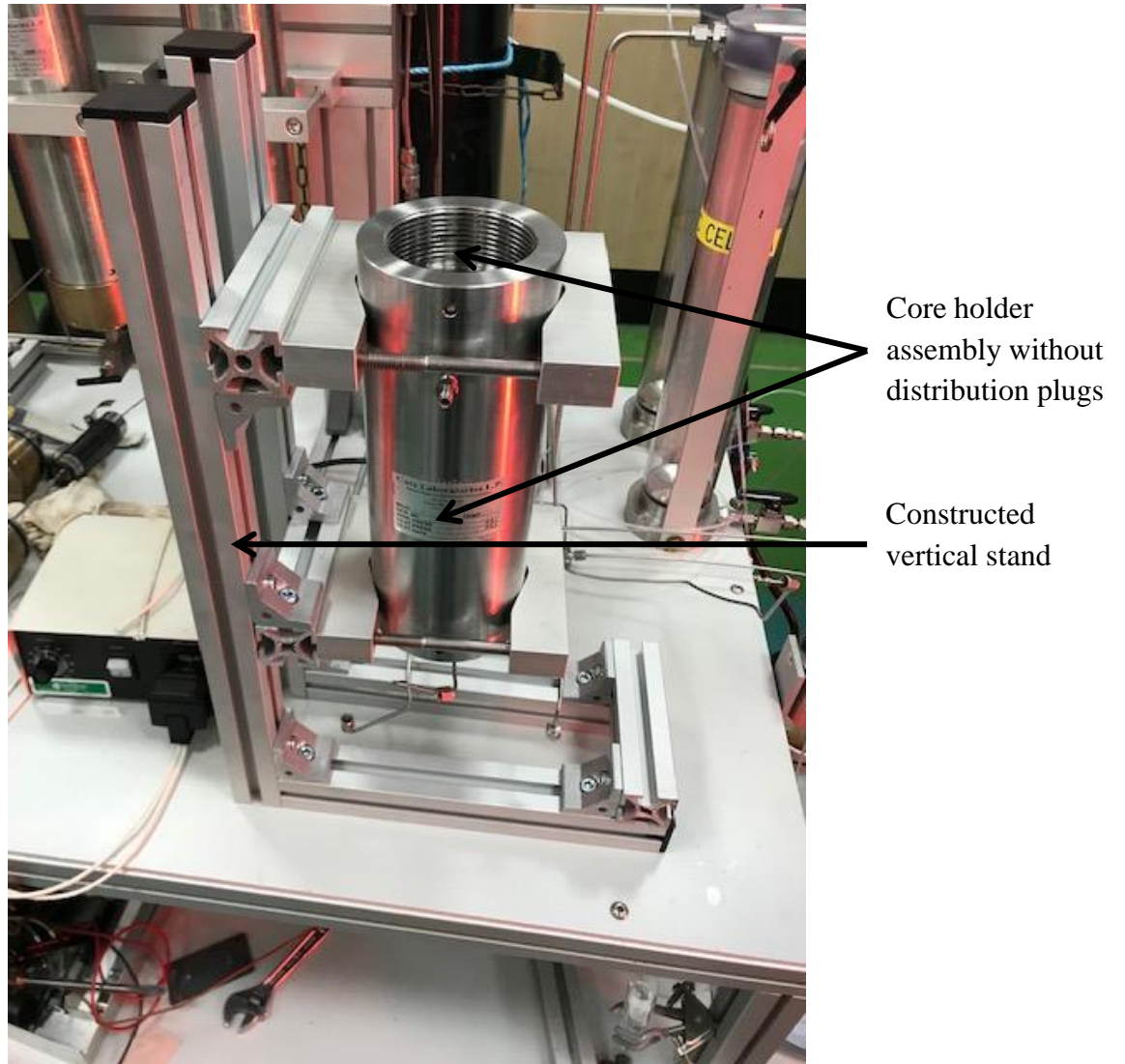
Figure 4.27 Core holder installed in the stand
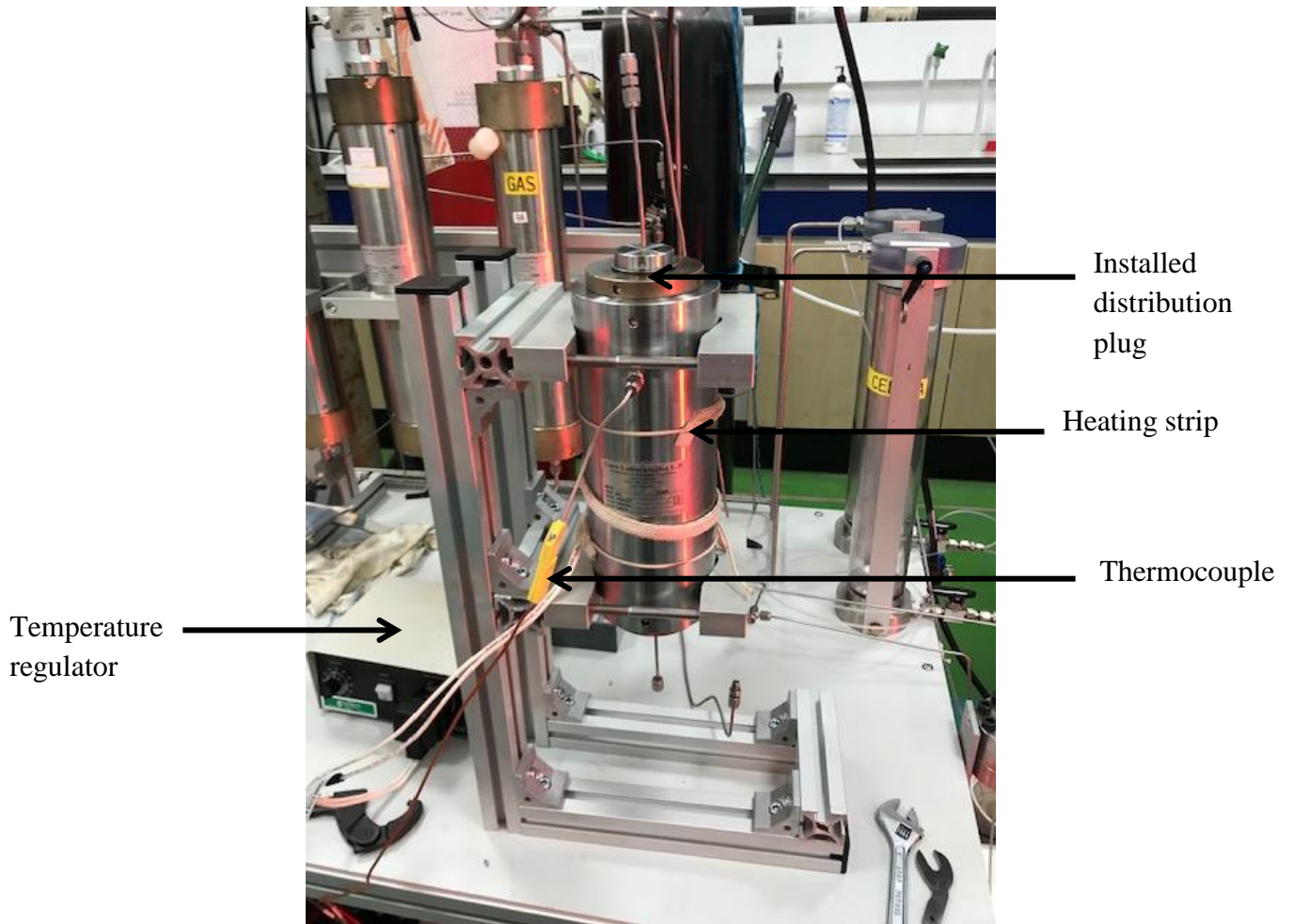
Figure 4.28 Core sample inserted and tubing coupled
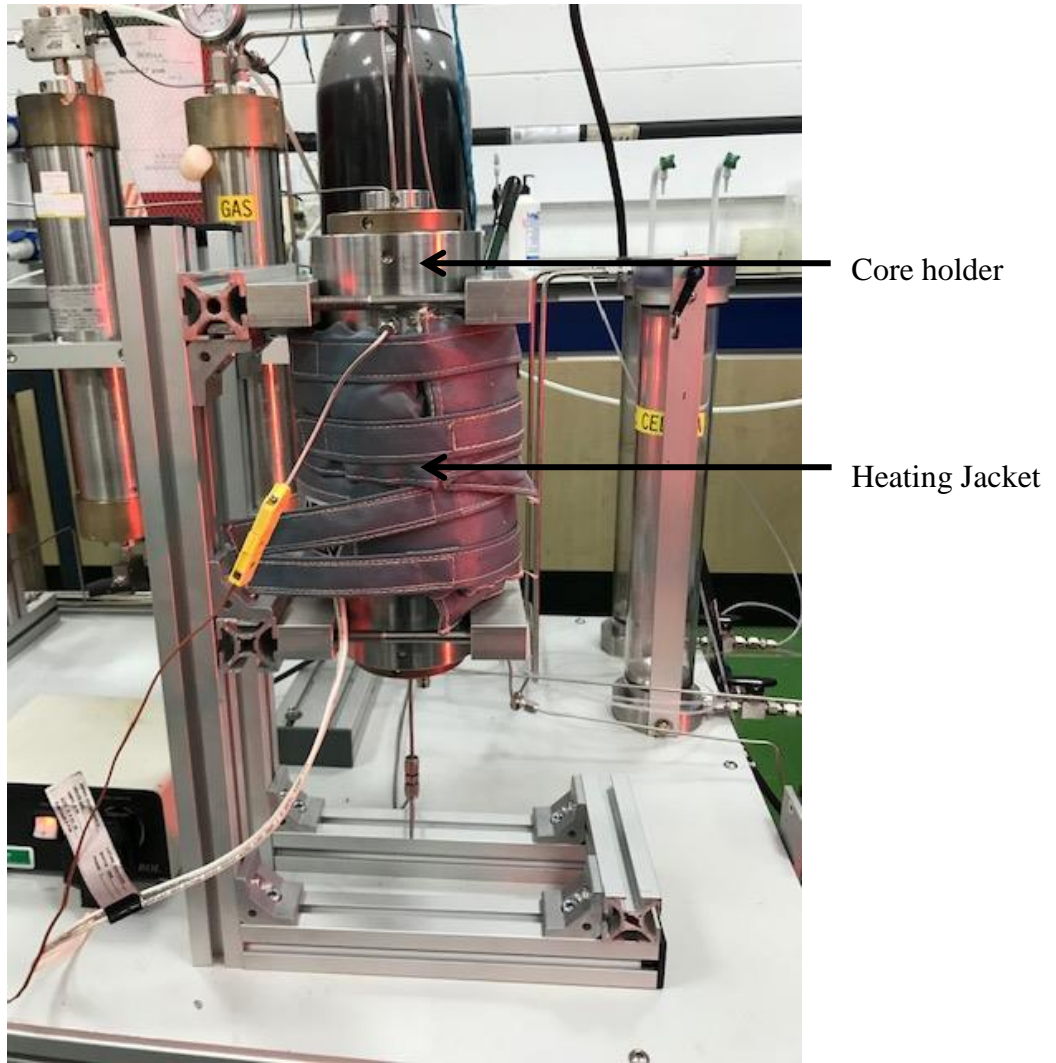
Figure 4.29 Core holder wrapped with heating jacket and ready for core flooding

4.4.4 Effluent analysis

An Agilent Gas chromatograph (GC) 7890 A with serial number CN12241131 was employed in this work. This GC is configured to analyse natural gas according to the ASTM (American Standard for Material and Testing) method 1945 and the GPA (Gas Processors Association) method 2261 on a sour gas sample. The analyser is a three-valve system using 1/8-inch packed columns with four columns for a multicomponent separation. A plumbing diagram is shown in Figure 4.30. The GC is plumbed in nickel tubing. Columns have nickel tubing. The gas inlet filter is in Hastelloy material. These materials are chosen to reduce corrosion due to acidic components of the sour gas samples.
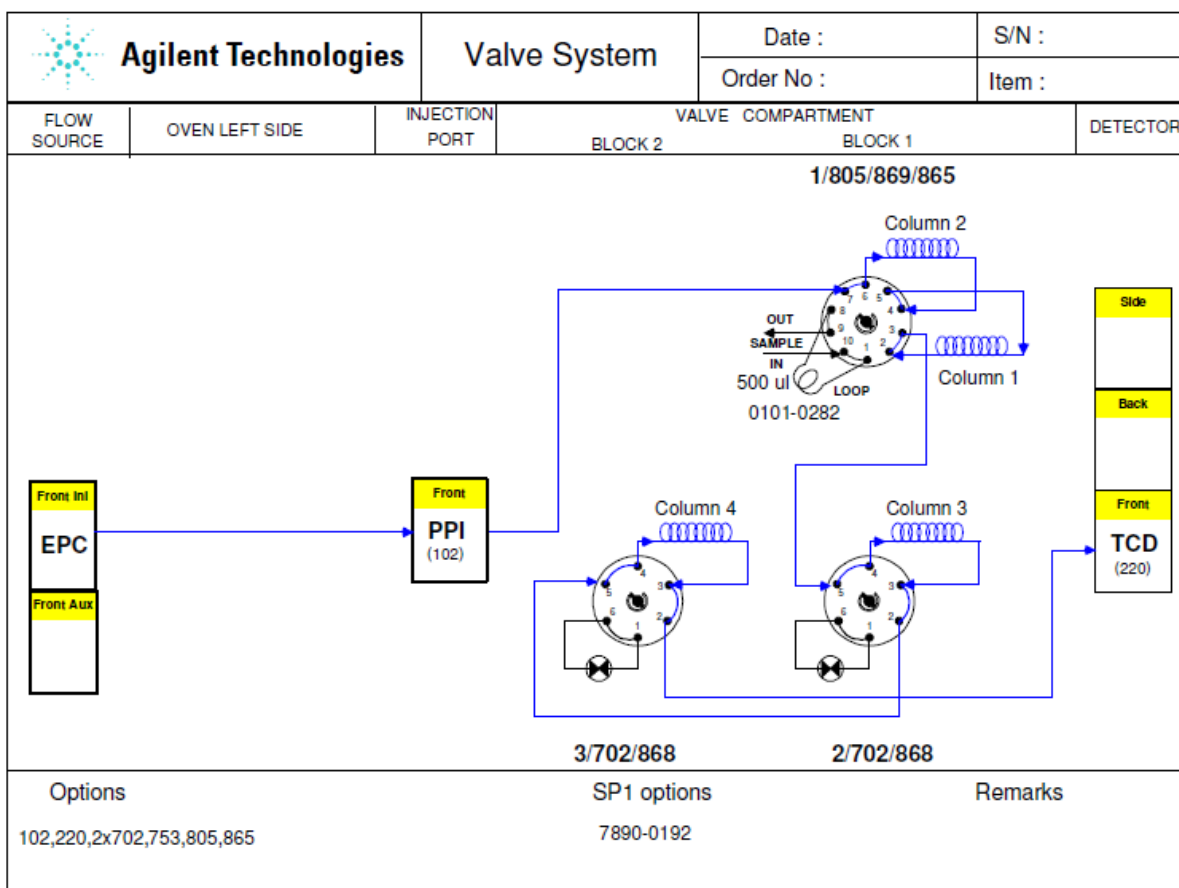
Figure 4.30 Plumbing schematics of the GC (Agilent, 2010)

The plumbing schematic shows a packed inlet as the flow source for the valves. The pneumatics control module can also be used as a flow source. Valve 1 is a 10-port valve configured as a gas sampling with sequence reversal and backflush of the pre-column. Valves 2 and 3 are column isolation valves and in this case assigned as others. This particular application can be combined into more complex systems, allowing the inclusion of more inlets, detectors, etc.

Nevertheless, the basic design can always be traced down because the plumbing, flow sources and general function will not change. However, a modified method was adopted for the Enhanced Gas recovery application as shown in Chapter three where the run time was trimmed down to 5 minutes as against the 30 minutes run time for the default sour natural gas with heavy components separation. This was achieved by increasing the oven temperature from originally 90°C to 130°C taking precautions not to create a condensing phenomenon at the front inlet by also increasing the temperature of the inlet to about 120°C. The flowrate of the carrier gas was also increased from 27ml/min to 40ml/min for reduce the elusion time of the CO_2 and CH_4. Column 4 – Molecular sieve was by passed by shutting off the valve 3

before the commencement of the injection as shown in the modified method in chapter three as CO_2 will not elute from it. It is designed to separate light gases.

4.4.5 Columns

Agilent 7890A GC utilises packed column design to cater for the sensitivity of the application. It is more rigorous than the capillary columns in the separation of natural gas components.

The columns used in this GC are as follows, as shown in Figure 4.34;

- Column 1- 2 Foot 12% UCW982 on PAW 80/100 mesh
- Column 2 - 15 Foot 25% DC200 on PAW 80/100 mesh
- Column 3 - 10 Foot HayesepQ 80/100 mesh
- Column 4 - 10 Foot Molecular Sieve 13X 45/60 mesh

Each column is designed with a specific type of packing composition. The Molecular Sieve 13X is made up of a form of synthetic zeolite packing with specific pore size mesh of 80/100. The column is made from a nickel material that can withstand a temperature of up to 350°C. it is used to separate light gases like oxygen, methane, nitrogen, and carbon dioxide and also inert gases like krypton, neon, argon, and helium. The design of the column provides an adequate retention for better separation and consistency.

The HayesepQ column is composed of a Divinylbenzene polymer as the packing material in a nickel alloy with a maximum operating temperature of 275°C. It has large surface area owing to its porous morphology, being that it has a variety of porous structure ranging from micropore to mesopores thereby making it suitable for separation and analysis of gases, amines, water, and other organic low carbon number components. Furthermore, it is quite inert and exhibits hydrophobicity.

Methyl vinylpolysiloxane is the packing material in the UCW 982 column which is made up of stainless steel. It has an operating temperature of 200°C.

4.5.2 Thermal Conductivity Detector (TCD)

The thermal conductivity detector (TCD) works based on the differences in thermal conductivity between carrier gas and sample components i.e. column effluent flow, and a reference flow of carrier gas alone. It produces a voltage proportional to this difference. The

voltage then becomes the output signal to the connected chart recording or integrating device. The two gas streams are switched over the filament at a rate of about 5 times per second, by the switching solenoid valve. An audible "clicking" can be heard when the detector is on. Crucial to the proper response of the TCD is:

- Temperature of the detector
- Flow rate ratio of the column + makeup gas flow and the reference flow
- Filament resistance

If either of these factors is not optimal, then the response of the TCD will be compromised.

4.5.3 Signal Analysis

The OpenLab Chemstation software (v.01.19.00), developed by Agilent Technologies, processes the raw data obtained from the separation analysis and component detection in the gas chromatograph and displays the results as peaks in the chromatography. It is user friendly and provides an interface for method and sequence modification. The interface is shown in Figure 4.31. The method can be modified using the instrument control window shown in the schematics.
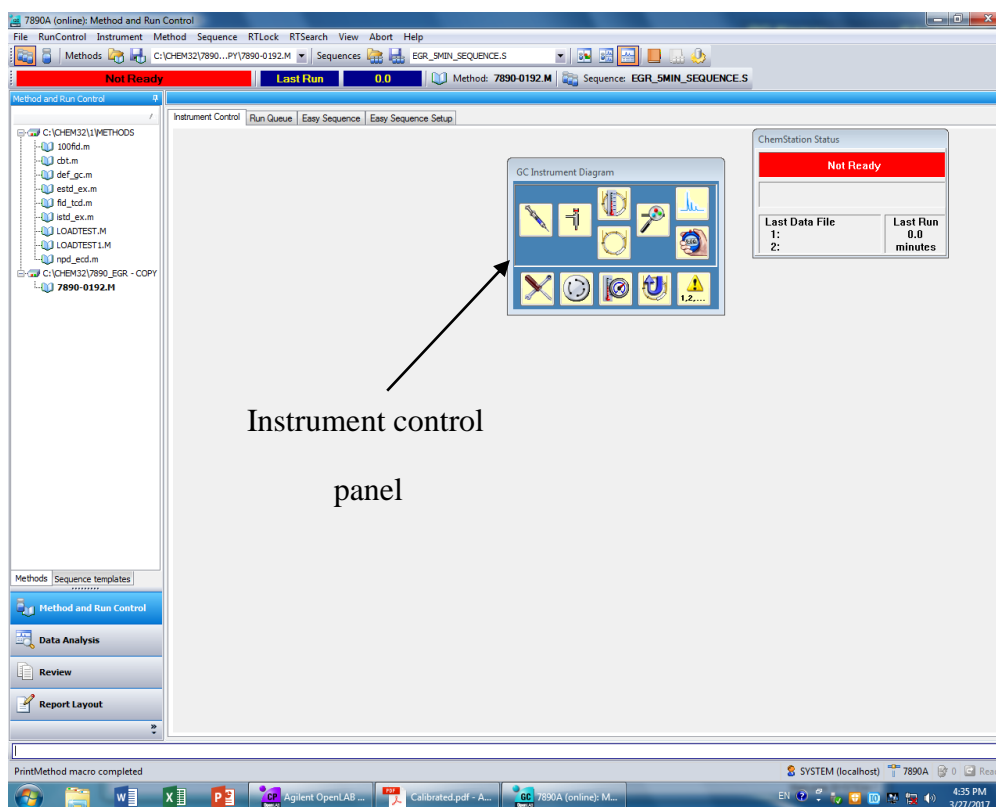
Figure 4.31 Interface of the OpenLab Chemstation software
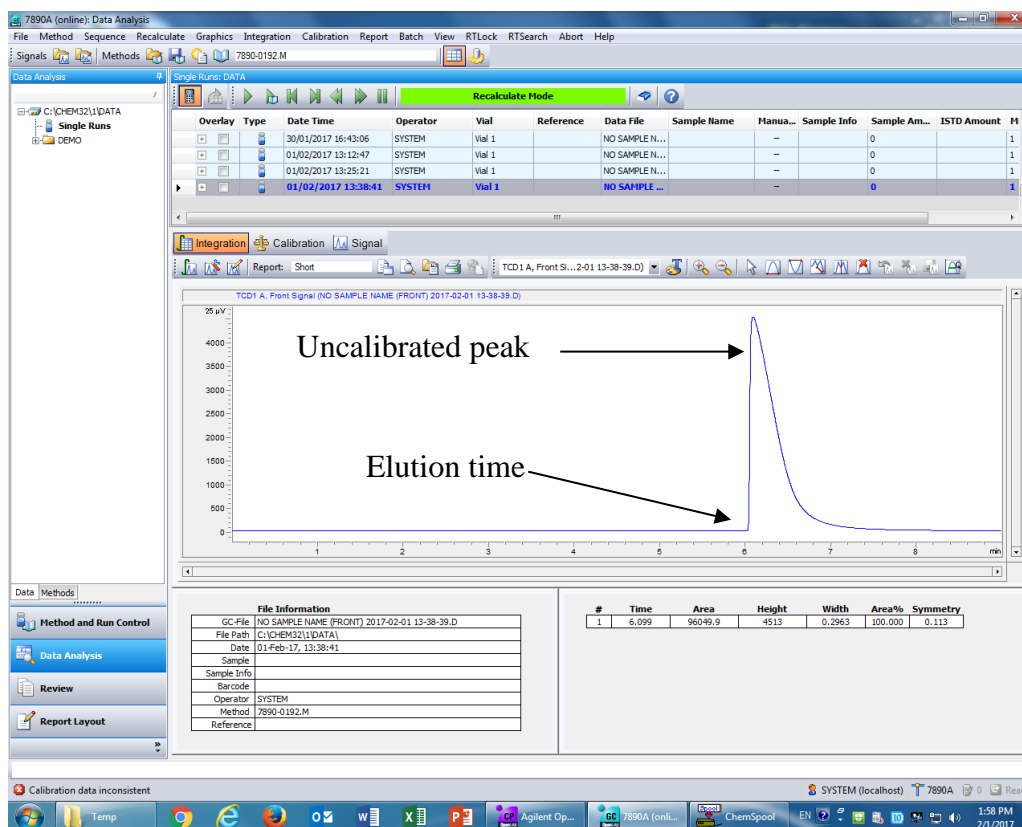
Figure 4.32 Chromatogram showing an uncalibrated methane peak

An uncalibrated peak of an unknown gas species is shown in Figure 4.32 with an elution time of about 6 minutes. This window provides the platform to calibrate the system with the desired calibration gas for the desired application. In this case, CO_2, CH_4, N_2, and O_2 were calibrated to create the concentration profiles required for the dispersion evaluation. The standalone GC system set up is shown in Figure 4.33 with the data acquisition PC which records the chromatogram.

GC

Data

Acquisition

system
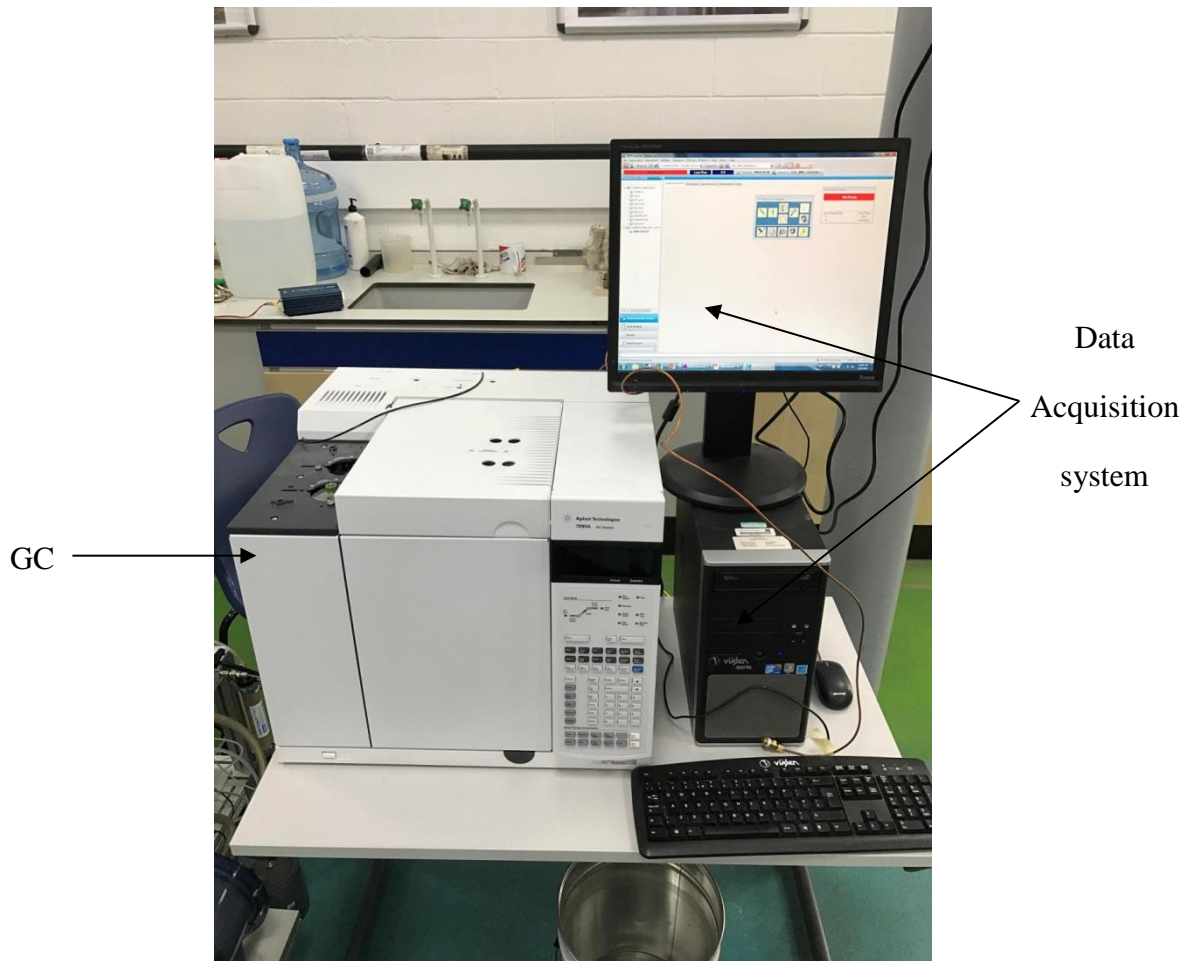
Figure 4.33 Agilent GC with data acquisition station
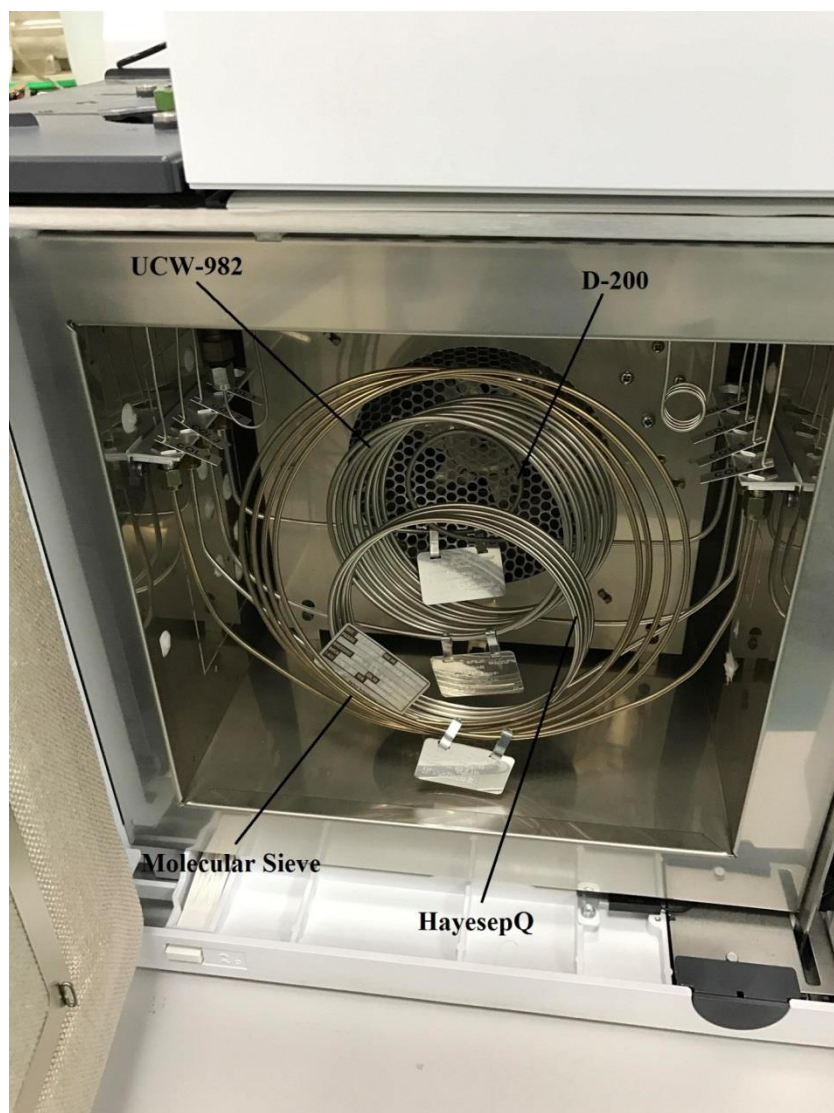
Figure 4.34 GC oven showing the four columns
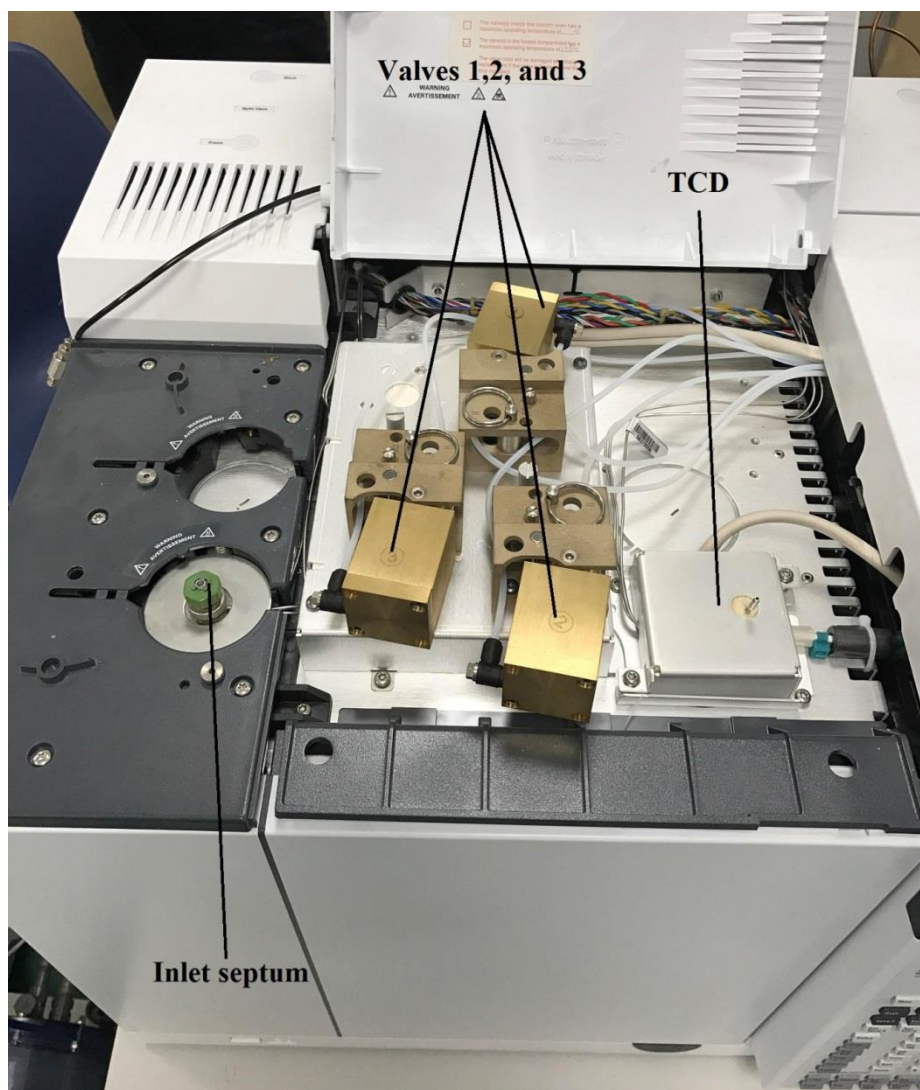
Figure 4.35 Pneumatic valves and the detector

4.5   Interfacial tension measurement

A Corelab high pressure high temperature surface interaction energy experimental set up was used in this research. The setup is shown below in Figure 4.36:
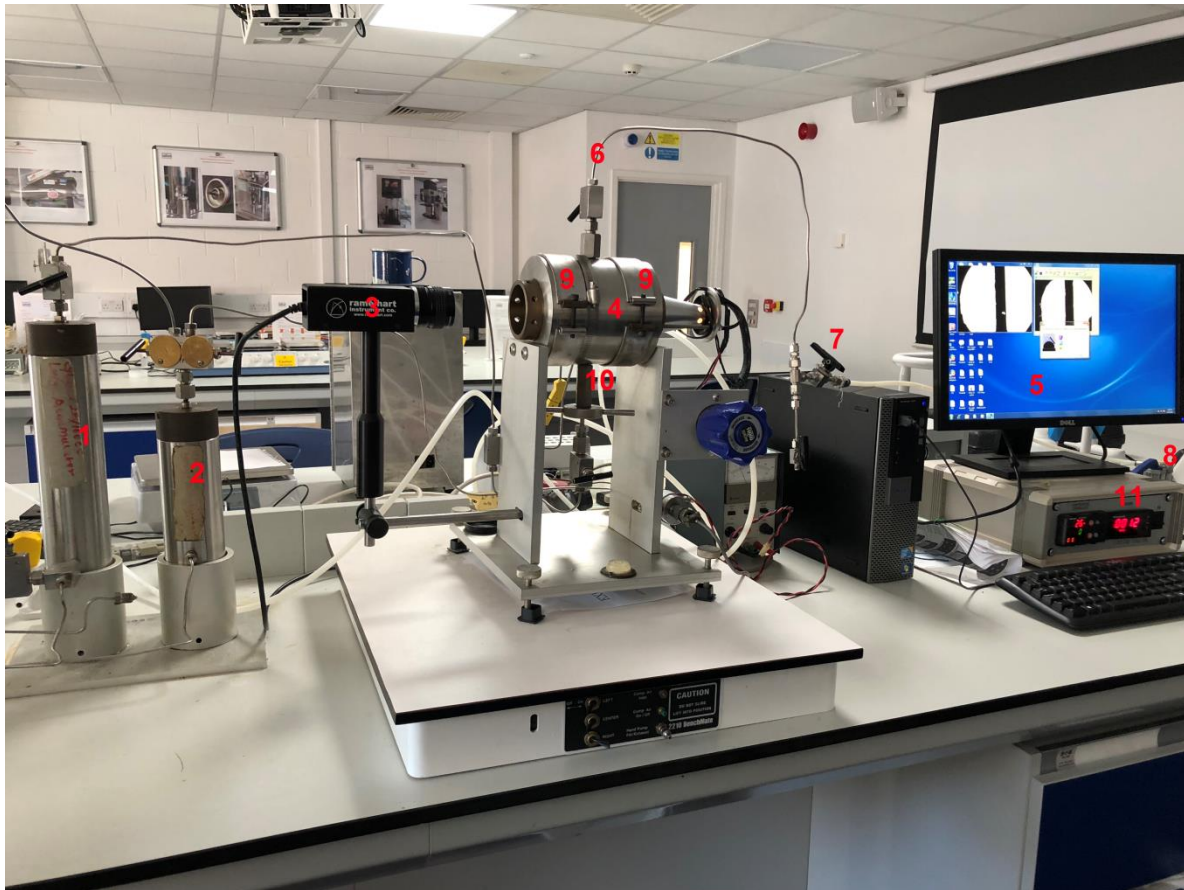
Figure 4.36 IFT set up

*(1&2) accumulators (3) Rame hart digital camera (4) IFT cell (5) Monitor (6) Vent Valve (7) Vacuum Valve (8) Vacuum pump (9) Heating element (10) Injection Needle (11) data logger and temperature controller

It is made up of a high pressure measurement cell with a pressure rating of up to 12,000 psig, a Rame-Hart optical video camera system for onscreen real time image display which is connected to a computer and interfaced with a digital image processing software (DropImage software developed by Rame-hart Instruments Co.) used for the IFT determination using image analysis of the gas bubble captured by the camera, a high pressure HiP 62-6-10 manual pump with a pressure rating of 10,000 psig for charging the external phase (brine) and a Temco temperature controller used to set the temperature of the system and maintains it within a range of $\pm$ 0.3°C of the set temperature. The IFT is measured using DropImage software which uses a theoretical algorithm to evaluate the IFT based on the bubble profile generated and the dimensions.

4.5.1 Procedure

Before each measurement, precautionary steps were taken to rid the system of any contaminant to ensure good experiments and to obtain reliable results. The accumulators (1&2), the IFT cell (4), the injection needle (10), the delivery tubing were soaked in acetone

for 2 hours, and this step was repeated for all new samples being investigated. These components were coupled back together and then evacuated using vacuum pump (8). Hot distilled water was then placed inside the accumulators and then injected into IFT cell to flush the whole system. Dry compressed air was then used to dry the entire system. The external phases (brine/distilled water) was then charged into the cell using the manual pump till the desired pressure was attained and also the temperature was set using Corelab temperature controller. After the pressures and temperatures have stabilised, the gases (CH_4 or CO_2) were then introduced into the drop phase accumulator. Then the manual pump was used to pressurise the gas to the desire test pressures. Creating the bubble inside the test cell was done by gently opening the injection needle valve and monitoring the development of the bubble. The bubble development and collapse were recorded.

This bubble measurement was repeated for 5 bubbles in each experiment using the DropImage software for repeatability and acquired data reliability and the IFT measurement was made repeatedly on each bubble image obtained.

CHAPTER 5

5   RESULTS AND DISCUSSION

5.1   Overview

This research entailed a concept of and relevant literature on enhanced gas recovery by CO_2 injection and characterisation of the acquired core samples. The aim of the core flooding is to investigate the efficiency of the displacement of CH_4 by supercritical CO_2 and also the parameters responsible for the excessive mixing of the injected CO_2 and the nascent CH_4 during enhanced gas recovery.

The Phase I of the research work was to characterise the samples accurately using state of the art techniques. The mean grain diameter determination provided an alternative to the conventional characteristic length of mixing, α, then a comparative analysis was made to investigate which property better presented the mechanism of dispersion/mixing during CO_2 displacement of CH_4 for enhanced gas recovery.

The second phase of the research comprised the experimental laboratory core flooding process which involved the injection of supercritical CO_2 to displace CH_4 at simulated reservoir conditions as stated in Chapter 4. The effect of the injection orientation was also determined and analysed in this phase to ascertain the sensitivity of the injection pattern on the displacement process.

Phase 3 is the final phase of the experimental design in this research which buttresses the effect of connate water salinity on the dispersion of CO_2 during EGR. Furthermore, the investigation of the solubility trapping as the secondary mechanism of CO_2 storage during EGR was highlighted in this phase. Therefore, the results obtained were presented in the sequence of the experimental design as follows:

5.2   Phase I: Core sample characterisation

As already discussed in section 5.1, the sequence of the experiments will be highlighted in accordance with the experimental design of established in Chapter 3. After the core sample cleaning using Soxhlet extraction, the characterisation of the core sample was the next step to determine the petrophysical properties of the core samples. Furthermore, this section highlighted the results obtained from the core sample characterisation. These include porosity measurements, permeability evaluation, and grain diameter determination using various

techniques as were presented. They are discussed and presented in the order as aforementioned.

5.2.1 Porosity Determination

The techniques used in this determination include Helium Porosimetry, CT technique, and saturation methods. Each technique has its peculiarity and the results are compared to see the accuracy of each measurement.

5.2.1.1 Helium Porosimetry

The pore volume was obtained by the relationship between grain volume and bulk volume.

Table 5.1 shows the results obtained from the helium Porosimetry technique.

Table 5.1 Pore volume evaluation

Core Samples	Bulk Volume (BV) (cm³)	Grain Volume (GV) (cm³)	(PV) PV = BV - GV (cm³)	Porosity (%)
Bandera Grey	38.7	32.1	6.6	17.05
Grey Berea	38.1	30.6	7.5	19.75
Buff Berea	37.3	27.5	9.8	26.27

Grain volume was obtained from gas porosimetry using the Helium porosimeter based on Boyle's law and results generated from a built-in Microsoft excel program.

5.2.1.2 X-Ray CT for Porosity determination

From (Akin & Kovscek, 2003), Porosity can be determined using CT X-ray from equation 4.4 in Chapter 4:

The samples were scanned using the CT settings shown in Table 5.2. The choice of these settings was based on the core sample composition (quartz) which has high density, the sensitivity of the detector in the CT scanner, and the intensity of the protons to penetrate the core sample and obtain a good scan.

Table 5.2 CT parameters used for scanning

SN	Parameter	Value
1	Tube Voltage (kV)	100
2	Tube Current (µA)	200
3	Power (W)	20
4	Timing (ms)	200
5	Average	4
6	Skip	1
7	Sensitivity	4

For all the scans, these settings were used for consistency of results to evaluate the porosity using the contrasts and intensities during the scans. The results from the evaluated CT numbers using Eq. 4.6 are shown in Table 5.3.

Table 5.3 Porosity results from X-ray CT

Core Samples	CT Numbers (WET)	CT Numbers (DRY)	Porosity (%)
Bandera Grey	15623	2103	17.6
Grey Berea	14138	1835	20.3
Buff Berea	9438	1343	26.6

Taking the CT Numbers of water and air as 11118 and 6909 respectively, the porosities were evaluated using the expression depicted in Eq. 6.

The images from the CT scan for the dry core scans are shown in Figure 5.1 to 5.3 for Bandera grey, Grey Berea, and Buff Berea, respectively. There was not obvious change visually but only the attenuations due to increase in density of the saturated core samples.

Figure 5.1 Bandera grey 3D CT Image

Figure 5.2 Grey Berea 3D CT image
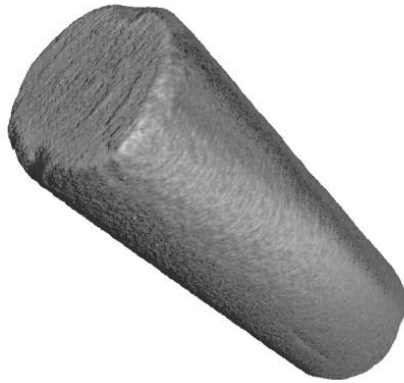
Figure 5.3 Buff Berea 3D CT Image

5.2.1.3 Saturation method of porosity determination

The weights of the dry core samples prior to the saturation were measured. They are then saturated under vacuum with distilled water and their weights were measured after every 30 minutes until there was no change in the weights. This indicated that the saturation limit of the core samples was reached, and it was safe to say the samples were 100% saturated with water.

The 100% saturated core sample was then placed in a beaker with distilled water of known volume and the increase in weight of the total weight of the beaker + water + saturated core sample to measure the bulk volume.

The results are given in Table 5.4.

Table 5.4 Core Saturation results and liquid pore volumes

Core samples	Dry weight (g)	Saturated weight (g)	Pore Volumes (cm³)	Wet Bulk Volume (cm³)	Porosity (%)
Bandera Grey	81.42	86.29	4.87	57.72	16.69
Grey Berea	80.10	85.44	5.34	58.17	20.10
Buff Berea	73.58	80.03	6.45	55.22	26.20

Taking the density of distilled water as 0.998 g/cm^3

$$V = \frac{m}{\rho} \qquad (5.1)$$

Where, *V is volume in cm^3, m is mass in g, and ρ is density in g/cm^3*

Table 5.5 shows the overall porosity measurements of the sample using all the techniques in this study. The measured porosities using both x-ray CT and helium porosimetry show a trend of consistency which goes on to present the measured porosities are more accurate than the one given by the company where the samples were sourced. The core samples were saturated under vacuum using the set up shown in Chapter 4.

Comparing the pore volumes obtained from all the methods, there is a discrepancy in the values from the different methods. This is as a result of the gas compressibility. Water is an incompressible fluid; hence the effective pore volumes are usually lower than a compressible fluid such as gases.

Table 5.5 Porosity Results from different Methods

Core samples	Length (mm)	Diameter (mm)	*Porosity (%)	Porosimetry Porosity (%)	CT Porosity (%)	Saturation Porosity (%)
Bandera Grey	76.00	25.47	21	17	17.6	16.69
Grey Berea	76.27	25.22	19-20	20	20.3	20.10
Buff Berea	76.18	24.95	24	26.27	26.6	26.20

*Determined by Kocurek industries from where the samples were sourced

5.2.2 Permeability measurement

Using the set up for permeability determination shown in chapter 4, core sample absolute permeability to air was computed based on Darcy's law. Due to the low pressures used, different permeability at different pressures and flowrates were determined so as to apply Klinkinberg's correction i.e. plotting the permeability against flowrates. This was applied to the Buff Berea with high porosity. For Bandera G rey sample, the sleeve in the core holder could not withstand pressures above 100 psig owing to its very low permeability; hence, an overburden of 200 psig was applied to keep the containing sleeve in place so as to obtain the necessary permeability at different pressures being cautious not to affect the absolute

permeability of the core sample. Taking viscosity of N_2 to be 1.98 x 10^{-2} cP, length of the core to be 7.618 cm, and area as 4.89 cm^2, the permeability (md) of each core sample was evaluated.

Permeability was evaluated using the expression for gases;

$$k = 2000 \frac{L}{A} \mu Q \frac{P_{atm}}{\Delta P}$$

(5.2)

Plotting the measured permeability against the flow rates will help evaluate the core samples absolute permeability by obtaining the intercept of the line of best fit through the points on the permeability axis.
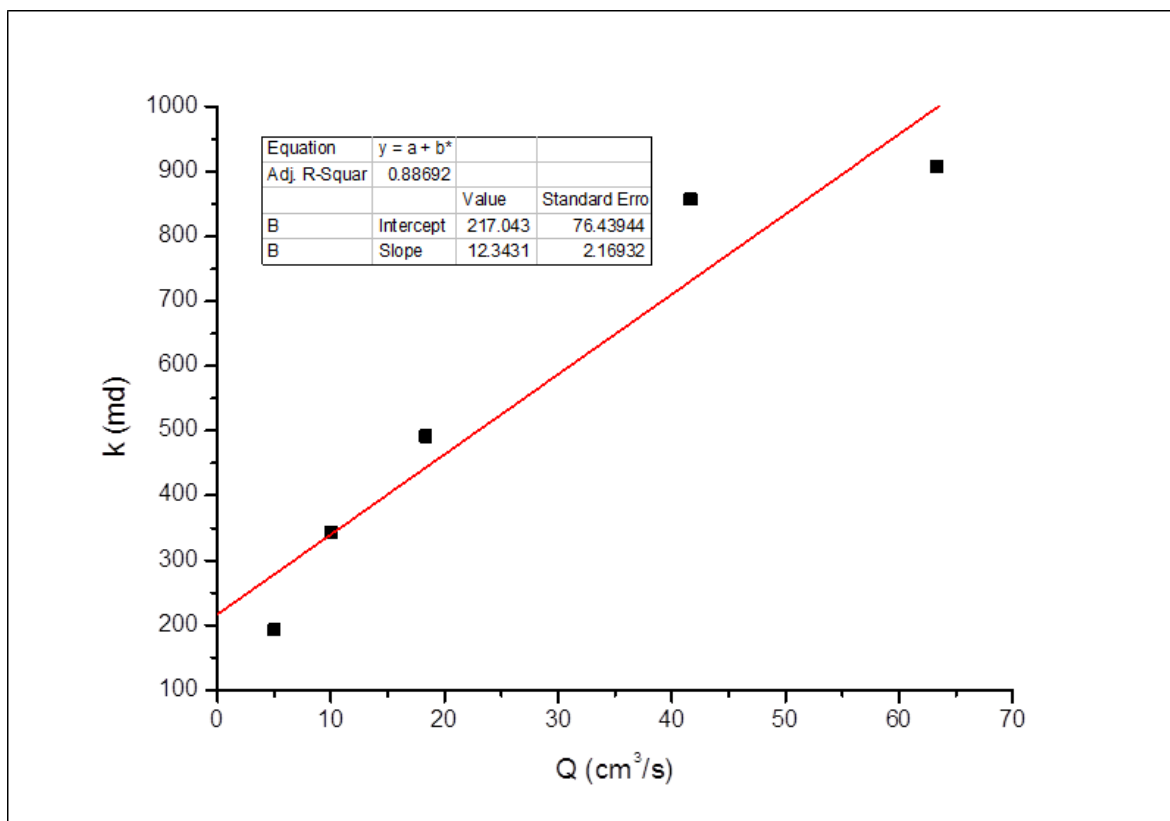
Figure 5.4 Graph of k as a function of Q for Grey Berea Sandstone sample

94
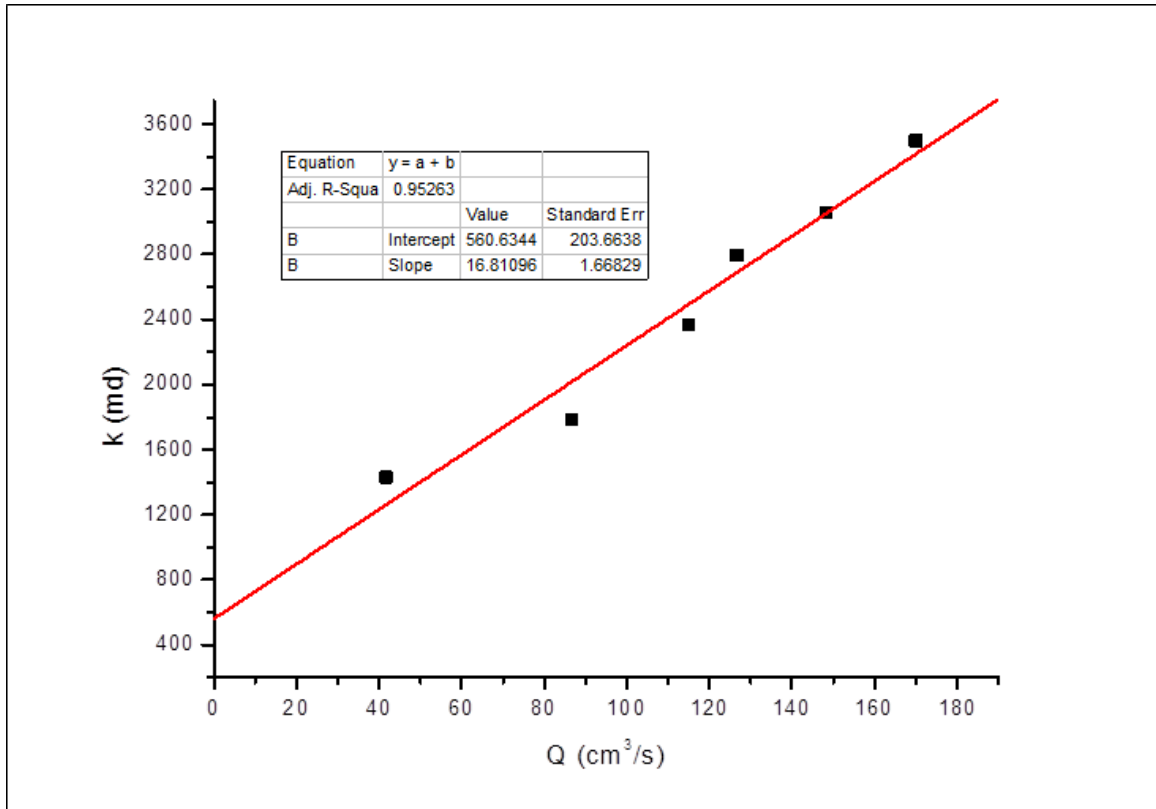
Figure 5.5 Graph of k as function of Q for Buff Berea Sandstone sample
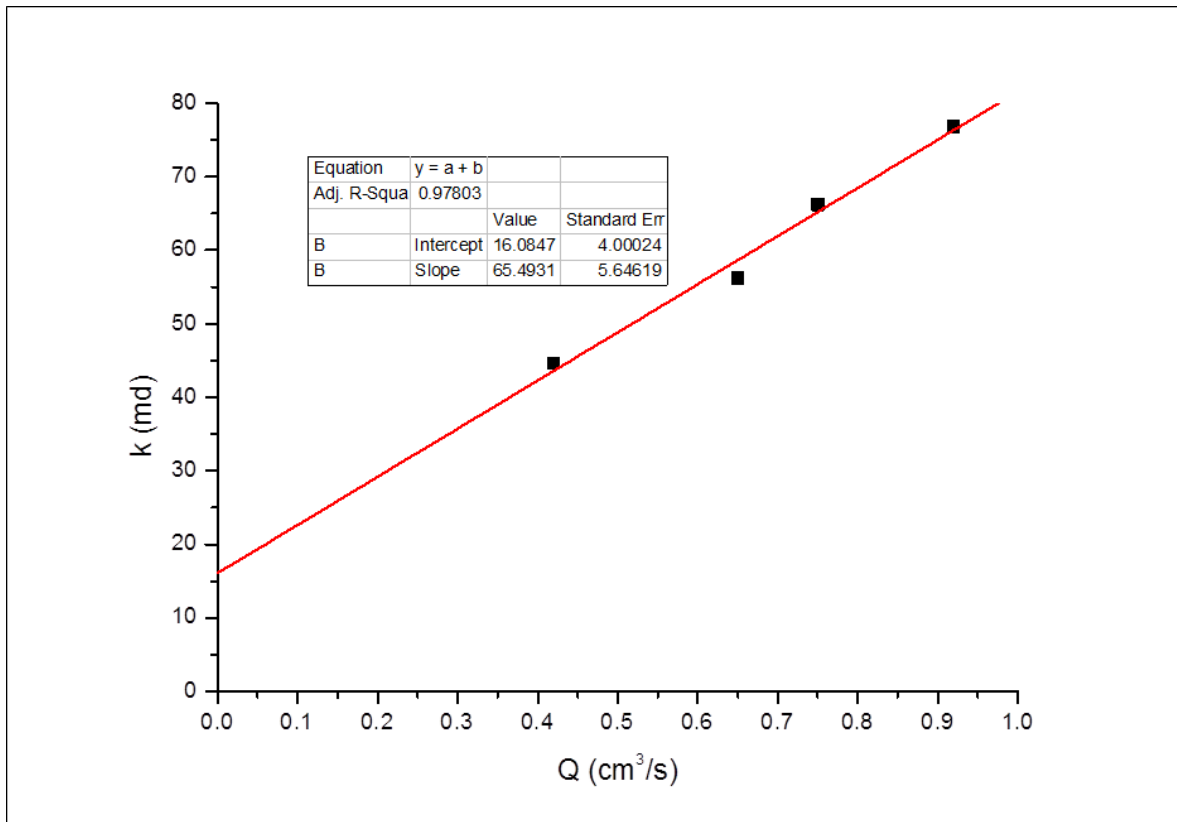
Figure 5.6 Graph of k as a function of Q for Bandera Grey Sandstone sample

The laboratory measured absolute gas permeability for each core sample is summarised in Table 5.6. All the values are within the given permeability from where the core samples were

sourced. However, referring to the results obtained for the Bandera grey which is significantly lower than the source permeability, this can be attributed to the overburden pressure applied during the measurement to exert pressure on the sleeve around the core sample within the core holder to prevent the simulated pore pressure build up from overpowering the sleeve enclosure. The overburden pressure lowers the permeability of the formation by compressing the pore openings and interconnected pore channels of the pore structure. These results will be the benchmark for all subsequent experiments.

Table 5.6 Summary of measured permeability of sandstone core samples

Core samples	Length (mm)	Diameter (mm)	*Permeability (mD)	Measured Permeability (mD)
Bandera Grey	76.00	25.47	30	16.08
Grey Berea	76.27	25.22	200-315	217.04
Buff Berea	76.18	24.95	350-600	560.63

*Determined by Kocurek industries from where the samples were sourced

5.2.3 Grain diameter determination

Using SEM images of sections of the core sample and ImageJ software for image processing, the mean grain diameter was obtained by equivalent circle diameter method (Olson, 2011). The grain particles at a magnification of 500um are irregular as shown in Figure 5.7. Post processing of these images is shown in Figure 5.8 and Figure 5.9.

The SEM images of sections of the core sample at different magnifications are shown in Appendix C. These SEM images were analysed with the image processing software ImageJ and the areas of each of the particles was obtained. Furthermore, there equivalent circle diameter was evaluated in Microsoft Excel and imported into IBM SPSS to generate the mean grain diameter as shown in Figure 5.10 to Figure 5.12.

Each core sample SEM images were obtained at different magnifications. This will help in determining the measurements more accurately and reliably. The steps to follow in carrying out the measurement are as discussed in the Section 4.2.5.
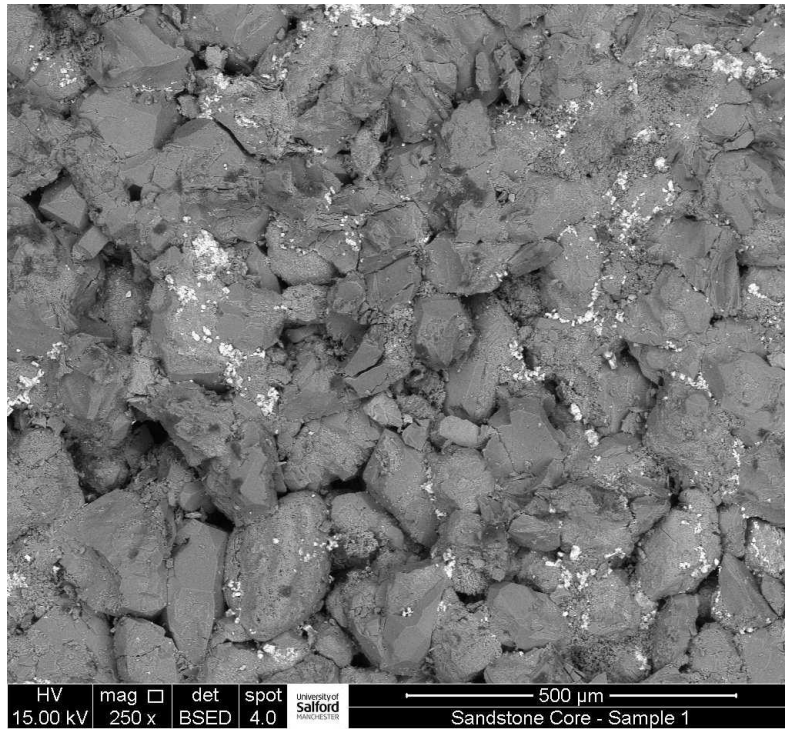
Figure 5.7 SEM image of a section of Grey Berea at 500 µm
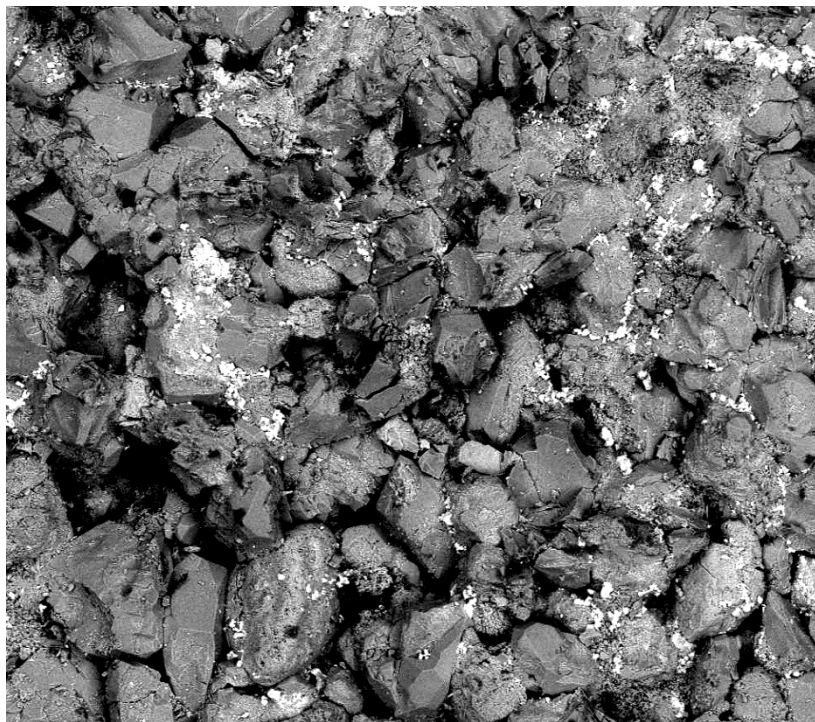
Figure 5.8 Post processed SEM image of Grey Berea showing threshold adjustment

97
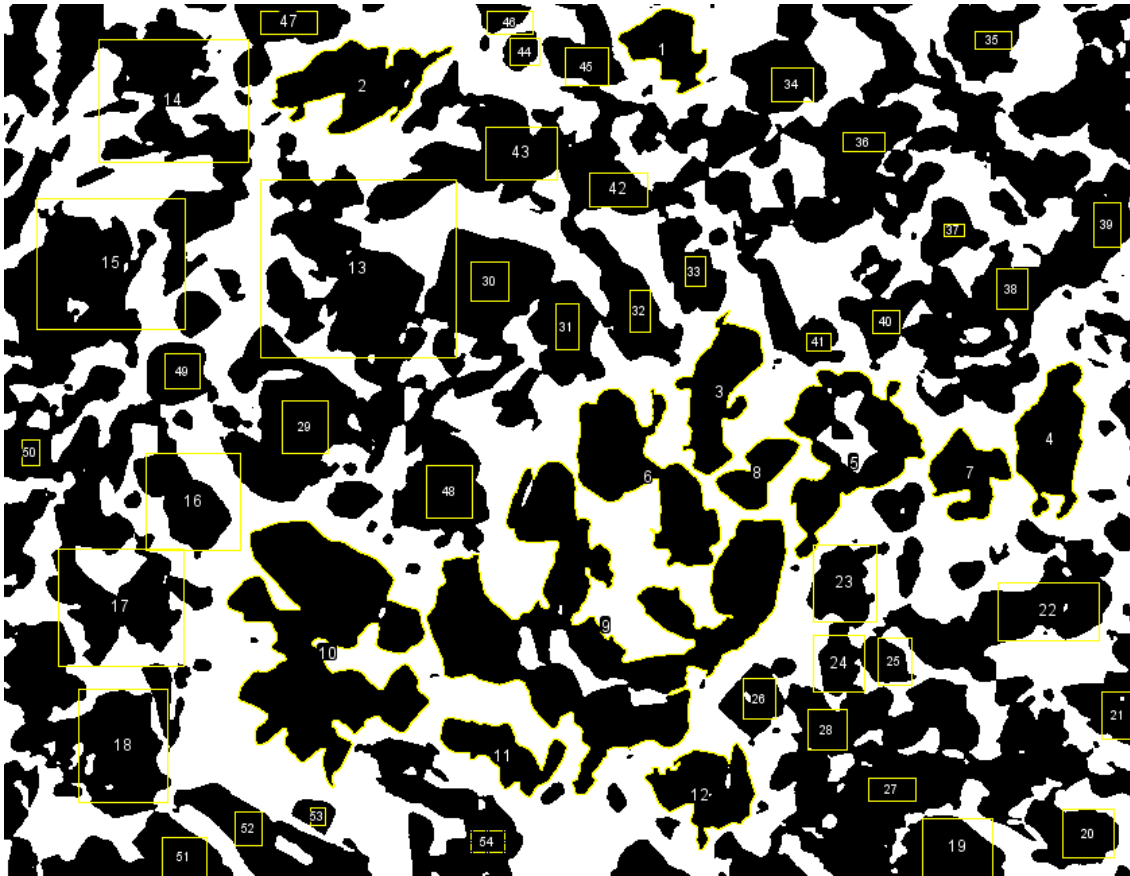
Figure 5.9 Image processing of SEM images to measure grain diameter of Grey Berea

All measurements on the core samples were carried out using the same procedure used in determining the grain diameter of Grey Berea. The data analysis follows in the next section.

5.2.3.1 Data analysis
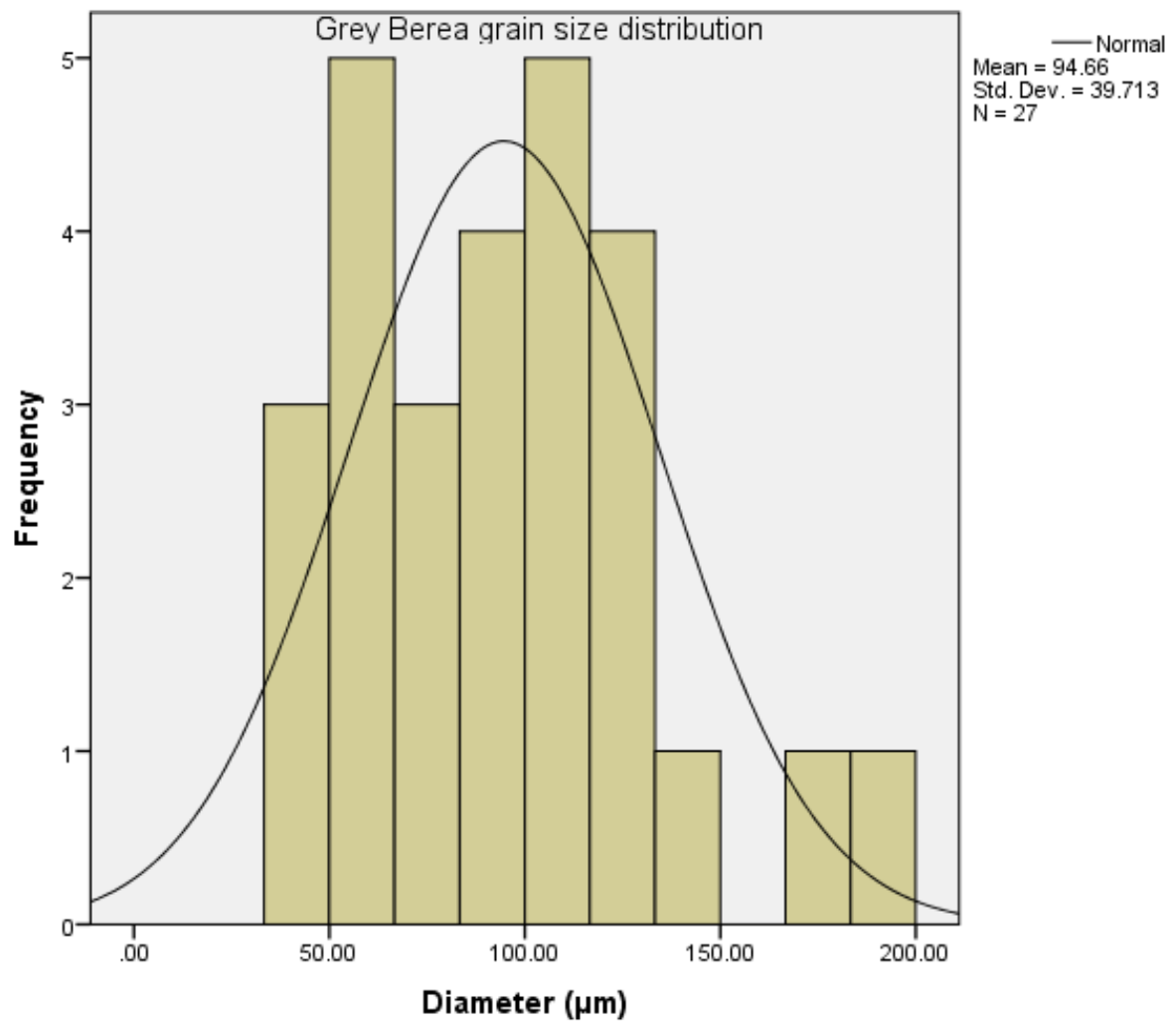
Figure 5.10 Grey Berea grain size distribution showing the mean grain diameter
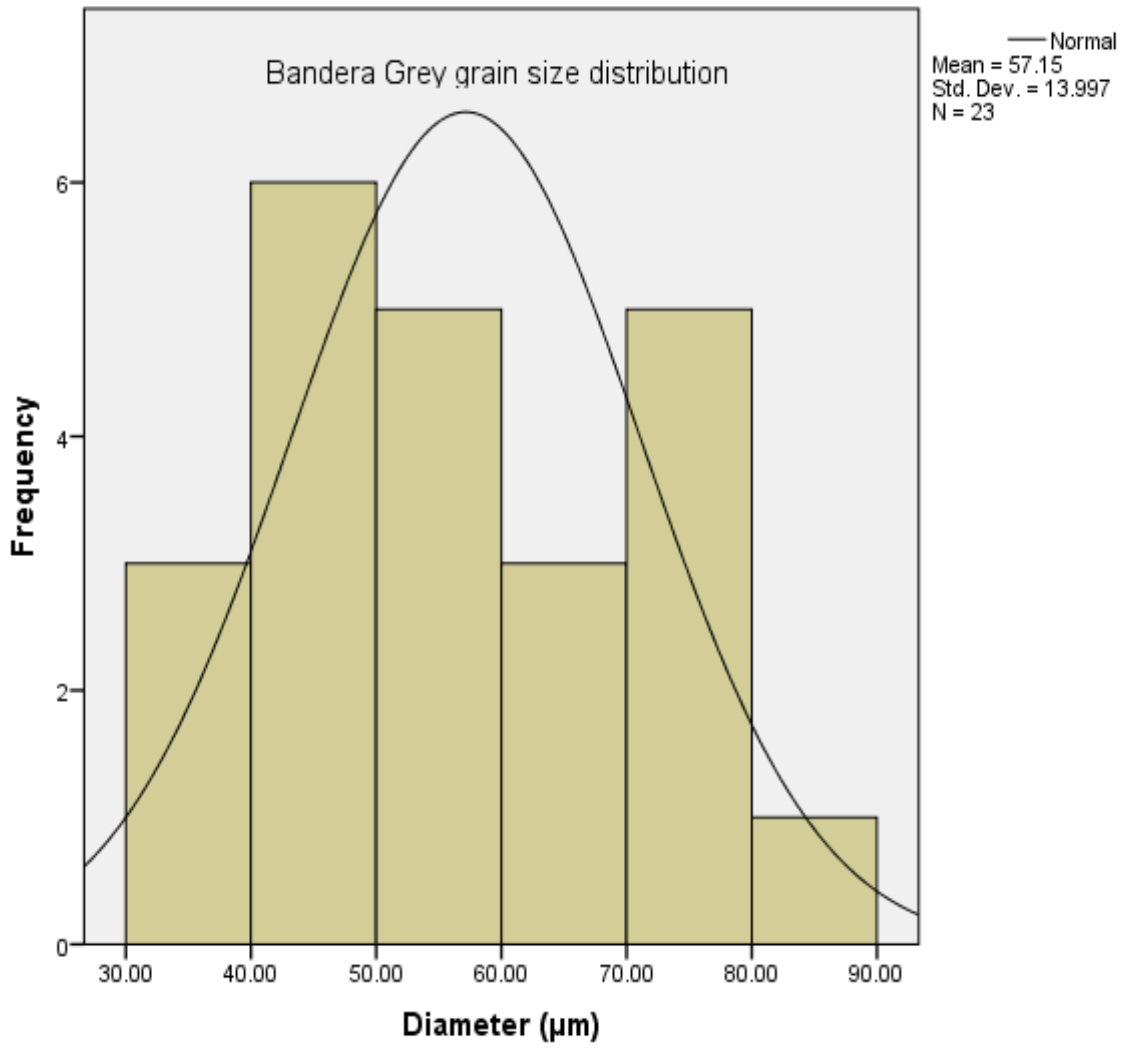
Figure 5.11 Bandera Grey grain size distribution showing the mean grain diameter
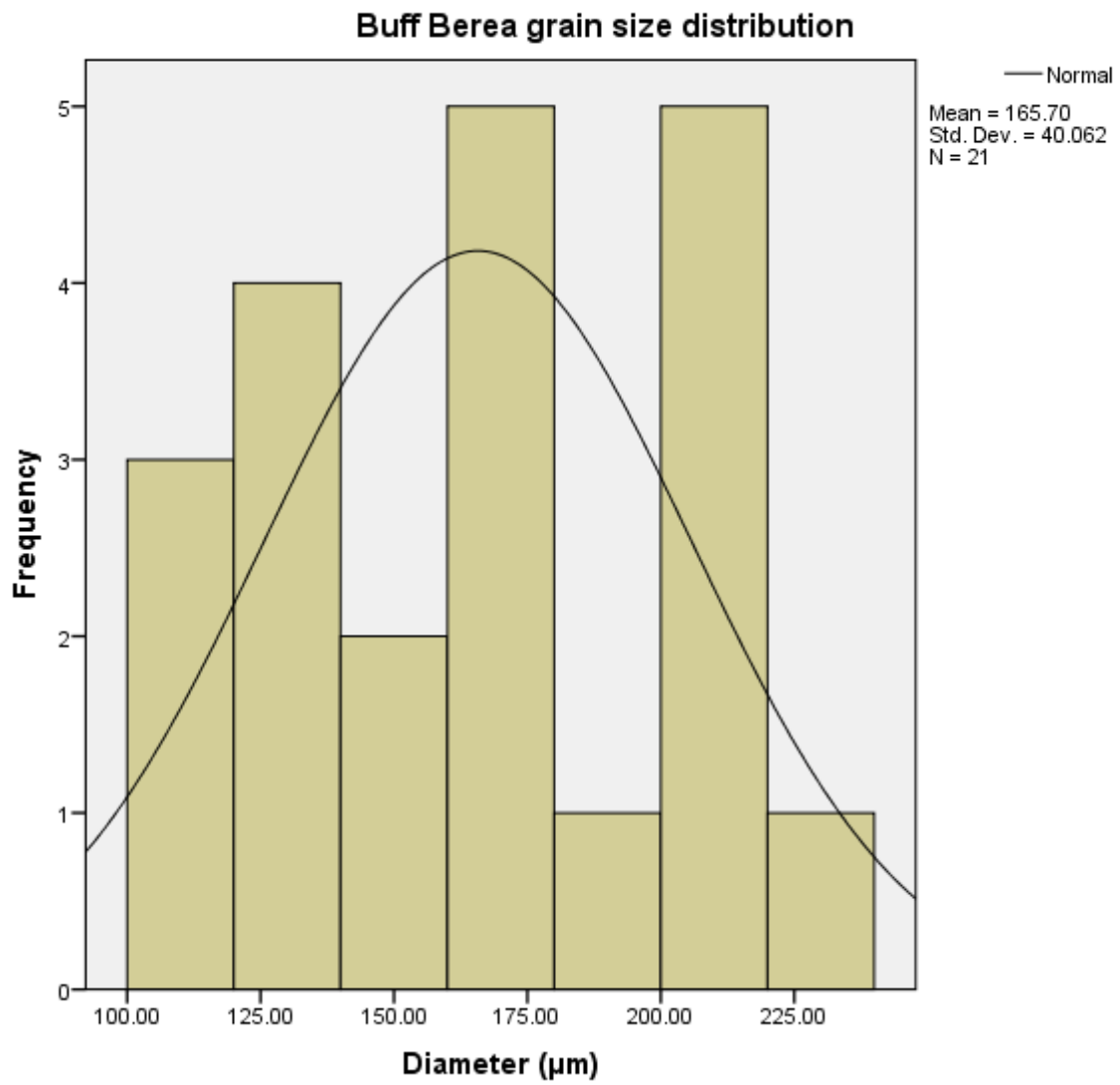
Figure 5.12 Buff Berea grain size distribution showing the mean grain diameter

Table 5.7 Result of mean grain diameter of core samples

S/N	Sample type	Mean grain diameter (µm)	Porosity (%)
1	Buff Berea	165.70	24
2	Grey Berea	94.66	20
3	Bandera Grey	57.15	17

From Table 5.7, it can be seen that the higher the porosity of the core samples the bigger the grain sizes therein. This is in line with the arrangement of the grain particles in that the larger the grain sizes, the larger the spaces between them, hence the larger the porosity. These results will be used as the characteristic length of mixing parameter in place of either the reservoir quality index (RQI) which is square root of the ratio of permeability to porosity ($\sqrt{\frac{k}{\phi}}$) or the dispersivity to compute the medium *Péclet* number for mechanism of displacement during the core flooding experimentation.

5.3 Phase II: Core flooding process

The determination of the petrophysical properties and the grain diameter of the core samples is a prerequisite for the core flooding process which is the Phase II of the thesis design. This facilitates the experimental investigation of the effects of systematic properties of the injection technique. The investigation of the effects of these systematic properties will be based on the displacement efficiency, flow behaviour, injection orientation, and dispersion of the injected CO_2. All core samples will be used in the core flooding and the results obtained will be compared to each individual run to evaluate the sensitivity of different petrophysical properties on the variation systematic properties as aforementioned.

As discussed in Chapter 4, section 4.3.2, the core flooding procedure, an overburden of 2200 psig was maintained by adjusting the drain valve intermittently throughout the core flooding process. The reservoir temperature of 50°C was kept steady by monitoring the heat jacket enclosure and a constant flowrate was maintained throughout the core flooding experimental runs.

Note that injection rates and flowrates are going to be used interchangeably as both describe the inflow of the CO_2 injected to displace the CH_4.

The petrophysical properties of the core samples are presented in Table 5.8 which were obtained from methodical core analysis in the first phase of the research.

Table 5.8 Petrophysical properties of core sample

Core sample	Length (mm)	Diameter (mm)	Porosity (%)	Permeability (md)	d (μm)
Grey Berea	76.27	25.22	20.10	217.04	94.66
Buff Berea	76.18	24.95	26.20	560.63	165.70
Bandera Grey	76.00	25.47	17.01	16.08	57.15

5.3.1   Reproducibility and Repeatability of the experimental setup and method

As stated, the determination of the dispersion coefficient will be highlighted here and the corresponding mechanism of displacement will be evaluated for each of the core samples using the dispersion coefficient as a function of the medium *Péclet* number. This will help determine the CO_2 injection pattern chosen for further investigations.

Prior to the actual experimental runs, the integrity and repeatability of the experimental set up and method was tested by running several runs on *Grey Berea* sandstone at an arbitrary injection rate of 0.25 ml/min at 1300 psig and 50°C for consistency. Several concentration profiles were obtained, and the dispersion coefficient evaluated.

Table 5.9 Repeatability test dispersion coefficients

Runs	K_L ($10^{-8}m^2/s$)
1	3.34
2	3.32
3	7.07
4	5.06
5	2.13
6	2.81
7	2.41
8	3.33
9	4.21
10	4.11

Before the curve fitting was carried out, the equation utilises the interstitial velocity and one of the principles in applying the 1D ADE is that the interstitial velocity is constant through the porous medium. The injection rate here however is in the form of volumetric and must be converted to interstitial velocity in order to provide the input variable in the equation for curve fitting. Therefore, the relationship between interstitial velocity and volumetric flow rate can be expressed as follows:

$$Q = V_s A \qquad (5.4)$$

Where Q is volumetric flow rate (cm^3/s), V_s is the superficial velocity (cm/s), and A is the cross-sectional area (cm^2).

and,

$$V_s = u\phi \qquad (5.5)$$

Where u is the interstitial velocity (cm/s) and ϕ is the porosity of the porous media.

So substituting Eq. (5.2) into Eq. 5.3 becomes

$$Q = u\phi A \qquad (5.6)$$

$$u = \frac{Q}{A\phi} \qquad (5.7)$$

From the table, Runs 1, 2, and 8 have fitted dispersion coefficients of 3.34, 3.32, and 3.33 x 10^{-8} m^2/s respectively with the highest relative difference in the fitted value of 1.13% and a standard deviation of 1.101%. These statistical evaluations imply that the method and experimental set up have good repeatability and reliability. The fitted curved are shown in Figure 5.13.
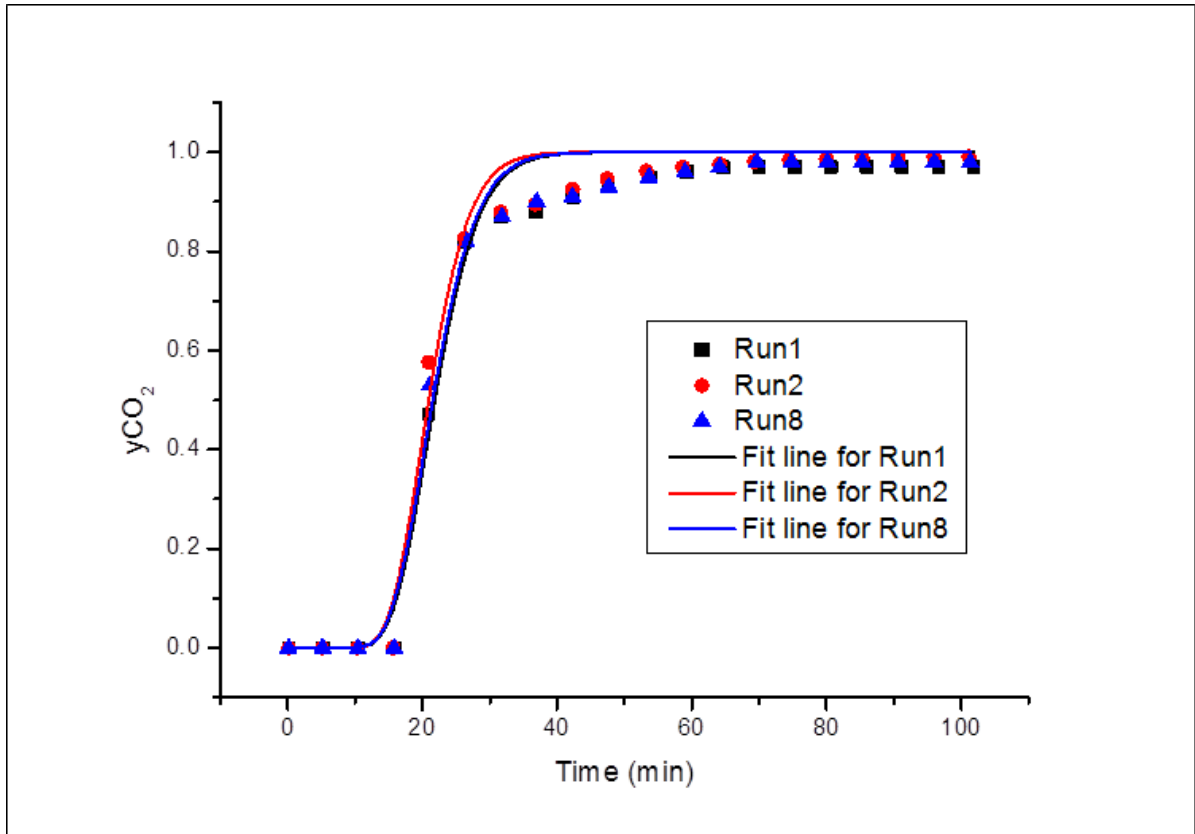
Figure 5.13 Concentration profile to evaluate the repeatability of the set up and method

From the evaluation of the grain diameters for individual core samples helped provide the dominant displacement mechanism during the experimental runs through determining the P_{ex}. In order to evaluate individual displacement mechanism for each core sample of interest, three repeated tests were carried out at 0.35 ml/min (average test flow rate) and the average of the obtained dispersion coefficient was used to compute the medium *Peclet* number of the core samples using Eq. 2.4. A comparison was made of the P_{ex} values using the conventional methods of using the RQI and dispersivity and also the technique used in this work i.e. grain diameter as the characteristic length scale of mixing. The results are presented in Table 5.10.

Table 5.10 Peclet number comparison for displacement mechanism evaluation

Core sample	Mean grain diameter (μm)	K_L (10^{-8}m²/s)	D (10^{-8} m²/s)	P_{ex} (d)	P_{ex} RQI	P_{ex} α
Bandera Grey	57.15	6.32	21.3	0.019	0.000133	0.483
Grey Berea	94.66	3.86	21.3	0.026	0.000287	0.124
Buff Berea	165.70	3.12	21.3	0.035	0.000303	0.128

At low flow velocities in porous media, solute transport is diffusion dominant and, conversely, at higher flow velocities dispersion takes precedence (Huysmans & Dassargues, 2005; Yu, Jackson, & Harmon, 1999). Identifying the displacement mechanisms in fluid transport in porous media is very important especially when investigating solute transport in porous media. For numerical simulation purposes, concise and accurate input parameters are prerequisites to obtaining precise results which will provide blueprints for which field applications of technique under investigation are adopted. Overestimation or underestimation of these input parameters leads to poor depiction of a technique of EGR which may have detrimental impact of the investigated technique either in terms of economics and or efficiency. Table 5.10 gives a range of P_{ex} using different characteristic length scales of mixing.

As seen, the values of the medium Peclet number, P_{ex}, for all the core samples fall below 0.1 using the grain diameter as the length scale of mixing which is indicative of diffusion dominant flow (discussed in Chapter 2 Sections 2.3) in the test core samples. The P_{ex} evaluated from the RQI gave an indication of diffusion dominant flow but showed categorically low values of P_{ex}. Furthermore, using the dispersivity α as the length scale, the values of the P_{ex} fell in the transition zone between molecular diffusion and mechanical dispersion displacement mechanisms. In both cases where the displacement was diffusion dominant, the injection rate plays a vital role as this will affect the factors that influence the mixing of the displacing and displaced gases. As aforementioned, overestimation and underestimation of Pex is clearly the case from the table. At low P_{ex} values where diffusion is the dominant displacement mechanism, flow is concentration driven and as such transport is aided by mobility of the molecules through the flow velocity (Perkins & Johnston, 1963). The choice of the flow velocity in EGR thus becomes imperative as higher injection rates leads to incessant mixing of the gases and lower injection rates provide longer resident times for the gases in contact and hence increases the mixing of the gases yet again (Hughes et al., 2012). The P_{ex} values give an indication of the optimum injection rates which translates into the better displacement and lower dispersion during EGR.

This affords an insight into the injection strategy adopted in this research. Given that the displacement mechanism is diffusion dominant, the choice of lower injection rates provided smoother concentration profiles for proper analysis as opposed to higher injection rates. Low P_{ex} values, like those obtained from RQI, drive for lower injection rates and are likely to

propagate higher mixing, and high values of P_{ex} as those evaluated from α needs a higher injection rates during displacement and this will also increase the mixing of the gases and instil poor sweep efficiency. However, P_{ex} values obtained from the d lie between the P_{ex} obtained from both methods and will help in adopting an optimum range of injection rates which will be adopted in this work.

5.3.2 Investigation of injection rates and injection orientations

The core holder orientation was switched from horizontal to vertical orientations for all the core samples to ascertain the impact of these patterns on the mixing/dispersion and also the flow behaviour of supercritical CO_2 during EGR.

5.3.2.1 Grey Berea

The effects of injection rates and the orientation of the core sample was carried out and analysed to highlight the influence of the injection orientation on the displacement. First, the orientation investigation will be carried out in the horizontal procedure.

5.3.2.1.1 Horizontal orientation

The CO_2 injection/flow rates were varied from 0.2, 0.3, 0.4 to 0.5 ml/min. These flowrates were chosen based on the P_{ex} evaluated and reaffirmed by literature data (Hughes et al., 2012; S. Liu et al., 2015) and with respect to the size/scale of the laboratory experimental set up and core samples relative to actual field tracer tests. This was carried out to investigate the effects of injection rate variation on the mixing/dispersion between the injected CO_2 and the nascent CH_4. This provided a dependable way of determining the best or optimum flowrate during EGR investigations.

Table 5.11 shows the effluent composition for each of the runs obtained from the GC. It shows the percentages by volume of CO_2 at each injection point at 5 minutes interval to create a concentration profile (Figure 5.14). This was used to curve fit the experimental results with Eq. 2.8 to obtain the longitudinal dispersion coefficient.

Table 5.11 Core flooding effluent percentage composition by volume for horizontal orientation

Q = 0.2 ml/min		Q = 0.3 ml/min		Q = 0.4 ml/min		Q = 0.5 ml/min	
Time (min)	CO_2 (%)	Time (min)	CO_2 (%)	Time (min)	CO_2 (%)	Time (min)	CO_2 (%)
0.16	0	0.17	0	0.16	0	0.16	0
5.49	0	5.5	0	5.16	0	5.32	0
10.83	0	10.83	0.25	10.49	0.41	10.66	30.62
16.17	4.99	15.99	18.58	15.66	55.04	15.99	81.79
21.51	63.15	21.5	65.51	21.16	79.32	21.16	89.93
26.67	73.52	26.67	78.46	26.32	85.1	26.5	96.26
32.17	78.31	32.17	82.94	31.66	91.12	31.82	98.93
37.32	81.24	37.33	87.34	36.99	96.05	37.16	99.73
42.67	83.79	42.66	93.35	42.32	96.94	42.32	99.64
47.99	85.45	47.99	95.82	47.49	97.05	47.66	99.81
53.67	87.14	54	96.56				
58.99	88.54	59.33	96.66				
64.33	89.44	64.66	97.72				
69.47	91.23						

From Table 5.11, it can be seen that the breakthrough times of CO_2 for each set of results decreased with increasing flowrates. This is obvious as increase in the injection rate invariably increases the interstitial velocity in porous media which in turn increases the kinetic energy of the gas molecules which invariably leads to more dispersion.

The mole fractions of CO_2 were extracted from Table 5.11 to ascertain the rate of mixing between the injected CO_2 and the CH_4 insitu using Eq. (2.8) as to fit the equation to the experimental data and using the longitudinal dispersion coefficient K_L as the fitting parameter. The L_{exp} too was adjusted in the regression to provide a better fit as advised by Hughes et al. (2012) and adopted by Liu et al. (2015) in that the interstitial velocity was held constant as assumed in the 1D advection dispersion equation (ADE). Least square regression analysis was the method employed in the curve fitting process.

The curve fitting was carried out using OriginPro 8 software and the curve fitted concentration profiles for each test flowrates are shown in Figure 5.14. The dispersion coefficients were evaluated and are shown in Table 5.10 and as discussed earlier, the K_L increases with increase in the interstitial velocity. Eq. 5.4 was used to calculate the interstitial velocities using the individual injection flow rates, Q and used in the software as the input parameter.

$$u = \frac{Q}{\phi A} \tag{5.8}$$

Table 5.12 CO_2 mole fractions for each experiment in the horizontal orientation at differrnt injection rates

Q = 0.2 ml/min		Q = 0.3 ml/min		Q = 0.4 ml/min		Q = 0.5 ml/min	
Time (min)	yCO_2	Time (min)	yCO_2	Time (min)	yCO_2	Time (min)	yCO_2
0.16	0	0.17	0	0.16	0	0.16	0
5.49	0	5.5	0	5.16	0	5.32	0
10.83	0	10.83	0.0025	10.49	0.0041	10.66	0.3062
16.17	0.0499	15.99	0.1858	15.66	0.5504	15.99	0.8179
21.51	0.6315	21.5	0.6551	21.16	0.7932	21.16	0.8993
26.67	0.7352	26.67	0.7846	26.32	0.851	26.5	0.9626
32.17	0.7831	32.17	0.8294	31.66	0.9112	31.82	0.9893
37.32	0.8124	37.33	0.8734	36.99	0.9605	37.16	0.9973
42.67	0.8379	42.66	0.9335	42.32	0.9694	42.32	0.9964
47.99	0.8545	47.99	0.9582	47.49	0.9705	47.66	0.9981
53.67	0.8714	54	0.9656				
58.99	0.8854	59.33	0.9666				
64.33	0.8944	64.66	0.9772				
69.47	0.9123						

There was early breakthrough for 0.5 ml/min and late breakthrough at 0.2 ml/min as expected. The fitting of the 1D ADE to the experimental results was meagre as a result of systematics errors like entry and exit effects and capillary tailing as described in the works of (Hughes et al., 2012). This was noted for all the runs in the entire experiments. However, these do not affect the evaluation of the parameter – dispersion coefficient. For all subsequent experiments, these systematic effects are noticed and are presented as such.
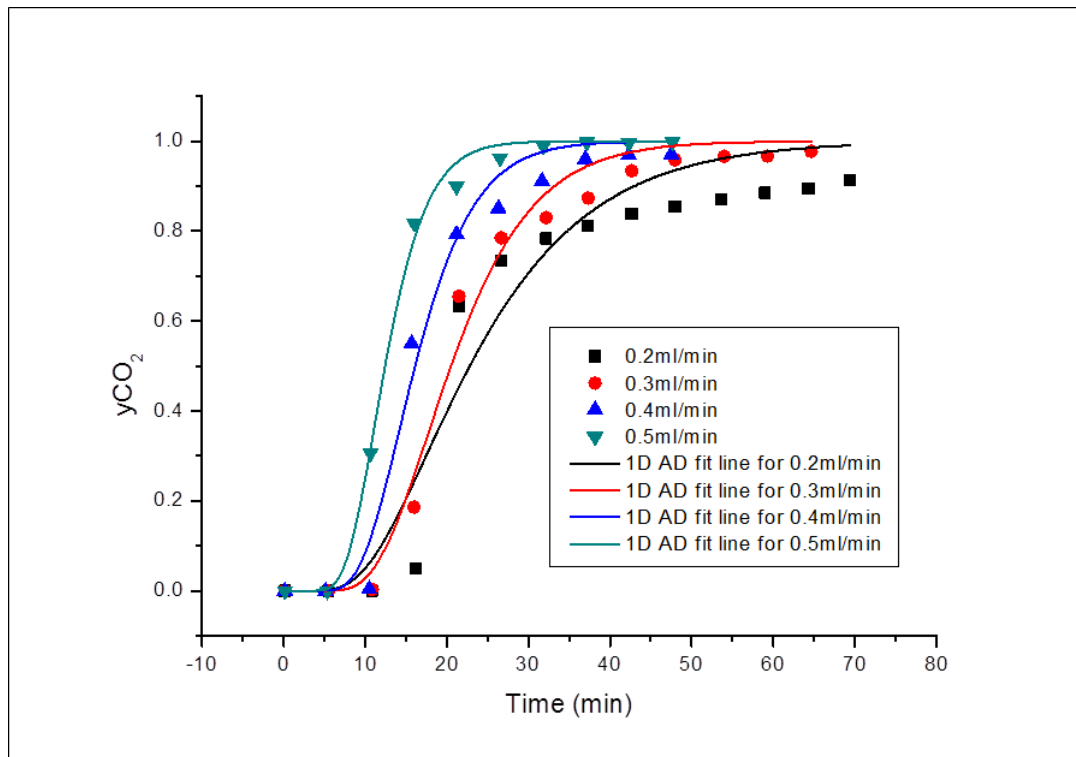
Figure 5.14 Concentration profile for Grey Berea in horizontal orientation

Using Eq. 2.9, the diffusion coefficients, D, were evaluated at the experimental conditions and were also presented in Table 5.10. It is essential when describing the dispersivity, α, and the Pex of the core sample and also compare the results to those in literature which will further reaffirm the accuracy of the experiments.

Table 5.13 Dispersion coefficients of CO_2 in CH_4 as functions of concentration profiles

Q (ml/min)	Pressure (psig)	Temperature (°C)	u (10^{-5} m/s)	K_L (10^{-8} m^2/s)	D (10^{-8} m^2/s)	u/D	k/D
0.2	1300	50	3.350	3.11	5.33	621.5857	0.583489681
0.3	1300	50	5.025	3.64	5.33	938.2001	0.682926829
0.4	1300	50	6.700	4.01	5.33	1250.683	0.750469043
0.5	1300	50	8.376	5.51	5.33	1564.293	1.031894934

The dispersivity can be analytically evaluated by fitting Eq. (2.5) to the plots of u/D against k/D which is a straight line as shown in Figure 5.15.

The equation shown in the figure:

$$\frac{K_l}{D} = \frac{1}{\tau} + \alpha \frac{u_m^n}{D}$$

Equation	y = a + b*x		
Adj. R-Square	0.84755		
		Value	Standard Error
B	Intercept	0.26777	0.12344
B	Slope	4.49494E-4	1.06904E-4
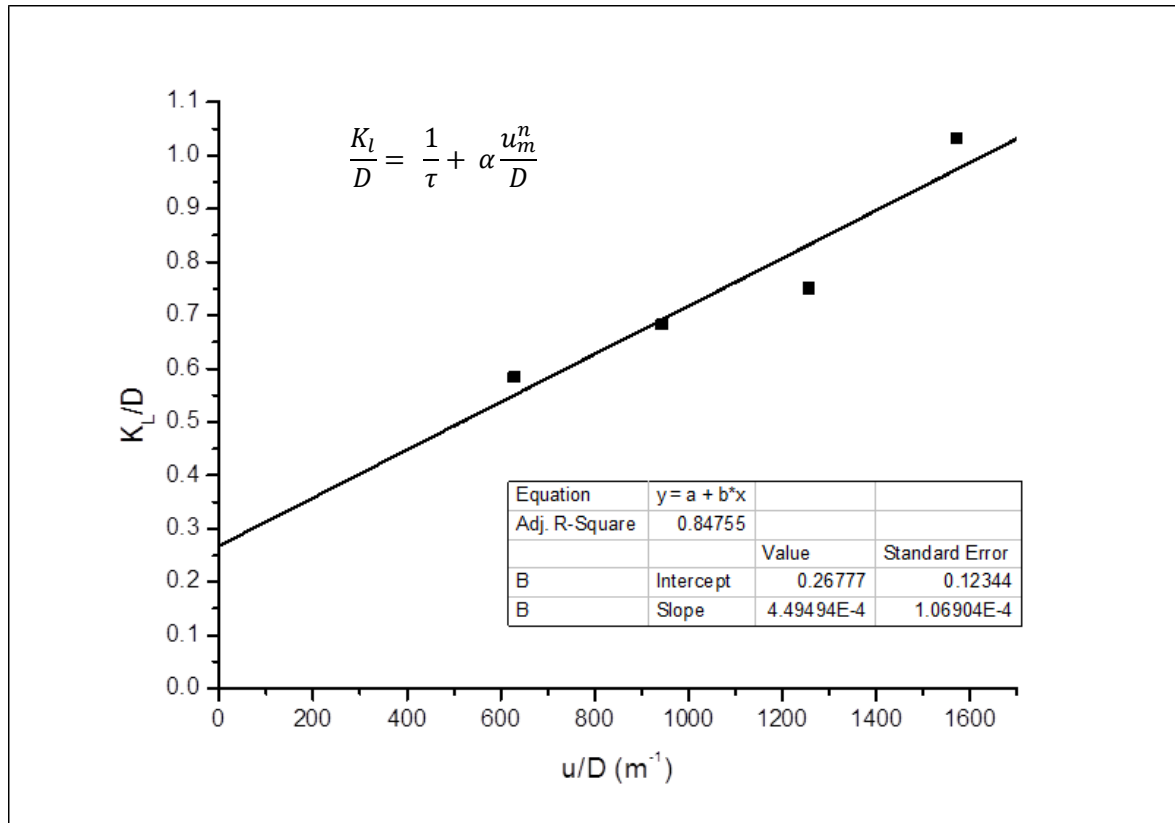
Figure 5.15 Dispersion to diffusion coefficient ratio against interstitial velocity

From the works of (Coats & Whitson, 2004; Coats et al., 2009; Honari et al., 2013; Hughes et al., 2012), they presented that the values of the apparent dispersivity in consolidated porous media are generally smaller than 0.01 ft (0.003 m). Hughes et al (2012) obtained dispersivity in a range of 0.0001 m to 0.0011m using a core sample (Donny brook) with similar petrophysical properties as the ones used in this work. This provided a practical input variable for EGR simulations. As dispersivity is a very important porous media property, its accurate determination can provide a befitting technique to actually simulate the fluid flow in the matrix of the reservoir.

From Figure 5.15, the dispersivity obtained in this work (slope) is 0.00045m which lies within the range of those obtained in literature. Invariably, this is also an indication that the results obtained from the analyses carried out in this research are practically accurate.

111

Using the measured grain diameter (99.6μm) as the characteristic length scale of mixing, the P_{ex} was determined from Eq. 2.4, taking the average interstitial velocity of the runs as an input variable. P_{ex} was evaluated and presented as 0.06 which shows that diffusion is the dominant mechanism in the entire runs using Grey Berea. All flow is concentration driven as opposed to advection which is velocity driven. However, if the dispersivity obtained here, 0.00045m was used to evaluate the medium P_{ex}, the value will be 0.2 which clearly is an over estimation of the *Péclet* number here and therefore the displacement mechanism lies in the transition zone between molecular diffusion and mechanical dispersion. Thereby providing wrong characterisation and hence over compensation of the transport parameters.

5.3.2.1.2 Vertical orientation

The same procedures were adopted here as those employed in the horizontal orientation. The only difference being the orientation of the core samples hence the injection pattern. The concentration profiles obtained are shown in Table 5.14

Table 5.14 Mole fractions of CO2 at all injection rates in the vertical orientation

Q = 0.2 ml/min		Q = 0.3 ml/min		Q = 0.4 ml/min		Q = 0.5 ml/min	
Time (min)	yCO_2	Time (min)	yCO_2	Time (min)	yCO_2	Time (min)	yCO_2
0.15	0	0.15	0	0.16	0	0.16	0
5.49	0	5.49	0	5.33	0	5.49	0
10.99	0	10.99	0	10.65	0	10.83	0.3667
16.19	0	16.19	0.2199	15.99	0.3601	16.16	0.7788
21.48	0.1253	21.48	0.6439	21.33	0.7032	21.49	0.8671
26.83	0.6186	26.83	0.7419	26.49	0.7914	26.83	0.9372
31.84	0.7602	31.84	0.8019	31.99	0.8467	32.16	0.9728
37.12	0.8164	37.12	0.8613	37.33	0.8934	37.33	0.9736
42.32	0.8589	42.32	0.9326	42.49	0.9151	42.66	0.9736
47.83	0.8839	47.83	0.9676	47.83	0.919	47.99	0.9752
53.49	0.9339	53.49	0.9917	54.16	0.9231		
58.52	0.9839						

There certainly are similarities between the vertical and horizontal orientations results as can be seen in both Tables –Table 5.12 and Table 5.14. There was an early breakthrough at lower injection rates in the horizontal orientation compared to those of the vertical orientations. The reason behind this trend can be attributed to the significant gravity effect per the horizontal orientation. Details of this systematics are discussed in Section 5.3.7 of this chapter.

Table 5.15 Dispersion coefficients and diffusion coefficients at different flow rates

Q (ml/min)	Pressure (psig)	Temperature (°C)	u (10^{-5} m/s)	K_L (10^{-8} m²/s)	D (10^{-8} m²/s)	u/D	k/D
0.2	1300	50	3.350	2.46	5.33	621.5857	0.46153846
0.3	1300	50	5.025	3.03	5.33	938.2001	0.56848030
0.4	1300	50	6.700	3.30	5.33	1250.683	0.61913696
0.5	1300	50	8.376	4.02	5.33	1564.293	0.75422138
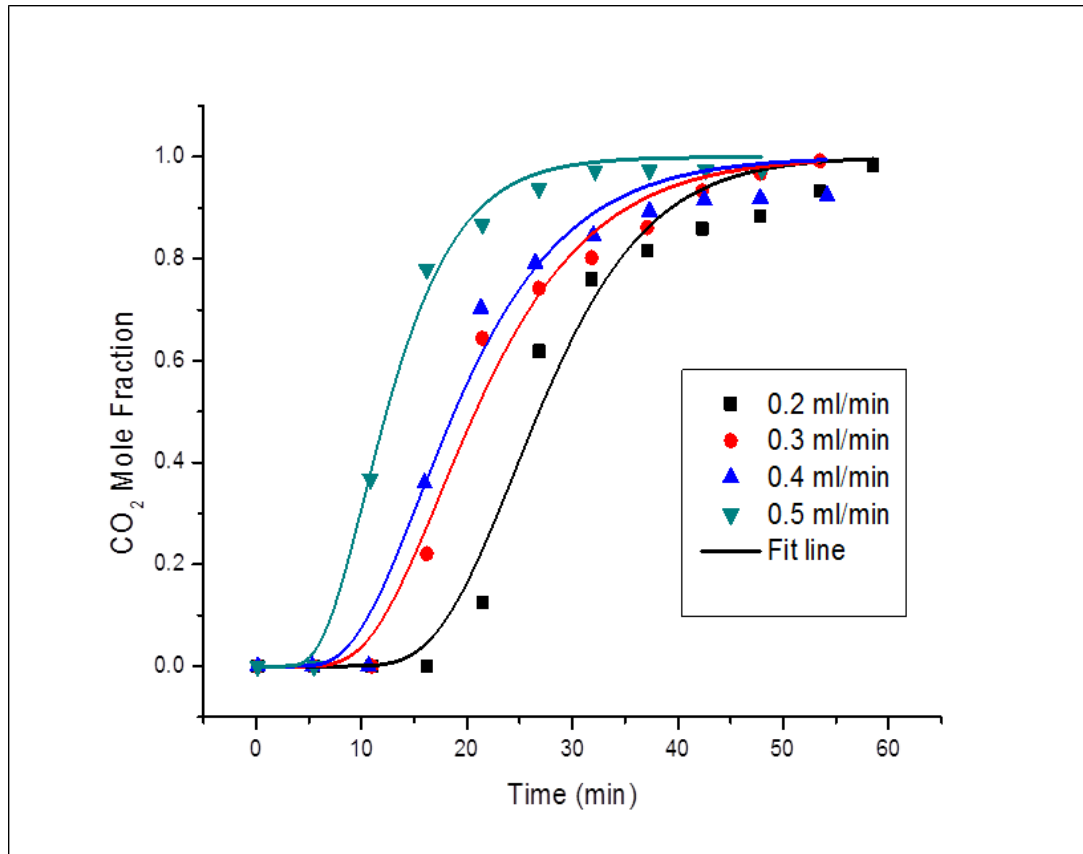
Figure 5.16 Concentration profile for all Grey Berea runs Vertical orientation

From Figure 5.17, the dispersivity – a function of the porous medium was the still within the same range of practical values regardless of injection orientation of the core sample. The dispersivity was found to be 0.0003 m which is the slope of the plot of the ratio of dispersion coefficient to the diffusion coefficient as a function of interstitial velocity. This shows the reliability of the experiments even further.

113

The graph shows the equation:

$$\frac{K_l}{D} = \frac{1}{\tau} + \alpha \frac{u_m^n}{D}$$

With data table:

Equation	y = a + b*x		
Adj. R-Square	0.95984		
		Value	Standard Error
D	Intercept	0.27584	0.04002
D	Slope	2.95475E-4	3.46545E-5

Axes: y-axis K_L/D, x-axis u/D (m^{-1})
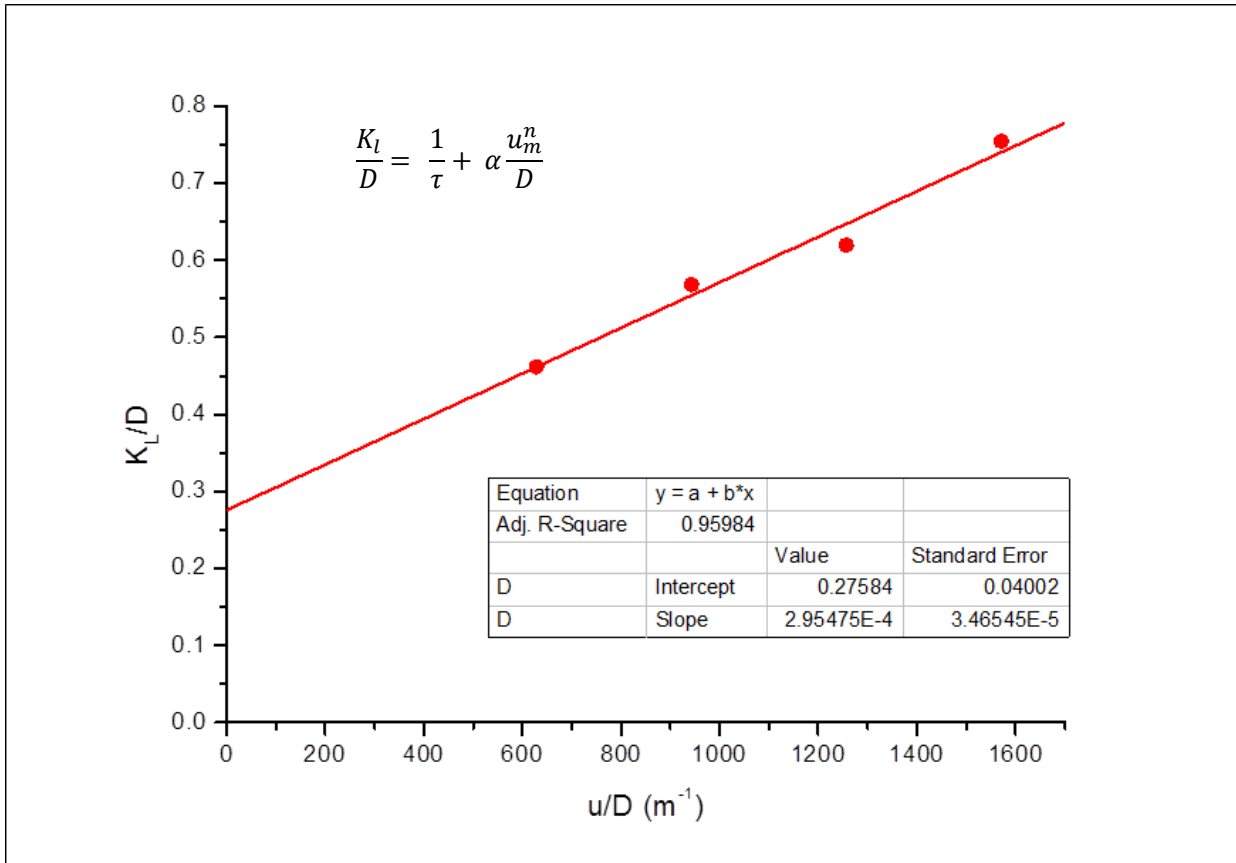
Figure 5.17 Dispersivity evaluation using the dispersion coefficient & interstitial velocity

The tortuosity (inverse of the intercept on the y-axis of the straight line) was similar in both cases (Figure 5.18), indicating that regardless of the injection orientation of the core sample, the tortuosity (a property of the core sample) remained unchanged. This shows that core orientation does not alter the pathways of the matrix of the porous media when fluid transverses, further attributing the fluid behaviour to mainly a function of the fluid properties and not the rock.

114

$$\frac{K_l}{D} = \frac{1}{\tau} + \alpha \frac{u_m^n}{D}$$
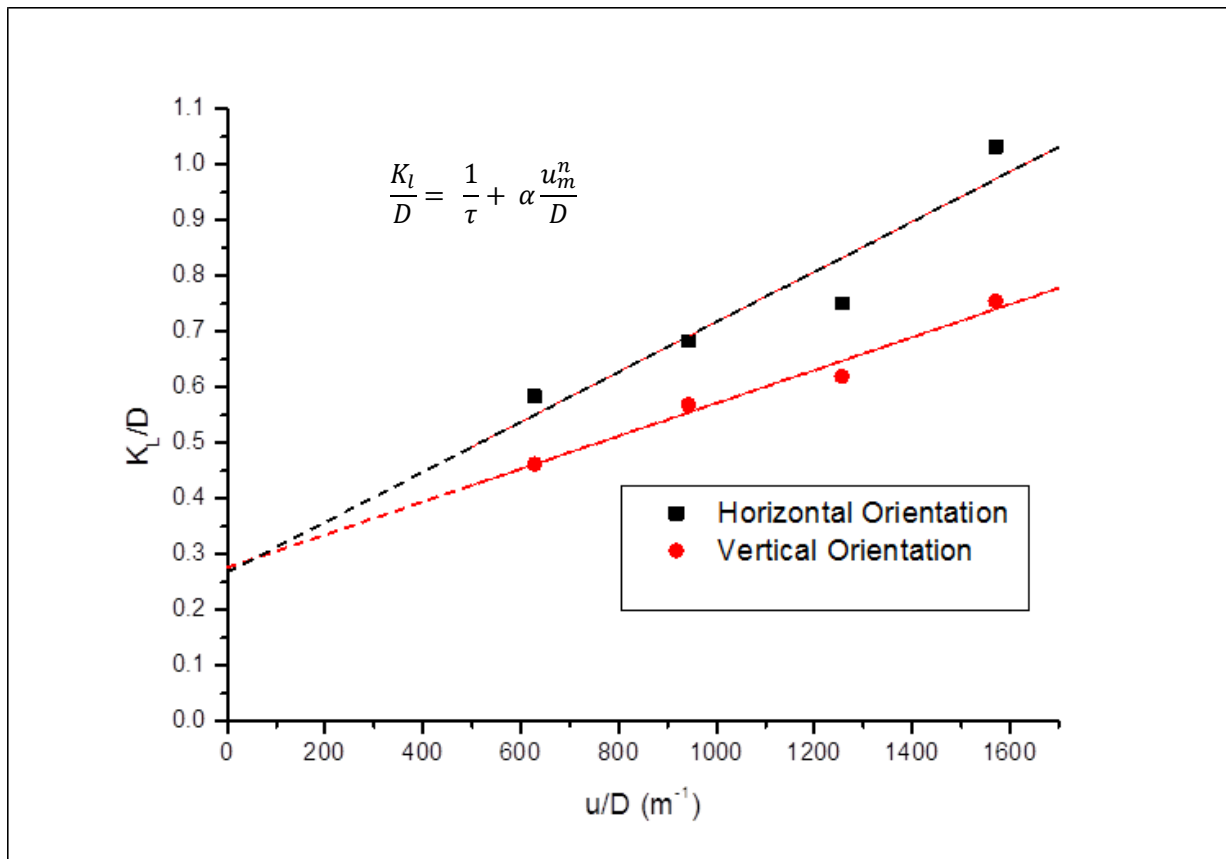
Figure 5.18 Comparison of the dispersivities in both orientations for Grey Berea

5.3.2.2 Buff Berea core sample

The same procedure as the preceding investigation using *Grey Berea* was adopted here. Varying injection rates of 0.2, 0.3, 0.4, 0.5 ml/min were used at the same test conditions. The results are as follows.

5.3.2.2.1 Horizontal orientation

The horizontal concentration profiles for all the test flow rates are shown in Table 5.16 and as expected the break through times increased with increase in the injection rates.

Table 5.16 Mole Fractions of CO_2 at different flow rates in horizontal orientation

Q = 0.2 ml/min		Q = 0.3 ml/min		Q = 0.4 ml/min		Q = 0.5 ml/min	
Time (min)	yCO_2	Time (min)	yCO_2	Time (min)	yCO_2	Time (min)	yCO_2
0.15	0	0.16	0	0.16	0	0.15	0
5.49	0	5.48	0	5.33	0.0042	5.48	0.0046
10.83	0	10.68	0.6223	10.66	0.572	10.82	0.7172
16.16	0.2065	15.99	0.71121	15.82	0.8127	15.98	0.8152
21.33	0.5611	21.32	0.7971	21.33	0.8814	21.32	0.8401
26.66	0.6825	26.83	0.831	26.49	0.9077	26.82	0.8836

115

31.99	0.7568	31.99	0.8606	31.82	0.9355	31.98	0.9281
37.19	0.8181	37.16	0.9019	37.16	0.9458	37.32	0.9384
42.66	0.8852	42.49	0.9334	42.49	0.9497	42.65	0.9429
47.83	0.9444	47.82	0.9479	47.83	0.9511	47.98	0.9433
53.33	0.9801	64.66	0.9491	54.99	0.9518		
59.67	0.9904						

The dispersion coefficients were also evaluated from the plot of the mole fraction of CO_2 as a function of time by the 1D ADE to the experimental concentration profile per Figure 5.19.
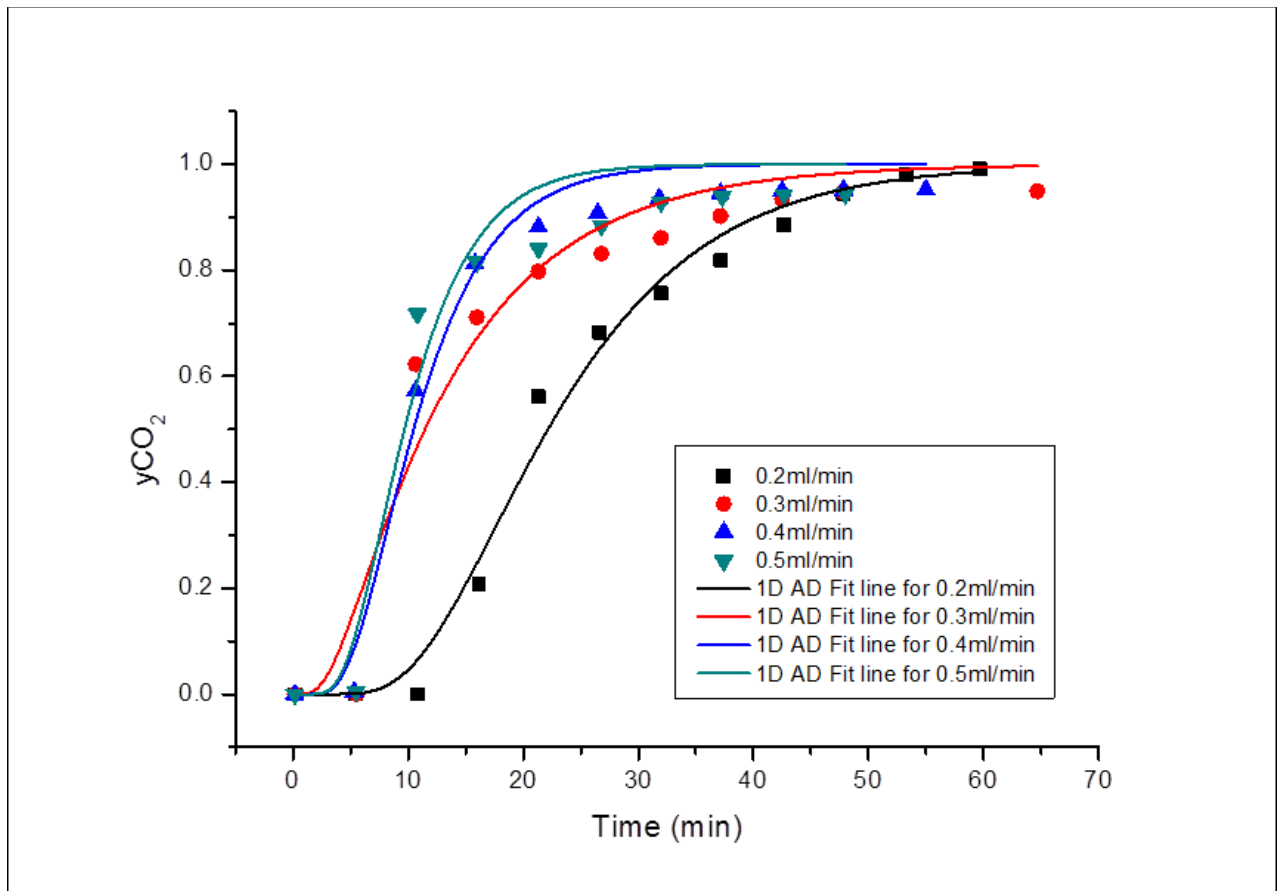
Figure 5.19 Concentration profile of all the runs for Buff Berea in horizontal orientation

From the fitting technique in Figure 5.19, the dispersion coefficients were evaluated and presented in Table 5.17.

Table 5.17 Dispersion and diffusion coefficients in the horizontal orientation

Q (ml/min)	Pressure (psig)	Temperature (°C)	u (10^{-5} m/s)	K_L (10^{-8} m²/s)	D (10^{-8} m²/s)	u/D	k/D
0.2	1300	50	2.62	2.38	5.33	492.16	0.44
0.3	1300	50	3.93	3.13	5.33	738.24	0.58
0.4	1300	50	5.25	3.51	5.33	984.32	0.65
0.5	1300	50	6.56	4.89	5.33	1230.40	0.91

Using the dispersion coefficients from Table 5.17, the dispersivity of the core sample was evaluated from the relationship between the dispersion coefficient and interstitial velocity.

Equation	y = a + b*x	
Adj. R-Square	0.91281	
	Value	Standard Error
B Intercept	0.13302	0.09578
B Slope	6.03074E-4	1.05938E-4

$$\frac{K_l}{D} = \frac{1}{\tau} + \alpha \frac{u_m^n}{D}$$
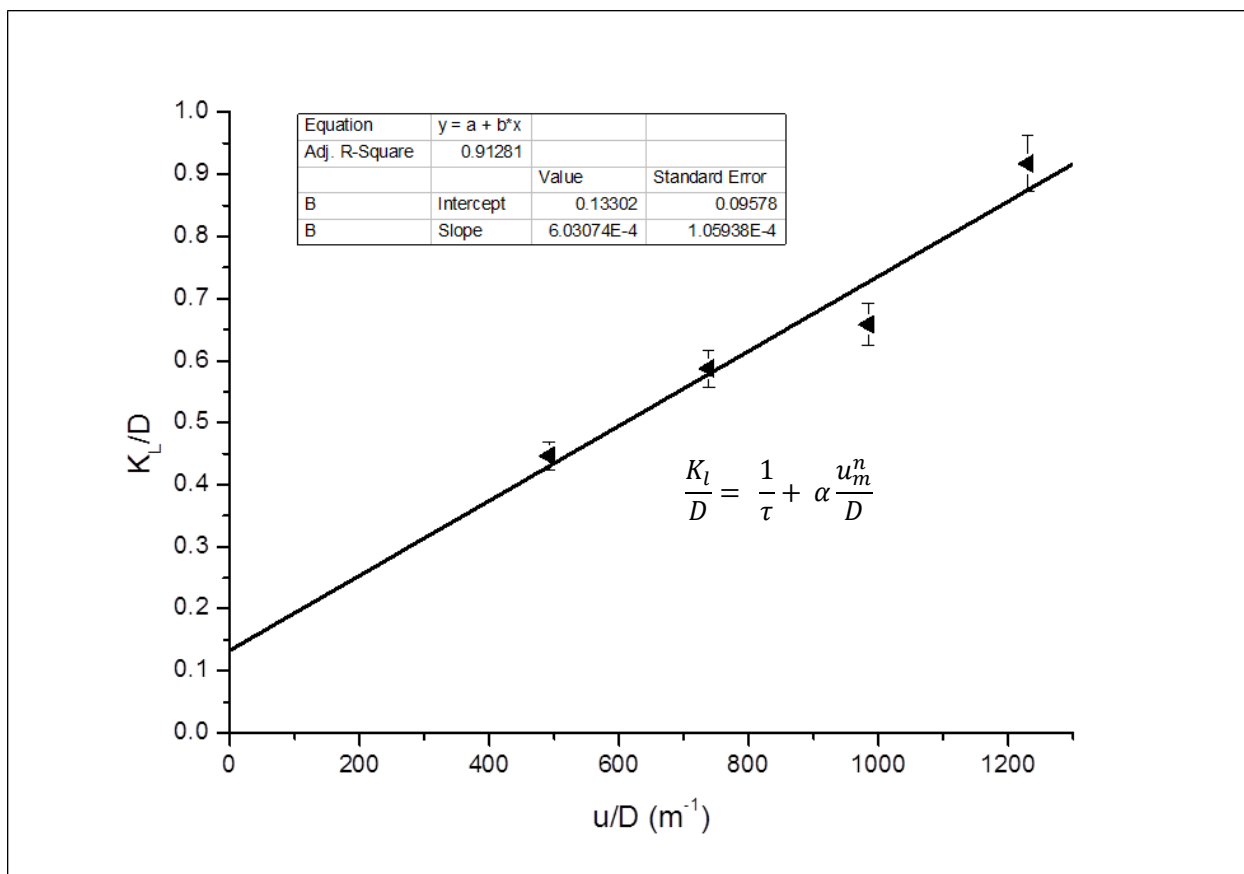
Figure 5.20 Dispersivity evaluation for Buff Berea in the horizontal orientation

From Figure 5.20, the dispersivity of Buff Berea for this application is 0.0006. This value further reinstates the practicality of the experiments given that it falls within the range of those obtained in literature for similar core samples with similar petrophysical properties.

5.3.2.2.2 Vertical Orientation

The fitted ADE for the vertical displacement of CH_4 by supercritical CO_2 in buff Berea core sample is shown in Figure 5.21.
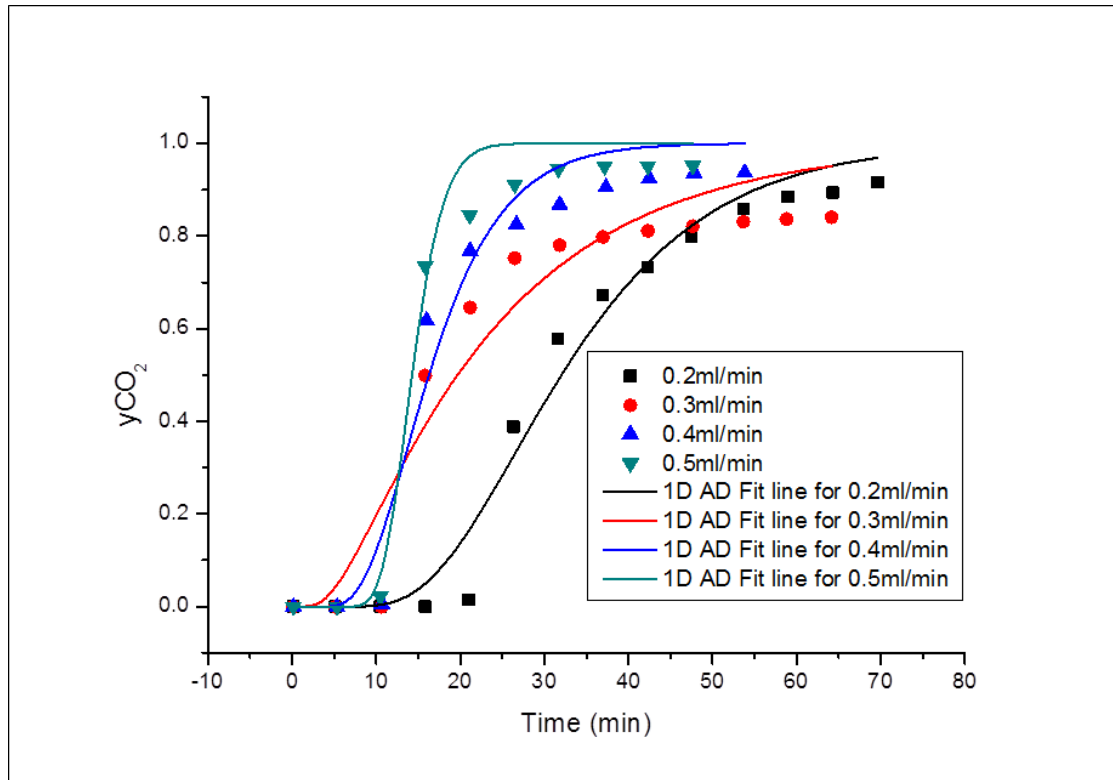
Figure 5.21 Concentration profile for all Buff Berea runs in vertical orientation

As stated earlier, the conformance stemming from the systematic effects makes a meagre fitting of the experimental results and the 1D ADE.

$$\frac{K_l}{D} = \frac{1}{\tau} + \alpha \frac{u_m^n}{D}$$

Equation	y = a + b*x	
Adj. R-Square	0.80475	
	Value	Standard Error
D Intercept	0.11966	0.09998
D Slope	4.04235E-4	1.10575E-4
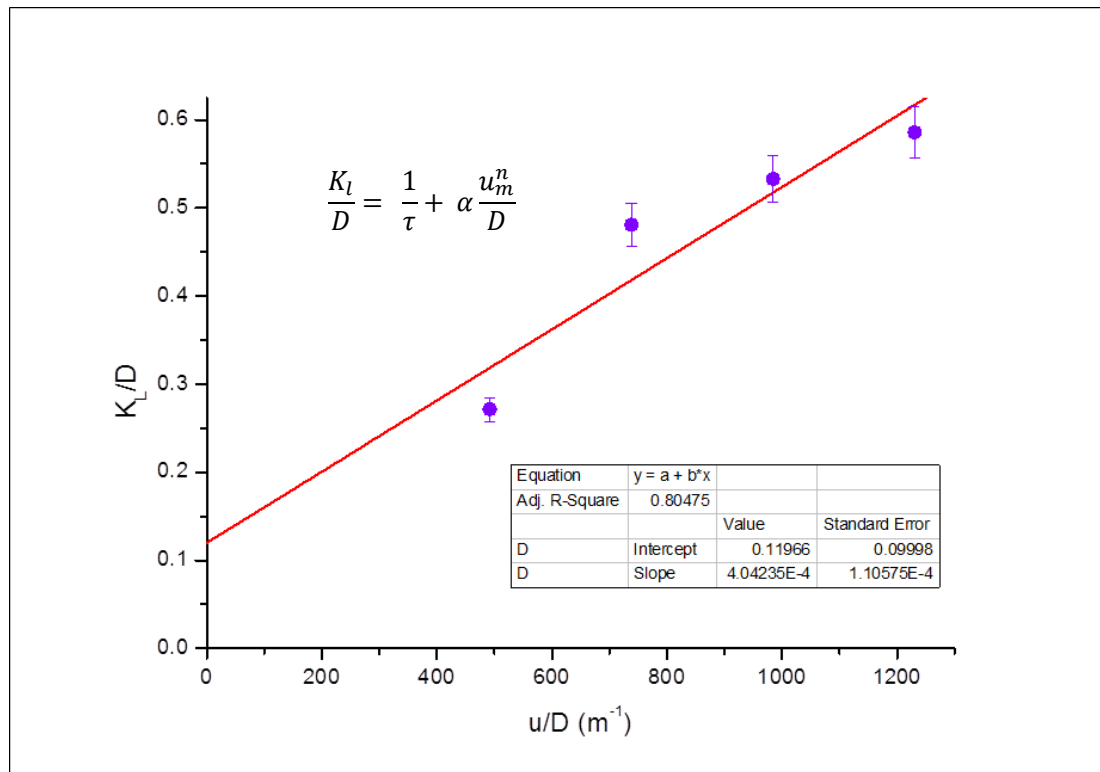
Figure 5.22 Dispersivity evaluation for Buff Berea in the vertical orientation

Table 5.18 shows the dispersion and diffusion coefficients in the vertical orientation. These were then used to relate the dispersion coefficient as a function of the interstitial velocity to evaluate the dispersivity at that orientation and conditions.

Table 5.18 Dispersion and diffusion coefficient in vertical orientation for Buff Berea

Q (ml/min)	Pressure (psig)	Temperature (°C)	u (10^{-5} m/s)	K_L (10^{-8} m²/s)	D (10^{-8} m²/s)	u/D	k/D
0.2	1300	50	2.62	1.447	5.33	492.16	0.27
0.3	1300	50	3.93	2.564	5.33	738.24	0.48
0.4	1300	50	5.25	2.841	5.33	984.32	0.53
0.5	1300	50	6.56	3.122	5.33	1230.40	0.58

A comparison of the dispersivity of the buff Berea was depicted in Figure 5.23 and as already seen in the case of Grey Berea, the horizontal dispersivity is higher than the vertical one. This is also true in that there was higher dispersion in the horizontal orientation than the vertical orientation as observed.
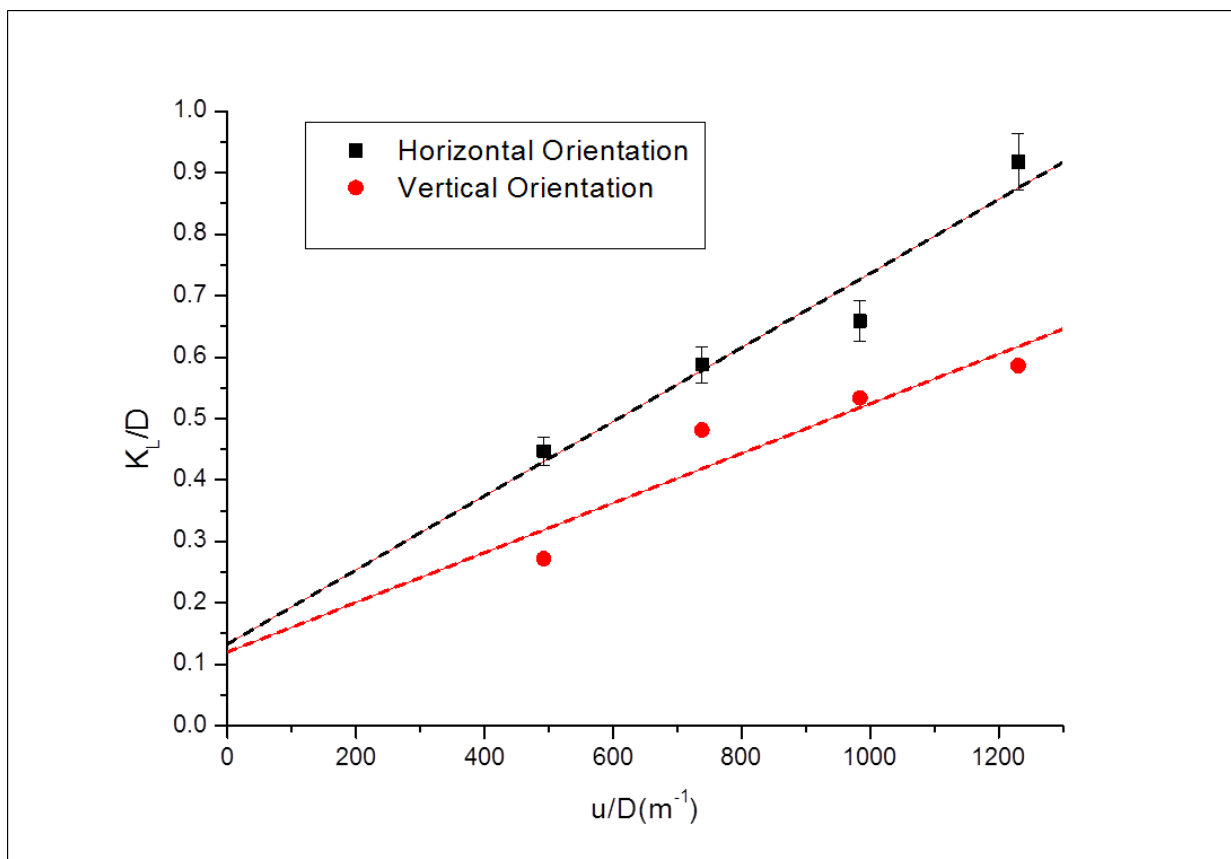
Figure 5.23 Comparison of the dispersivities in both orientations for Buff Berea

5.3.2.3 Bandera Grey

This core sample has the lowest permeability and porosity amongst the core samples investigated. This low porosity also means higher interstitial velocity (Eq. 5.4) which invariably means higher dispersion coefficient at each injection rate compared to the other core samples – Buff Berea and Grey Berea. The horizontal and vertical analyses were also carried out to evaluate the extent of the variation.

5.3.2.3.1 Horizontal orientation

The fitted concentration profiles for all the test runs for Bandera grey are shown in Figure 5.24. The profiles are characteristically quite steep showing that the displacement front is short and also higher dispersion of CO_2 in CH_4. Here also, the 1D ADE fitting of the

experimental results was not perfect as seen in previous curve fits which is due to the systematics errors as earlier explained.
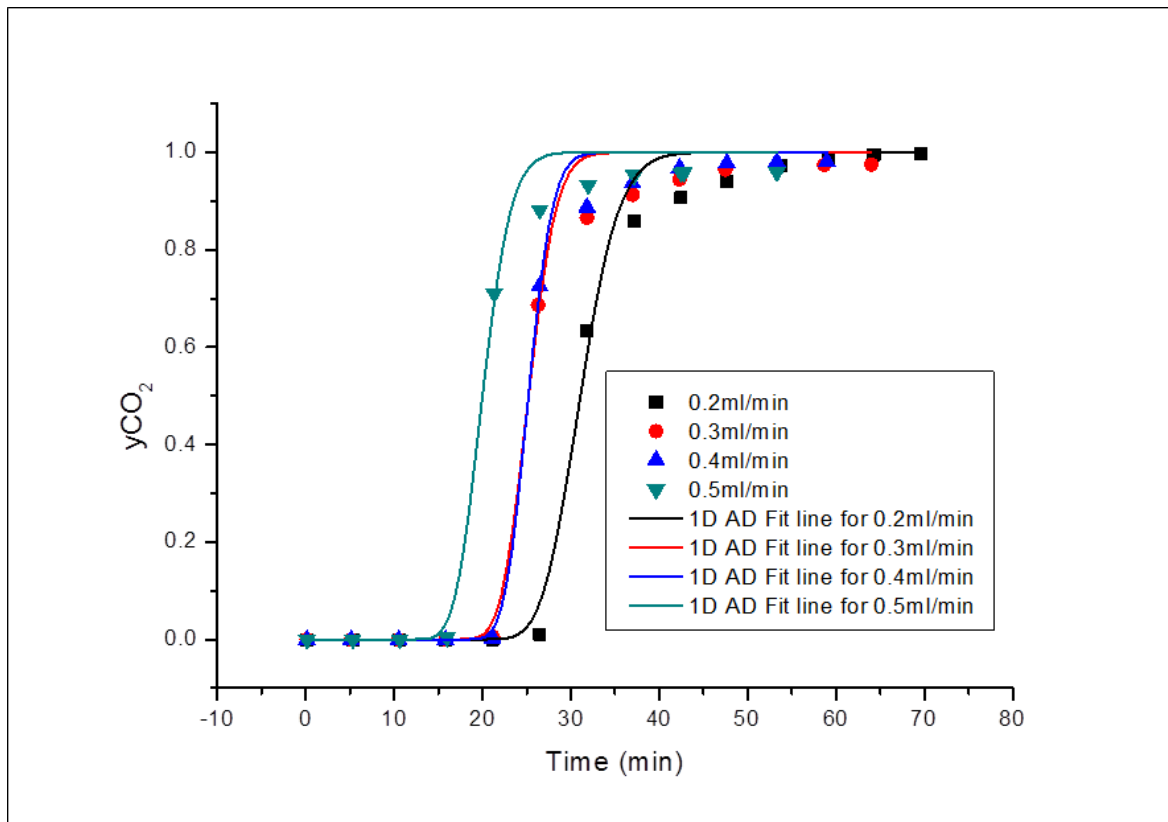
Figure 5.24 Concentration profile for Bandera Grey in horizontal orientation

From Table 5.19, the dispersion coefficients are higher than the dispersion coefficients of the preceding core samples by at least a factor of 2.5 for all the test runs.

Table 5.19 Dispersion & diffusion coefficient in horizontal orientation for Bandera Grey

Q (ml/min)	Pressure (psig)	Temperature (°C)	u (10^{-5} m/s)	K_L (10^{-8} m²/s)	D (10^{-8} m²/s)	u/D	k/D
0.2	1300	50	3.93	7.01	5.33	741.70	1.32264
0.3	1300	50	5.90	8.97	5.33	1112.55	1.69245
0.4	1300	50	7.86	13.20	5.33	1483.40	2.49057
0.5	1300	50	9.83	15.23	5.33	1854.25	2.87358

Invariably, the dispersivity was quite low (Figure 5.25) given the lower permeability and porosity of the core sample compared to the other core samples. This shows that a lower

volume of a fluid passes through the core sample as a result of the restrictive type flow from the core samples.
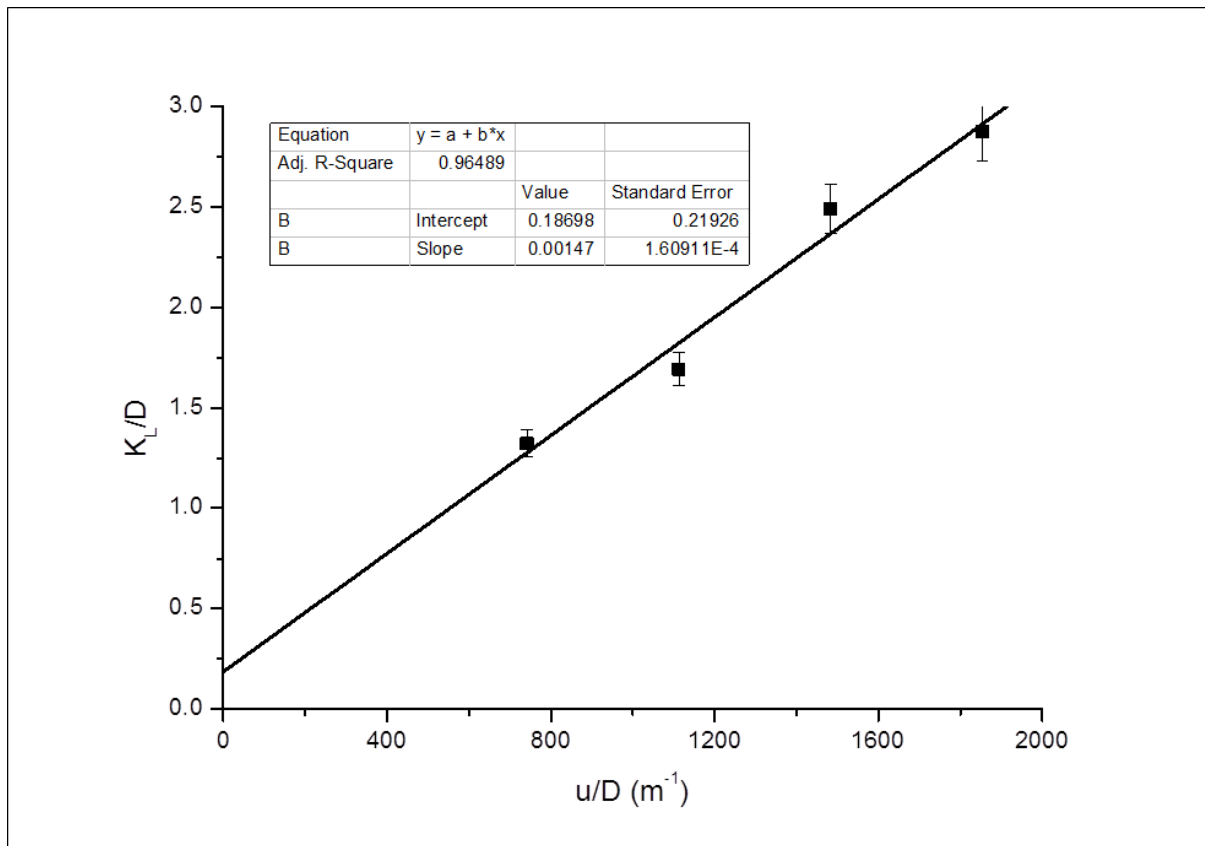
Figure 5.25 Dispersivity evaluation for Bandera Grey in the horizontal orientation

5.3.2.3.2 Vertical Orientation

Similar trend as the horizontal orientation was realised here when analysing the vertical orientation results. The breakthrough times are as expected with 0.2 ml/min having the late breakthrough and 0.5 ml/min having the earliest breakthrough. Steep concentration profiles are visible denoting higher dispersion of the gas during displacement (Figure 5.26).
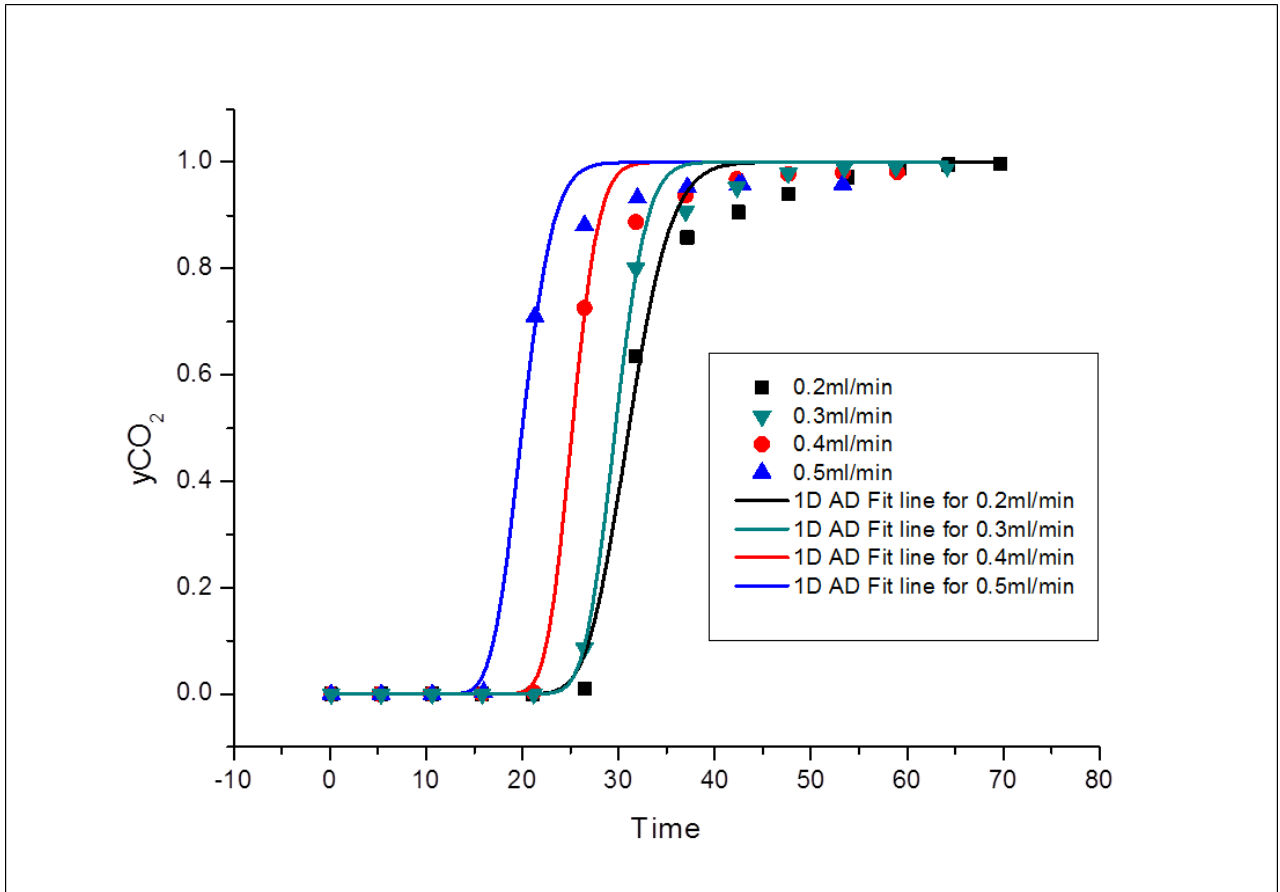
Figure 5.26 Concentration profile for Bandera Grey runs in vertical orientation

The dispersion is seemingly lower than that observed in the horizontal orientation from Table 5.20. Further investigations on the flow behaviour of CO_2 during EGR was carried out to explain these trends observed due to the variation of the injection orientation and discussed in detail in section 5.3.7.

Table 5.20 Dispersion & diffusion coefficient in vertical orientation for Bandera Grey

Q (ml/min)	Pressure (psig)	Temperature (°C)	u (10^{-5} m/s)	K_L (10^{-8} m²/s)	D (10^{-8} m²/s)	u/D	k/D
0.2	1300	50	3.93	4.56605	5.33	741.70	0.86152
0.3	1300	50	5.90	5.19316	5.33	1112.55	0.97984
0.4	1300	50	7.86	7.03657	5.33	1483.40	1.32765
0.5	1300	50	9.83	9.35058	5.33	1854.25	1.76426

Using the results obtained in Table 5.20, the dispersivity at this orientation was evaluated and plotted in Figure 5.27, where the slope was obtained which represents the rock longitudinal dispersivity. The value was 0.0008.

123

Equation	y = a + b*x		
Adj. R-Square	0.91998		
		Value	Standard Error
D	Intercept	0.16371	0.18848
D	Slope	8.24064E-4	1.38328E-4
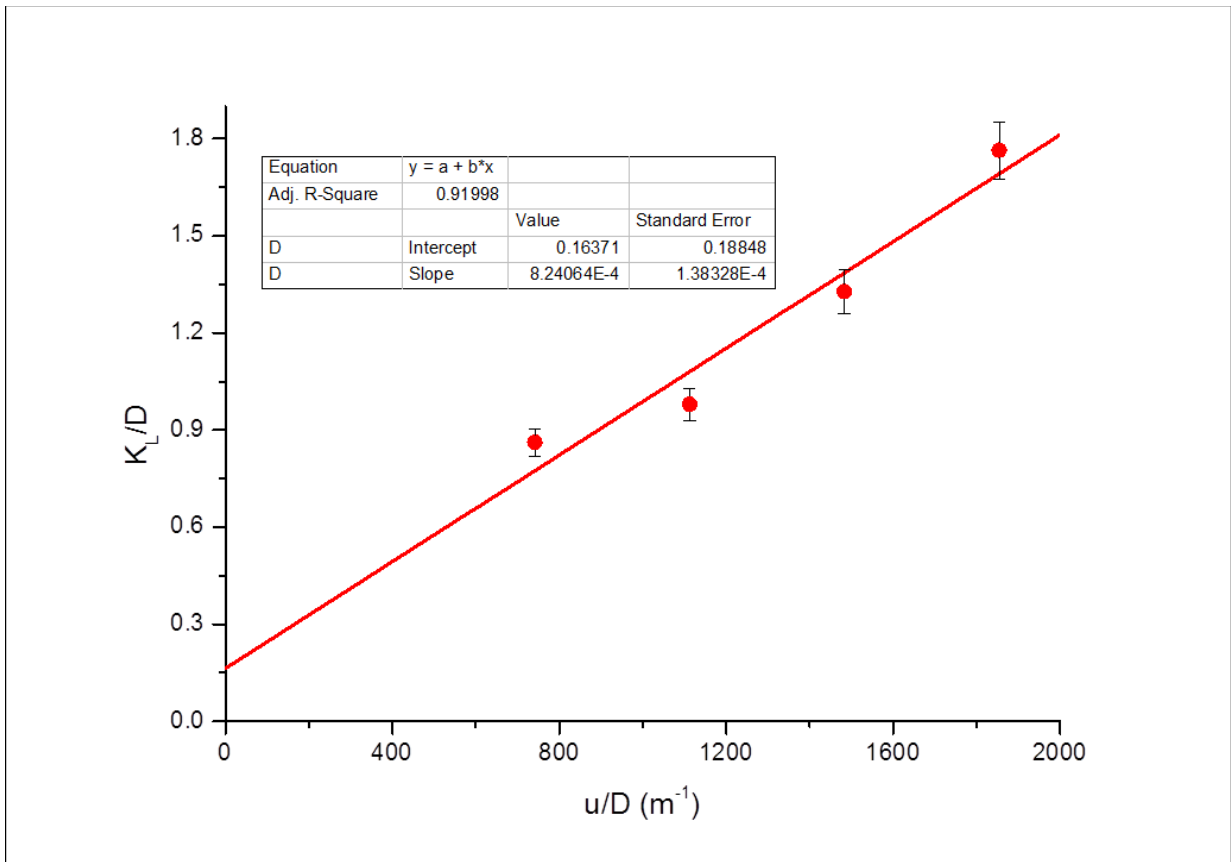
Figure 5.27 Dispersivity evaluation for Bandera Grey in the vertical orientation

It is apparent that the horizontal dispersivity is higher than the vertical dispersivity for all the core samples investigated. This is shown (Figure 5.28) in the comparison between the vertical and horizontal dispersivities of Bandera Grey core sample.
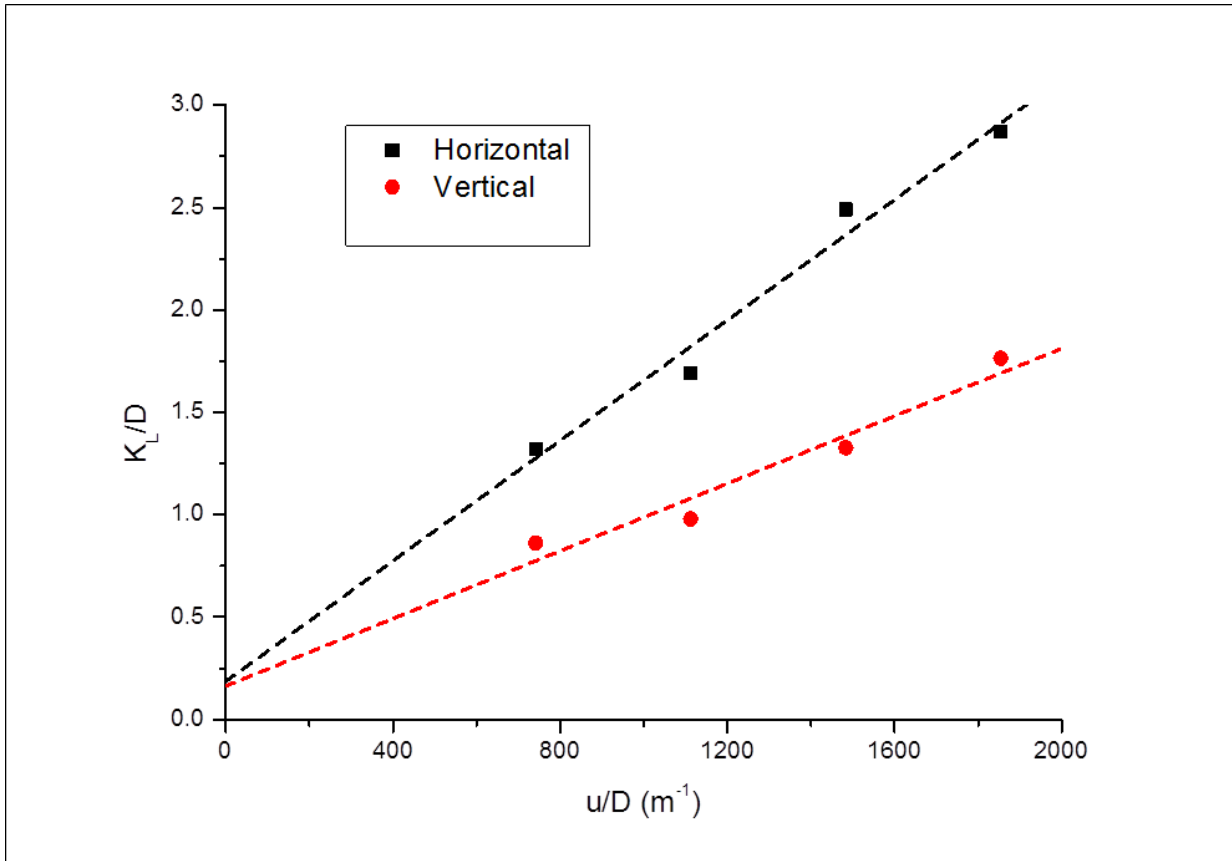
Figure 5.28 Comparison of the dispersivities in orientations for Bandera Grey

5.3.2.4 Summary of the dispersion coefficient investigation

Table 5.21 Summary of the dispersion coefficients of all the core samples

S/N	Core sample	Orientation	u (10^{-5} m/s)	K_L (10^{-8} m^2/s)
1	**Bandera Grey**	Horizontal	3.93	7.01
			5.90	8.97
	(K = 16.08 md)		7.86	13.20
			9.83	15.23
		Vertical	3.93	4.56
			5.90	5.19
			7.86	7.03
			9.83	9.35
2	**Grey Berea**	Horizontal	3.35	3.11
			5.03	3.64
	(K = 217.04 md)		6.70	4.01
			8.38	5.51
		Vertical	3.35	2.46
			5.03	3.03
			6.70	3.70
			8.38	4.02

3	**Buff Berea**	Horizontal	2.62	2.38
			3.93	3.13
	(K = 560.63 md)		5.25	3.51
			6.56	4.89
		Vertical	2.62	1.44
			3.93	2.56
			5.25	2.84
			6.56	3.12

Dispersion coefficient generally decreases with increase in permeability as seen in Table 5.21. So, the core sample with the least permeability (Bandera Grey) showed significantly higher dispersion coefficient. Another realisation from the table is that in all the runs, those in the horizontal orientation appear to have the higher dispersion coefficient. This can be attributed to the effect of gravity on the CO_2 as it traverses the core sample. This will further be discussed in section 5.3.7. Also, since the interstitial velocity is a function of porosity, the core sample with the most porosity had the lowest interstitial velocity and hence a lower dispersion coefficient at lower flowrates. The dispersion coefficient increases significantly at higher injection rates in all the runs – regardless of the orientation.

The dispersivity also increases with increase in permeability. This being a function of the core sample is evident with this trend as the absolute permeability of the core sample is also a property of the core sample. Basically, the higher the permeability of the core sample, the higher the rate of mixing when CO_2 is injected to displace CH_4. However, dispersivity is scale dependent (Bjerg, 2008; Schulze-Makuch, 2005) and albeit being at laboratory scale, this finding is an indication of the effects of the petrophysical properties on the mixing taking place during EGR. Finding the right injection scenario is vital in achieving the best recovery efficiency whilst storing substantial volumes of CO_2.

5.3.3 Flow behaviour of supercritical CO_2 during EGR

Evaluating the flow behaviour of supercritical CO_2 is vital in understanding the flow mechanics during EGR. This will help better develop an injection strategy based on the CO_2 injection rate for CH4 displacement. The effect CO_2 permeability can also be assessed based on the differential pressure (dP) across the core sample during the displacement. This was obtained during the previous test for evaluating the dispersion coefficient in different injection orientation. Since dP is directly inversely proportional to the permeability of the fluid through the core sample, direct interpretation of the dP as a function of the flow behaviour will be carried out to explain the trends observed.

Individual core samples were analysed at the test flow rates and then a comparison was made to effectively highlight the influence of the petrophysical properties of the different core samples on the flow behaviour, specifically permeability variation with injection orientation.

5.3.3.1 Grey Berea

The absolute permeability of the core sample was evaluated as 217.04 md as shown in section 5.2.2. A comparison of all the dP changes with time for all the test injection rates and orientation is shown in Figure 5.29 and Figure 5.34.
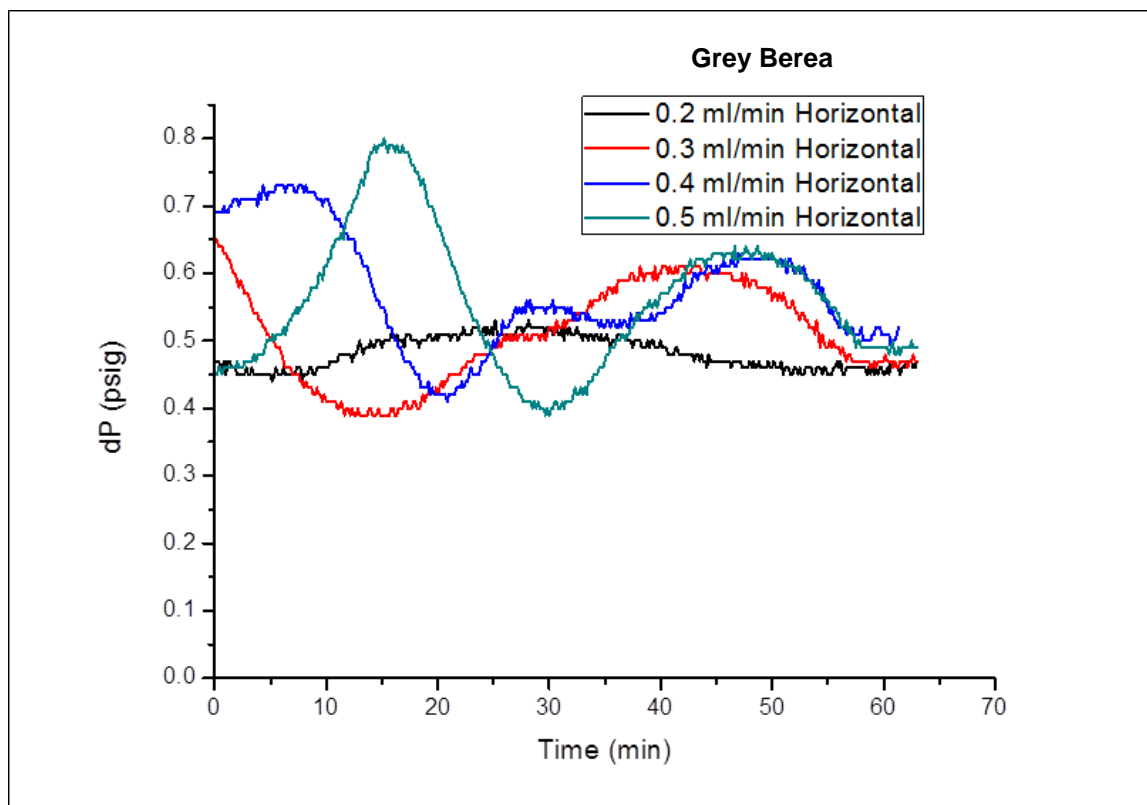
Figure 5.29 dP changes as function of time for grey Berea in horizontal orientation

From Figure 5.29, the flow of supercritical CO_2 follows a pattern in which there are higher average pressure drops (dP) as the flow rates increase. This is expected due to the direct relationship between the injection rate and the dP in Darcy equation. This same pattern is observed in the vertical orientation shown in Figure 5.30. The only difference is that in the vertical orientation, there seem to be a bit more conformity in term of the fluctuations in all the runs unlike those observed in the vertical orientation.
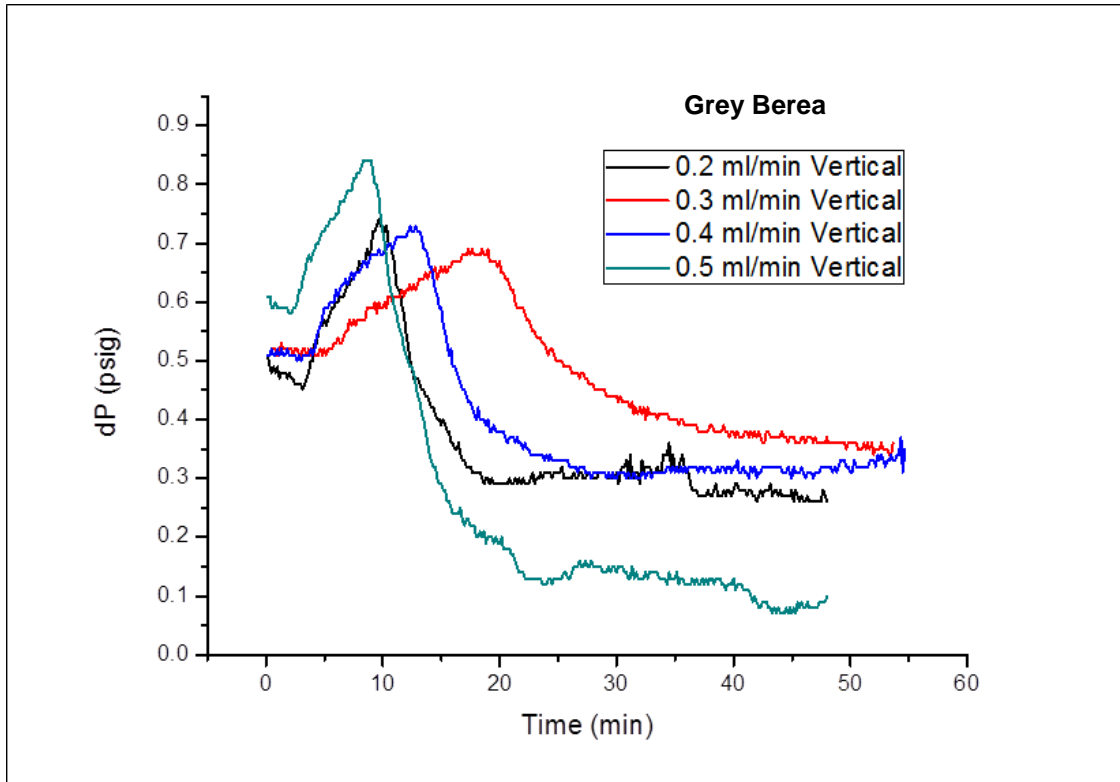
Figure 5.30 dP changes as function of time for grey Berea in vertical orientation

In order to properly evaluate the difference in flow behaviour of supercritical CO_2 in Grey Berea core sample at different injection rates and injection orientation, a comparison was made to assess these trends at individual flow rate at different orientations. Figure 5.31 shows the dP fluctuation as a function of time at 0.2ml/min but at different orientations. In the vertical run, there was a high pressure drop at the onset of the injection where it peaked, indicative of CO_2 breakthrough during the displacement and then a sharp drop in the dP and stabilised till the end of the run. When this trend was compared to the horizontal run, there seem to be no much difference in the dP fluctuations, but CO_2 permeability k was lower in the horizontal orientation compared with the vertical orientation.

On further evaluation, Figure 5.32 Figure 5.33, Figure 5.34 for 0.3, 0.4, 0.5 ml/min respectively, show similar trend but as the injection rates increased, the k was not much off with respect to injection orientation.

128
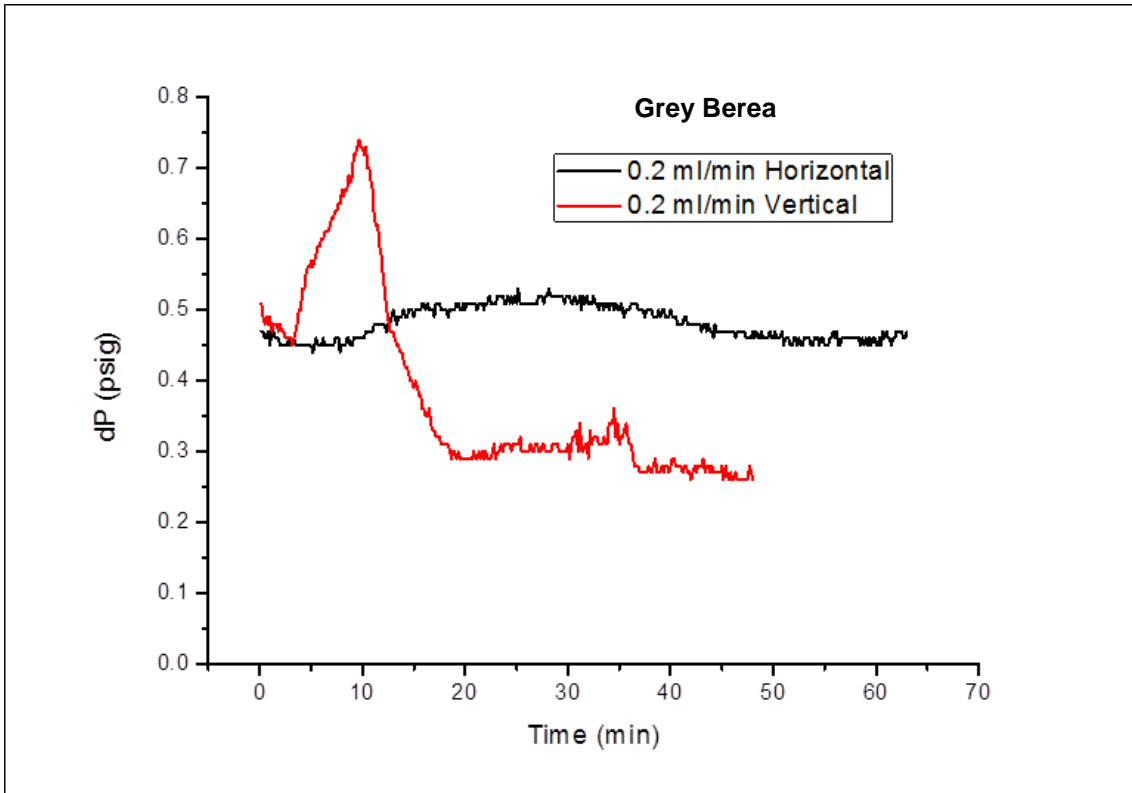
Figure 5.31 Comparison of dP changes with time at 0.2 ml/min in both orientations
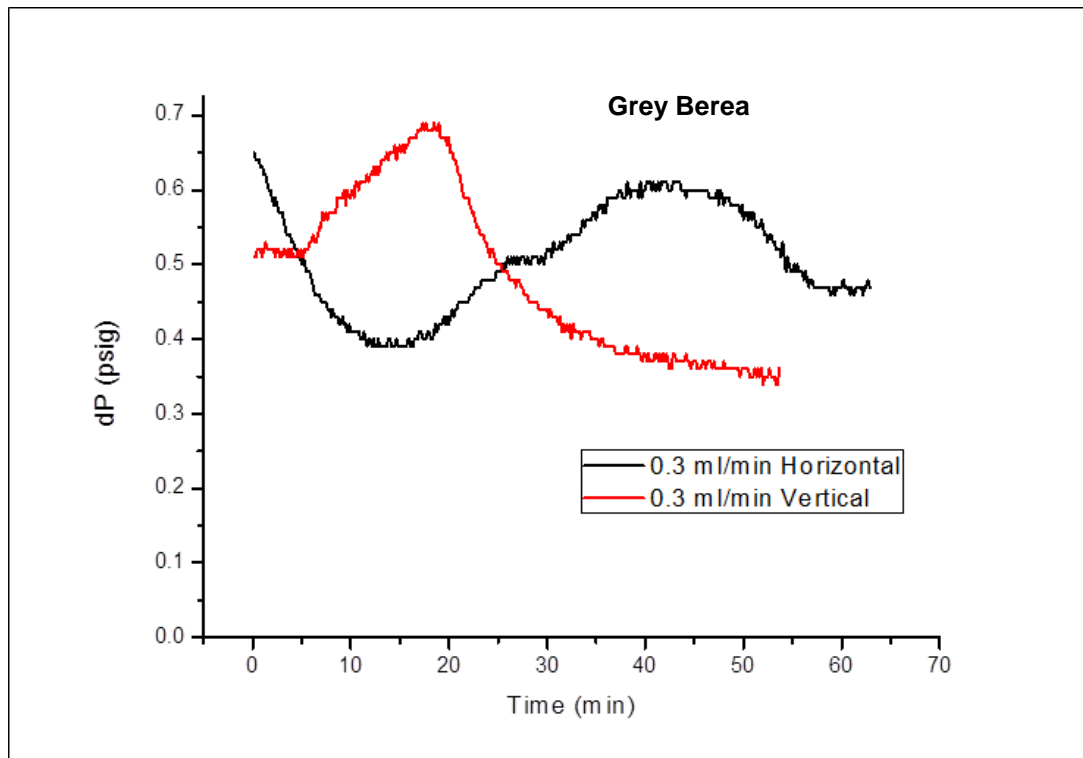
Figure 5.32 Comparison of dP changes with time at 0.3 ml/min in both orientations
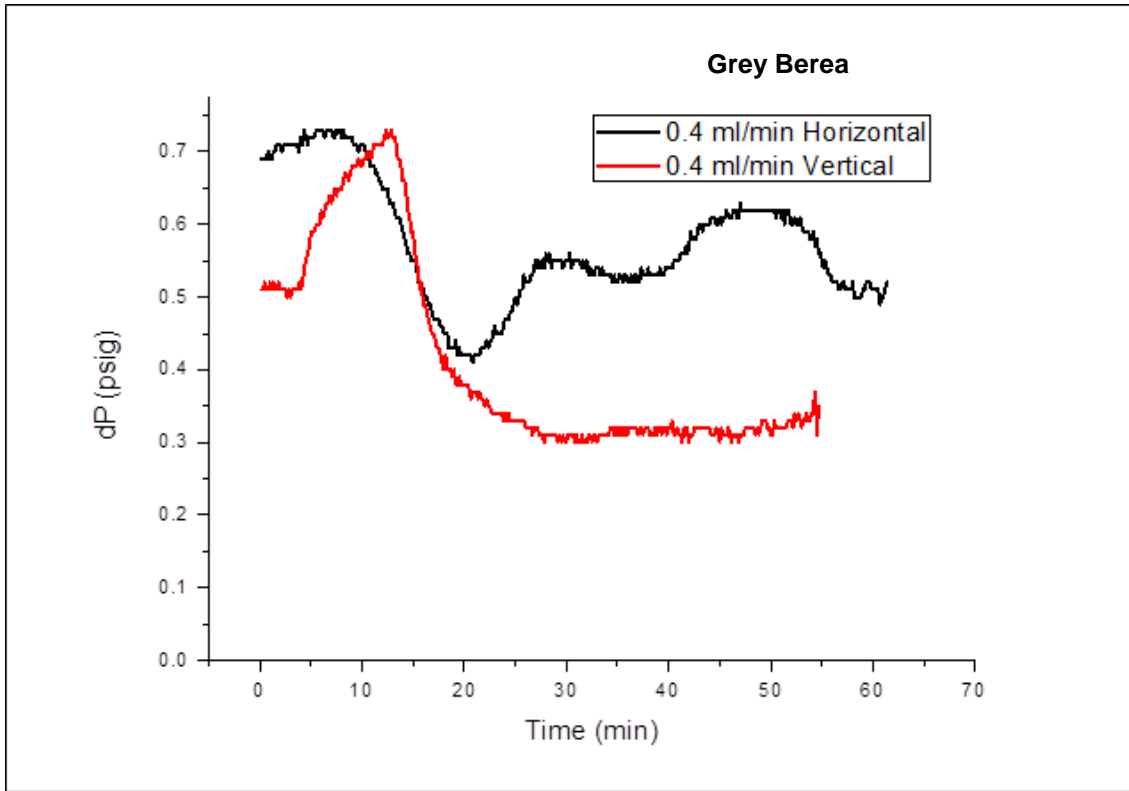
Figure 5.33 Comparison of dP changes with time at 0.4 ml/min in both orientations
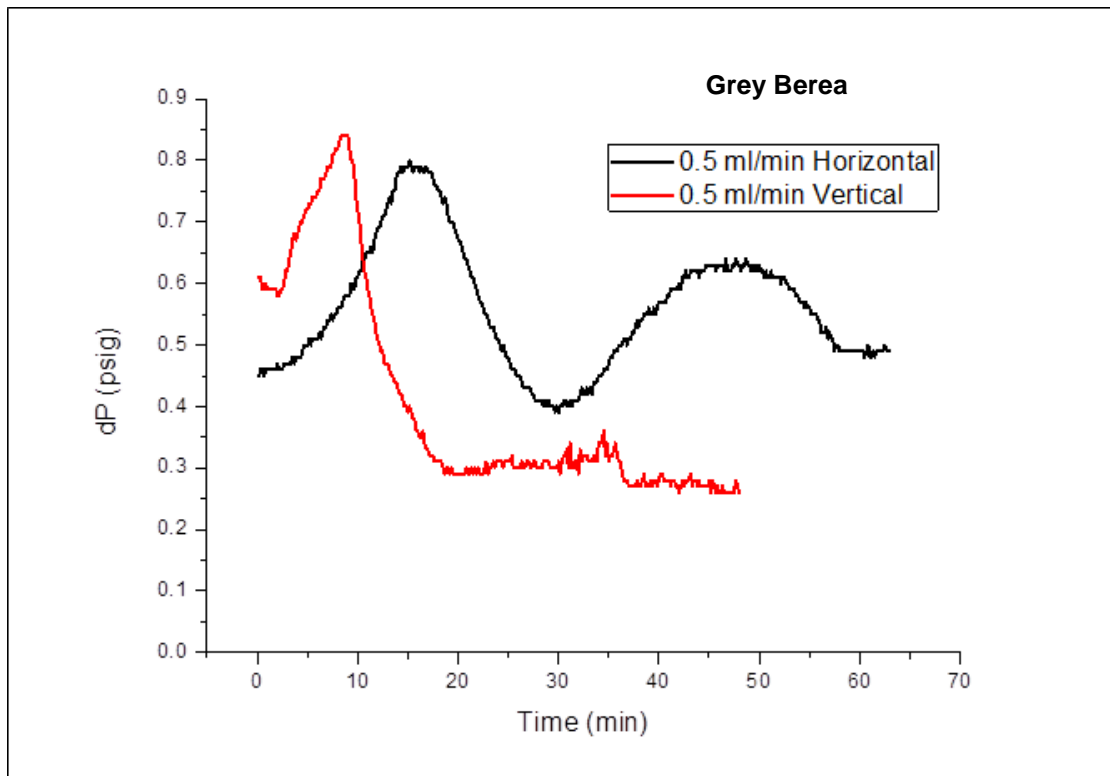
Figure 5.34 Comparison of dP changes with time at 0.5 ml/min in both orientations

130

5.3.3.2 Buff Berea

The flow behaviour of CO_2 in Buff Berea with the highest permeability amongst the core samples of interest was investigated by evaluation of the dP changes of the CO_2 as it displaces CH_4. This gives vital insight into the inter relationship between the CO_2 at the operating conditions and the porous medium through which it passes. The trends of the CO_2 dP with time are comparable to those seen in Grey Berea as in the case of both horizontal (Figure 5.35) and vertical (Figure 5.36) orientations as the injection rates were increased from 0.2-0.5 ml/min. There was apparent deviation of the trends in the horizontal injection orientation at lower injection rates compared to those observed in the vertical pattern.
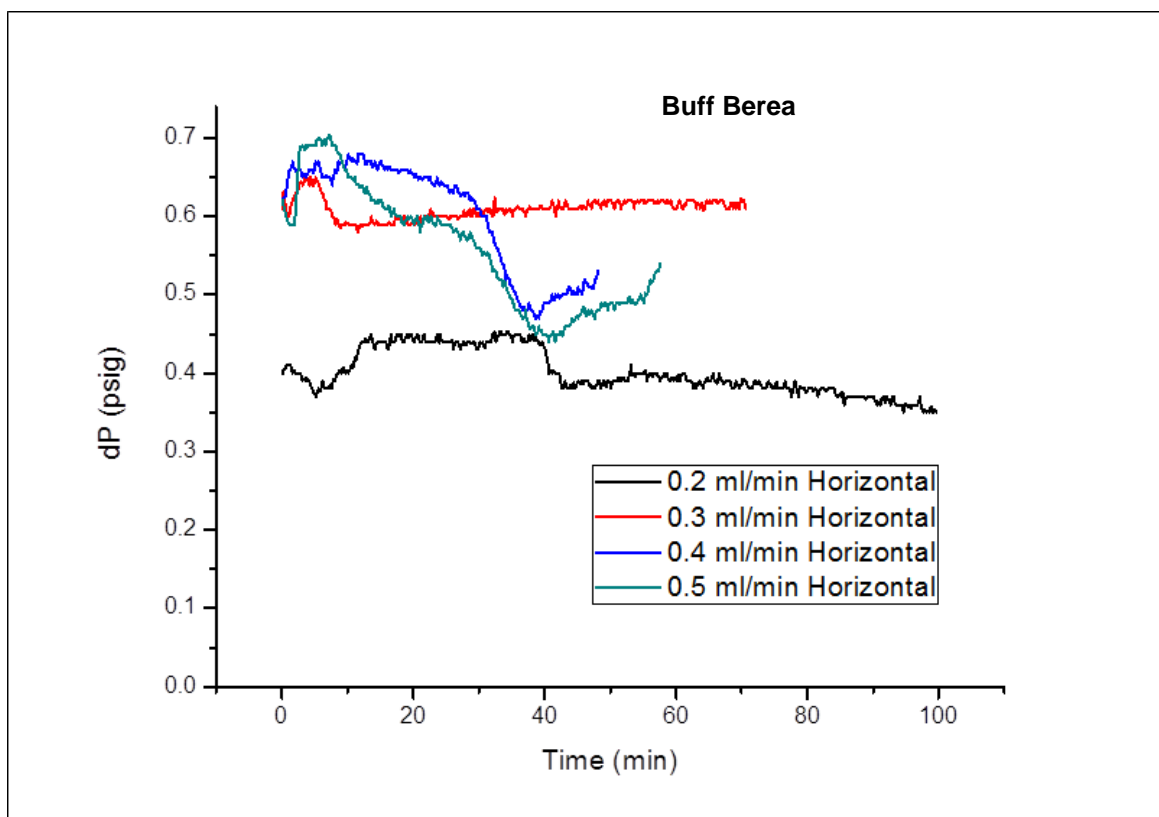
Figure 5.35 dP changes as function of time for Buff Berea in horizontal orientation

In both cases, the permeability at 0.2 ml/min appeared to be higher with the lowest dP.
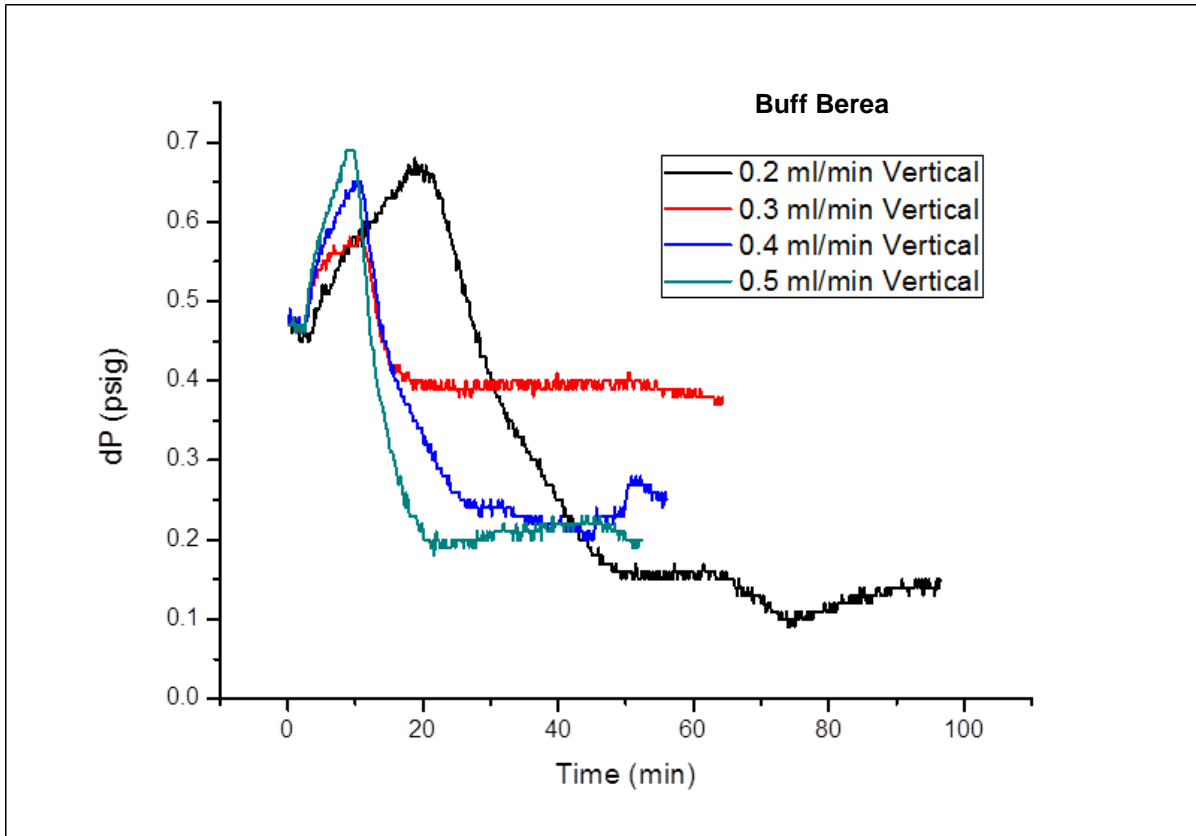
Figure 5.36 dP changes as function of time for Buff Berea in vertical orientation

Figure 5.37, Figure 5.38, Figure 5.39, and Figure 5.40 show the individual comparison of the flow behaviour at the same injection and different orientations. They all have one thing in common- the core sample permeability to the injected CO_2 tends to be lower in the vertical orientation compared to the horizontal orientation. There appears to be a strong influence of gravity on the flow of CO_2 through the porous media.

To further reaffirm this effect of gravity, these analyses were conducted in the case of *Bandera Grey* with the lowest absolute permeability amongst the core samples and explanations were made as to the trends observed.
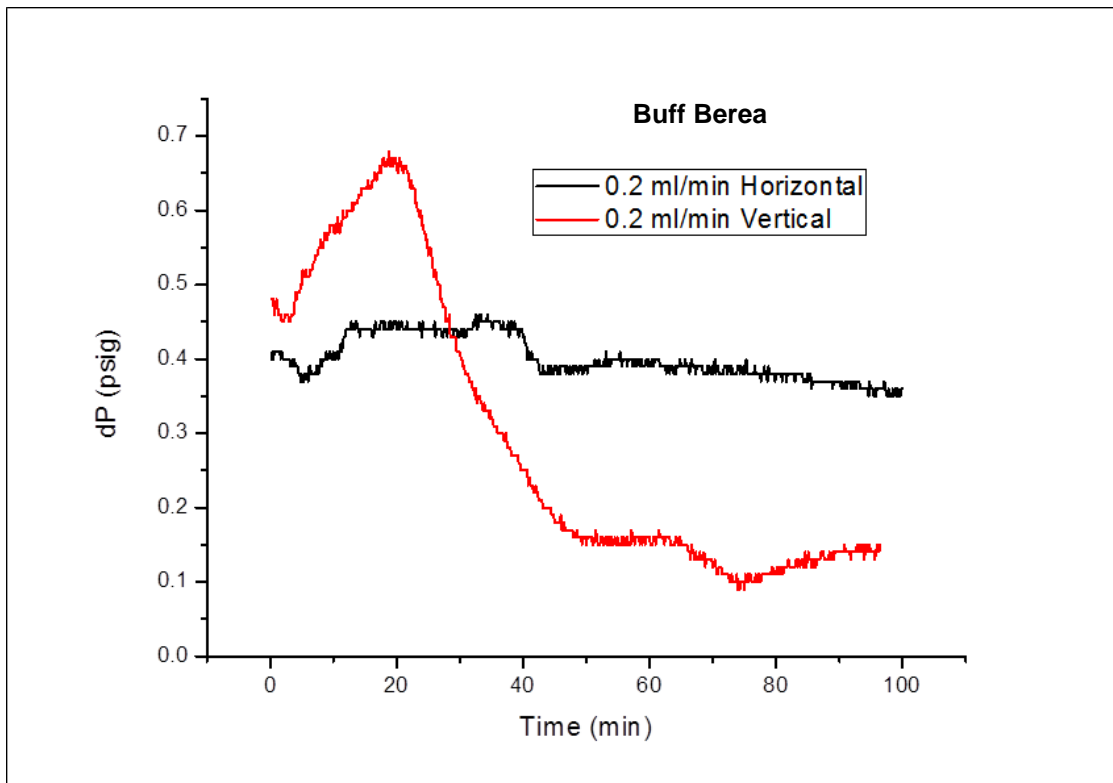
Figure 5.37 Comparison of dP changes with time at 0.2 ml/min in both orientations
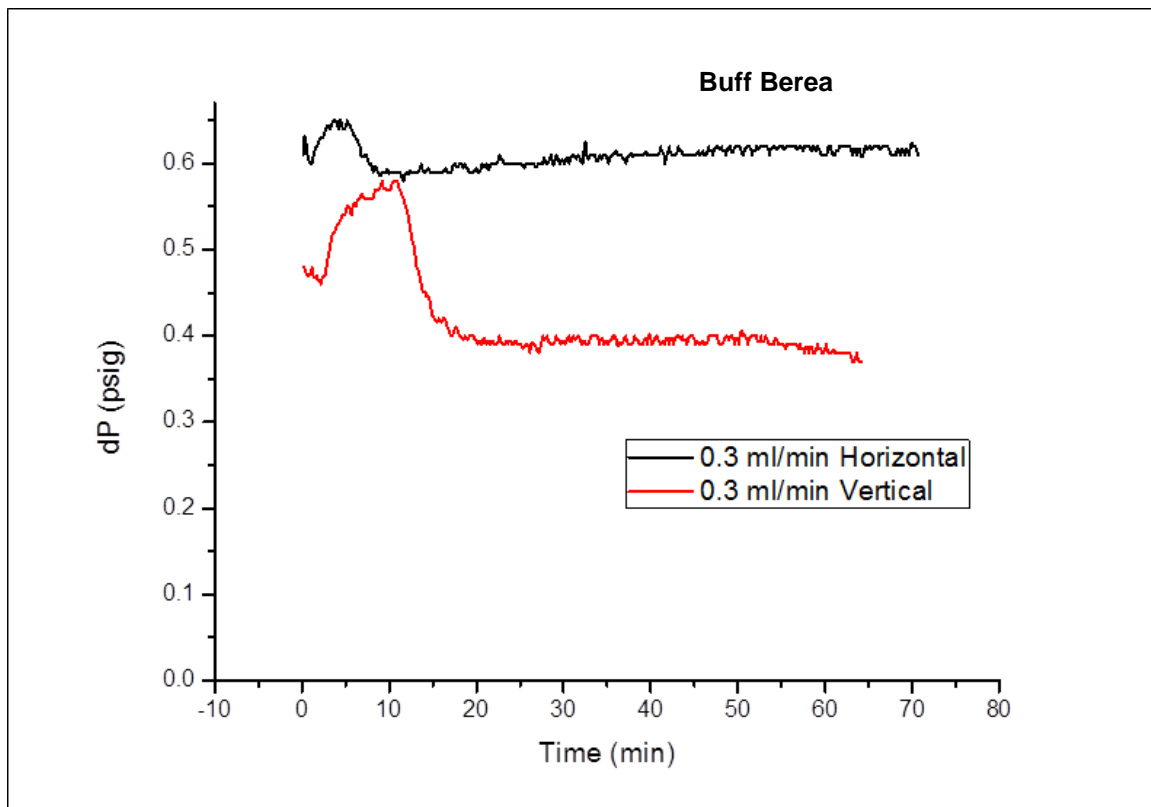
Figure 5.38 Comparison of dP changes with time at 0.3 ml/min in both orientations

133
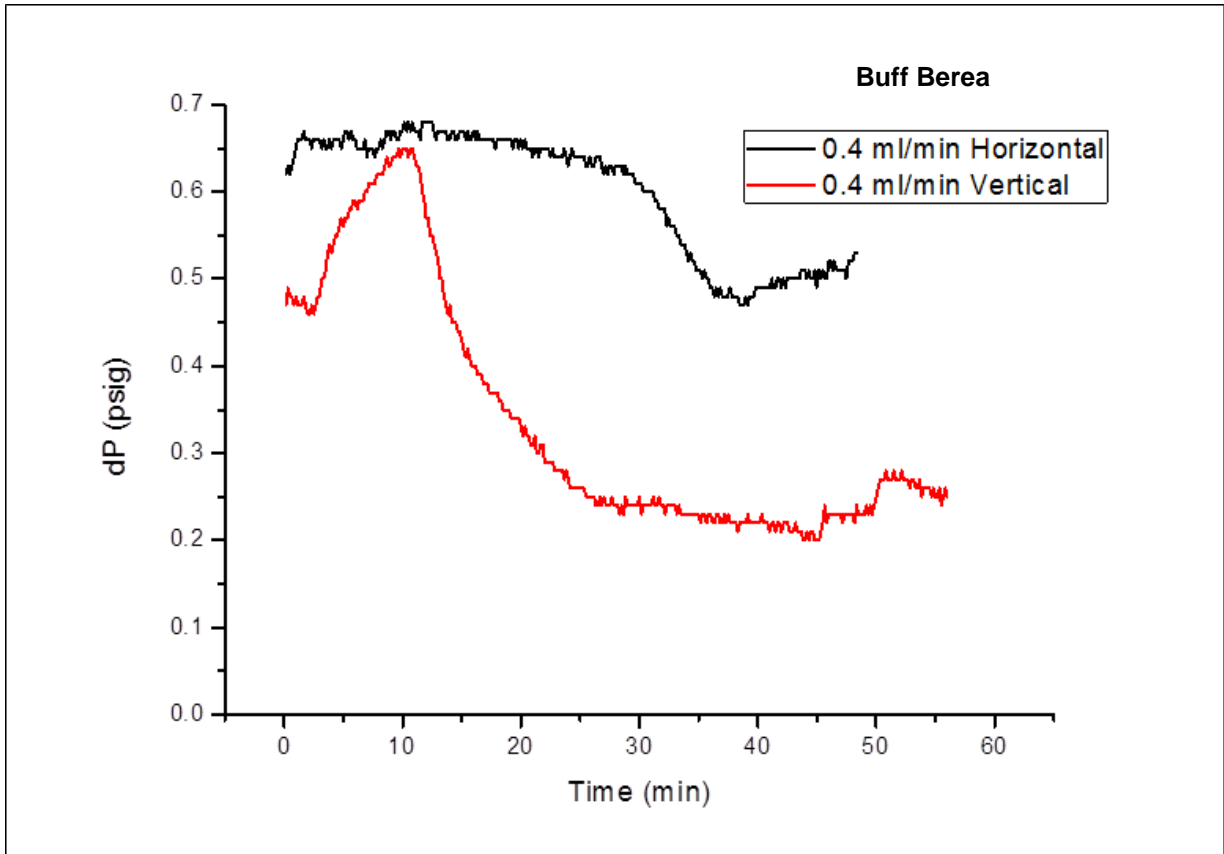
Figure 5.39 Comparison of dP changes with time at 0.4 ml/min in both orientations
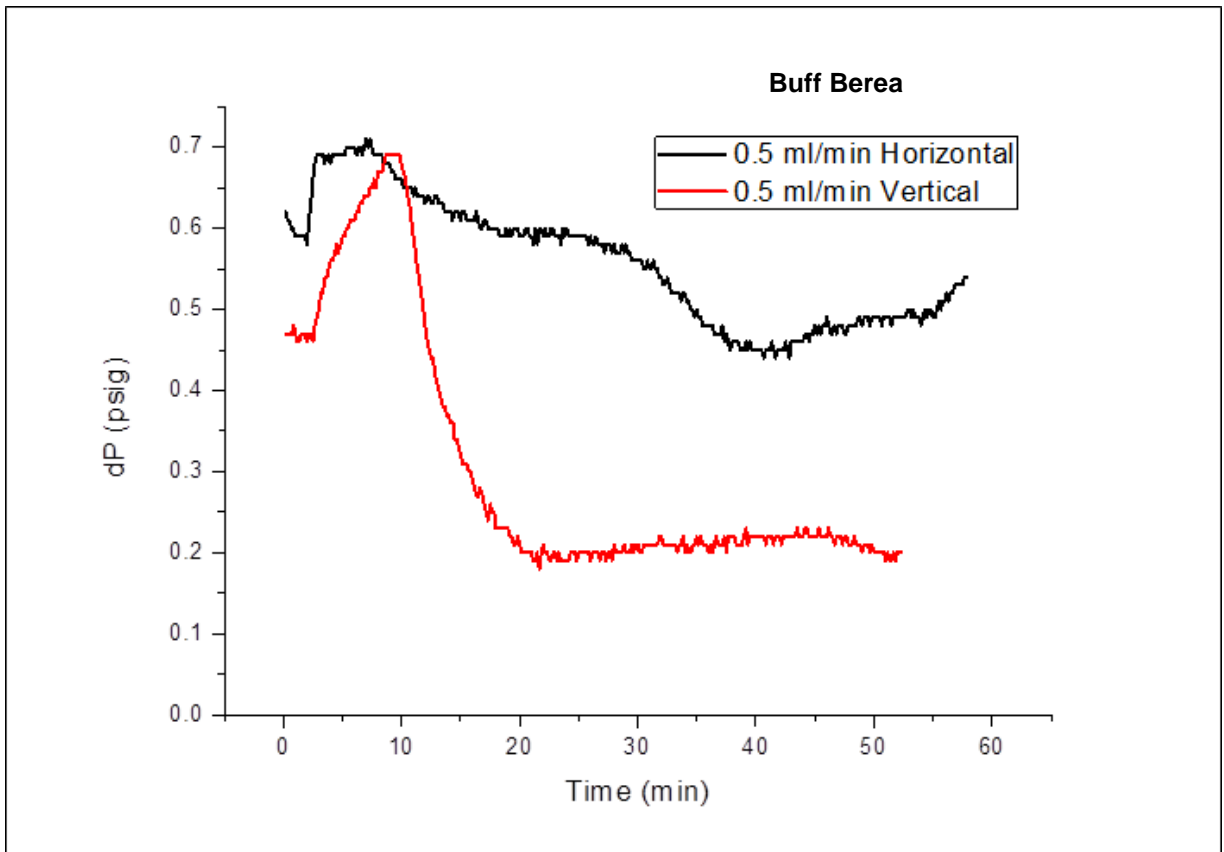
Figure 5.40 Comparison of dP changes with time at 0.5 ml/min in both orientations

134

5.3.3.3 Bandera Grey

There appeared to be more consistency in the dP trends for all the runs in both as functions of time. Bandera grey with the lowest absolute permeability shows no apparent deviations in magnitude for all the injections regardless of injection orientation. However, in Figure 5.41 and Figure 5.42, the highest permeability at the end of the experimental runs was realised in the 0.5ml/min experimental run. The high compressibility of CO_2 (Zhang et. al., 2011) and its high diffusivity in smaller pores (Dickerson et. al., 2014), can be used to explain this high permeability at high injection rate at the end of the experimental run. However, the mean dP was significantly higher compared to the other runs at lower injection rates which shows conformance to the Darcy law.
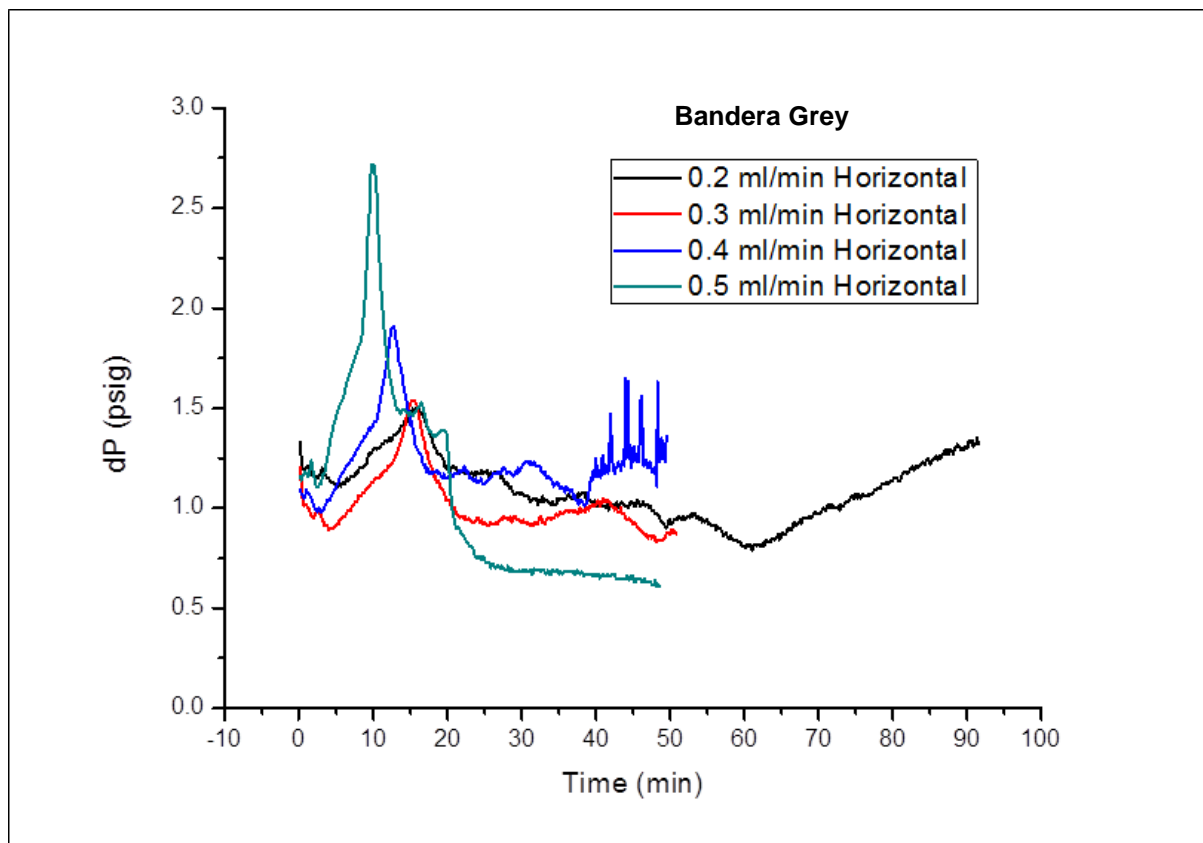
Figure 5.41 dP changes as function of time for Bandera Grey in horizontal orientation
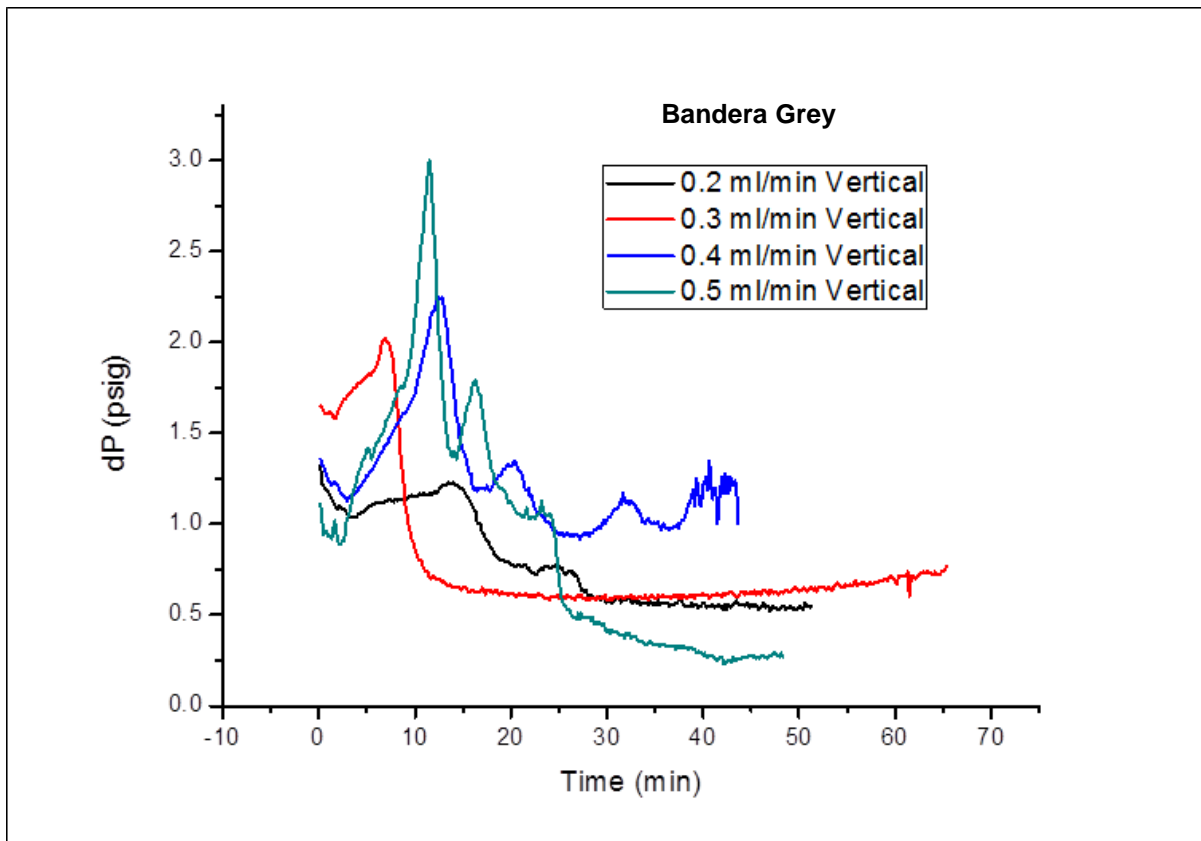
Figure 5.42 dP changes as function of time for Bandera Grey in vertical orientation

Analysing the individual injection runs at different orientations for *Bandera Grey*, the same trend also was observed in that the vertical orientation experiment, CO_2 had higher permeability compared to the horizontal runs at all the injection rates. However, as seen with the other core samples, the flow behaviour of CO_2 became similar at higher injection rates regardless of the injection orientations.

From Figure 5.43, Figure 5.44, Figure 5.45, and Figure 5.46, the dP trend started off similarly and then after the CO_2 breakthrough, there were divergence in trends especially in 0.2 and 0.3 ml/min runs at both orientations which are the low injection rates. This behaviour was minimised when the injection rates increased to 0.4 and 0.5 ml/min – an indication that at higher injection rates, the flow behaviour became similar irrespective of the injection orientation.

An attempt was made in the next section to explain the seemingly similar trends on the flow behaviour of supercritical CO_2 during EGR in terms of permeability variation and also injection orientation.
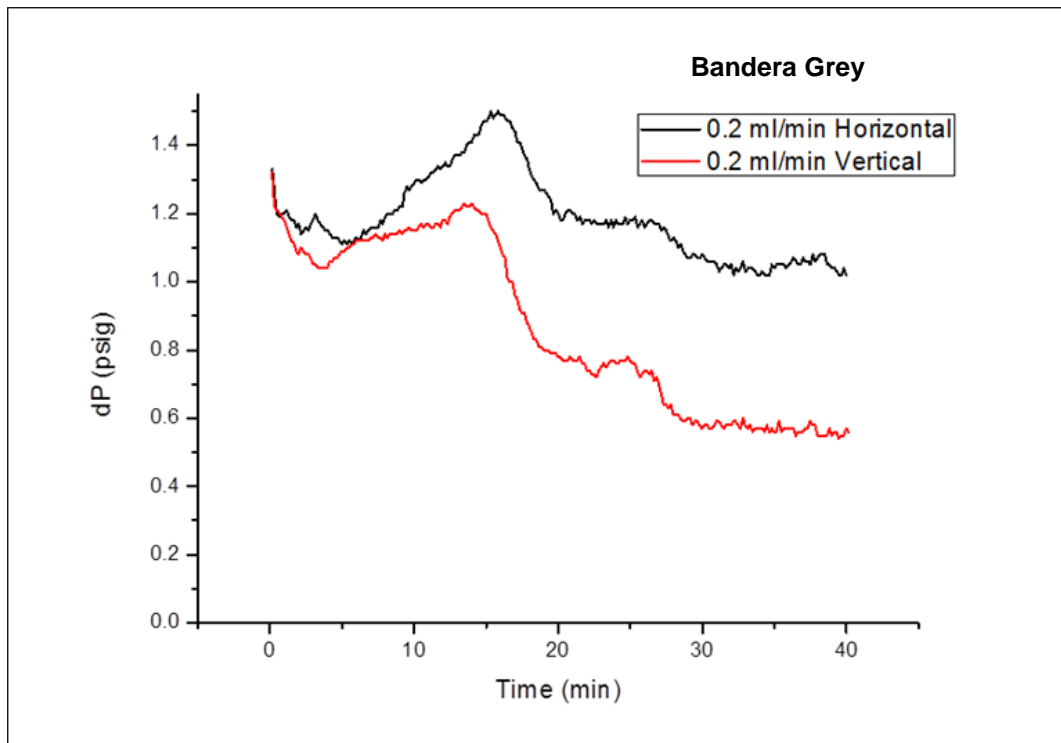
Figure 5.43 Comparison of dP changes with time at 0.2 ml/min in both orientations
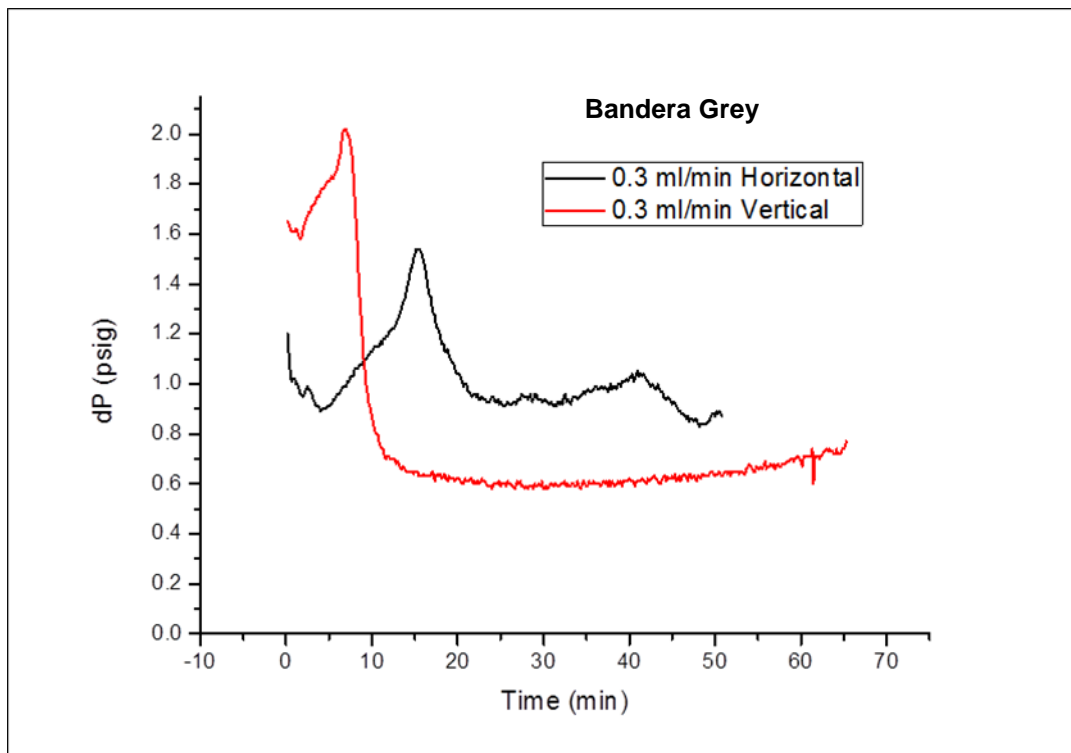
Figure 5.44 Comparison of dP changes with time at 0.3 ml/min in both orientations
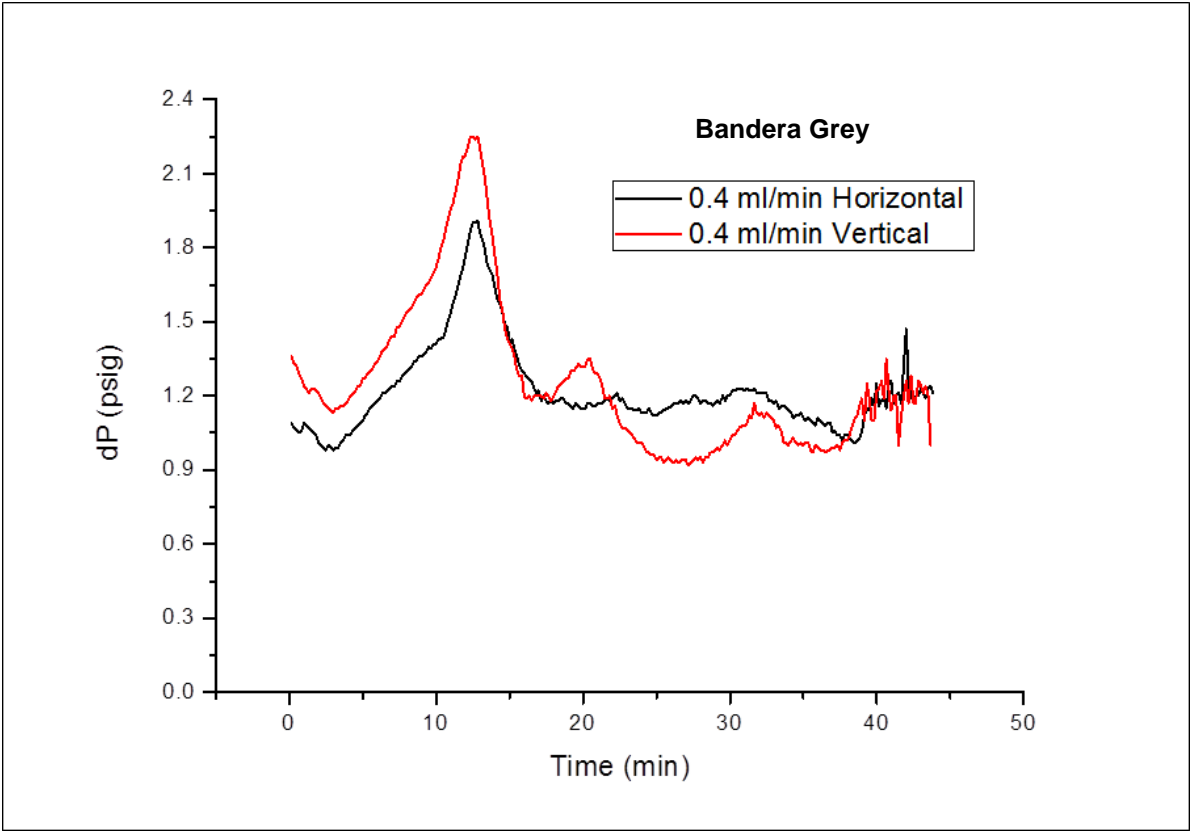
Figure 5.45 Comparison of dP changes with time at 0.4 ml/min in both orientations
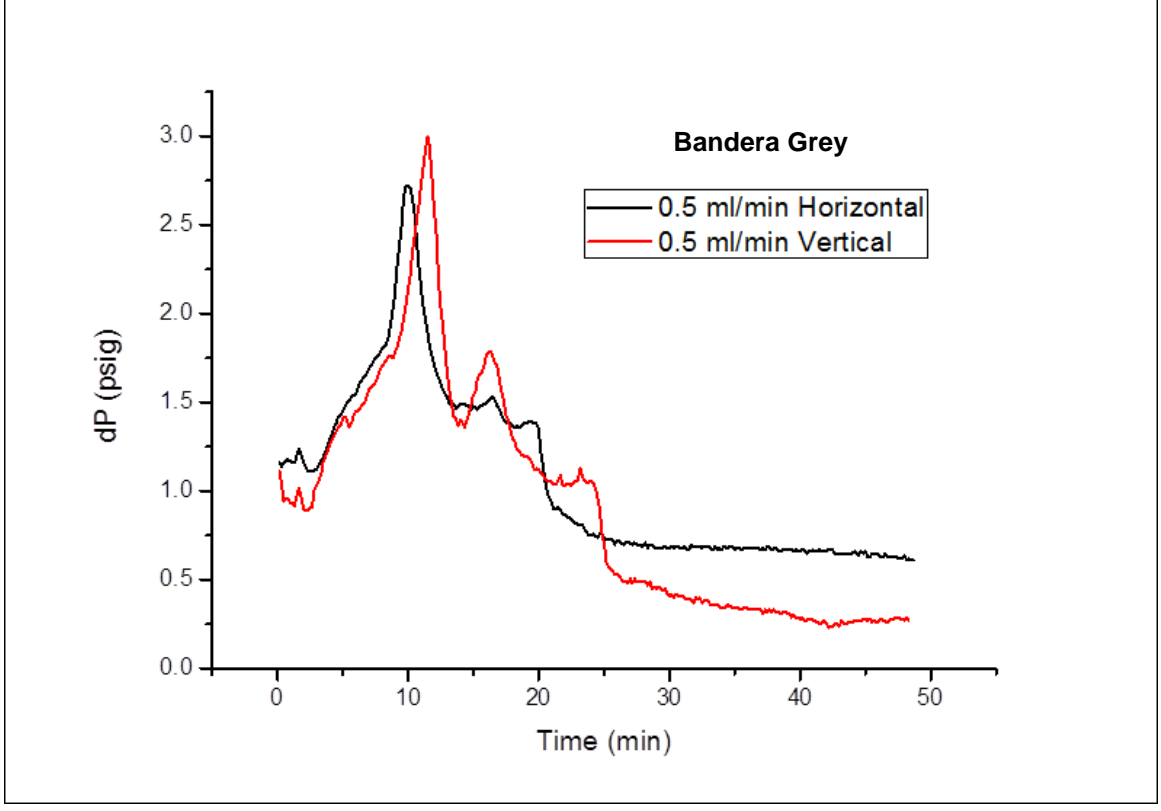
Figure 5.46 Comparison of dP changes with time at 0.5 ml/min in both orientations

138

5.3.3.4 Comparison of the flow behaviours of test cores

Figure 5.47 to Figure 5.54 are comparisons made of the core samples at the same injection rates and injection orientation. *Buff Berea* core samples behaved quite similarly to the Grey Berea and remarkably different from Bandera grey. At 0.2 ml/min injection rate, the dP changes in the horizontal orientation deviated towards the end of the flow in *Bandera grey*. This is as a result of the tailing effect of the remnants of the displaced CH_4 which slowly enters the flow stream of the injected CO_2 plume as it exits the core sample. This was not observed in the vertical run which was characterised by a very high dP at the onset, meaning that the since the flow was against gravity, the pressure build up at the inlet of the core sample was significantly higher and after which this dP rapidly decreased after CO_2 breakthrough. All the vertical runs - Figure 5.48 Figure 5.50 Figure 5.52 Figure 5.54 – were characterised by this trend and provided the less dispersion (Table summary) compared to their horizontal counterparts for all the core samples tested.
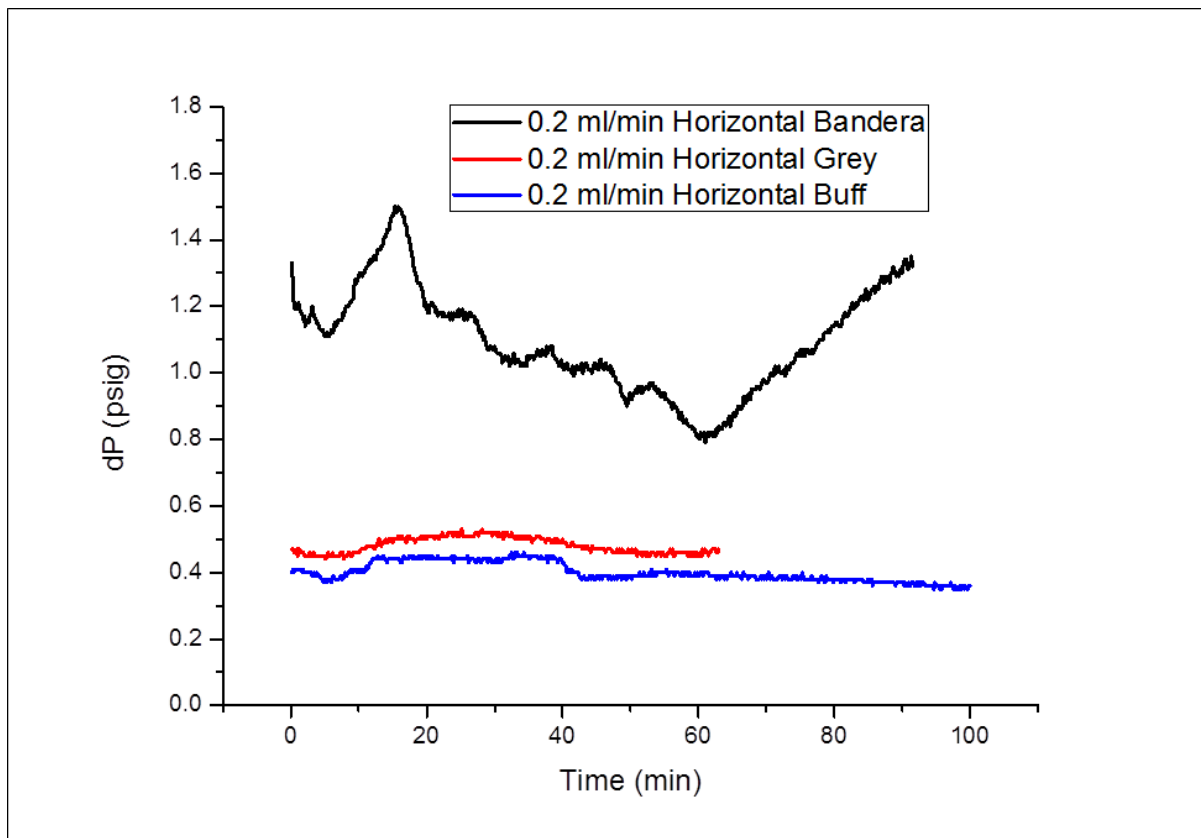
Figure 5.47 dP comparison between all samples at 0.2 ml/min in horizontal orientation

139
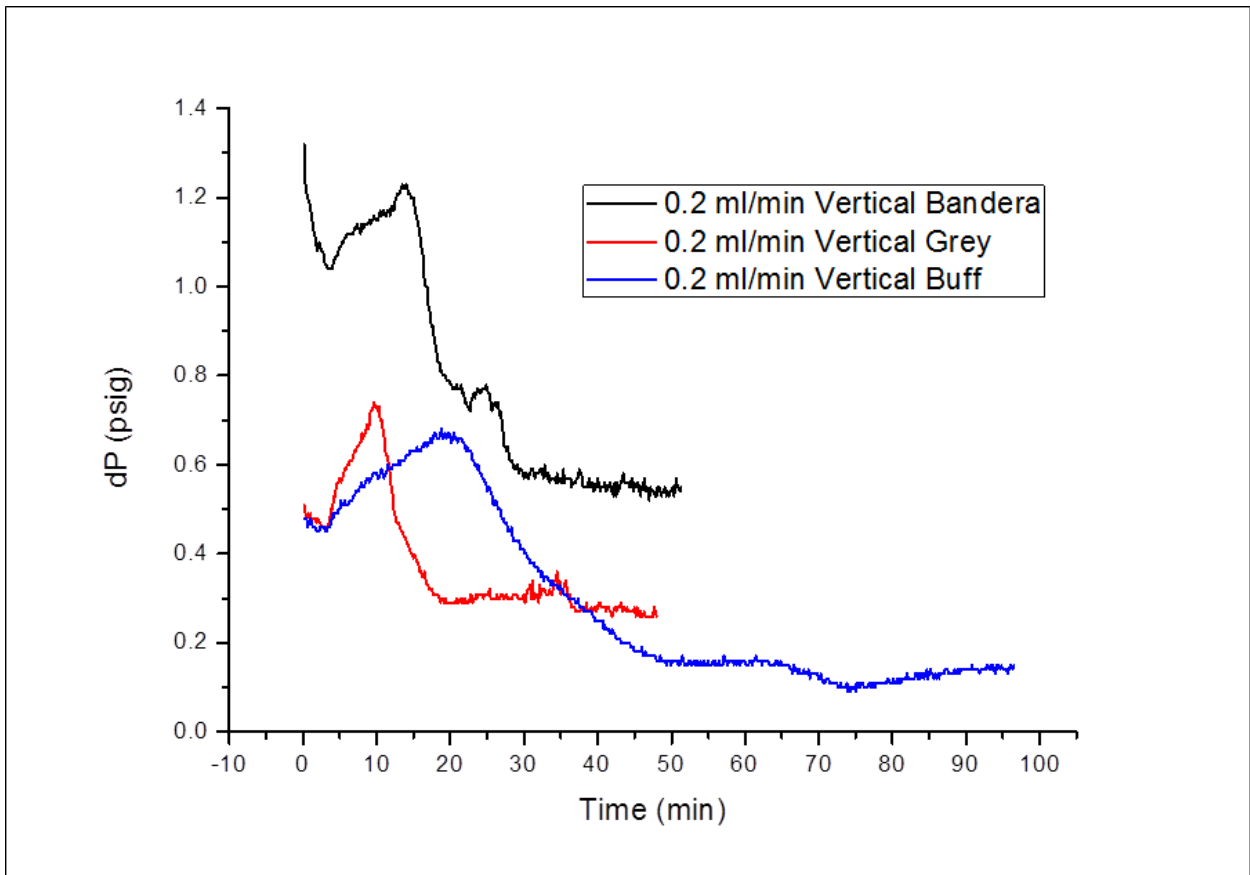
Figure 5.48 dP comparison between all samples at 0.2 ml/min in vertical orientation

For the horizontal orientation - Figure 5.47, Figure 5.49 Figure 5.51 and Figure 5.53- the flows did not follow a specified pattern with regards to the uniqueness of their petrophysical assertions, with *Bandera Grey* having the most consistency when it comes to relating the flow and dP changes as functions of time.
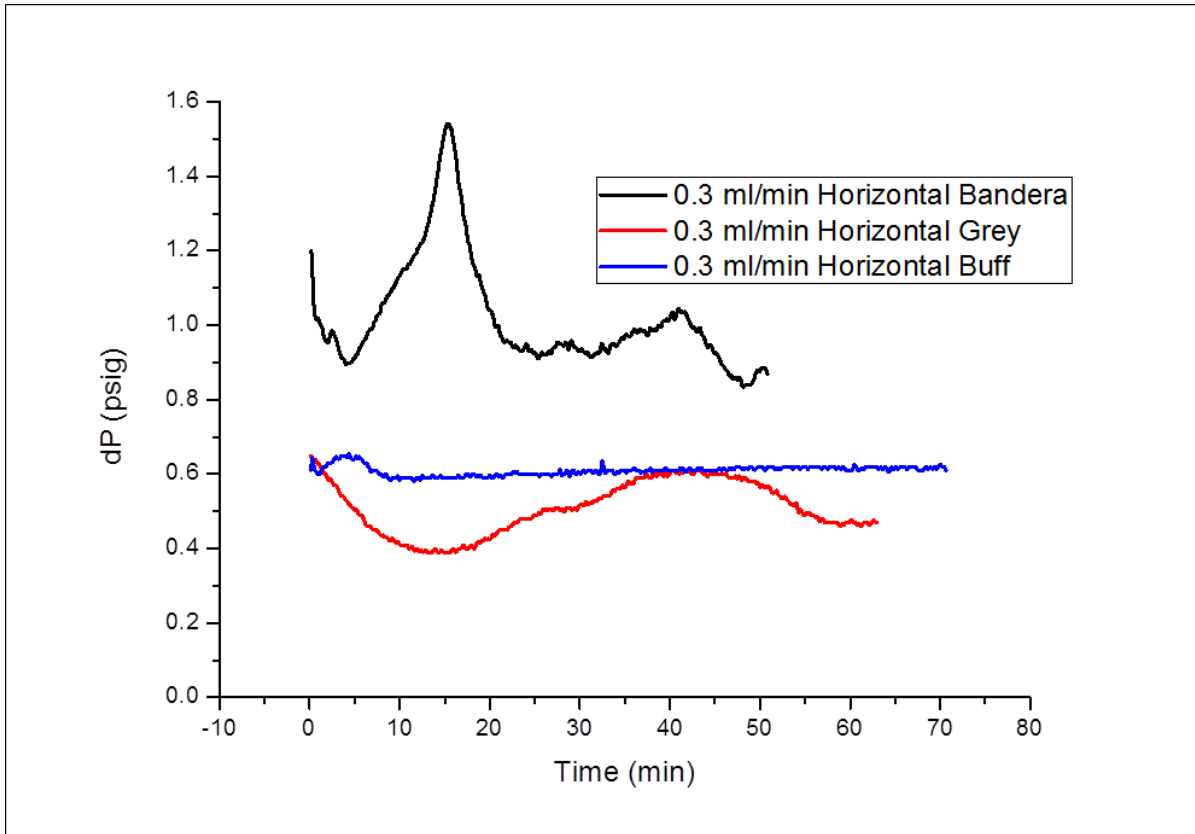
Figure 5.49 dP comparison between all samples at 0.3 ml/min in horizontal orientation
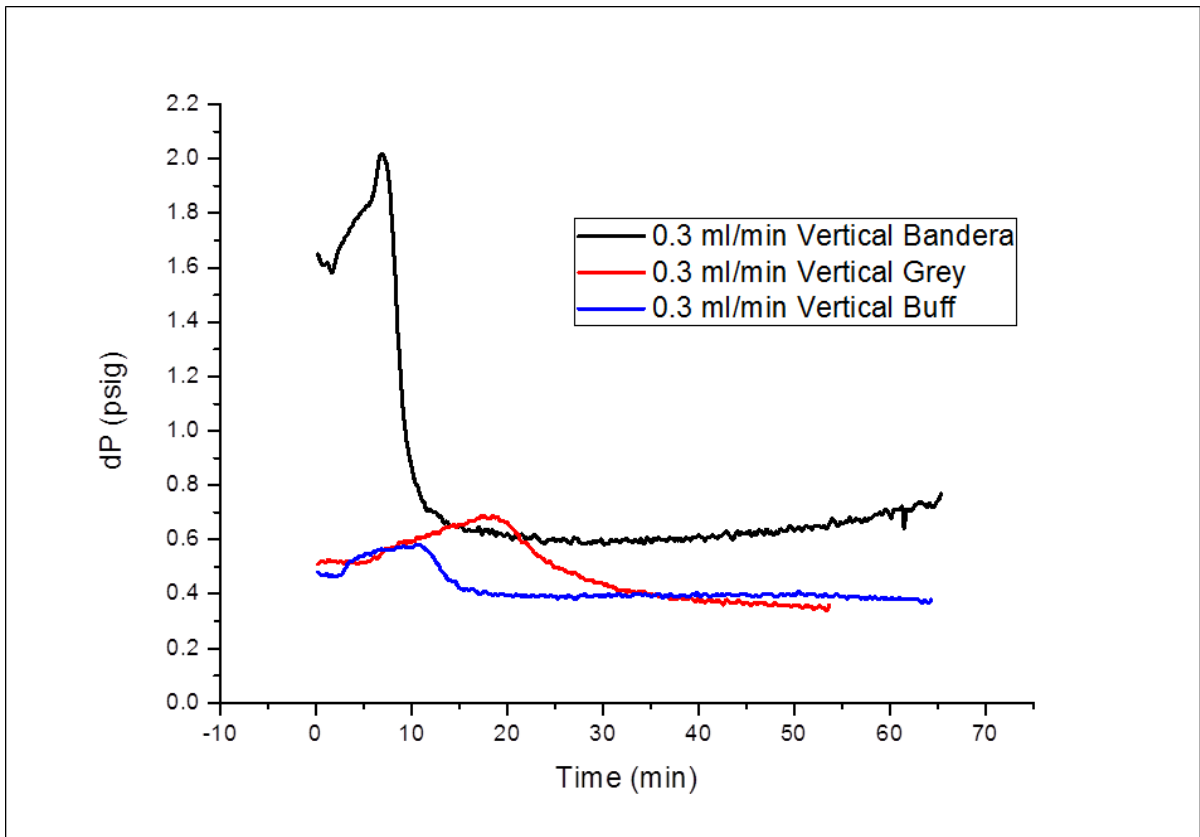
Figure 5.50 dP comparison between all samples at 0.3 ml/min in vertical orientation

141
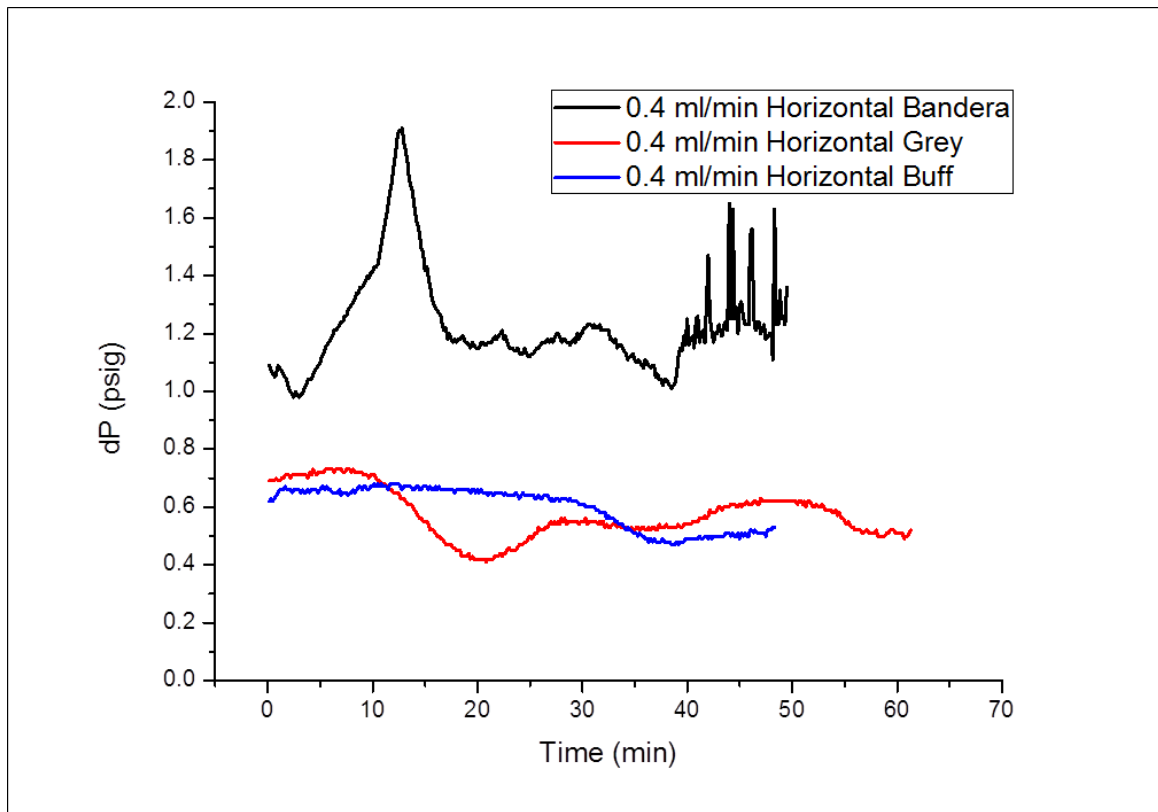
Figure 5.51 dP comparison between all samples at 0.4 ml/min in horizontal orientation
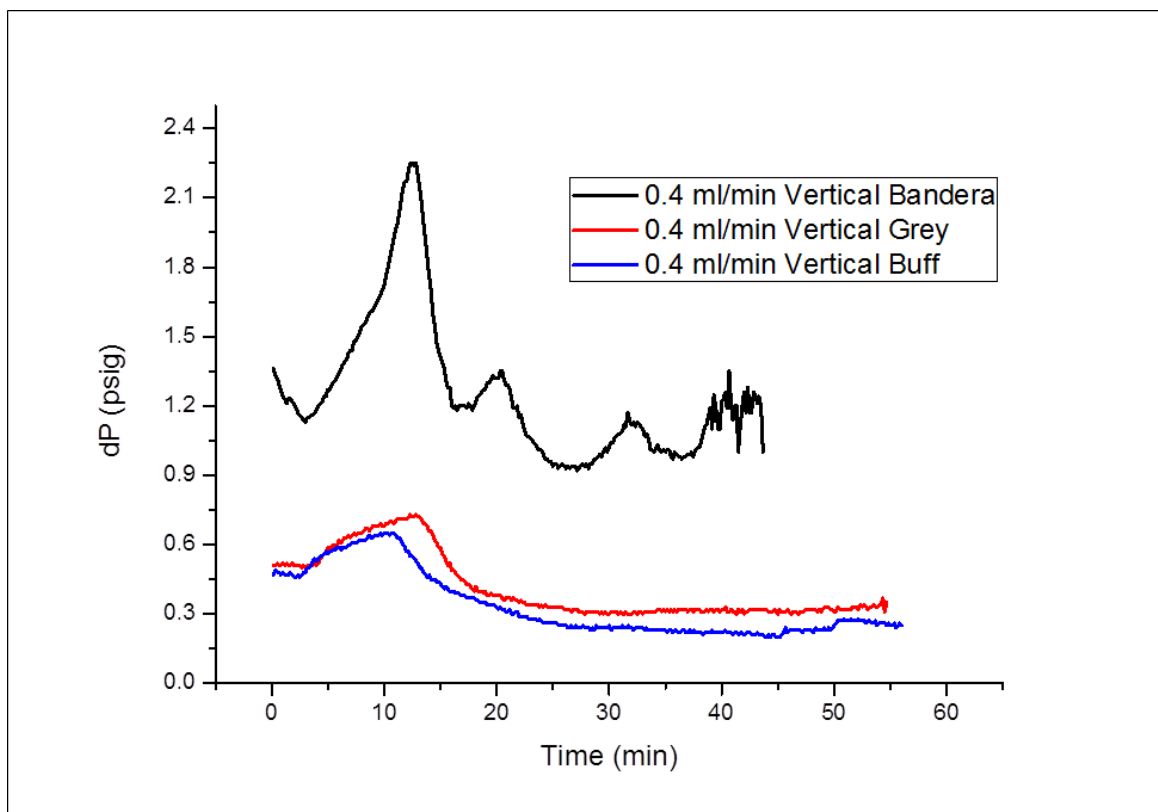
Figure 5.52 dP comparison between all samples at 0.4 ml/min in vertical orientation

142
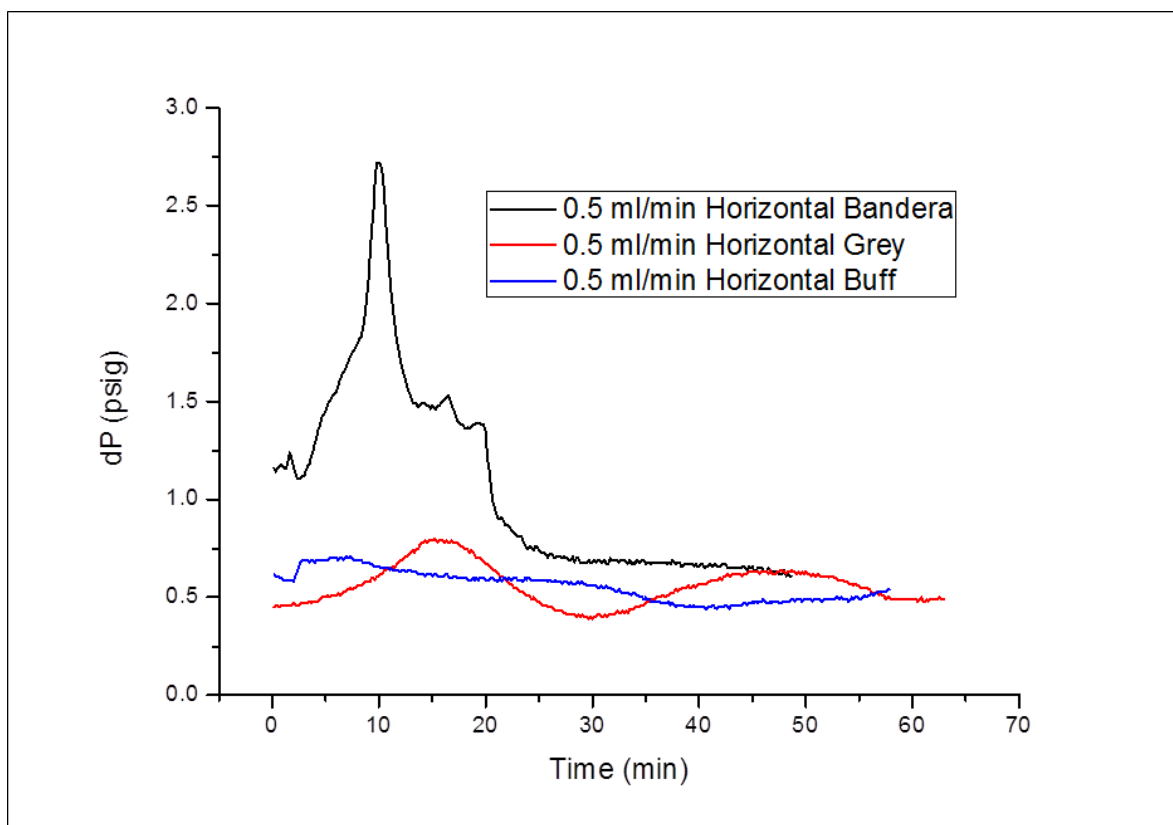
Figure 5.53 dP comparison between all samples at 0.5 ml/min in horizontal orientation
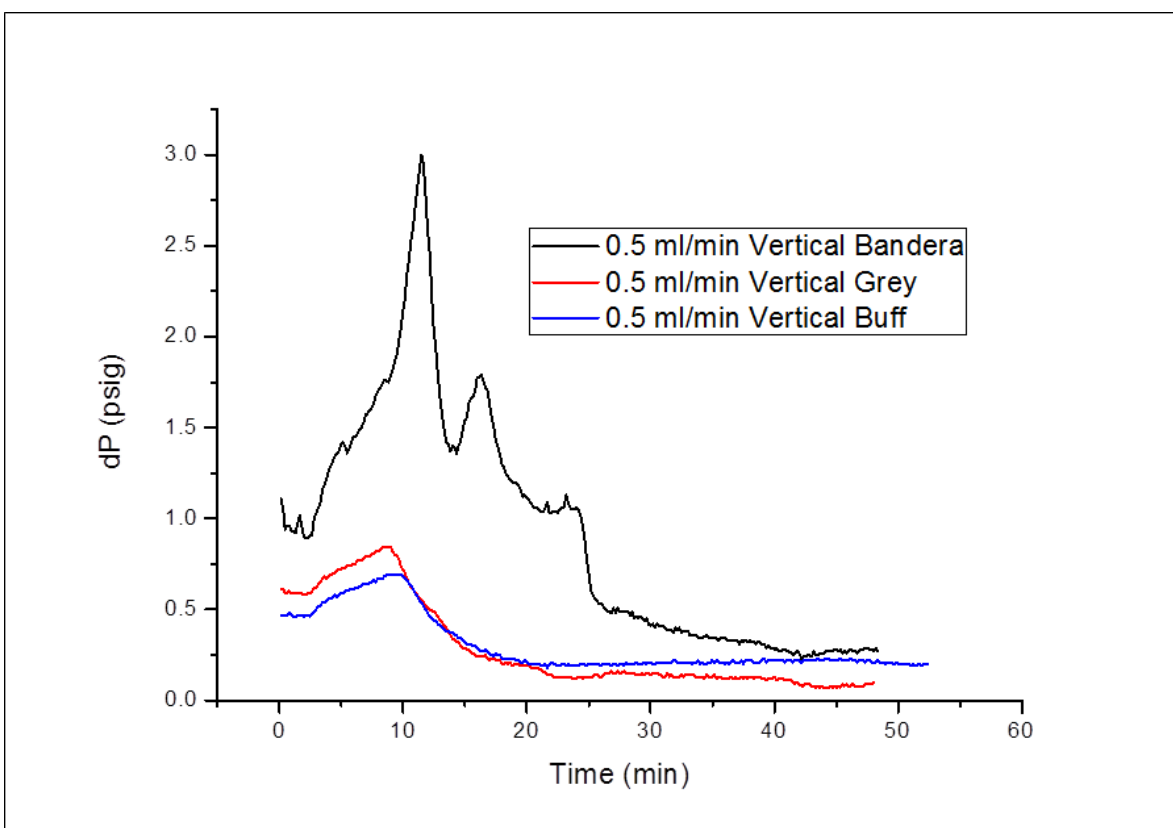
Figure 5.54 dP comparison between all samples at 0.5 ml/min in vertical orientation

143

As mentioned in Section 2.6 of Chapter 2, CO_2 at conditions above a pressure of 1070 psia and 31°C is in its supercritical state and in this state exhibits a rather peculiar property deviating from the normal gas behaviour to a quasi-gas behaviour in that it attains a density close to that of a liquid but still retains the viscosity of a gas. This behaviour comes with a lot of complexity when describing the flow behaviour in this region. As with CO_2, CH_4 is also in its supercritical state at 667 psia and -82°C pressure and temperature respectively. However, CH_4 does not deviate from gas behaviour and its supercritical state showed no significant effect on its transport through porous media as seen in this research.

The significant "activity" seen in the dP trends during the displacement of CH_4 in EGR in the horizontal orientation in all the test injection rates can be attributed to the effect of gravity on the CO_2 as it traverses the core sample. CO_2 flows longitudinally along the entire length of the core sample thereby creating higher pressure drops as it loses its energy within the core sample's pore matrix.

Given the closeness in permeability and porosity of Buff and Grey Berea, this realisation of similar dispositions in dP fluctuations in these core samples is expected. Generally, the horizontal orientations experiments exhibited the most unstable flow (from the dP plots) of CO_2 as it displaces the CH_4, mainly as a result of CO_2 density relative to that of CH_4. At those conditions, the density of CO_2 is substantial that as it invades the core sample at the inlet, it "sinks" to the bottom of the core sample and accumulates as it transverses through the core sample and displaces CH_4 upwards and towards the outlet. The densities of the gas at the specified conditions of interest in this research was simulated using PVTSim 8 and is shown in Figure 5.55. This segregation of CO_2 to the bottom of the porous medium as a result of its higher density will be more pronounced in the horizontal orientation as seen in the relationship between the density and the permeability through a modification of Darcy law by Muscat (1937) as reported by Thusyanthan & Madabushi (2003) and given as:

$$k = K \frac{\rho g}{\mu} \tag{5.9}$$

Where K is the intrinsic permeability (a function of arrangement, diameter and shape of the porous medium), k is Darcy permeability, ρ is the density of the fluid, μ is the dynamic viscosity of the fluid, and g is acceleration due to gravity. Given the nature of the fluids (CH_4 and CO_2) under investigation, there is a significant difference in their densities and overall

properties and invariably their weights and viscosities which will obviously alter their flow behavior and transport properties.
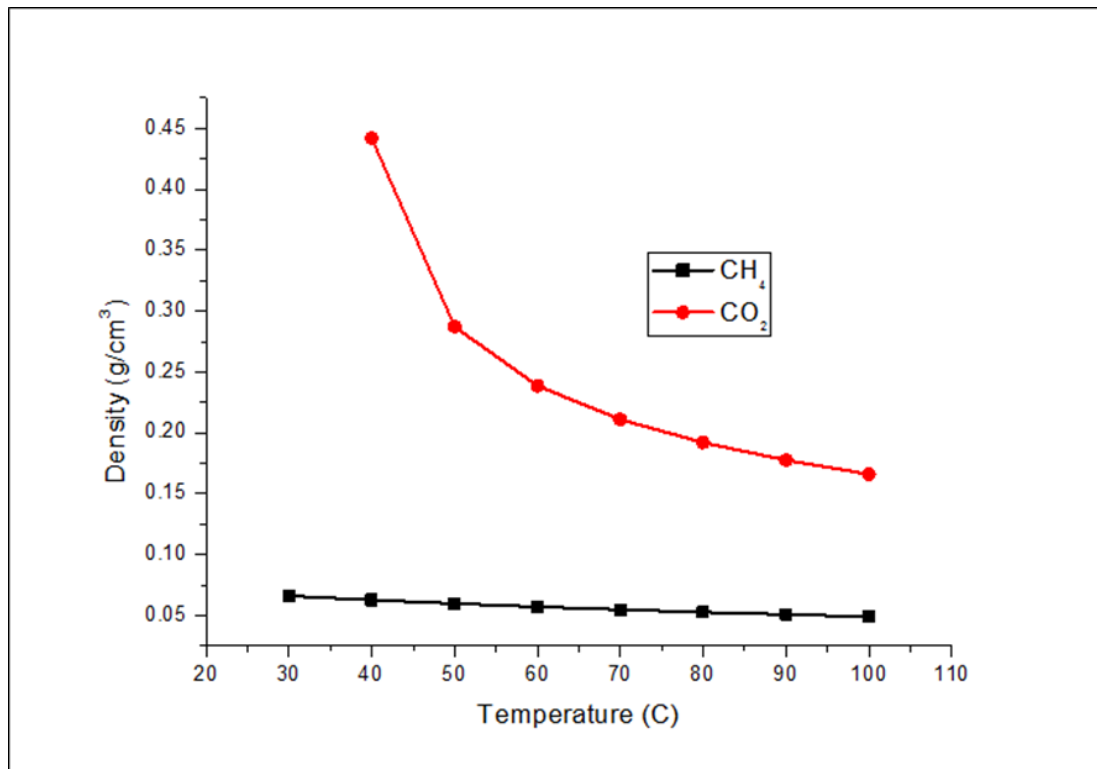
Figure 5.55 CH_4 and CO_2 densities as functions of temperature at 1400 psig

To further buttress these points, CO_2 permeability, as observed in the aforementioned figures, drastically decreased with characteristically higher dP in the horizontal orientation as a result of the increased gravity effect on the gases in porous media which unequivocally affected the recovery efficiency of CH_4 during the displacement by providing a rather poor sweep efficiency. Mixing of the gases is more severe in the horizontal orientation as seen in Section 5.3.3.

From these analyses it is noteworthy to infer that gravity has substantial influence on the flow behaviour of CO_2. For this reason, the subsequent investigations on the parametric analysis will be carried out in the vertical orientation as gravity effects are not as pronounced as in the horizontal runs which could affect the outcome of further tests.

5.3.4 CH_4 recovery determination

Having evaluated the individual dispersion coefficients for each core sample at test flowrates, and also investigated the effect of injection orientation, the next step is to evaluate the recovery efficiency of the injection process on each core sample. As stated in the previous

section, this investigation was carried out in the vertical orientation to reduce the gravity effects on the injected CO_2. This helps to eliminate the systematics errors emanating from CO_2 transport through the porous medium as it displaces CH_4 to set up a benchmark for other factors under investigation. The recovery efficiency will be based on the CH_4 recovered after the displacement run.

5.3.4.1 Grey Berea

The mass flow controllers/meters measured the gas effluents produced during the core flooding experiments. Measurements of the gas effluents production rates were in sccm (standard cubic centimetres per second) and the conversion to actual flowrate at experimental conditions of 50°C and 1300 psig was carried out using the correlation contained in the technical manual of Honeywell (2012).

$$Q_X = Q_S \cdot \frac{P_s}{P_X} \cdot \frac{T_X}{T_s} \qquad (5.10)$$

Where Q_x is the volumetric flowrate (ccm) at experimental conditions, Q_s is volumetric flowrate (sccm) at standard conditions measured by the flow meter, P_s, P_x are pressures at standard and experimental conditions respectively in atm, T_s, T_x are temperature at standard and experimental conditions respectively. The reference condition for the design of the flow meter is 0°C and 14.69 psi. However, the effluent exit pressure from the back-pressure regulator was 80 - 100 psig and the gas flowing temperature is the as that of the core holder, 50°C.

This was used to calculate the instantaneous volume produced at each time stamp which invariably computed the cumulative volume produced for each core flooding process. And the percentage by volumes of the gas produced obtained from the GC was used to calculate individual gas produced at each time in each run.

In order to assess the percentage recovery of the CH_4 and recovery factor of each injection rate, the original gas in place OGIP must be determined. Employing Eq. 2.18 to 2.20, the Gas formation volume factor was calculated at the experimental conditions using the compressibility factor, z, of the gas.

To determine the z factor from the chart, the pseudo-reduced properties/conditions of CH_4 at the experimental conditions must be deduced. A correlation for the pseudo pressure is presented as follows:

$$P_{pr} = \frac{P}{P_c} \qquad (5.11)$$

And for the temperature;

$$T_{pr} = \frac{T}{T_c} \qquad (5.12)$$

Where P_{pr} the dimensionless Pressure, P is the average experimental pressure (1300 psig) in psi, P_c is the critical pressure (46.7 bar or 670.13 psi) – this was obtained from Figure 2.4 which is a simulation of the phase envelope of CH_4 using PVTsim - of the gas (CH_4) in psi, T_{pr} is the dimensionless temperature, T_c is the critical pressure of the gas (from Figure 2.6 – 190.2K) in K. These parameters input variables to evaluate the z factor using the Standing and Katz chart.

$$P_{pr} = \frac{1314.69}{670.13} = 1.97$$

$$T_{pr} = \frac{323.15}{190.2} = 1.70$$

Using the values, the gas compressibility factor, z, was obtained from the Standing and Katz chart as 0.92. Similarly, there are more robust models to accurately estimate the CO_2 compressibility derived from modified Peng Robinson Equation of state (EOS) presented by (Ziabakhsh-Ganji & Kooi, 2012) and later improved and adopted by (Shabani & Vilcáez, 2017). This is given as:

$$Z^3 - (1 - B)Z^2 + (A - 2B - 3B^3)Z - (AB - B^2 - B^3) = 0 \qquad (5.13)$$

Where the parameters A and B are dimensionless and also defined as

$$A = \frac{aP}{(RT)^2} \qquad (5.14)$$

And

$$B = \frac{bP}{RT} \qquad (5.15)$$

The constants, a and b are defined as

$$a = 0.45724 \frac{R^2 T_c^2}{P_c} \alpha \qquad (5.16)$$

$$b = 0.07780 \frac{R T_c}{P_c} \qquad (5.17)$$

$$\alpha = [1 + (0.37646 + 14522\omega - 0.26992\omega^2)(1 - \sqrt{\frac{T}{T_c}})]^2 \qquad (5.18)$$

R is the universal gas constant, w is acentric factor. A MATLAB program was written to evaluate the z. The coding and scripts written are presented in Appendix G. The z obtained from this model was 0.94.

The obtained z factor was then used in Eq. (2.18) and B_g was computed as:

$$B_g = \frac{0.94 \times 323.15}{20 \times 1314.7} = 0.01204 \; cm^3/scm^3$$

Next step in to insert the B_g into Equation 2.19 to compute the OGIP, the porosity value of the core sample (Grey Berea) was 20.1% from Table 5.1, and the bulk volume, V_b was found to be 37.75cm³ using the core sample dimension in Table 5.1. Since the core sample is dry, $S_w = 0$

$$OGIP = \frac{37.75 \times 0.203 \times (1 - 0)}{0.01204} = 629.78 \; cm^3$$

The value of the OGIP was then used to calculate the CH_4 percentage recovery. The CH_4 production recovery was evaluated and plotted as a function of time which was shown in Figure 5.56.

Recovery was calculated using the expression:

$$\%CH_4 = \frac{CH_4 \; Recovered \; @ \; time \; t}{OGIP} \times 100$$

This was used to calculate the instantaneous CH4 recovered and used to plot the graphs in all the runs.

Table 5.22 Flow properties and recovery efficiency of the experimental run at 0.2 ml/min

			0.2 ml/min			
Time (min)	Qs (sccm)	Qx (ccm)	Cum. Vol (cm³)	CH₄ (cm³)	CH4 Pv	CH₄ % Rec
0.16	289	49.97	49.97	47.97	6.0	12.09
5.49	461	80.21	194.18	194.18	24.3	30.82
10.83	392	68.21	262.39	212.39	26.5	37.65
16.17	354	61.60	323.99	233.82	29.2	40.86
21.51	132	22.97	346.96	127.85	16.0	20.30
26.67	80	13.92	360.88	95.56	11.9	15.17
32.17	52	9.05	369.92	80.24	10.0	12.74
37.32	35	6.09	376.01	70.54	8.8	11.20
42.67	30	5.22	381.23	61.80	7.7	9.81
47.99	32	5.57	386.80	56.28	7.0	8.93
53.67	41	7.13	393.94	50.66	6.3	8.04
58.99	64	11.14	405.07	46.42	5.8	7.37
64.33	141	24.53	429.61	45.37	5.7	7.20
69.47	290	50.46	480.07	42.10	5.3	6.68

Table 5.23 Flow properties and recovery efficiency of the experimental run at 0.3 ml/min

			0.3 ml/min				
Time (min)	Qs (sccm)	Qx (ccm)	Cum. Vol (cm³)	CO₂ (%)	CO₂ (cm³)	CH₄ (cm³)	CH₄ % Rec
0.17	655	113.97	113.97	0	0	113.97	18.09
5.50	469	81.61	195.58	0	0	195.58	31.05
10.83	400	69.60	265.18	0.25	0.66	304.51	58.99
15.99	282	49.07	314.24	18.58	58.39	285.86	40.62
21.50	96	16.70	330.95	65.51	216.80	114.14	18.12
26.67	68	11.83	342.78	78.46	268.95	73.83	11.72
32.17	82	14.27	357.05	82.94	296.14	60.91	9.67
37.33	289	50.29	407.33	87.34	355.77	51.57	8.19
42.66	319	55.51	462.84	93.35	432.06	30.78	4.89
47.99	197	34.28	497.12	95.82	476.34	20.78	3.30
54.00	427	74.30	571.42	96.56	551.76	19.66	3.12
59.33	318	55.33	626.75	96.66	605.81	20.93	3.32
64.66	305	53.07	679.82	97.72	664.32	15.50	2.46

Table 5.24 Flow properties and recovery efficiency of the experimental run at 0.4 ml/min

			0.4 ml/min				
Time (min)	**Qs (sccm)**	**Qx (ccm)**	**Cum. Vol (cm^3)**	**CO_2 (%)**	**CO_2 (cm^3)**	**CH_4 (cm^3)**	**CH_4 % Rec**
0.16	374	65.08	65.08	0	0	65.07	10.33
5.16	199	34.63	99.70	0	0	99.70	15.82
10.49	193	33.58	133.28	0.41	0.546	132.73	21.07
15.66	62	10.79	144.07	55.04	79.29	64.77	10.28
21.16	40	6.96	151.03	79.32	119.79	31.23	4.95
26.32	59	10.27	161.29	85.1	137.26	24.03	3.81
31.66	162	28.19	189.48	91.12	172.65	16.82	2.67
36.99	174	30.28	219.76	96.05	211.08	8.68	1.37
42.32	132	22.97	242.73	96.94	235.30	7.42	1.19
47.49	126	21.92	264.65	97.05	256.84	7.80	1.23

Table 5.25 Flow properties and recovery efficiency of the experimental run at 0.5 ml/min

			0.5 ml/min				
Time (min)	**Qs (sccm)**	**Qx (ccm)**	**Cum. Vol (cm^3)**	**CO_2 (%)**	**CO_2 (cm^3)**	**CH_4 (cm^3)**	**CH_4 % Rec**
0.16	242	42.11	42.11	0	0	42.11	6.686
5.32	167	29.06	71.17	0	0	71.17	11.300
10.66	105	18.27	89.44	30.62	27.39	62.05	9.853
15.99	39	6.79	96.22	81.79	78.70	17.52	2.782
21.16	87	15.14	111.36	89.93	100.15	11.21	1.781
26.5	59	10.27	121.63	96.26	117.08	4.55	0.722
31.82	70	12.18	133.81	98.93	132.37	1.43	0.227
37.16	75	13.05	146.86	99.73	146.46	0.40	0.063
42.32	72	12.53	159.38	99.64	158.81	0.57	0.091
47.66	69	12.01	171.39	99.81	171.06	0.33	0.052
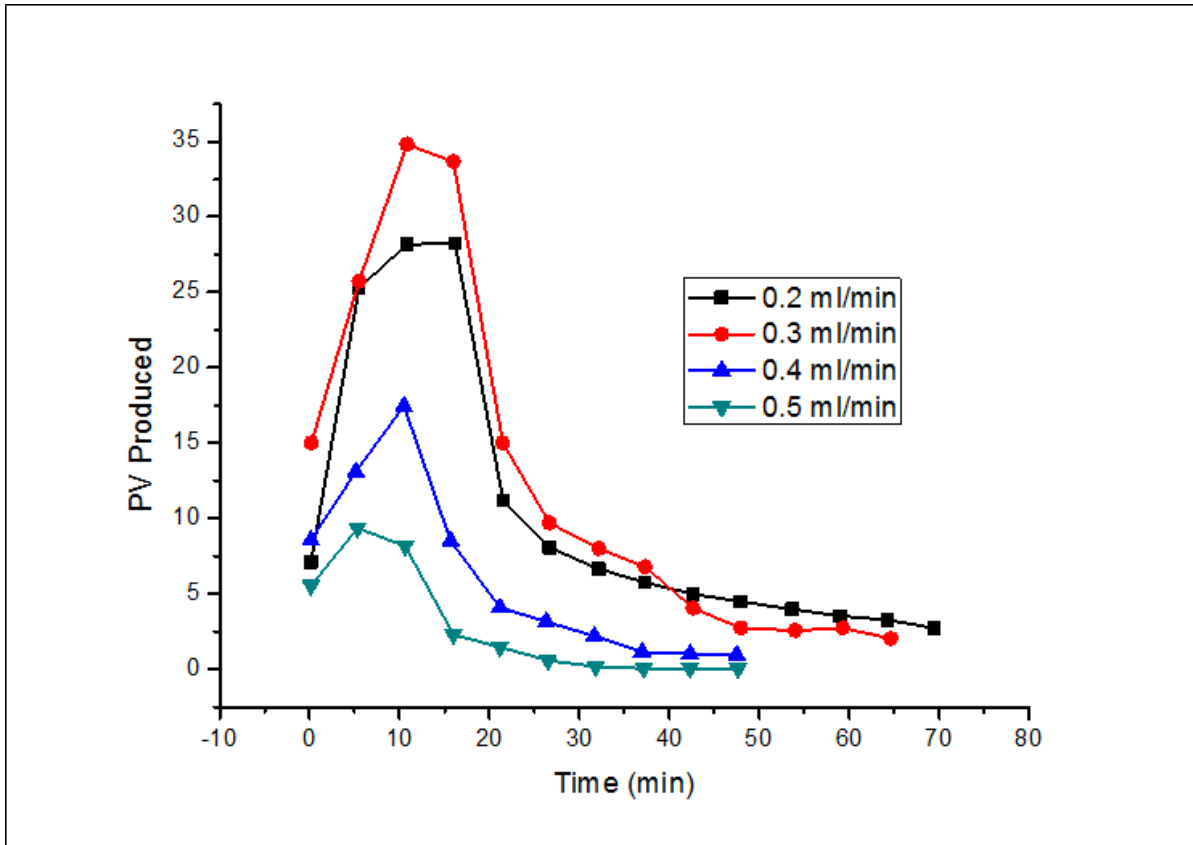
Figure 5.56 Comparison of CH$_4$ recovery in pore volumes as function of time for Gre

Figure 5.56 is a graphical representation of the results obtained for the CH$_4$ production recovery efficiency from the core flooding experimental runs through the application of different injection rates at the same experimental reservoir conditions adopted for this study. The run with 0.3 ml/min had the best recovery efficiency followed by the experimental run at 0.2 ml/min with substantial recovery too but the resident time for the displacement was longer, given that there was extensive mixing between the displaced and displacing gases taking into consideration. This is not conceivably an economic outcome as more CH$_4$ will be produced which will be grossly contaminated with the injected CO$_2$ thereby undermining the sequestration idea using EGR. There was good sweep efficiency and a substantial CH$_4$ recovery in the experimental run with 0.3 ml/min as the injection rate compared to the runs with 0.4 ml/min and 0.5 ml/min which show a rather poor trend in terms of CH$_4$ recovery and sweep efficiency. Higher injection rates presented early breakthroughs of CO$_2$ and high dispersion coefficients.

With these results, it is clear that the optimum flowrate/injection rate for CO_2 injection for this experiment is the 0.3 ml/min based on the volume of CH_4 recovered.

5.3.4.2 Buff Berea

The same steps were taken as those employed in the Grey Berea evaluation in Section 5.3.4.1 to analyse the recovery efficiency of the process in Buff Berea with a higher porosity and permeability. The differences are the porosity and bulk volume to evaluate the OGIP in the Buff Berea core sample. The evaluation of the OGIP is as follows:

From Eq. 5.6:

$$P_{pr} = \frac{1314.69}{670.13} = 1.97$$

$$T_{pr} = \frac{323.15}{190.2} = 1.70$$

Using the values, the gas compressibility factor, z, was obtained modified model as employed in Grey Berea experiments.

$$B_g = \frac{0.94 \times 323.15}{20 \times 1314.7} = 0.01204 \ cm^3/scm^3$$

And as for the OGIP, and at $S_w = 0$

$$OGIP = \frac{37.002 \times 0.262 \ (1 - 0)}{0.01204} = 805.15 \ cm^3$$

The value of the OGIP was then used to calculate the CH_4 percentage recovery. The CH_4 production recovery was evaluated and plotted as a function of time which was shown in Figure 5.57.

152
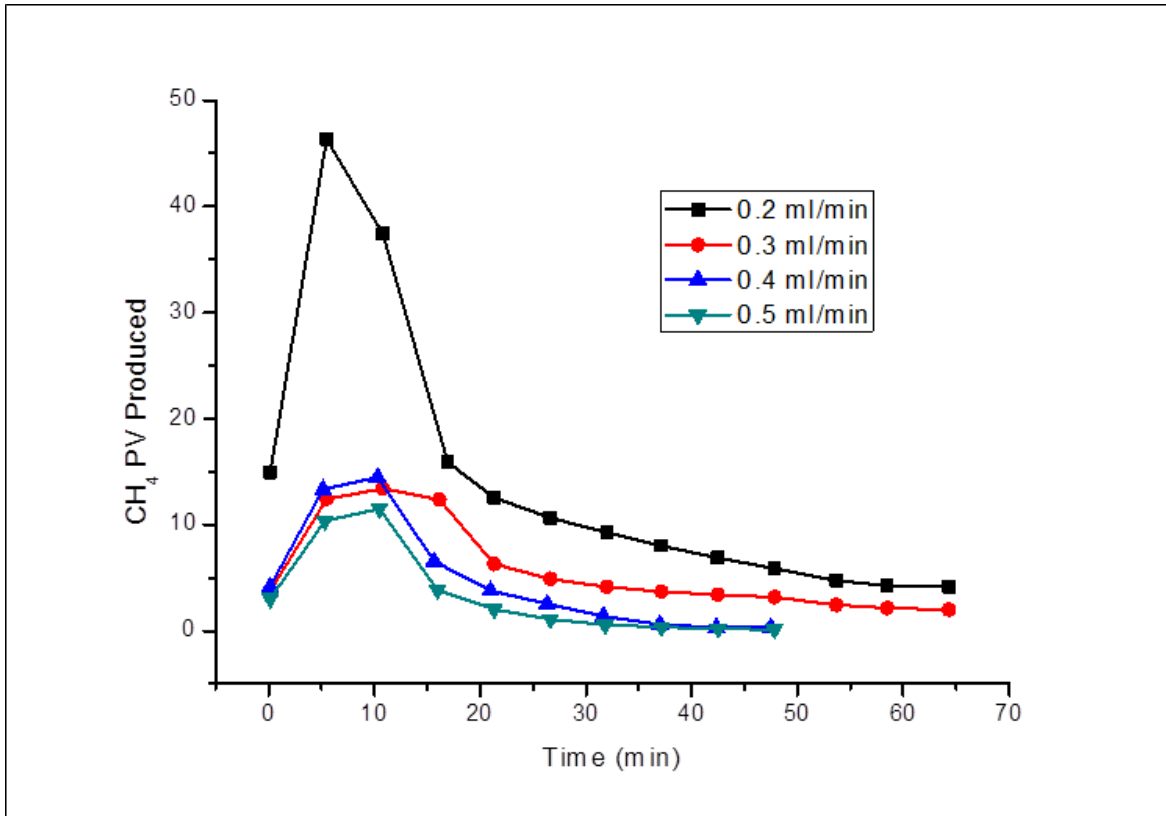
Figure 5.57 Recovery efficiency of the experimental runs on Buff Berea

Total CH4 volume produced was highest during the investigation on Buff Berea when the injection rate was 0.2 ml/min. other rates showed significant poor sweep efficiency, given the higher interstitial velocities at higher injection rates.

5.3.4.3 Bandera Grey

The same steps were taken as those employed in the Grey Berea evaluation in Section 5.3.4.1 to analyse the recovery efficiency of the process in Bandera Grey with a lowest porosity and permeability.

The pseudo-reduced properties of the system were also evaluated as done in the previous sections. These are as follows:

$$P_{pr} = \frac{1314.69}{670.13} = 1.97$$

$$T_{pr} = \frac{323.15}{190.2} = 1.70$$

153

And the gas formation volume factor was also evaluated to obtain the OGIP in Bandera Grey sample and followed the same procedure as those adopted in the cases of the other core samples.

$$B_g = \frac{0.91 \times 323.15}{20 \times 1314.7} = 0.01204 \ cm^3/scm^3$$

Now plugging the B_g into Equation 2.20 to compute the OGIP, the porosity value of the core sample (Bandera Grey) was 17.05% from Table 5.1, and the bulk volume, V_b was found to be 37.54 cm^3 using the core sample dimension in Table 5.1. and at $S_w = 0$

$$OGIP = \frac{37.54 \times 0.1705 \ (1 - 0)}{0.01204} = 531.61 \ cm^3$$

The value of the OGIP was then used to calculate the CH$_4$ percentage recovery. The CH$_4$ production recovery was evaluated and plotted as a function of time which was shown in Figure 5.58.
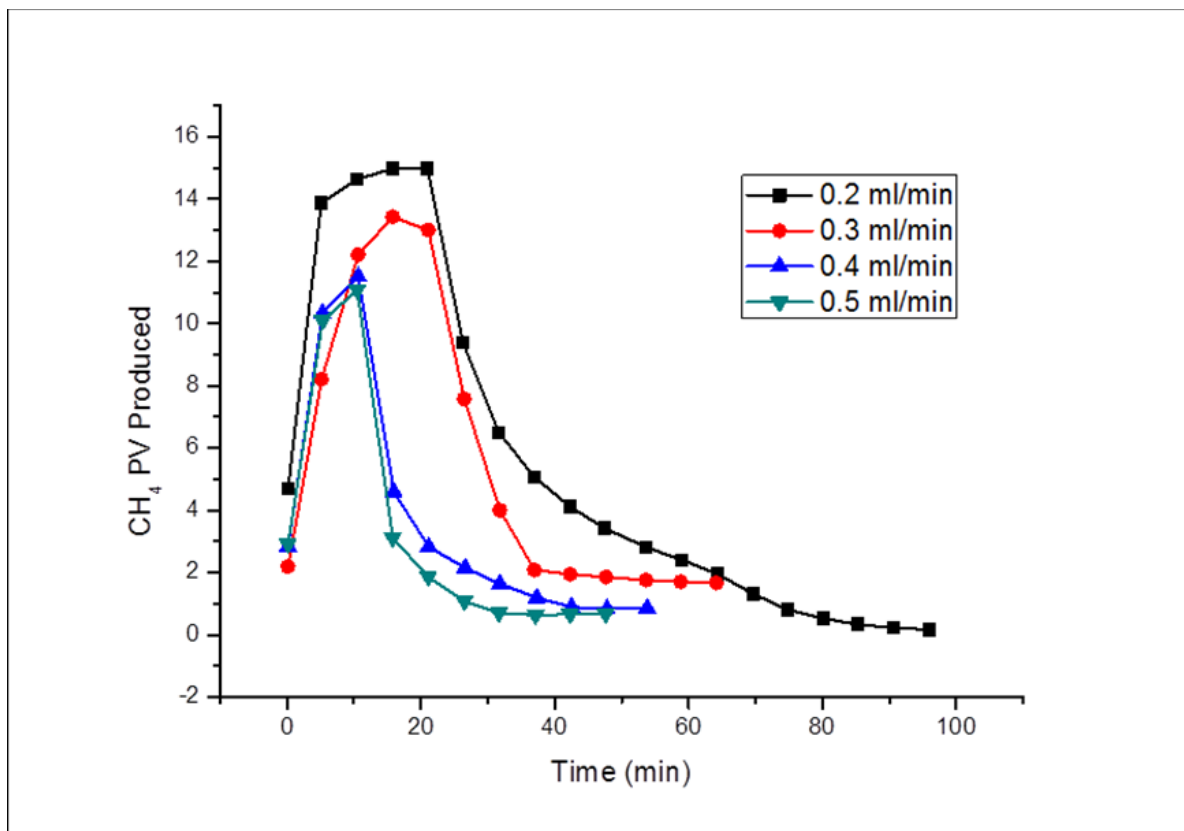
Figure 5.58 Recovery efficiency of the experimental runs on Bandera Grey

The most CH$_4$ volume produced was realised during the 0.2 ml/min run similar to that evaluated in Bandera grey.

The recovery efficiency of each individual run at different flow rates will be measured in terms of the recovery factor i.e.

$$RF = \frac{Vproduced}{OGIP} \times 100 \qquad (5.19)$$

Table 5.26 Calculated OGIP of the core samples at 1300 psig and 50°C

S/N	Core Sample	OGIP (cm^3)
1	Bandera Grey	531.60
2	Grey Berea	629.78
3	Buff Berea	805.15

From the OGIP calculated, the recovery factors were also determined using the total CH$_4$ volume recovered. These values are shown in Table 5.27 and depicted in Figure 5.59.

Table 5.27 Summary of recovery factors of all the experiments at all test flow rates

Bandera Grey		
Injection rates (ml/min)	Total CH$_4$ Recovered (cm^3)	Recovery factor (%)
0.2	476.49	89.6
0.3	331.48	62.3
0.4	266.55	50.1
0.5	172.27	32.4
Grey Berea		
Injection rates (ml/min)	Total CH$_4$ Recovered (cm^3)	Recovery factor (%)
0.2	417.51	66.2
0.3	523.59	83.1
0.4	185.29	29.4
0.5	84.94	13.4

Buff Berea		
Injection rates (ml/min)	Total CH₄ Recovered (cm³)	Recovery factor (%)
0.2	596.94	74.1
0.3	445.60	55.3
0.4	313.27	38.8
0.5	217.09	27.1
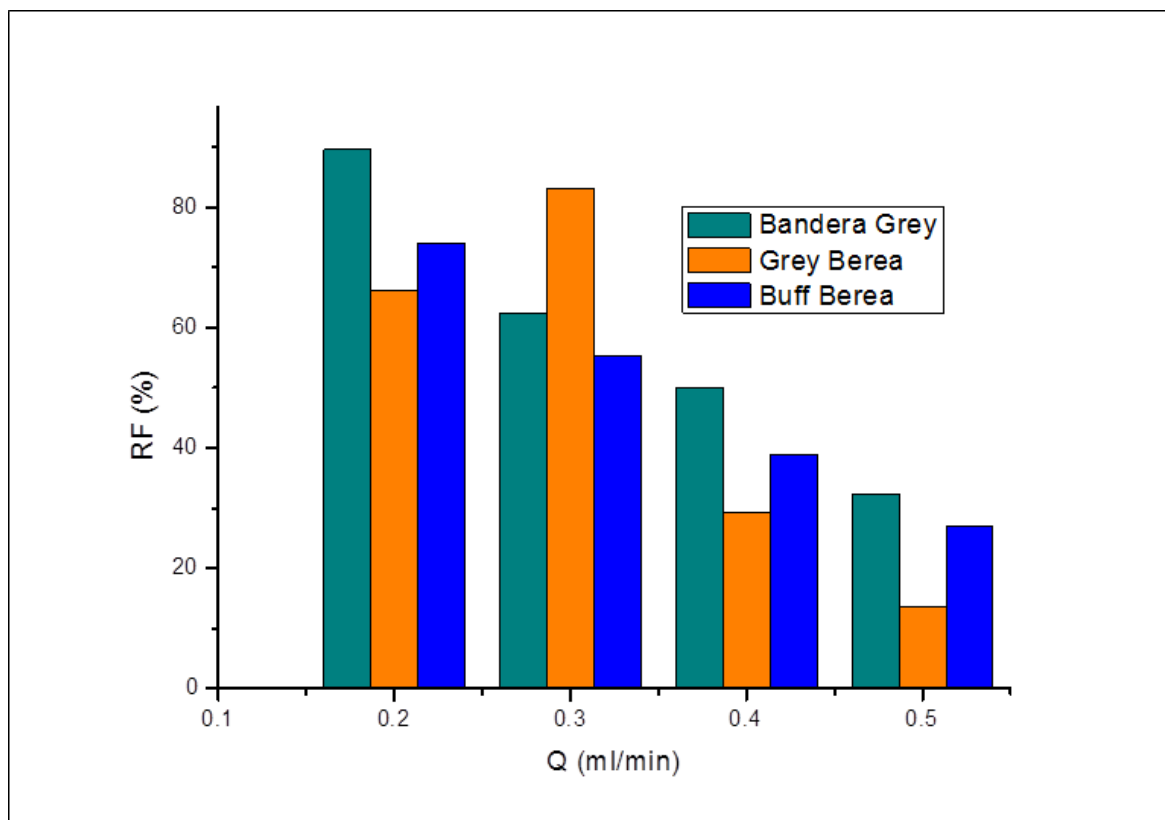
Figure 5.59 Recovery factors of all the core samples at different flowrates

From Table 5.27 and Figure 5.59, the process recovery factor at 0.2 ml/min was realised in the Bandera Grey core sample followed by Buff Berea and the least recovery factor was realised in the case of Grey Berea. However, at 0.3 ml/min Grey Berea had the best RF. And at higher flow rates, as seen in the recovery volumes as functions of time had the worse sweep efficiency and recoveries will be poor. This is, as already mentioned, resulting from the higher interstitial velocities of the CO_2 gas molecules through the pore matrix of the core sample.

Overall, the core sample with the best and consistent dispersion coefficient values was Grey Berea sandstone sample compared to the other core samples as seen in Table 5.27. Bandera grey had the highest dispersion coefficients, and this is as mentioned as a result of the narrower pore channels due to the lower permeability. Buff Berea however had lower dispersion than Grey Berea, but dispersion appeared not to be as consistent. This is alluded to the fact that there was more room for the gases to mix given the larger pore channels of Buff Berea which is characterised by larger pore spaces and also the larger grain diameters as seen in Section 5.2.3. Thus, as seen from the analysis, dispersive mixing increased with increase in flow rates in all the core samples.

Flow behaviour of the CO_2 in all the core samples was investigated and the most consistent behaviour was observed to be at an injection flow rate of 0.3 ml/min as all the permeability seem to have reliable conformance (Figure 5.50). After CO_2 breakthrough, characterised by the high-pressure build-up and a sudden drop, the permeability to the core samples became quite similar in all the core samples at that flow rate and indicative of the optimum flow behaviour of CO_2 at test conditions. Permeability decreased with increase in injection rate signified by the higher dP as the runs proceeded.

Furthermore, in terms of the recovery efficiency, the best recovery factors were seen at lower injection rates – 0.2 and 0.3 ml/min. Higher flowrates had very poor sweep efficiencies in all the core samples. At 0.2 ml/min, higher RF was obtained in Bandera Core sample with the least OGIP compared to Buff and Grey Berea, this is because of the CO_2 segregation at a lower rate and the plume will spread longitudinally transversely which will displace the CH_4 in the smaller pore spaces within the pore matrix which is characterised by the higher dP Figure 5.48 compared to the same runs in Buff and Grey Berea core samples. As a result, most of the CH_4 will be displaced from the core sample as the CO_2 plume rises through the core sample. Invariably, at 0.3 ml/min, Grey Berea had the best RF compared to the other core sample.

From all these three assertions – dispersion coefficient measurements and injection orientation, flow behaviour of supercritical CO_2 in different core orientations, and lastly the recovery efficiency of the displacement process in all the core samples and injection rates, it suffices to say that the best results in terms of all the assertions were obtained in vertical orientation and with Grey Berea core sample. Thus, in the last analysis based on the RF, 0.3 ml/min provided the best efficiency but Bandera Grey at 0.2 ml/min gave the best RF but had

157

the highest dispersion coefficient, meaning more mixing was observed in that the ratio of the injected CO_2 and the recovered CH_4 was substantially higher in the effluents. The resident time at this lower flowrate aided in the substantial recovery of the CH_4 but ironically allowed more mixing of the injected CO_2 and the recovered CH_4 and hence the higher mixing observed. This was the reason why the Grey Berea at 0.3 ml/min in the vertical orientation was deemed the best scenario in the whole experiments. Therefore, Grey Berea at 0.3ml/min and vertical orientation will be used to benchmark the effects of salinity on the dispersion coefficient which will be next and subsequent tests.

5.4   Phase III: Parametric sensitivity analysis

For this phase, the sensitivity of the parameters of interest was investigated by carrying out a core flooding process in which the same core sample was used throughout the experiment. The core sample chosen for this analysis was Grey Berea as it provided the best case in terms of recovery efficiency and flow behavior as well as the optimum injection rate as seen in the previous section. This provided the benchmark as it will afford less interference from other systematic influences compared to the other core samples. The next step is to investigate the effect of connate water salinity on dispersion coefficient and also the recovery efficiency.

5.4.1   Connate water salinity in EGR investigation

The connate water saturation in the Grey Berea core sample was set to 10% to have enough pore volume for evaluation given the scale of the core samples used. This provided more surface area for the initial equilibrium between the CH_4 and the connate water during initial pressurisation. The mimicking of water saturation was done with distilled water, brine (5 wt%), and brine (10 wt%) to fill up 10% of the core samples pore volume under vacuum for effective distribution throughout the pore matrix of the core sample.

The dispersion coefficient of each run at a given salinity was highlighted to evaluate the effect of the parameter on the extent of mixing during EGR.

5.4.1.1   Dispersion coefficient measurements

These experiments were performed on Grey Berea at a constant flow rate of 0.3 ml/min and at test conditions. Table 5.28 summarises the dispersion coefficients of each of the runs under investigation.

158

Table 5.28 Results of the dispersion coefficients at different salinities at 0.3 ml/min

Run	S_{wi} (%)	Salinity (wt%)	Pressure (psig)	Temperature (^{o}C)	K_L (10^{-8} m^2/s)
1	10	10	1300	50	0.44
2	10	5	1300	50	0.59
3	10	0	1300	50	3.61
4	0	0	1300	50	2.82

These results are consistent with the findings of (Abba et. al., 2017). They elucidated that the trends spotted were as a result of reduction in the tortuous flow channels or paths of the consolidated core samples when there was inclusion of connate water in the experimental runs. However, when distilled water was employed as the connate water saturation, the dispersion coefficient was noticeably highest, and this observation was explained by (M. K. Abba et al., 2017; Abba et al., 2018) in that the low density of the connate water compared to the higher salinity brines was responsible for higher dispersion coefficient observed.

The fitted experimental results of the concentration profiles are shown in Figure 5.60. Early breakthrough of CO_2 was evident in the runs with saturations of 10% by volumes, given that the pore volume of the core sample was reduced by 10% due to the inclusion of the saturation of the connate water.
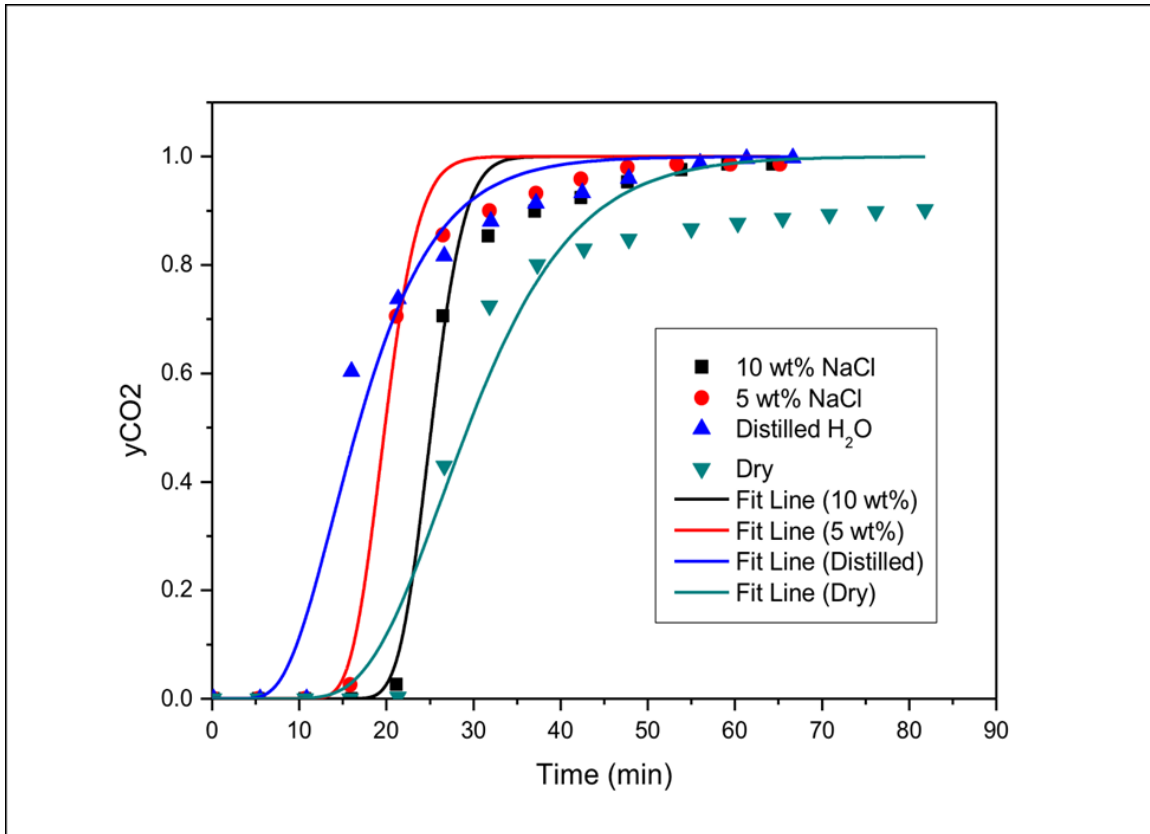
Figure 5.60 Concentration profiles of different salinities and air at test conditions

The densities of the different connate water salinities were simulated and shown in Figure 5.61 to 5.63. This was carried out to observe the interplay between the dispersion coefficients and the connate water salinities. This relationship between the connate water salinity and the dispersion coefficient is first established in this study to the knowledge of this research.
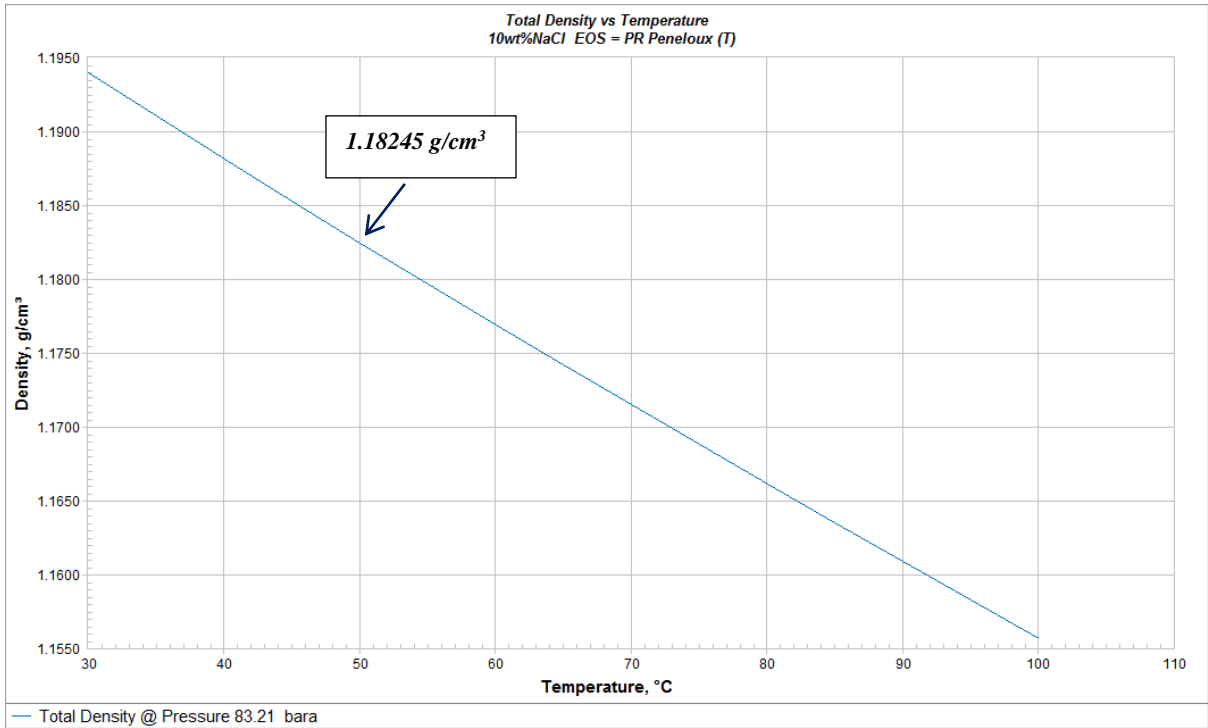
Figure 5.61 10wt% NaCl brine density as a function of temperature
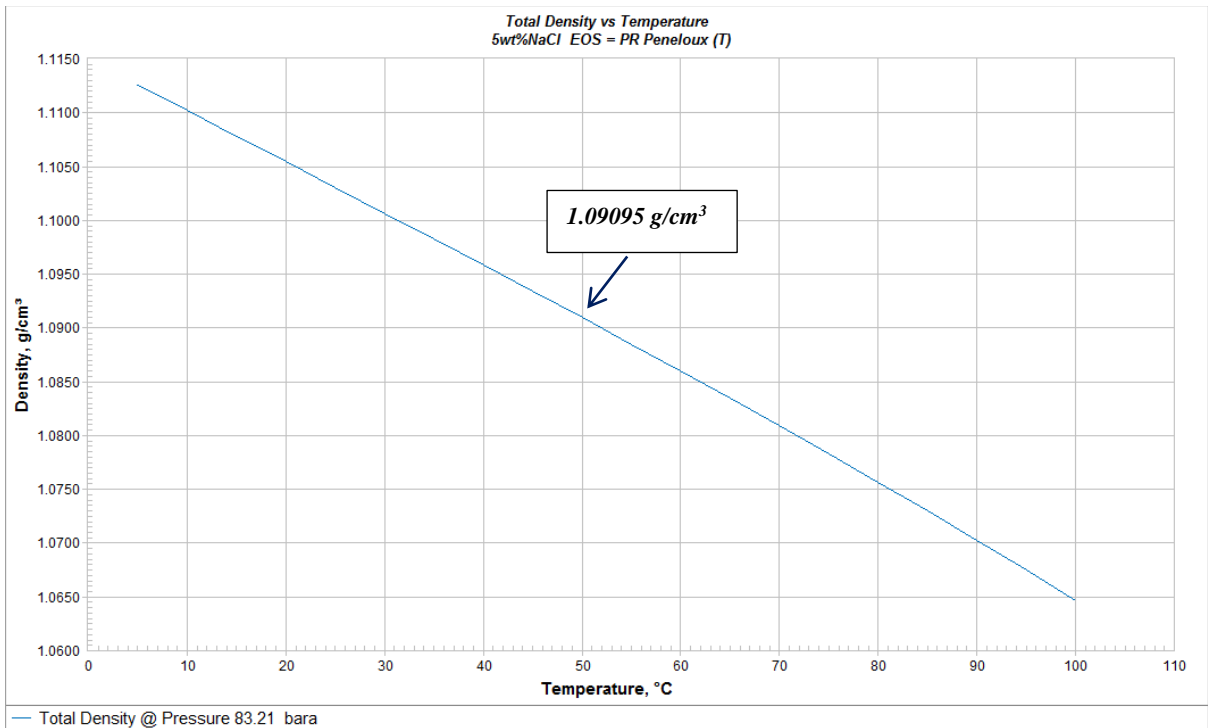
Figure 5.62 5wt% NaCl brine density as a function of temperature

161
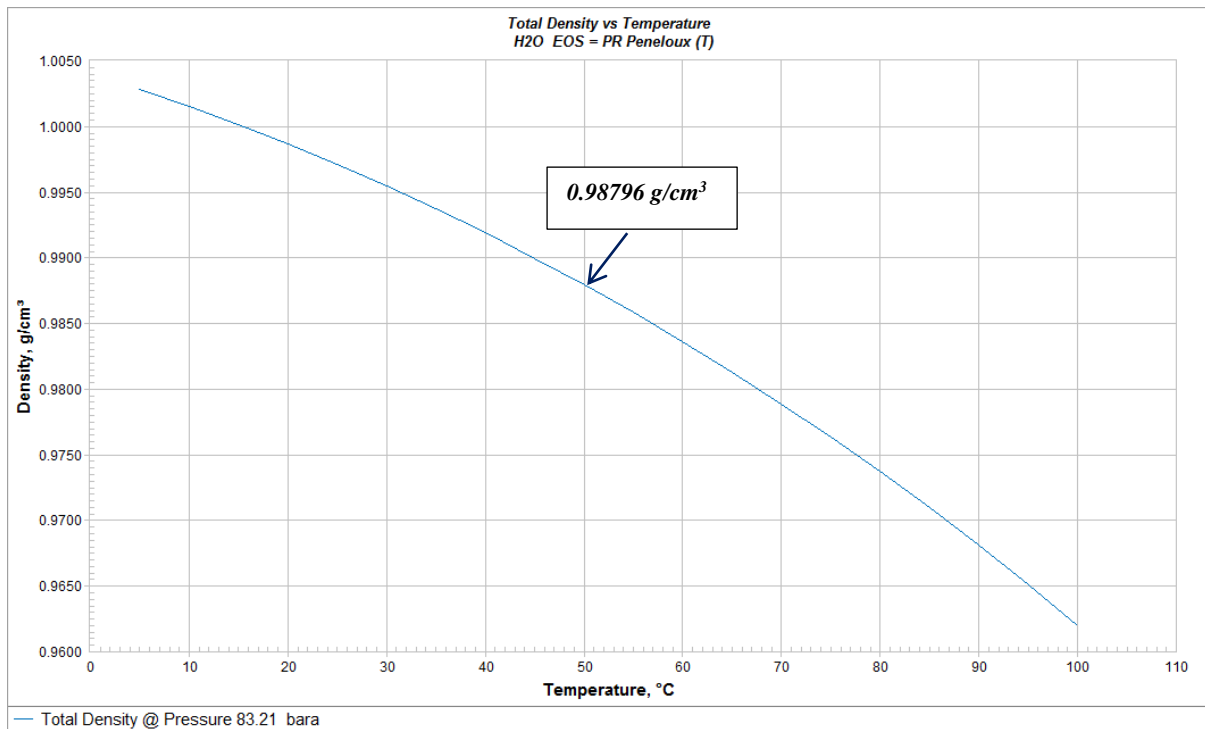
Figure 5.63: Distilled density as a function of temperature

From the simulation results, Figures 5.61 to 5.63, the densities were extracted at the desired conditions and tabulated below in Table 5.29.

Table 5.29 Brine concentration with corresponding densities

Salinity (wt%)	Temperature (ºC)	Pressure (psig)	Density (g/cm3)
10	50	1300	1.18245
5	50	1300	1.09095
0	50	1300	0.98796

The dispersion coefficients of the runs with their corresponding parameters are tabulated as follows in Table 5.30.

Table 5.30 Fluid densities and their corresponding dispersion coefficients.

Run	Salinity (wt%)	Density (g/cm3)	K_L (10^{-8} m^2/s)
1	10	1.18245	0.44
2	5	1.09095	0.59
3	0	0.98796	3.61

The properties shown in Table 5.30 clearly indicate the observed relationship between

connate water densities and their various longitudinal dispersion coefficients. This indicates that as the density of the connate water within the pore spaces of the core sample increases, the dispersion coefficient seemingly decreases. This relation can graphically be represented in the Figure 5.64 below:
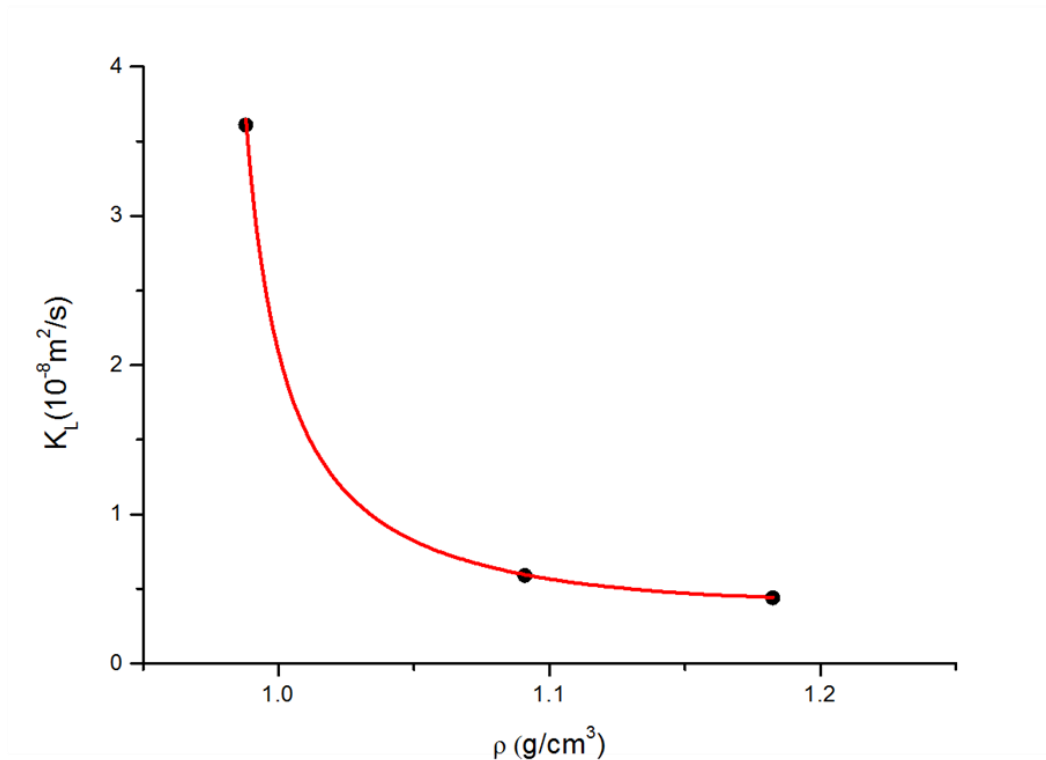
Figure 5.64 Dispersion as a function of connate water density

Albeit the large dispersion of the data in the graphical representation, the standard error of the line of best fit was well within 5% of the average of the experimental data obtained. The relationship represented in Figure 5.64 however, is mainly for representation purposes and not intended to describe a model which relates these two parameters as there is no data, to the knowledge of this study, found in literature which categorically tried to validate or back up this finding. Nonetheless, this is a new data which further infer the description of the CO_2 dispersion in CH_4 in consolidated sandstone porous media at conditions in which EGR is relevant.

Furthermore, when there is an inclusion of connate water in the pore matrix of the porous medium, the apparent narrowing of the tortuous flow paths of the porous media will lead to a

decrease in the tortuosity of the porous medium due to the reduction in porosity. These parameters are related as follows (Yi Zhang et al., 2014);

$$\tau = Aln\left(\frac{1}{\phi}\right) + 1 \qquad (5.20)$$

The A is an empirical constant, ϕ porosity of the porous medium.

The time it took for the injected CO_2 to traverse the length of core sample longitudinally will grossly be reduced given that the tortuosity is reduced as a result of the inclusion of connate water which occupied some of the pore channels in the porous medium. This realisation can be attributed to what was observed in the experimental runs where higher density connate water (10wt%) was used to mimic the connate water saturation. Per Darcy law, permeability is a directly proportional to the differential pressure across a core sample. Therefore, the injected CO_2 permeability increased with increase in the salinity of the connate water as shown in Figure 5.65.
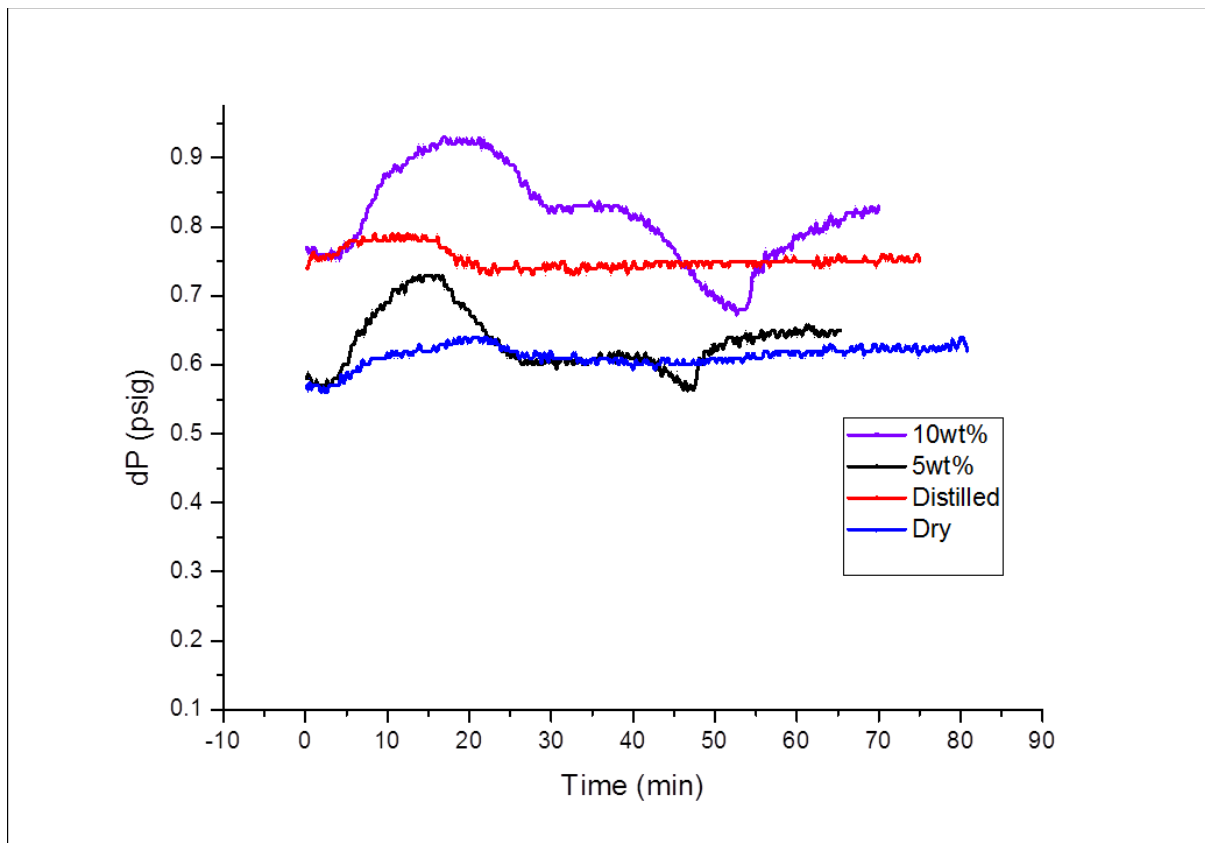
Figure 5.65 Differential pressure of the experimental runs as a function of time

164

Conversely, the experimental run where distilled water was used, which has 0wt% salinity, showed a higher differential pressure across the core sample, invariably indicating higher permeability, compared to that of the 5wt% salinity run. This can be explained by the works of (M. K. Abba et al., 2017; Abba et al., 2018) who inferred that due to the low density of the distilled water, it did not entirely seal off the narrower flow channels of the core sample but instead, made it narrower and that increased the interstitial velocity through the core sample and this phenomenon also explains the high dispersion coefficient observed with the distilled water experimental run.

5.4.2 Solubility trapping mechanism for EGR investigation

In this thesis, a core flooding experiment was carried which involved the injection of CO_2 through a core sample saturated with CH_4 and connate water at different salinities. The core sample used was *Grey Berea* sandstone. The salinities of the connate water used were 0, 5, 10wt% NaCl.

A series of experiments were carried out to achieve the aims set out in this study. The core sample was first characterised to evaluate the petrophysical properties of the core sample for a more dependable measure of the parameters under investigation. Brines of different test salinities were prepared which were used for the investigation. After these preliminary preparatory tasks were done, a core flooding process was conducted on the core sample to evaluate the displacement efficiency of the process in the presence of the test connate water prepared. The effluent compositions were analysed using the gas chromatography at different time intervals using the configured sampling valve. Details of the procedure and set up are presented in our earlier work (Abba et al., 2017). The effluent rates were measured and recorded by the downstream flow meters. These provided the volumes produced by displacement of CH_4 by the injected CO_2 and paved a way to quantify the trapped or stored CO_2 in the core sample after substantial recovery of the desired C_{H4}. The solubility and interfacial interaction between the different gases in different brine salinities for all the experiments was studied using the rising bubble method of interfacial tension measurement. Details of the experimental set up and procedure is shown in section 2.2.4.

Prior to every experiment, the core sample was cleaned using Soxhlet extraction were a reflux of methanol cycles was used to remove any traces of inorganic compounds (in this case NaCl salts) to restore the original state of the core sample for consistency. Drying in the

oven at 100°C overnight follows. This ensured the removal of any moisture and reagents used in the cleaning process.

5.4.2.1 Core flooding experiment

The recovery efficiency of the experiment is investigated using a laboratory simulated displacement experiment to determine the concentration profiles of the interacting gas species. This entails injection of the CO_2 into the core sample saturated with CH_4 and connate water. A number of test runs were carried out to assess the repeatability of the experimental methodology and set up.

5.4.2.2 Methane Recovery

First, the CH_4 produced was evaluated based on the total volume of effluents produced after the core flooding experiment was stopped. These volumes were fractions of the OGIP in the core sample. The results obtained are presented in Table 5.31 below.

Table 5.31 CH_4 production in pore volumes for all the runs

Time (min)	PV Produced 10 wt% CH_4	Time (min)	PV Produced 5 wt% CH_4	Time (min)	PV Produced Distilled $H2O$ CH_4	Time (min)	PV Produced Dry CH_4
0.17	2.03	0.17	5.13	0.15	7.07	0.16	7.02
5.32	8.31	5.33	21.13	5.49	23.62	5.33	27.82
10.66	9.16	10.67	24.00	10.83	26.27	10.67	29.64
15.99	9.57	15.82	17.12	15.99	10.82	15.83	9.94
21.16	9.90	21.16	7.78	21.32	7.27	21.16	6.86
26.49	3.15	26.49	3.86	26.66	5.10	26.49	5.63
31.66	1.63	31.83	2.70	31.98	3.35	31.82	4.97
37.01	1.16	37.16	1.86	37.16	2.46	37.16	4.53
42.32	0.89	42.33	1.15	42.48	1.91	42.32	4.17
47.66	0.57	47.67	0.58	47.82	1.17	47.82	3.75
53.82	0.31	53.33	0.41	55.98	0.35	54.66	3.31
59.16	0.18	59.49	0.41	61.33	0.11	60	2.99
64.32	0.19	65.16	0.42	66.66	0.08	65.16	2.85

These results are presented better in a graphical form in Figure 5.66 which shows the trends observed. As can be seen, the poorest CH_4 recovery in all the runs was realised in the run where 10 wt% of connate water was used. This can be attributed to the poor sweep efficiency of the injected because of the restrictive flow when CO_2 transverses the core sample. This restriction is as a result of the higher salinity connate water sealing off the narrower pore

166

spaces within the pore matrix due to its density compared to the other runs with lower connate water concentration. Because of the forced-homogeneity actualised by the presence of the connate water in the pore matrix, less time was taken by the CO_2 as it was injected through the core sample and also early CO_2 breakthrough as seen in the concentration profile in Figure 5.67.
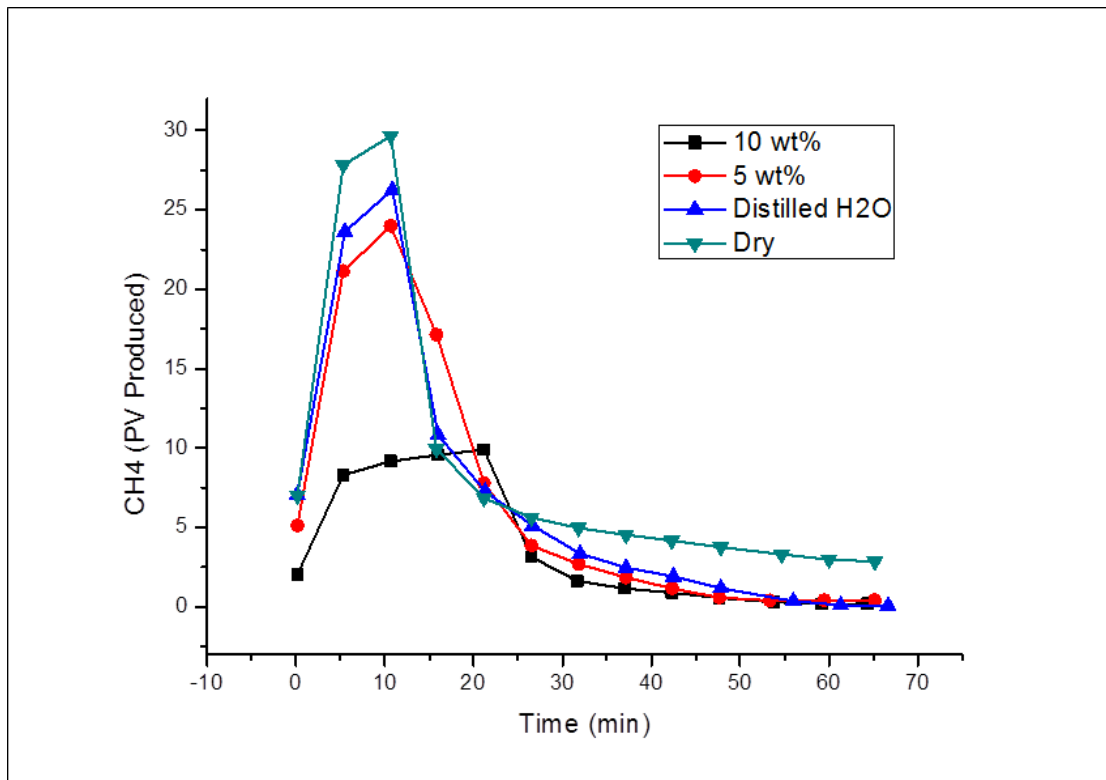
Figure 5.66 Graphical representation of CH_4 volumes produced from all the experiments
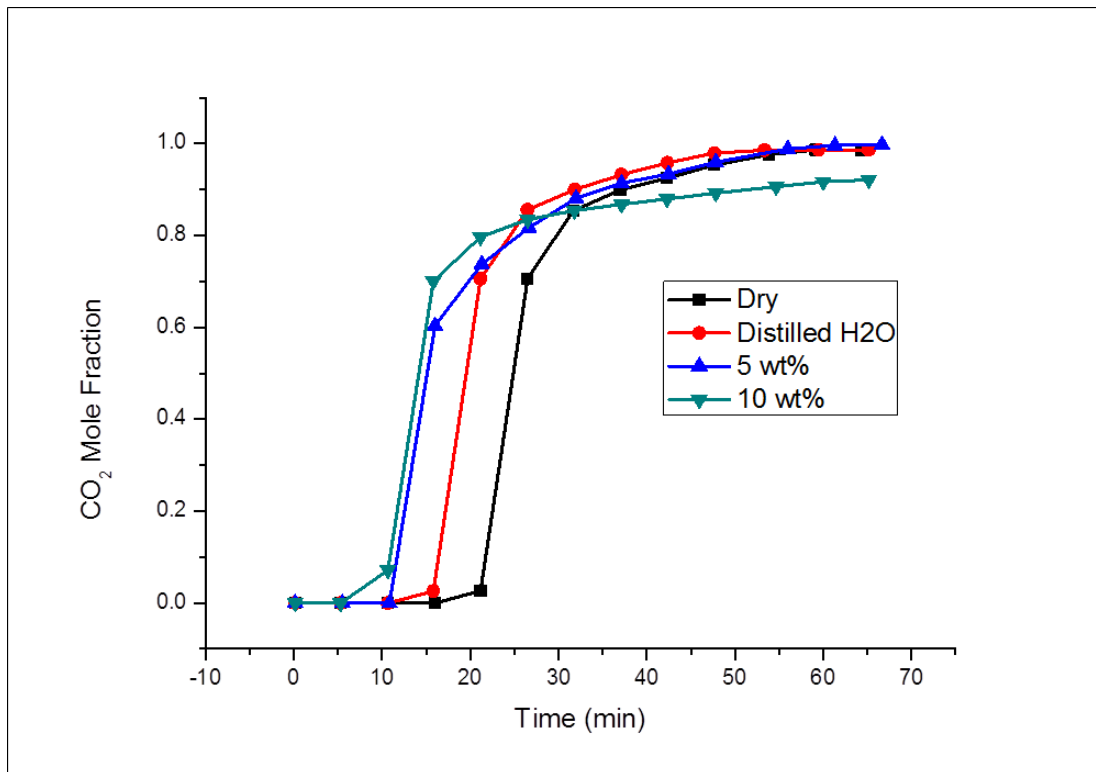
Figure 5.67 Concentration profiles of CO_2 produced

Furthermore, the CH_4 recovery was highest when there was no connate water saturation. This is obvious because there was no reduction in the original pore volume for the gas to occupy and hence more volume for nascent CH_4. Higher volume of CH_4 was realised in the core sample and thus higher recovery was observed. This will serve as the benchmark to which other tests are pitted against. So, analyses were accentuated in the runs with 10% of their pore volumes saturated with connate water of different salinities (0, 5, 10 wt%). The concentration profile also presented, notably, the variation of the breakthrough times with the salinities. This variation was explained in our previous works where significant pressure drop was seen when CO_2 was displacing CH_4 at a 10wt% connate condition (Figure 5.65). The same restrictive flow comes into play when explaining the variation in breakthrough times. The higher the salinity of the connate water the more pore throat sealing effect was noticed. Distilled water saturated run did not fully plug the pore throats instead it made it narrower and the flow channels became more tortuous. Similarly, 5wt% connate water run had lower pressure drop compared to the 10wt% connate water runs. This means that the pore channels were not significantly reduced thereby allowing more unrestricted flow through the pore matrix.

168

5.4.2.3 Carbon dioxide injection and recovery

Using a simple form of gas material balance and mass conservation, the volume of CO_2 injected, and CO_2 produced can be evaluated to assess the production efficiency of each injection strategy.

$$\sum V_{CO2\ in} = \sum (V_{CO2\ Accumulated} + V_{CO2\ Produced}) \tag{5.21}$$

Here, CO_2 was injected at a constant flowrate rate and the effluents produced were recorded and analysed. Produced CO_2 results obtained and analysed are shown in Table 5.32.

Table 5.32 CO_2 produced during EGR for all the experimental runs

Tests	Swi %	PV injected	Pv Produced	Pv Accumulated	% CO$_2$ Stored
10wt%	10	36.10	13.31	22.79	63.05
5wt%	10	36.10	29.44	6.66	18.45
Distilled	10	36.10	27.72	8.38	23.21
Dry	0	36.10	33.65	2.45	6.69

From Table 5.32, it suffices to say that the experimental run with 10wt% connate water yielded the most significant results in terms of CO_2 storage with 63.05% of the total pore volumes injected stored in the core sample. This is further established and reaffirmed in Figure 5.68 where the same run yielded the least CO_2 recovered compared to the other runs. Also, the restrictive flow during the run as a result of the sealing effect by the connate water aided the storage of the injected CO_2 which was characterised by the large pressure drop observed during the injection. Next, experimental run with the core sample saturated with distilled water provided stored 23.21% of the total pore volumes injected. This was followed closely by the run with 5wt% connate water and the least efficient storage scenario was the core sample with no connate water with the storage of 6.69% of the total pore volume injected. Given the similar flow behaviour of the injected CO_2 in terms of pressure drops between the distilled water and 5wt% runs, it was expected that the storage efficiency will be very close.
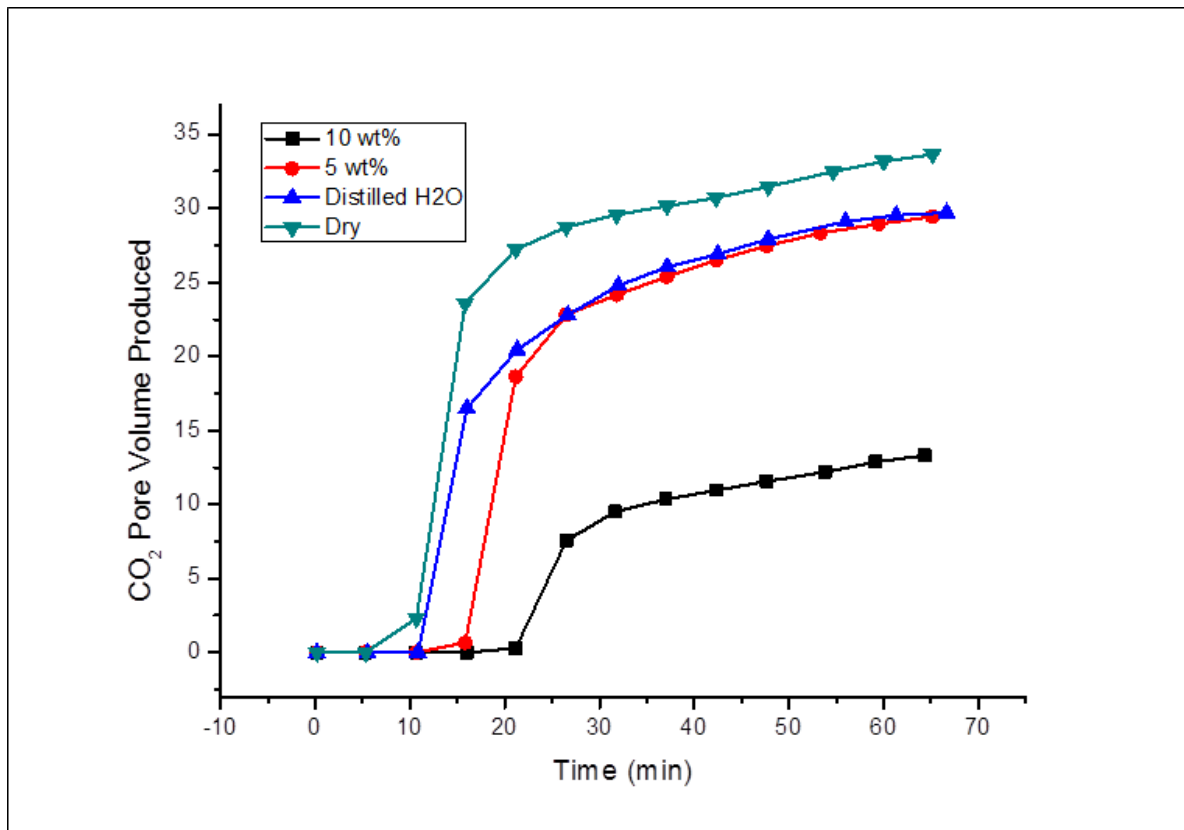
Figure 5.68 CO_2 volumes recovered in pore volumes as functions of time

However, distilled water run exhibited better storage efficiency and capacity. The reasoning behind this observed trend lies in the molecular interaction between the fluids in the core sample, more specifically, the dissolution of the injected CO_2 in the connate water. The primary trapping mechanism here is the structural and capillary trapping but the secondary mechanism – solubility trapping plays a role here as evident in the difference between the distilled and 5w% connate water experiments. It is a well-known fact that the CO_2 is highly soluble in water. The molecular interaction between the CO_2 and the connate water at different salinities is investigated next using IFT measurement to further drive and explain the narrative already established.

5.4.2.4 Interfacial tension measurement (IFT)

Several works have been carried out to measure the interfacial tension in CO_2-brine, CH_4-brine, CO_2-brine-CH_4 systems at different conditions (Amin et al., 2010; Arabloo et al., 2016; Bagalkot et. al., 2018; Barati-Harooni et al., 2016; Chow et. al., 2016; Dehghan et. al., 2015; Dittmar et. al., 2003; Duchateau & Broseta, 2012; Kamari et. al., 2017; Kashefi et al., 2016;

170

Khaksar et. al., 2016; Mohammad et. al., 2017; Mutailipu et al., 2018a; Zhang et. al., 2018b; Pereira et al., 2017; Rashid et al., 2017; Guo et. al., 2000; Stukan et. al., 2012; Yadali et. al., 2011; Yahaya et. al., 2018; Yasuda et. al., 2015) and the relationship between the interfacial tension and solubility highlighted. These investigations have shown that the forces that exist at the interfaces between two phases or fluids interacting are a function of the densities, the temperature and pressures of the fluids system. And there exist mass transfer between the phases in contact which can be well attributed to the solubility of one species of the fluids in another.

The experimental fluid-fluid IFT measurement was carried out using the rising bubble technique. This technique capitalises on the buoyancy of the gas bubble with respect to the brine used, in that its ability to rise through the denser fluid is exploited. The IFT measurement is evaluated based on the profile of the gas bubble in the brine created in the IFT cell which is deduced using the Young-Laplace equations:

$$\gamma = \frac{\Delta \rho g d_e^2}{H} \tag{5.22}$$

Where

$$\frac{1}{H} = f\left(\frac{d_s}{d_e}\right) \tag{5.23}$$

$\Delta \rho$ is the density difference between the two fluids, γ is the interfacial tension, g is the acceleration due to gravity, de is equatorial diameter of the drop, ds is the diameter of the bubble at de from the apex, H is the bond number which is a function of the ratio of ds/de. The densities of the phases were evaluated using PVTsim V20 at the test conditions of 1400 psig and 50°C. The IFT was first measured when the external phase (connate water) was not saturated with the drop phase (CO_2) to observe the development and collapse of the bubble generated. The results for all the test fluids are shown in Table 5.33 where measurements were taken continuously as the bubble shrunk and collapsed.

Table 5.33 IFT measurement of CO_2 at different brine salinities (1400 psig 50°C)

Time (s)	Distilled Water (mN/m)	5 wt% (mN/m)	10 wt% (mN/m)
0.0	55.23	62.30	65.51
1.0	54.89	61.10	64.53
1.9	52.12	59.89	63.63
2.9	48.11	57.19	63.51
4.0	44.22	55.22	63.48
5.0	38.16	53.45	63.41
6.0	33.67	52.32	63.40
6.9	28.32	51.75	63.38
8.0	24.33	50.11	63.07
9.0	22.12	48.29	62.36
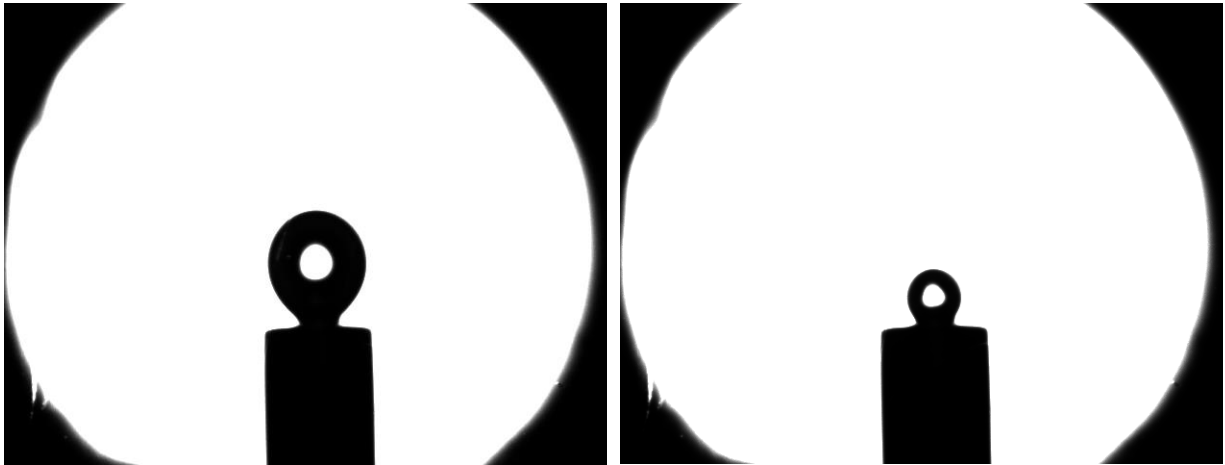
Figure 5.69 Bubble shrinkage of CO2 bubble in Distilled water L: Onset R: End
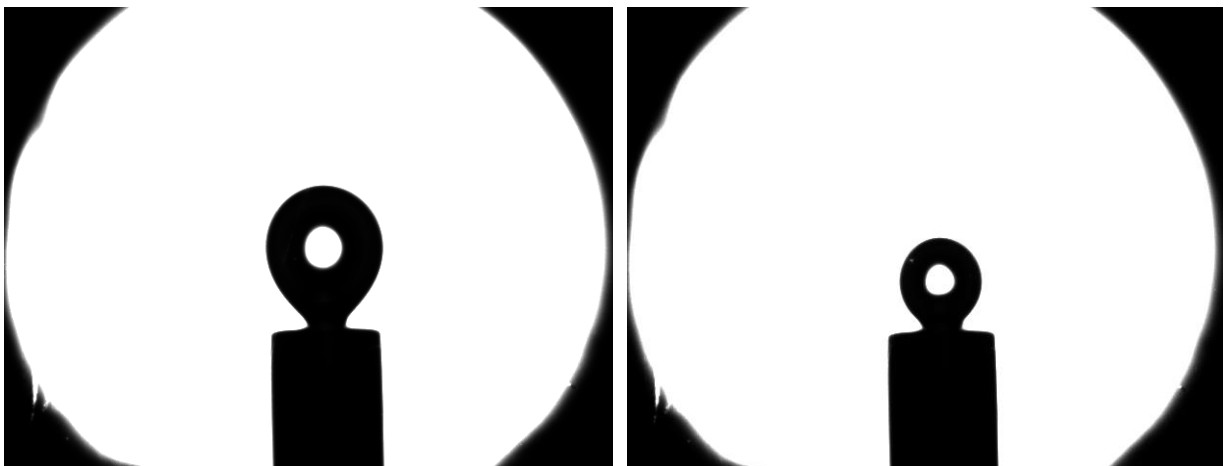
Figure 5.70 Bubble shrinkage of CO2 in 5wt% brine L: Onset R: End
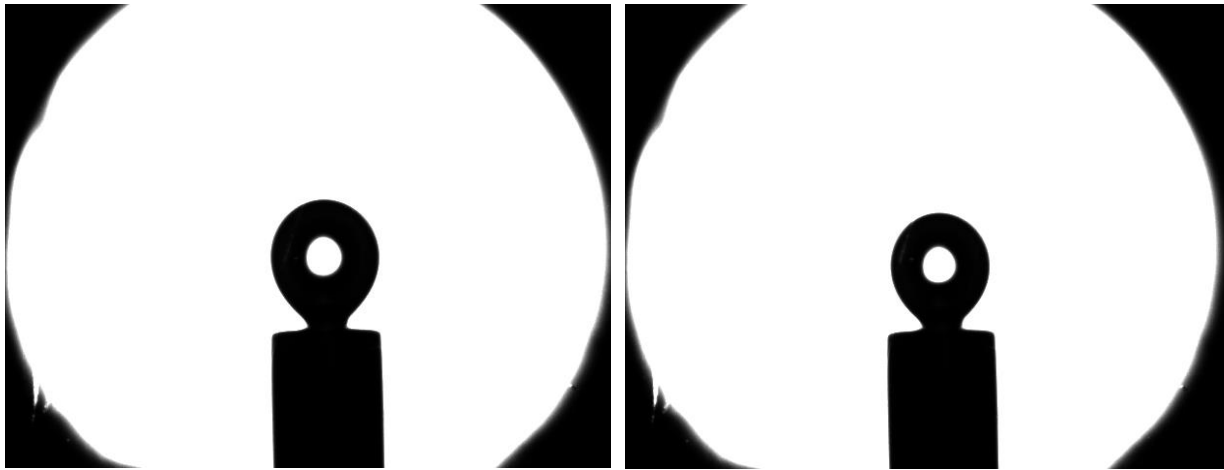
Figure 5.71 Bubble shrinkage of CO2 in 10wt% brine L: Onset R: End

The shrinking of the bubble signified the rate of mass transfer over the interface between the gas bubbles generated and brine phase in the cell. As seen in Figure 5.69, Figure 5.70, and Figure 5.71, the rate of shrinkage of the gas bubble is more pronounced in the distilled water experiment and the rate decreased as the salinity of the connate water sample increased. The IFT decreased rapidly in the distilled water which explained the shrinkage observed. However, IFT rate decreased at a slower rate when the salinity increased to 5 w% and even slowest at 10wt% connate water. This is represented graphically in Figure 5.72.
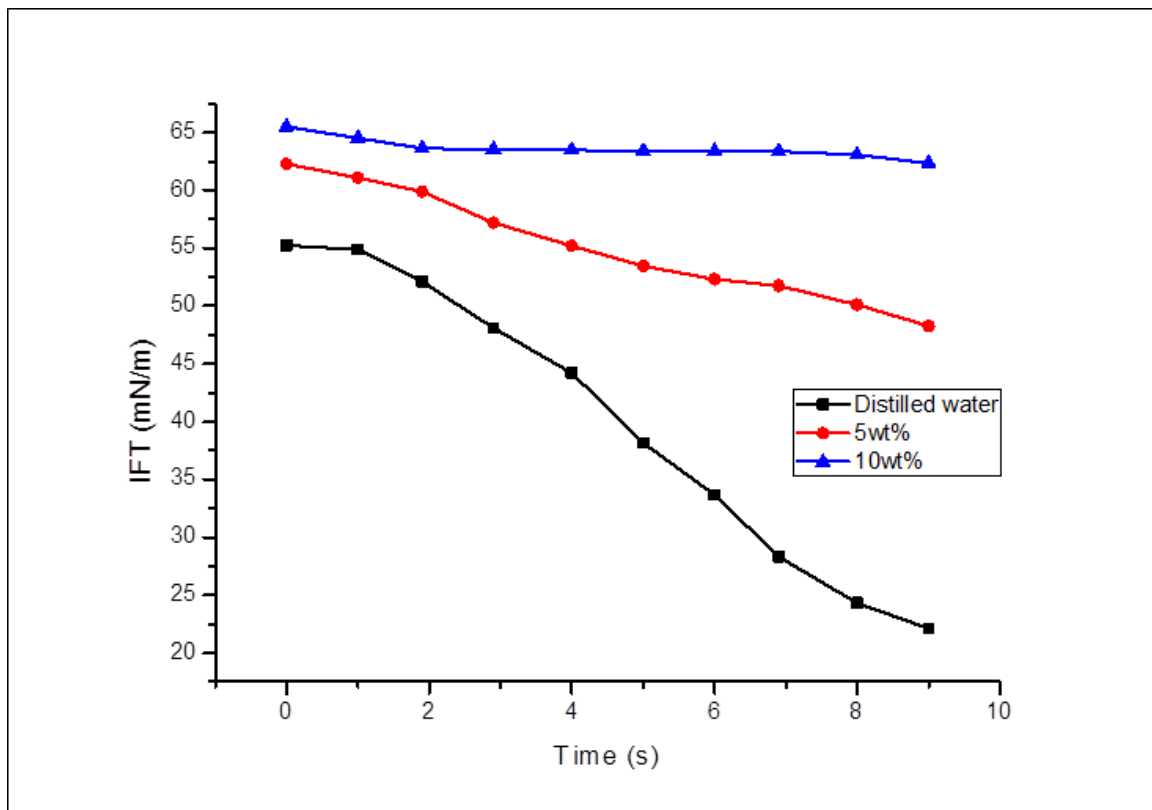
Figure 5.72 CO_2 IFT decrease as a function of time at under-saturated aqueous conditions

After the results of the rate of shrinkage and IFT variation with time in the unsaturated brine were obtained, the next step was to evaluate CO_2 IFT when the brine was saturated with the injected CH_4. The external phase of the experiment (brine) was saturated with the CH_4 by injecting the gas through the injection needle which pressurised the system to the test pressures. IFT measurements were taken at time intervals at the test conditions. Full equilibrium was achieved after about 3 minutes where the bubble sizes became constant and hence the IFTs. The CH_4 IFT results shown in Figure 5.73 are similar to those obtained by Yahaya et al. (2018) at the equilibrium conditions relevant to this work.

From the results, it follows the same trend as that observed when the measuring the CO_2 IFT in brine, in that the rate of IFT decrease is consequential to the brine salinity, with the lowest IFT measured between the CH_4 and the brine. This reaffirms that the higher the salinity of the brine the lower the gas solubility. The graphical representation of the IFT variation with time is shown in Figure 5.73.
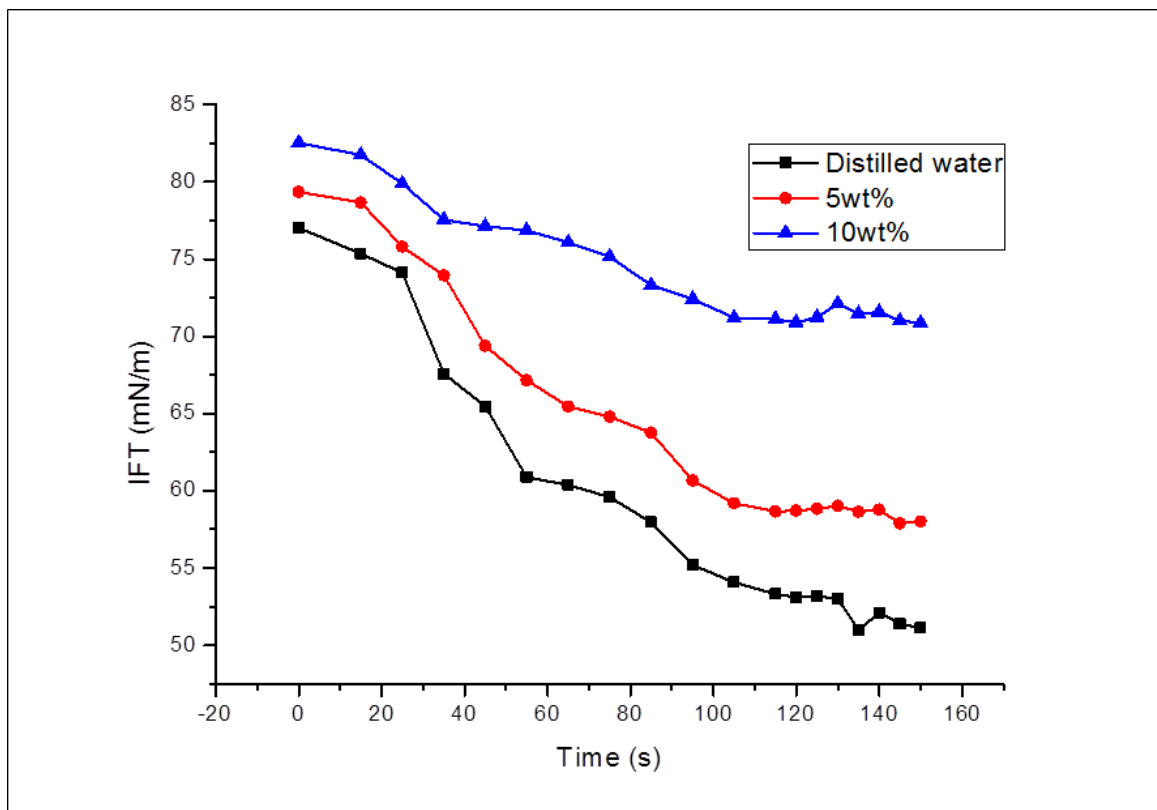
Figure 5.73 CH_4 IFT as function of time at equilibrium

174

Once the equilibrium between CH_4 and the brine was attained, CO_2 was now injected at the same pressure into the CH_4 saturated brine to evaluate its IFT. This was to simulate the rate of CO_2 dissolution in the reservoir during the displacement. It is noted that the connate water in the reservoir was saturated with the CH_4 prior to injection, so this step in IFT determination of the CO_2 in a CH_4 saturated brine gives a representation of the trends observed in Figure 5.74. The results from this step of the experiments are shown in Figure 5.74.
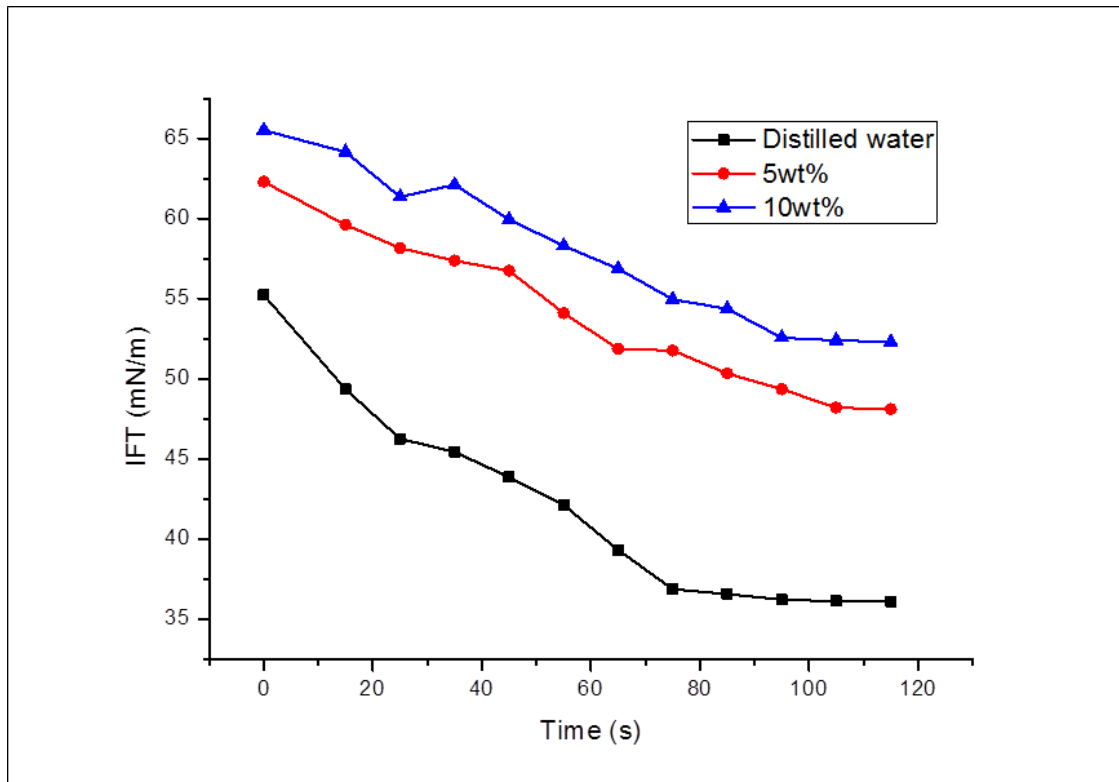
Figure 5.74 CO_2 IFT as a function of time at saturated conditions

It is clear that the gases had the highest interfacial tension in the brine with the highest salinity and lowest interfacial tension value in distilled water. This explains why more CO_2 seemed to accumulate during the run with distilled water (Table 5.32) compared to the run with 5wt%. That means in addition to structural trapping, solubility trapping is realisable during EGR.

CHAPTER 6

6 EGR FLOW PHYSICS MODELLING USING COMSOL MULTIPHYSICS®

6.1 Overview

Computer simulations have become the bedrock and prerequisites for science and engineering designs, their implementation and also optimisation (COMSOL, 2014). To develop new products and services, researchers use simulation study for feasibility and projection of all possible aspects of the spectrum in terms of economics and efficiency. There exists a wide array of simulations software with basic and advanced programming languages for modelling specific cases, the choice of which depends on the innate application.

It has been presented (Patel et al., 2016) that Finite Element Method (FEM) and Finite Volume Method (FVM) are possibly more accurate simulation methods used to discretise and solve the governing equations than Finite Difference Methods (FDM). With reasons stemming from conservation of mass and energy by design in FVM to less numerical dispersion due to annulling several assumptions in FEM. Albeit higher computational time, FEM and FVM compromise time management with accuracy. Thus, for this research application, COMSOL Multiphysics software will be adopted. COMSOL Multiphysics® software is a commercial simulation software package which is based on finite element method (FEM) of numerical analysis (Dickinson, Ekström, & Fontes, 2014). This will be employed as a tool to validate the experimental measurements by simulating the same flow physics adopted in the experiments. The results obtained will then be compared with those from the experiments. Comparison will be made on two parameters to evaluate the effect of the injection rate based on mass transfer and the gravity effects through the injection orientation of the study.

6.2 Model Assumptions

CO_2 with a density ρ and viscosity μ was injected at a constant interstitial velocity u, to displace CH_4 with density and viscosity in a 2D homogenous porous core sample which has a porosity ϕ and permeability k both of with are assumed constant. The dispersion is also assumed to be isotropic throughout the displacement and the fluids are, of course, miscible given that both are gases. Flow is compressible. Temperature is also assumed to be constant.

6.3 Model definition

The domain of the model in this work is described in Figure 6.1.
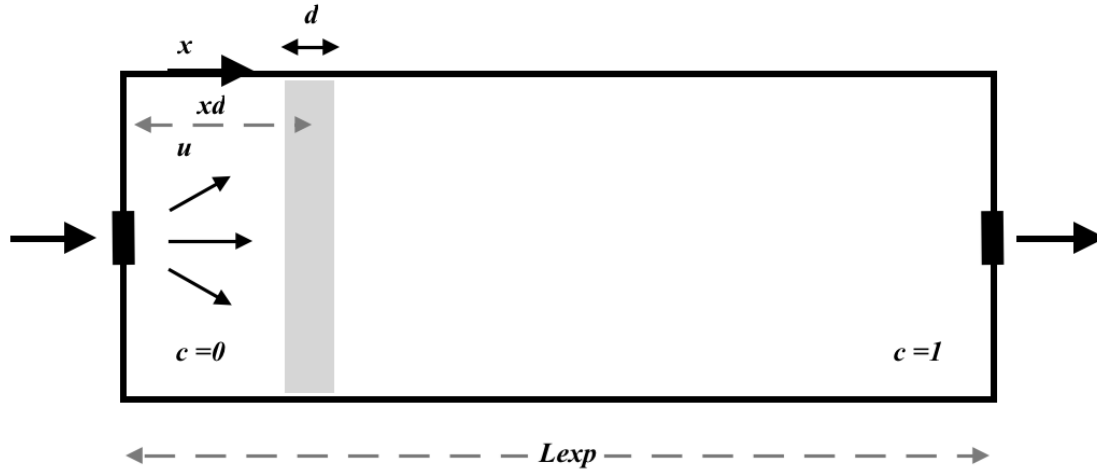
Figure 6.1 2D representation of the core sample

The concentration of CO_2 at the inlet of the core sample is denoted by c and is $c_{CO2} = 0$ mol/m^3, with density and viscosity also denoted by ρ μ respectively. The length of the core sample is *Lexp*. Given the miscible nature of the fluids, there exists a transition zone or rather a displacement front d as shown. The parameter x represents the displacement position for which $c = c_{CH4}/4$ mol/m^3.

In this study, the concentration and pressure gradient are the driving forces that initiate the flow of the gases. The overall governing equation that manages the gas flow are the convection-advection equations which governs the transport of solutes concentrations, the continuity equation that governs the conservation of mass, and finally the equation of fluid motion which is responsible for conservation of momentum. These aforementioned definitions of physical phenomena require a system of physics to solve any problem related to them; the hydrodynamic physics which describes the flow in porous media and the transport of solute within the porous media as a result of the injection.

For the porous media, Brinkman equation which is an extension of Darcy equation (Kumar et. al., 2016) fits the porous media modelling in this case as compressibility of the gases must be taken into account. This provides a better definition of the gas flow in porous media (Liu et. al., 2007). Brinkman equation is presented as

$$\nabla \cdot u = 0 \tag{6.1}$$

$$\Delta P = \frac{\mu(c)}{k}u + \frac{\mu(c)}{\varepsilon}\nabla^2 u \tag{6.2}$$

Where u is the superficial velocity, μ is the dynamic viscosity of the fluid, P is the hydrodynamic pressure, and ε is the porosity of the porous media. The boundary conditions for this application in the model are presented as:

$$u = Ux \; at \; x = 0 \tag{6.3}$$

$$P = 0 \; at \; x = Lexp \tag{6.4}$$

To describe the fluid motion in the porous medium, a slip boundary condition along with the boundary conditions aforementioned is required.

The dynamic viscosity of the fluids in the system is controlled by the transport of the solute which is described by the convection-diffusion equation. This is shown in Eq. 6.5;

$$\varepsilon \frac{\partial c}{\partial t} + u \cdot \nabla c = \varepsilon D \nabla^2 c \tag{6.5}$$

D is the diffusion coefficient; and the boundary conditions which satisfy the equation are as follows:

$$c = 0 \; at \; x = 0 \tag{6.6}$$

$$\frac{\partial c}{\partial t} = 0 \; at \; x = Lexp \tag{6.7}$$

Given that there exists a displacement front in the model denoted as *d*, the initial condition for the concentration of the injected specie is presented as

$$c(x,y)_{t=0} = \frac{c_{cH4}}{4}\left[1 + erf\left(\frac{x - x_d}{d}\right)\right] \tag{6.8}$$

And erf is the complimentary error function described as:

$$erf(x) = \int_0^x e^{\frac{z^2}{2}} dz \tag{6.9}$$

6.4 Implementation in COMSOL Multiphysics®

Two physics interfaces were used to model the EGR scenario at the core scale. The porous media fluid flow based on pressure and velocity was modelled using the Brinkman equation (br). Transport of concentrated species (tcs) is used to model the transport of solute concentration. These physics interfaces were coupled with a complex coupling system imbedded in the COMSOL Multiphysics ® program called reacting flow coupling. The parameters used in this simulation are given in Table 6.1.

Table 6.1 Parameters used in the simulation

Name	Expression	Value	Description
mu_CH4	*1.3962e-5[Pa*s]*	*1.3962E−5 Pa·s*	CH_4 viscosity
rho_CH4	*58.3[kg/m^3]*	*58.3 kg/m³*	CH_4 Density
k	*2.102e-13[m^2]*	*2.102E−13 m²*	Core sample permeability
phi	*0.231[1]*	*0.231*	Core Sample Porosity
vel	*3.e-5[m/s]*	*3E−4 m/s*	Velocity
pr	*8652660[Pa]*	*8.6527E6 Pa*	Pressure
t_step	*1[s]*	*1 s*	Time ramp
D	*5.33e-8[m^2/s]*	*5.33E−8 m²/s*	Diffusivity
T	*313.15[K]*	*313.15 K*	Temperature
Lex	*0.076[m]*	*0.076 m*	Length of core sample
Wex	*0.025[m]*	*0.025 m*	Height of core sample
x_d	*0.02[m]*	*0.02 m*	Displacement front

6.4.1 Brinkman model

The equation for the conservation of momentum in the Brinkman (br) model in COMSOL Multiphysics® is given by:

$$\rho \frac{\partial u}{\partial t} = \nabla \cdot \left[-PI + \mu \frac{1}{\varepsilon}(\nabla u + (\nabla u)^T) - \frac{2}{3}\mu \frac{1}{\varepsilon}(\nabla \cdot u)I \right] - \left(\mu k^{-1} + \beta_F |u| + \frac{Q_m}{\varepsilon^2} \right)u + F + \rho g \quad (6.10)$$

$$Q_m = \frac{\partial \varepsilon \rho}{\partial t} + \nabla \cdot (\rho u) \quad (6.11)$$

179

Where β_F is the Forchhimer drag coefficient, I is the identity vector, and Q_m is the mass source.

A triangular finer physics-controlled meshing was initiated for the domain discretization in the model. This is presented in Figure 6.2.
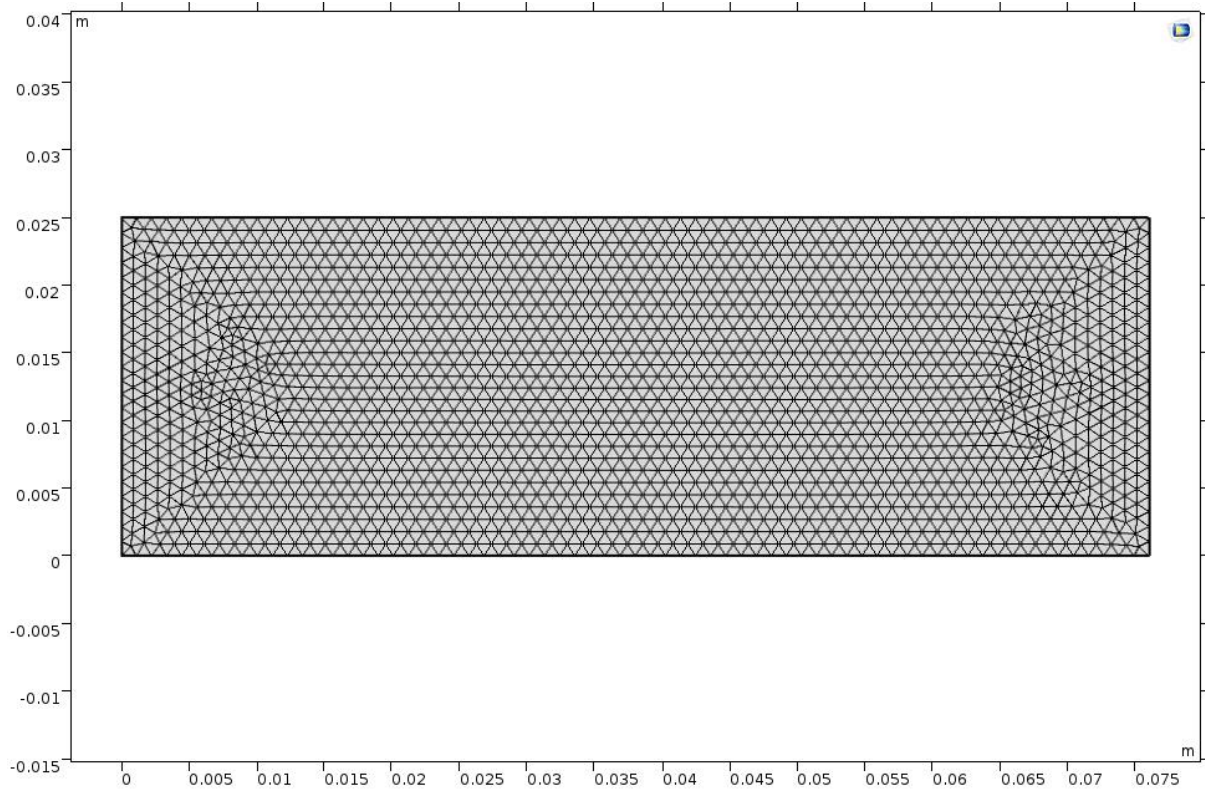
Figure 6.2 Discretization of the domain with finer triangular meshing in the model

6.4.2 Transport of concentrated species (tcs) in porous media

The reacting flow Multiphysics coupling employed in this study enables coupling of the Brinkman model with the transport of concentrated species to model solute transport in porous media. And in the tcs, the diffusion model chosen for the transport mechanism is the mixture-averaged model which entails convective transport and mass transfer in porous media. The equations used in the tcs in COMSOL Multiphysics® are as follows;

$$\rho \frac{\partial \omega_i}{\partial t} + \nabla \cdot j_i + \rho(u \cdot \nabla)\omega_i = R_i \tag{6.12}$$

$$N_i = j_i + \rho u \omega_i \tag{6.13}$$

$$j_i = -\left(\rho D_i^m \nabla \omega_i + \rho D_i^m \nabla \omega_i \frac{\nabla M_n}{M_n} - j_{c,i} + D_i^T \frac{\nabla T}{T}\right) \tag{6.14}$$

$$D_i^m = \frac{1 - \omega_i}{\sum_{k \neq i} \frac{x_k}{D_{ik}}} \qquad (6.15)$$

$$M_n = \left(\sum_i \frac{\omega_i}{M_i} \right)^{-1} \qquad (6.16)$$

$$j_{c,i} = \rho \omega_i \sum_k \frac{M_i}{M_n} D_k^m \nabla x_k \qquad (6.17)$$

Where Ri is the reaction rate, ω_i is the mass fraction of *i-th* component, *Ni* is the flux of specie *i*, *ji* is the diffusion flux vector of specie i, *Mn* is the molar mass of mixture, *Di* is the effective diffusion coefficient of the mixture, *Mi* is the molar mass of *i* species, *T* is the temperature of the system. The slip boundary condition was assumed here, also the there are no fluxes in any of the boundaries except for the inlet and out let of the core holder as shown in Figure 6.3.
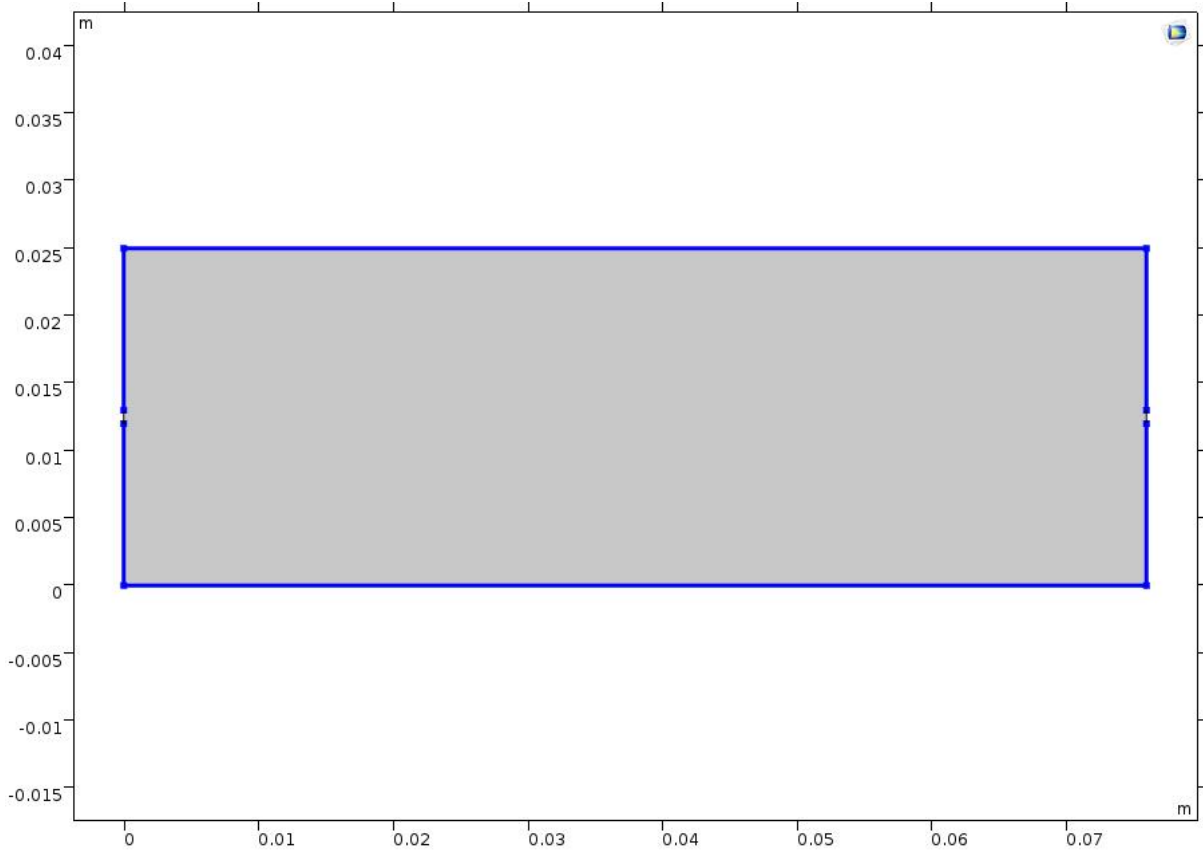
Figure 6.3 Slip and no flux boundary conditions in the model

Furthermore, for the effective diffusivity model, no correction was applied therefore $fe = 1$. Porosity and permeability of the core sample were also assumed to be constant. The

181

brinkman model coupled with the transport of concentrated specie in porous media modelled the miscible displacement of CH_4 by CO_2 for EGR.

6.5 Results and discussion

The displacement of CH_4 by CO_2 at test conditions was simulated in both vertical and horizontal orientation and compared to the experimental results for validation. An arbitrary point in the model space was chosen to measure the effluent concentration during the displacement. The point is shown in Figure 6.4. This enabled the generation of the concentration profile at the outlet of the core sample for the purpose of comparison.
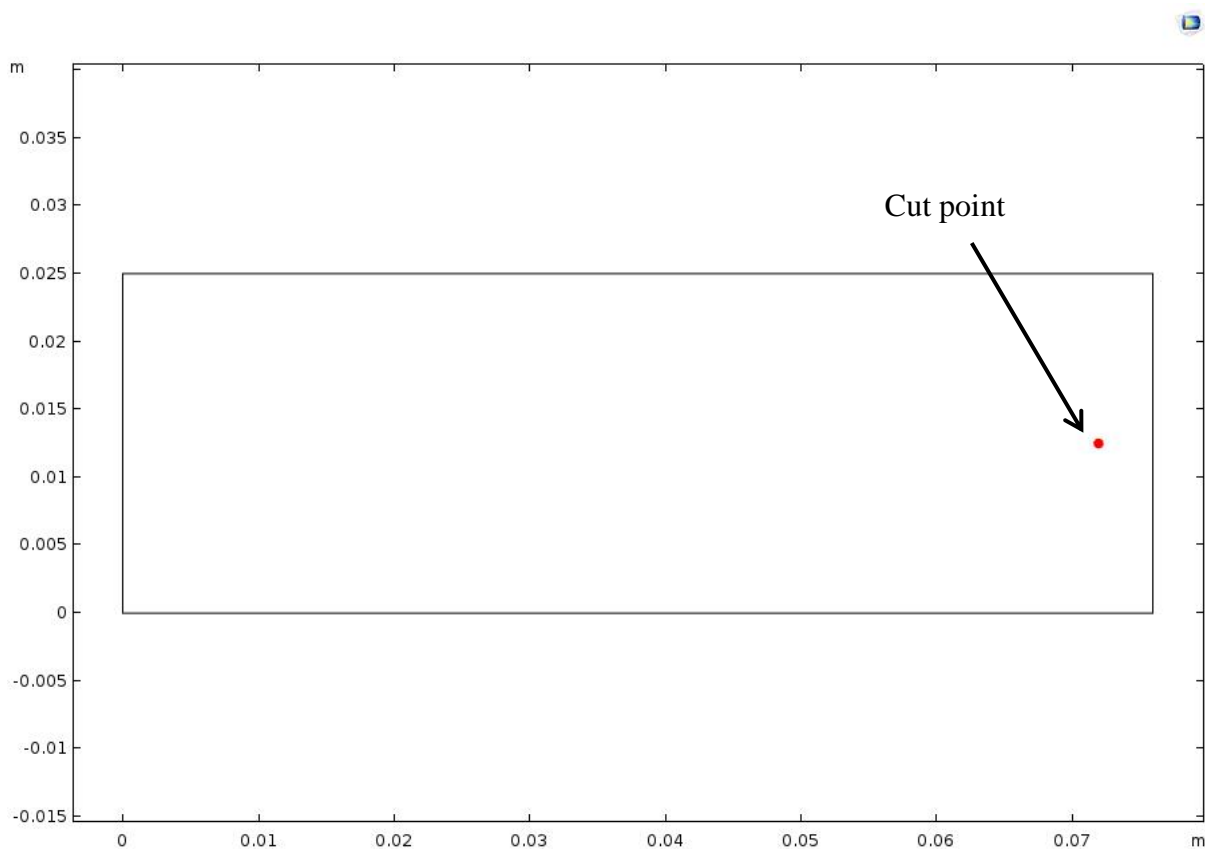
Figure 6.4 Cut point on the model for analysis

From the simulation, the concentration profile was obtained using the input parameters as those employed in the experimental runs. The results obtained are depicted Figure 6.5, where there is a good agreement between the experimental results and the simulated one. The breakthrough times are 3 minutes apart and with all the systematic effects experienced during the experimental run such as entry and exit effects, the results are very close in agreement. Gravity effects were also added to the brinkman model in order to simulate the effect of gravity on the flow behaviour of the injected CO_2.

182
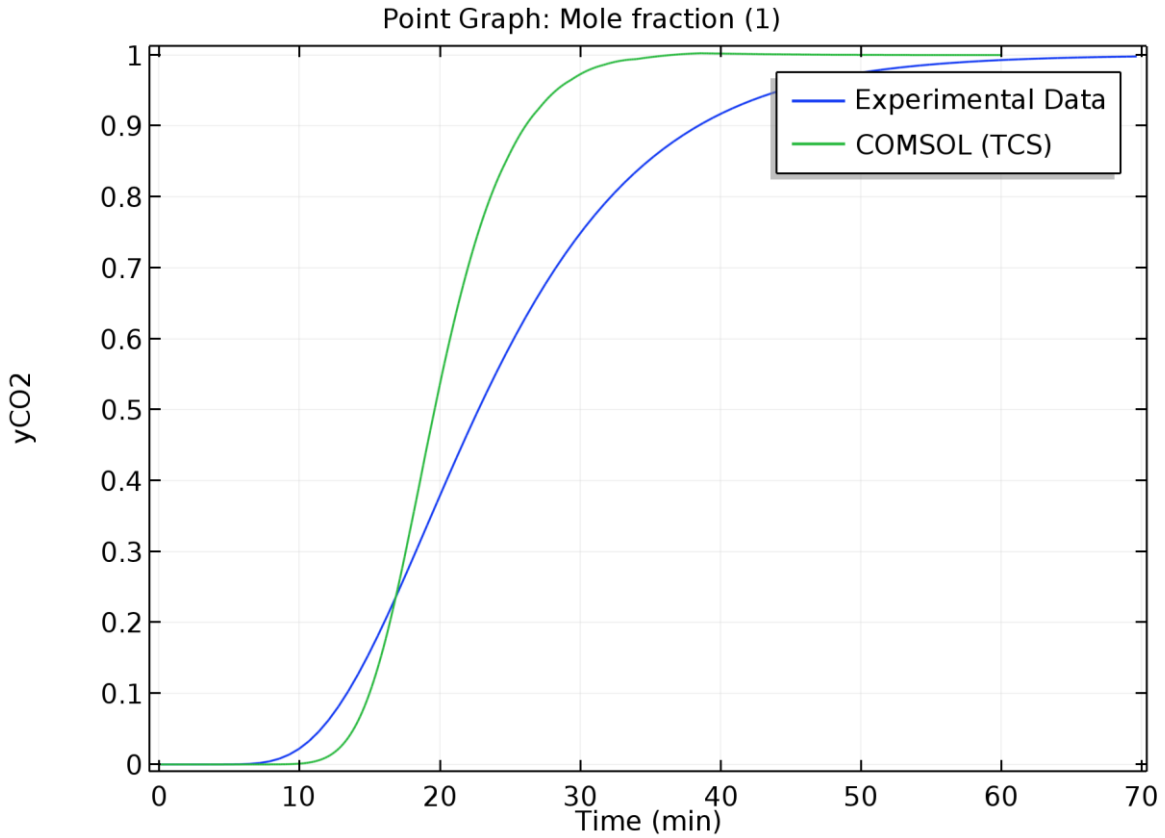
Figure 6.5 Comparison of simulated and experimental concentration profiles

The gravity effects are visually represented by the graphics interface of the COMSOL software. Each visual depiction of the flow behaviour was depicted at time intervals i.e. at the beginning of the simulation, the middle, and at the end over the period of 60 mins to visually assess the flow behaviour. Figure 6.6 shows the onset of the displacement and as can be seen, gravity segregation of the injected CO_2 is apparent in that the plume of the injected CO_2 moves downwards towards the bottom of the core sample in its flow path. Pressure seems to be higher towards the bottom as the injected proceeds. Velocity magnitude is higher at the inlet and the outlet of the core sample given the setup of the experiments.
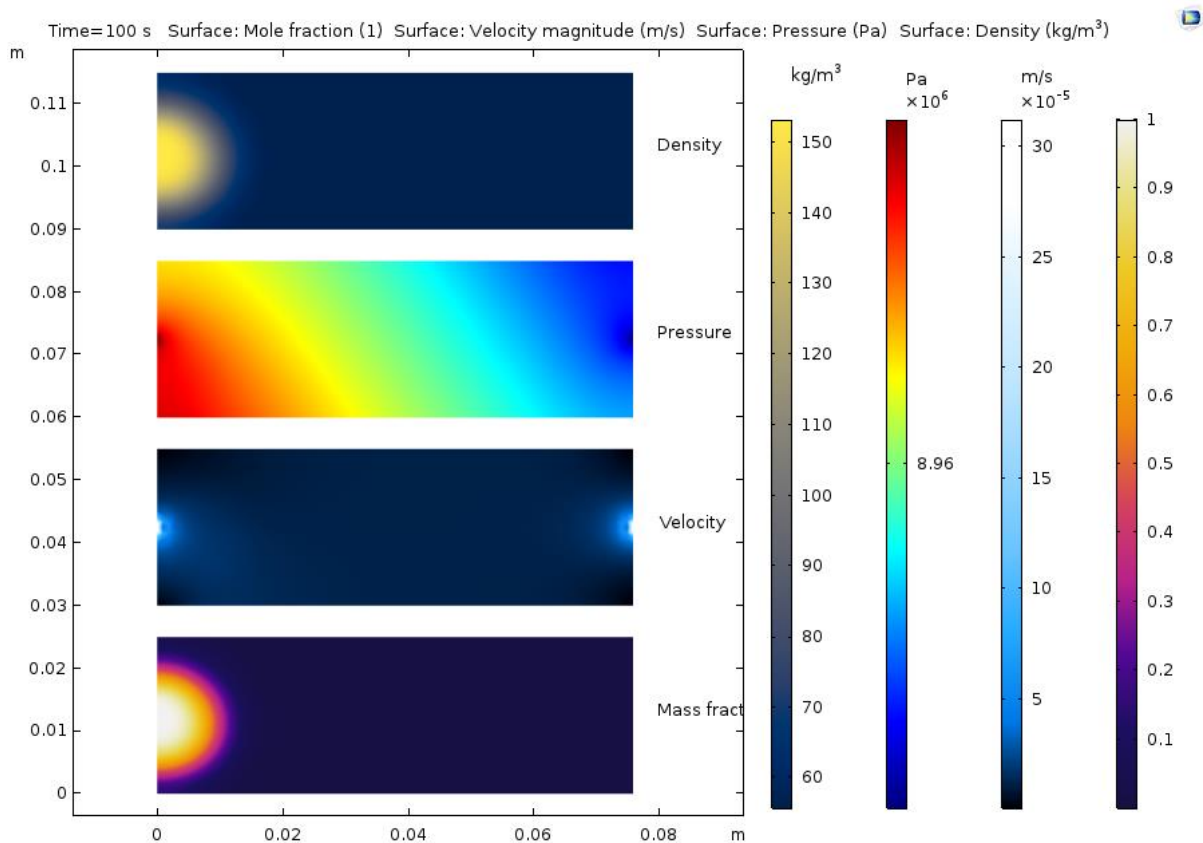
Figure 6.6 Visual graphics of parameters during simulation at 100s horizontal

Halfway through the simulation, the segregation progressed all through the length of the core sample towards the exit as shown in Figure 6.7 where the CO_2 pushed the CH_4 towards the uppermost part of the core sample because of the density gradient and also the density and viscosity difference.

Figure 6.8 show the end of the simulation where CO_2 gas completely occupied the core sample. One thing to note is that the velocity magnitude was not affected by gravity given that it was assumed to be constant all through the simulation to fit the postulate as presented in the ADE equation in the mathematical modelling.

This simulation of the effect of gravity on the behaviour of the injected CO_2 confirms the attributed segregation of the CO_2 during the experimental runs in the horizontal orientation. The sinking reduced the CO_2 permeability and hence affected the displacement of the CH_4 from the core sample. This also confirms the expected tailing effects seen during the curve fitting of the ADE to the experimental results which had a meagre fit towards the end of the regression.
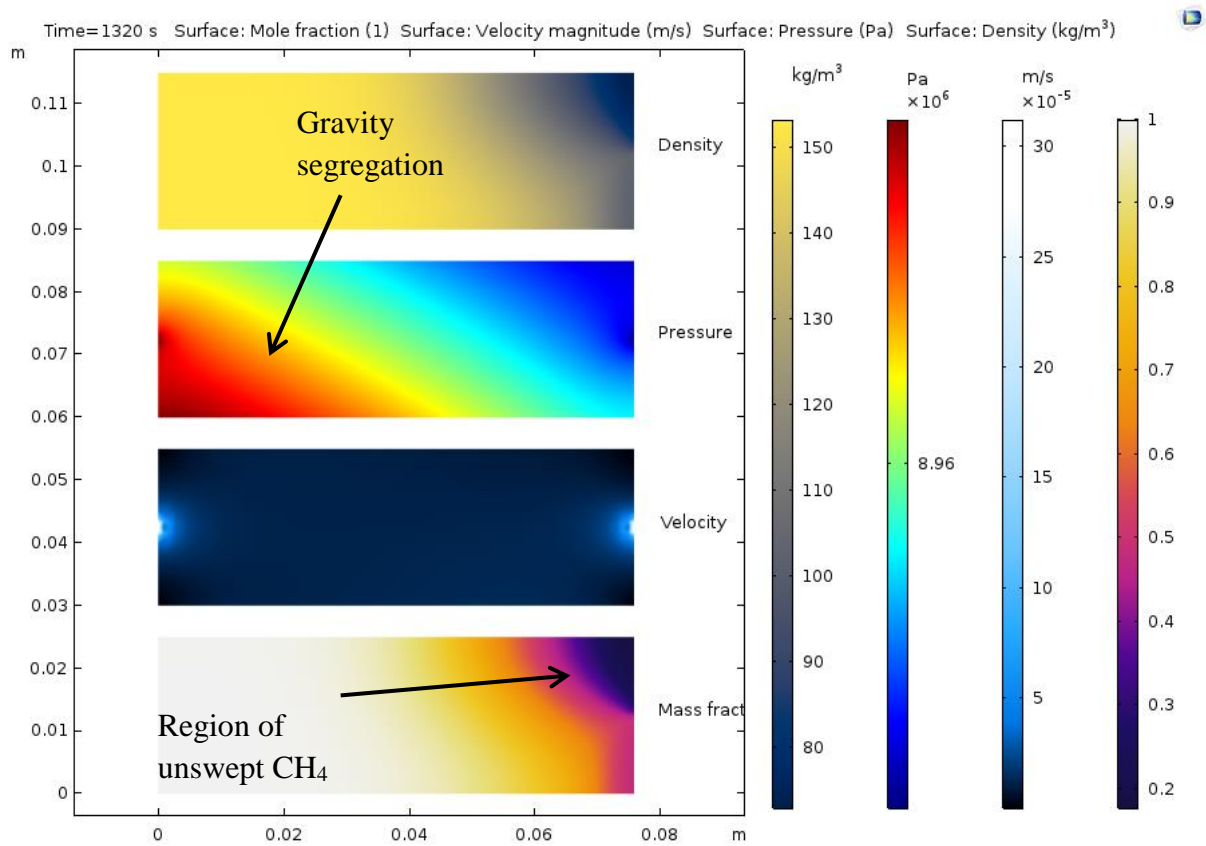
Figure 6.7 Visual graphics of parameters during simulation at 1320 s
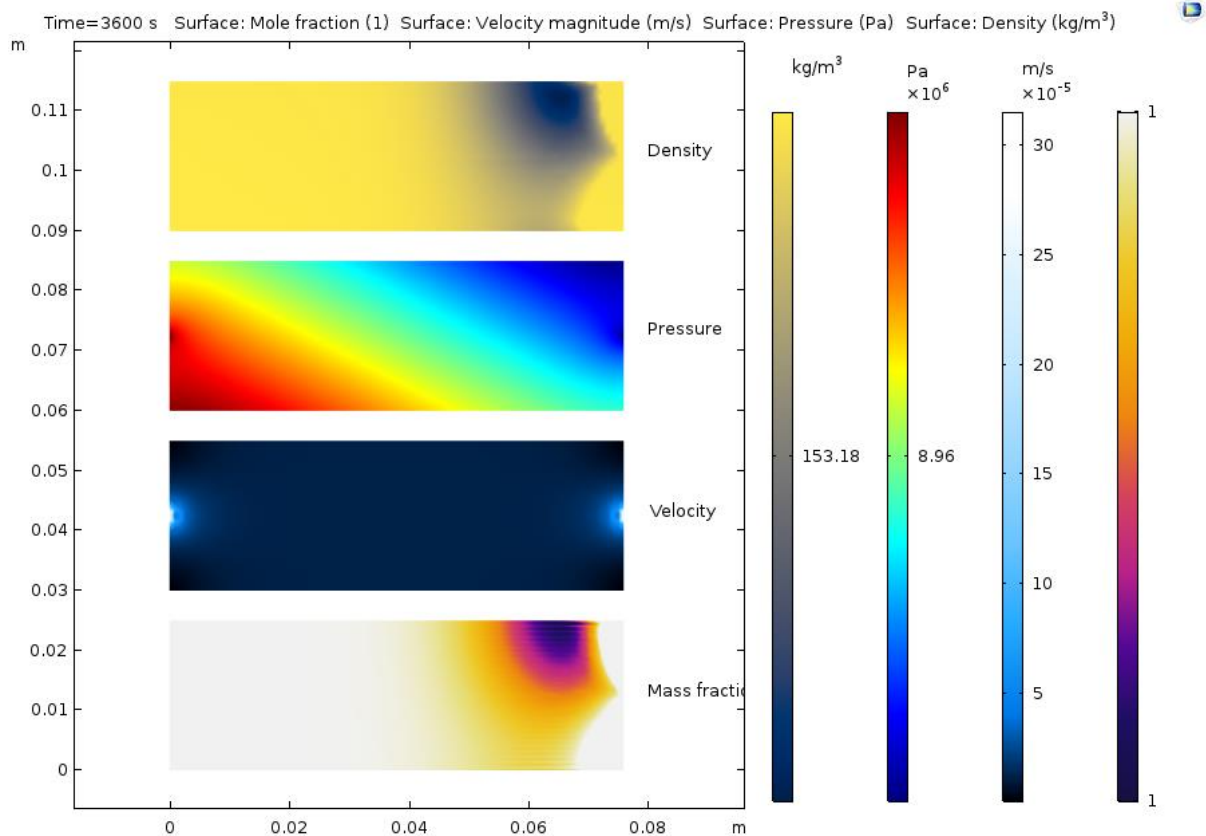
Figure 6.8 Visual graphics of parameters during simulation at 3600 s

185

Furthermore, a simulation on the vertical injection orientation was carried out using the same parameters as employed in the horizontal orientation. The result of the simulations at the onset of the run is described in Figure 6.9.
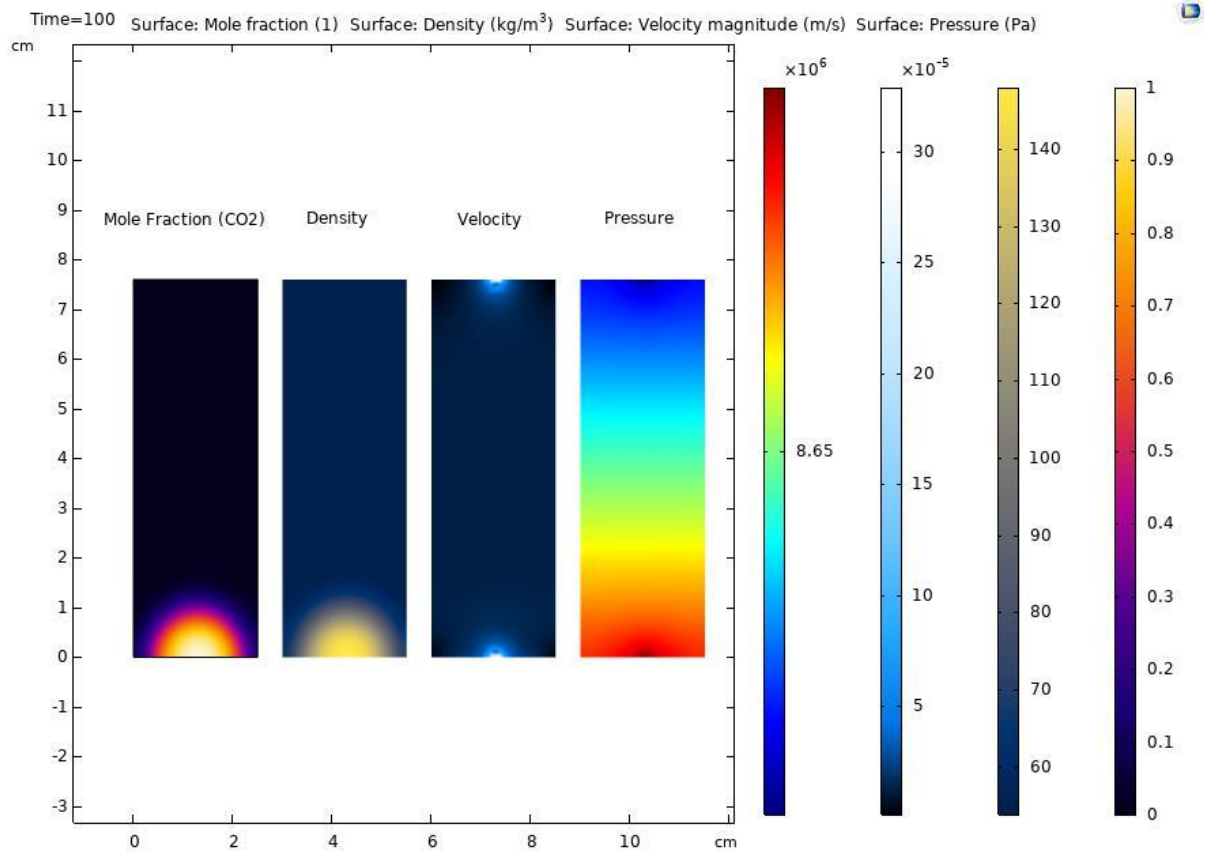
Figure 6.9 Visual graphics of parameters during simulation at 100s vertical

There is a uniform flow in the longitudinal path of the flow stream at the beginning of the simulation as seen in the mole fraction and density graphics of the injected CO_2 (Figure 6.9). This trend continued in the same cadence to the middle of the duration of the simulation shown in Figure 6.10. There was a slight profile in the middle of the plume which suggests the flow path and velocity at the middle of the core sample being higher.
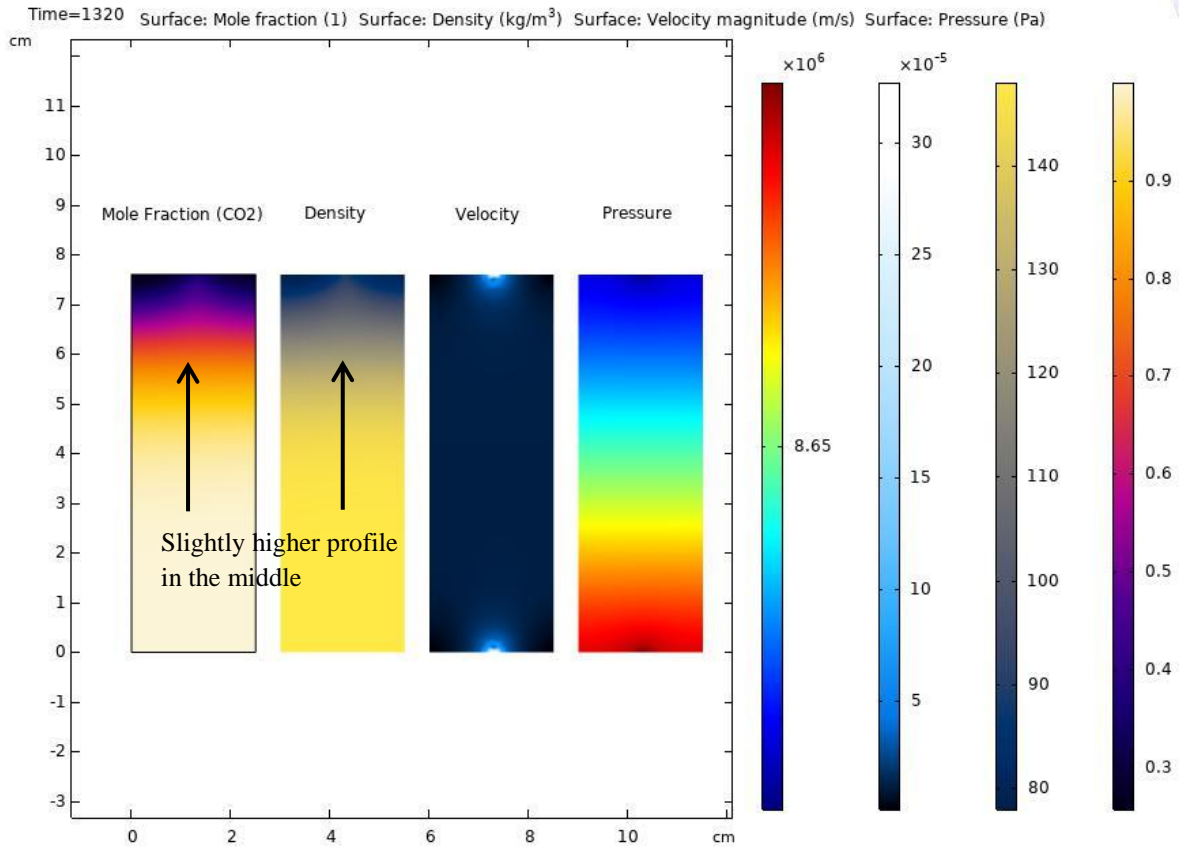
Figure 6.10 Visual graphics of parameters during simulation at 1320s vertical

In Figure 6.11, due to the buoyancy of the injected CO_2, there exists a time when the CO_2 will pass over the CH_4 in the core sample as a result of the small diameter of the inlet and outlet of the distribution plugs of the core holder housing the core sample. The rate of production at the outlet will be lower than the rate of the accumulation of the effluents exiting the core sample.
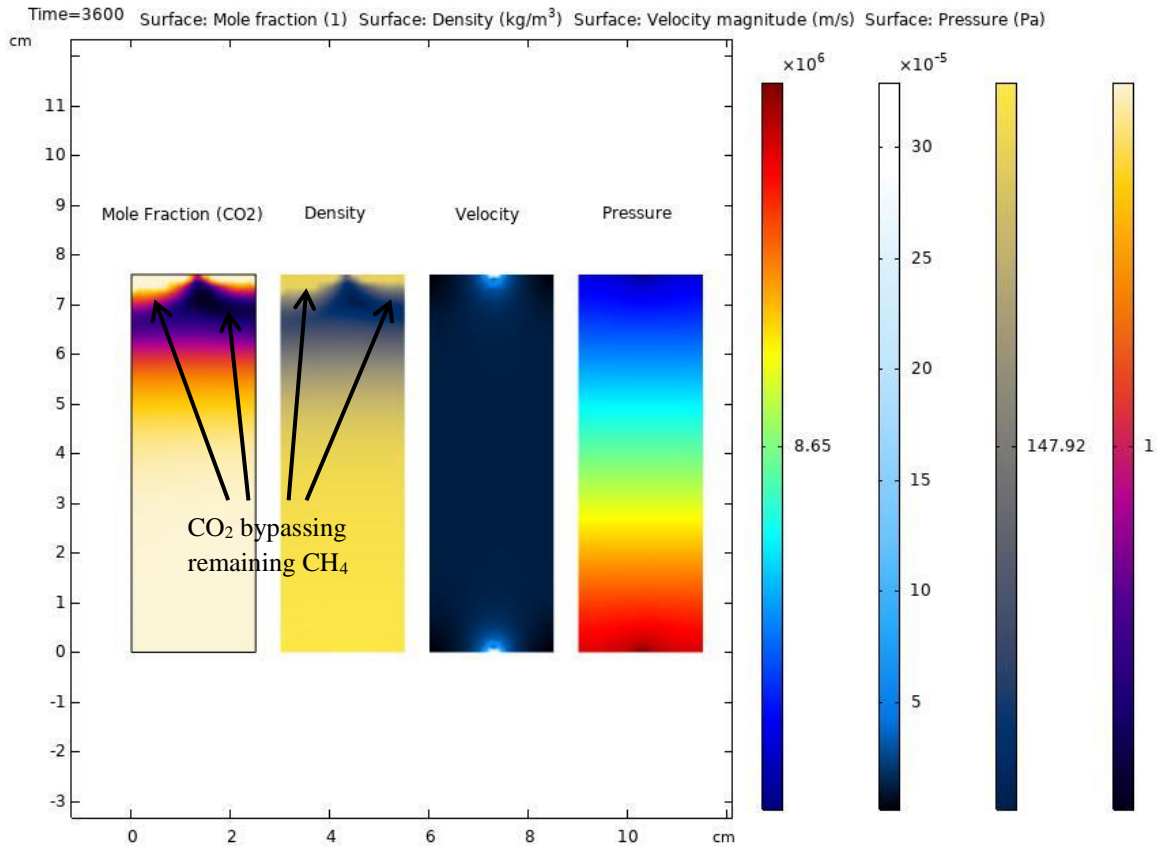
Figure 6.11 Visual graphics of parameters during simulation at 3600s vertical

6.6 Summary

A simulation was carried out using COMSOL Multiphysics® to compare the experimental results and further explain some of the trends observed in the experimental proceedings. Two physics in the modelling package were utilised; the Brinkman (br) model was used to define the porous domain of the model and the Transport of Concentrated Species (tcs) was used to model the solute transport using the reacting flow coupling to solve for the pressure and density gradient which provided a stable numerical modelling. The results show that the methodology employed in the experimental work in this thesis was robust and practical given the similarities between the concentration profiles of both simulation and experimental runs at the same conditions. Furthermore, the effect of gravity and the trends observed, and attributes postulated during the experimental runs were validated and shown using the simulation.

CHAPTER 7

7   CONCLUSION AND RECOMMENDATION

7.1   Conclusions

Having successfully carried out the objectives stated to achieve the aim of the research, a number of conclusions can be drawn to highlight the physics of mixing between CO_2 and CH_4 during with regards to injection orientation, injection rate, and connate water salinity inclusion. Also, the feasibility of solubility trapping as a secondary storage mechanism of CO_2 during enhanced gas recovery by CO_2 injection technique was emphasised. These conclusions are as follows:

- Using the grain diameter of rock as the characteristic length scale of mixing provided a more robust approach to the depiction of the dominant displacement mechanism when choosing displacement approach for EGR. Other approaches as shown in the study either overestimate or underestimate the P_{ex} which leads to poor choices of injection parameters especially the injection rate. The grain diameters measured for this purpose using SEM and image analysis were 165.70 µm for *Buff Berea*, 94.66 µm for *Grey Berea*, and finally 57.15 µm for *Bandera Grey*. For all the core samples used, this method of P_{ex} determination using the grain diameter as the length scale of mixing indicated that the dominant displacement mechanism during EGR was diffusion with $P_{ex} < 0.1$. This helped to determine the best injection rates based on the scale of the core samples employed for this application.

- The injection rates at the operating conditions of the experiments were obtained using within a range based on the P_{ex}, these are required to test the sensitivity of the injection orientation on CO_2 dispersion in CH_4. Hence, the injection orientation of the CO_2 was found to have significant effect on the displacement efficiency of EGR. Gravity effects are more pronounced in the horizontal orientation compared to the vertical orientation. Therefore, mixing/dispersion was observed to be more prominent in the horizontal orientation by a factor of 2.5.

- The core samples' permeability to supercritical CO_2 is generally higher in the vertical orientation. Noticeably, at lower injection rates the permeability was lower in the horizontal orientation with a characteristic higher pressure differential but similar at higher injection rates.

- The investigation of the sensitivity of the injection orientation provided an avenue where the optimum flow conditions based on injection rates and orientation were obtained so as to employ them in the connate water sensitivity experiments. This provided conditions where the experiments were unaffected by the systematic errors and also give the best situation where only salinity effects were more pronounced. *Grey Berea* at 0.3ml/min and vertical orientation gave the best results in terms of dispersion coefficient and CH_4 recovery and as such was used for the connate water sensitivity analysis during EGR. It was found that inclusion of connate water in EGR has substantial influence on the dispersion of the injected CO_2 into the CH_4. The connate water reduced or provided constrictions in the pore matrix in the rock thereby creating narrower flow paths in the core sample and hence increases the mixing between the gases.

- Connate water salinity profoundly changes the pore distribution of the core sample matrix and its effect on the mixing was rather peculiar. In the sense that, increase in salinity showed a decrease in the dispersion coefficient. This was attributed to the density of the connate water making the core sample more homogeneous which invariably provided a smother pathway for the gases to traverse.

- Solubility trapping is feasible as a potential secondary trapping mechanism for CO_2 injected in conjunction with primary structural trapping during EGR. This increases the storage capacity of natural gas reservoirs as sequestration site which makes EGR a more pragmatic approach as a technique for CO_2 emission reduction. At higher salinity of 10wt%, a storage of 63% of the injected CO_2 was realised as against 7% of the primary structural trapping albeit the low solubility of CO_2 in brine.

The investigation highlights the significance of the effect of inclusion of connate water and its salinity during EGR. This considerably impacts the extent of dispersion of the injected CO_2 into the nascent CH_4 during the displacement process. On the injection orientation, the importance of this highlight was to provide an insight into the dip angle of injection from injector to producer. These findings are aimed at providing knowledge for field scale application of EGR through computer simulations by including these systematic effects for a better representation of the process.

7.2 Recommendation and future work

Albeit the considerable breakthrough in this research, it is noteworthy to mention that there are still avenues to consider which are beyond the scope of this research work. Some recommendations are as follows:

- The use of more sophisticated imaging techniques like Nuclear Magnetic Resonance (NMR) could be employed to visualise the extent the pore distribution before and after the core flooding to analyse any dynamics therein as a result of the injection process.

- CO_2- brine, CH_4-brine relative permeability can help project the performance of CO_2 injection for EGR to evaluate the efficiency of the technique.

- The saturation of the connate water could be varied to also evaluate the effect of connate water saturation and salinity on both displacement efficiency and dispersion coefficient during EGR.

REFERENCES

Abba, M. K., Abbas, A. J., & Nasr, G. G. (2017). Enhanced Gas Recovery by CO_2 Injection and Sequestration: Effect of Connate Water Salinity on Displacement Efficiency. In *SPE Abu Dhabi International Petroleum Exhibition & Conference*. https://doi.org/10.2118/188930-MS

Abba, M.K., Abbas, A. J., Saidu, B., & Nasr, G. . (2018). Effects Of Gravity On Flow Behaviour Of Supercritical CO_2 During Enhanced Gas Recovery (EGR) By CO_2 Injection And Sequestration (pp. 1–5).

Abba, Muhammad Kabir, Al-Othaibi, A., Abbas, A. J., Nasr, G. G., & Mukhtar, A. (2018). Experimental investigation on the impact of connate water salinity on dispersion coefficient in consolidated rocks cores during Enhanced Gas Recovery by CO_2 injection. *Journal of Natural Gas Science and Engineering*. https://doi.org/10.1016/j.jngse.2018.10.007

Adepoju, O. O., Lake, L. W., Johns, R. T., & Energy, E. M. S. (2013). SPE 166390 Anisotropic Dispersion and Upscaling for Miscible Displacement, (1981), 421–432.

Ahmadi, P., & Chapoy, A. (2018). CO2solubility in formation water under sequestration conditions. *Fluid Phase Equilibria*, *463*, 80–90. https://doi.org/10.1016/j.fluid.2018.02.002

Ahmed, T. (2010). Gas Well Performance. *Reservoir Engineering Handbook*, 546–582. https://doi.org/10.1016/B978-1-85617-803-7.50016-X

Akin, S., & Kovscek, A. R. (2003). Computed tomography in petroleum engineering research, (215), 23–38.

Al-Abri, A., Hiwa, S., & Robert, A. (2009). Experimental investigation of the velocity-dependent relative permeability and sweep efficiency of supercritical CO2 injection into gas condensate reservoirs. *Journal of Natural Gas Science and Engineering*, *1*(4–5), 158–164. https://doi.org/10.1016/j.jngse.2009.10.002

Al-abri, A., Sidiq, H., & Amin, R. (2009). Enhanced Natural Gas and Condensate Recovery by Injection of Pure SCCO2 , Pure CH4 and Their Mixtures : Experimental Investigation. *SPE Annual Technical Conference and Exhibition, New Orleans, Lousiana, USA, 4-7 October*, 1–13.

Al-Abri, A., Sidiq, H., & Amin, R. (2012). Mobility ratio, relative permeability and sweep efficiency of supercritical CO2 and methane injection to enhance natural gas and condensate recovery: Coreflooding experimentation. *Journal of Natural Gas Science and Engineering*, *9*, 166–171. https://doi.org/10.1016/j.jngse.2012.05.011

Allen, R., Nilsen, H. M., Andersen, O., & Lie, K. A. (2017). Categorization of Norwegian Continental Shelf Formations in Terms of Geological CO2Storage Potentials. *Energy Procedia*, *114*(1876), 4583–4594. https://doi.org/10.1016/j.egypro.2017.03.1579

Amin, R., Sidiq, H., Kennaird, T., & Van der Steen, E. (2010). Gas-gas experimental interfacial tension measurement. *Fluid Phase Equilibria*, *295*(2), 230–236. https://doi.org/10.1016/j.fluid.2010.05.020

Arabloo, M., Ghazanfari, M. H., & Rashtchian, D. (2016). Wettability modification, interfacial tension and adsorption characteristics of a new surfactant: Implications for enhanced oil recovery. *Fuel*, *185*, 199–210. https://doi.org/10.1016/j.fuel.2016.06.088

Ayirala, S. C., & Rao, D. N. (2006). Solubility, miscibility and their relation to interfacial tension in ternary liquid systems. *Fluid Phase Equilibria*, *249*(1–2), 82–91. https://doi.org/10.1016/j.fluid.2006.09.020

Bagalkot, N., Hamouda, A. A., & Isdahl, O. M. (2018). Dynamic interfacial tension measurement method using axisymmetric drop shape analysis. *MethodsX*, *5*(June), 676–683. https://doi.org/10.1016/j.mex.2018.06.012

Barati-Harooni, A., Soleymanzadeh, A., Tatar, A., Najafi-Marghmaleki, A., Samadi, S. J., Yari, A., … Mohammadi, A. H. (2016). Experimental and modeling studies on the effects of temperature, pressure and brine salinity on interfacial tension in live oil-brine systems. *Journal of Molecular Liquids*, *219*, 985–993. https://doi.org/10.1016/j.molliq.2016.04.013

Bennaceur, K. (2013). CO2Capture and Sequestration. *Future Energy: Improved, Sustainable and Clean Options for Our Planet*, 583–611. https://doi.org/10.1016/B978-0-08-099424-6.00026-0

Bennion, D. B., & Bachu, S. (2008). A correlation of the interfacial tension between supercritical phase CO_2 and equilibrium brines as a function of salinity, temperature and pressure. *Proceedings - SPE Annual Technical Conference and Exhibition*, *1*, 224–237.

https://doi.org/10.2118/114479-MS

Benson, S., Cook, P., Anderson, J., Bachu, S., Nimir, H. B., Basu, B., … Deguchi, G. (2005). Underground geological storage. *Ipcc*, 195–276.

Biagi, J., Agarwal, R., & Zhang, Z. (2016). Simulation and optimization of enhanced gas recovery utilizing CO2. *Energy*, *94*, 78–86. https://doi.org/10.1016/j.energy.2015.10.115

Bjerg, P. (2008). Dispersion in aquifers. *Soil and Groundwater Pollution - Processes and Remediation*, (March), 6.

Blok, K., Williams, R. H., Katofsky, R. E., & Hendriks, C. A. (1997). Hydrogen production from natural gas, sequestration of recovered CO2 in depleted gas wells and enhanced natural gas recovery. *Energy*, *22*(2–3), 161–168. https://doi.org/10.1016/S0360-5442(96)00136-3

Chalbaud, C., Robin, M., Lombard, J. M., Martin, F., Egermann, P., & Bertin, H. (2009). Interfacial tension measurements and wettability evaluation for geological CO2storage. *Advances in Water Resources*, *32*(1), 98–109. https://doi.org/10.1016/j.advwatres.2008.10.012

Chen, L., Wang, M., Kang, Q., & Tao, W. (2018). Pore scale study of multiphase multicomponent reactive transport during CO2dissolution trapping. *Advances in Water Resources*, *116*(September 2017), 208–218. https://doi.org/10.1016/j.advwatres.2018.02.018

Chow, Y. T. F., Maitland, G. C., & Trusler, J. P. M. (2016). Interfacial tensions of the (CO2 + N2 + H2O) system at temperatures of (298 to 448) K and pressures up to 40 MPa. *Journal of Chemical Thermodynamics*, *93*, 392–403. https://doi.org/10.1016/j.jct.2015.08.006

CO2 Care. (2011). *D3 . 1 - Review of relevant trapping mechanisms based on site portfolio*.

Coats, K.H., Smith, B. D., van Genuchten, M. T., & Wierenga, P. J. (1964). Dead-End Pore Volume and Dispersion in Porous Media. *Soil Science Society of America Journal*, *4*(01), 73–84. https://doi.org/10.2118/647-PA

Coats, K.H., & Whitson, C. H. (2004). SPE 90390 Modeling Conformance as Dispersion.

Coats, Keith H., Whitson, C. H., & Thomas, K. (2009). Modeling Conformance as Dispersion. *SPE Reservoir Evaluation & Engineering*, *12*(01), 33–47. https://doi.org/10.2118/90390-PA

COMSOL. (2014). Introduction to COMSOL Multiphysics 5.3. *Manual*, 168. Retrieved from http://cdn.comsol.com/documentation/5.0.1.276/IntroductionToCOMSOLMultiphysics.pdf

Dake, L. P. (1978). *Fundamentals of resevoir engineering*. ELSEVIER SCIENCE. https://doi.org/10.1016/B978-0-08-098206-9.00004-X

Dehghan, A. A., Masihi, M., & Ayatollahi, S. (2015). Phase behavior and interfacial tension evaluation of a newly designed surfactant on heavy oil displacement efficiency; effects of salinity, wettability, and capillary pressure. *Fluid Phase Equilibria*, *396*, 20–27. https://doi.org/10.1016/j.fluid.2015.03.028

Dickinson, E. J. F., Ekström, H., & Fontes, E. (2014). COMSOL Multiphysics®: Finite element software for electrochemical analysis. A mini-review. *Electrochemistry Communications*, *40*, 71–74. https://doi.org/10.1016/j.elecom.2013.12.020

Ding, S., Xi, Y., Jiang, H., & Liu, G. (2018). CO_2 storage capacity estimation in oil reservoirs by solubility and mineral trapping. *Applied Geochemistry*, *89*(September 2017), 121–128. https://doi.org/10.1016/j.apgeochem.2017.12.002

Dittmar, D., Fredenhagen, A., Oei, S. B., & Eggers, R. (2003). Interfacial tensions of ethanol-carbon dioxide and ethanol-nitrogen. Dependence of the interfacial tension on the fluid density - prerequisites and physical reasoning. *Chemical Engineering Science*, *58*(7), 1223–1233. https://doi.org/10.1016/S0009-2509(02)00626-7

Duchateau, C., & Broseta, D. (2012). A simple method for determining brine-gas interfacial tensions. *Advances in Water Resources*, *42*, 30–36. https://doi.org/10.1016/j.advwatres.2012.03.008

Ekwere, P. J. (2007). Petrophysics, 1049.

He, W., Lv, W., & Dickerson, J. (2014). Gas Transport in Solid Oxide Fuel Cells. https://doi.org/10.1007/978-3-319-09737-4

Ho, C., & Webb, S. (2006). *Theory and Applications of Transport in Porous Media*.

Springer.

Holdich, S. A. (2004). Experimental and Simulation Studies of Sequestration of Supercritical Carbon Dioxide in Depleted Gas Reservoirs, (May).

Honari, A., Bijeljic, B., Johns, M. L., & May, E. F. (2015). Enhanced gas recovery with {CO2} sequestration: The effect of medium heterogeneity on the dispersion of supercritical CO2–CH4. *International Journal of Greenhouse Gas Control*, *39*(0), 39–50. https://doi.org/http://dx.doi.org/10.1016/j.ijggc.2015.04.014

Honari, A., Hughes, T. J., Fridjonsson, E. O., Johns, M. L., & May, E. F. (2013). Dispersion of supercritical CO2 and CH4 in consolidated porous media for enhanced gas recovery simulations. *International Journal of Greenhouse Gas Control*, *19*, 234–242. https://doi.org/10.1016/j.ijggc.2013.08.016

Honari, A., Zecca, M., Vogt, S. J., Iglauer, S., Bijeljic, B., Johns, M. L., & May, E. F. (2016). The impact of residual water on CH4-CO2 dispersion in consolidated rock cores. *International Journal of Greenhouse Gas Control*, *50*, 100–111. https://doi.org/10.1016/j.ijggc.2016.04.004

Honeywell. (2012). Mass Flow Sensors: Mass Flow versus Volumetric Flow and Flow Rate Unit Conversions, 1–4. Retrieved from http://sensing.honeywell.com/mass-flow-vs-volumetric-flow-and-unit-conversion-tn-008043-2-en-final-06nov12.pdf

Hughes, T. J., Honari, A., Graham, B. F., Chauhan, A. S., Johns, M. L., & May, E. F. (2012). CO2 sequestration for enhanced gas recovery: New measurements of supercritical CO2–CH4 dispersion in porous media and a review of recent research. *International Journal of Greenhouse Gas Control*, *9*, 457–468. https://doi.org/10.1016/j.ijggc.2012.05.011

Huysmans, M., & Dassargues, A. (2005). Review of the use of P??clet numbers to determine the relative importance of advection and diffusion in low permeability environments. *Hydrogeology Journal*, *13*(5–6), 895–904. https://doi.org/10.1007/s10040-004-0387-4

Iglauer, S. (2011). Dissolution Trapping of Carbon Dioxide in Reservoir Formation Brine A Carbon Storage Mechanism. *Mass Transfer - Advanced Aspects*, 836. https://doi.org/10.5772/20206

Jha, R. K., Bryant, S. L., Lake, L. W., & John, A. (2013). Investigation of Pore-Scale (Local)

Mixing. *SPE/DOE Symposium on Improved Oil Recovery*. https://doi.org/10.2118/99782-MS

Jin, L., Pekot, L. J., Smith, S. A., Salako, O., Peterson, K. J., Bosshart, N. W., … Gorecki, C. D. (2018). Effects of gas relative permeability hysteresis and solubility on associated CO2storage performance. *International Journal of Greenhouse Gas Control*, *75*(June), 140–150. https://doi.org/10.1016/j.ijggc.2018.06.002

Jones, E., & Lineweaver, C. (2010). Pressure-temperature Phase Diagram of the Earth. *Pathways Towards Habitable Planets ASP Conference Series*, *430*, 145–151. Retrieved from http://arxiv.org/abs/1005.2440

Kalra, S., & Wu, X. (2014). CO2 injection for Enhanced Gas Recovery. *SPE Western North American and Rocky Mountain …*, (April), 16–18. Retrieved from https://www.onepetro.org/conference-paper/SPE-169578-MS

Kamari, A., Pournik, M., Rostami, A., Amirlatifi, A., & Mohammadi, A. H. (2017). Characterizing the CO2-brine interfacial tension (IFT) using robust modeling approaches: A comparative study. *Journal of Molecular Liquids*, *246*, 32–38. https://doi.org/10.1016/j.molliq.2017.09.010

Kargarpour, M. A. (2017). Investigation of reservoir temperature in a gas reservoir in Middle East: case study. *Journal of Petroleum Exploration and Production Technology*, *7*(2), 531–541. https://doi.org/10.1007/s13202-016-0275-1

Kashefi, K., Pereira, L. M. C., Chapoy, A., Burgass, R., & Tohidi, B. (2016). Measurement and modelling of interfacial tension in methane/water and methane/brine systems at reservoir conditions. *Fluid Phase Equilibria*, *409*, 301–311. https://doi.org/10.1016/j.fluid.2015.09.050

Khaksar Manshad, A., Olad, M., Taghipour, S. A., Nowrouzi, I., & Mohammadi, A. H. (2016). Effects of water soluble ions on interfacial tension (IFT) between oil and brine in smart and carbonated smart water injection process in oil reservoirs. *Journal of Molecular Liquids*, *223*, 987–993. https://doi.org/10.1016/j.molliq.2016.08.089

Khan, C., Amin, R., & Madden, G. (2013). Carbon dioxide injection for enhanced gas recovery and storage (reservoir simulation). *Egyptian Journal of Petroleum*, *22*(2), 225–240. https://doi.org/10.1016/j.ejpe.2013.06.002

Koide, H., Tazaki, Y., Noguchi, Y., Iijima, M., Ito, K., & Shindo, Y. (1993). Underground storage of carbon dioxide in depleted natural gas reservoirs and in useless aquifers, *34*(3–4), 175–179. Retrieved from http://www.sciencedirect.com/science/article/B6V63-4808TV1-2G/1/07e8017ab41ca2d26dd639386097f63b

Kumar, A., Pramanik, S., & Mishra, M. (2016). COMSOL Multiphysics® Modeling in Darcian and Non-Darcian Porous Media. *COMSOL Conference*.

Li, B., Tchelepi, H. A., & Benson, S. M. (2013). Influence of capillary-pressure models on CO2 solubility trapping. *Advances in Water Resources*, *62*, 488–498. https://doi.org/10.1016/j.advwatres.2013.08.005

Liu, H., Patil, P. R., & Narusawa, U. (2007). On Darcy-Brinkman equation: Viscous flow between two parallel plates packed with regular square arrays of cylinders. *Entropy*, *9*(3), 118–131. https://doi.org/10.3390/e9030118

Liu, S., Zhang, Y., Xing, W., Jian, W., Liu, Z., Li, T., & Song, Y. (2015). Laboratory experiment of CO2-CH4 displacement and dispersion in sandpacks in enhanced gas recovery. *Journal of Natural Gas Science and Engineering*, *26*, 1585–1594. https://doi.org/10.1016/j.jngse.2015.04.021

Mamora, D. D., & Seo, J. G. (2002). Enhanced Recovery by Carbon Dioxide Sequestration in Depleted Gas Reservoirs. *SPE Annual Technical Conference and Exhibition*, 1–9.

Mehranfar, A., & Ghazanfari, M. H. (2014). Investigation of the microscopic displacement mechanisms and macroscopic behavior of alkaline flooding at different wettability conditions in shaly glass micromodels. *Journal of Petroleum Science and Engineering*, *122*, 595–615. https://doi.org/10.1016/j.petrol.2014.08.027

Michael, K., Golab, A., Shulakova, V., Ennis-King, J., Allinson, G., Sharma, S., & Aiken, T. (2010). Geological storage of CO2 in saline aquifers-A review of the experience from existing storage operations. *International Journal of Greenhouse Gas Control*, *4*(4), 659–667. https://doi.org/10.1016/j.ijggc.2009.12.011

Mohammad Salehi, M., Omidvar, P., & Naeimi, F. (2017). Salinity of injection water and its impact on oil recovery absolute permeability, residual oil saturation, interfacial tension and capillary pressure. *Egyptian Journal of Petroleum*, *26*(2), 301–312. https://doi.org/10.1016/j.ejpe.2016.05.003

Morra, G., & Yuen, D. A. (2008). Role of Korteweg stresses in geodynamics. *Geophysical Research Letters*, *35*(7). https://doi.org/10.1029/2007GL032860

Mutailipu, M., Liu, Y., Jiang, L., & Zhang, Y. (2018a). Measurement and estimation of CO2–brine interfacial tension and rock wettability under CO2 sub- and super-critical conditions. *Journal of Colloid and Interface Science*, *534*, 605–617. https://doi.org/10.1016/j.jcis.2018.09.031

Mutailipu, M., Liu, Y., Jiang, L., & Zhang, Y. (2018b). Measurement and estimation of CO2–brine interfacial tension and rock wettability under CO2 sub- and super-critical conditions. *Journal of Colloid and Interface Science*. https://doi.org/10.1016/j.jcis.2018.09.031

Narinesingh, J., & Alexander, D. (2014). CO2 Enhanced gas recovery and geologic sequestration in condensate reservoir: A simulation study of the effects of injection pressure on condensate recovery from reservoir and CO2 storage efficiency. *Energy Procedia*, *63*, 3107–3115. https://doi.org/10.1016/j.egypro.2014.11.334

Narinesingh, J., & Alexander, D. (2016). Injection Well Placement Analysis for Optimizing CO 2 Enhanced Gas Recovery Coupled With Sequestration in Condensate Reservoirs.

Newberg, M. ., & Foh, S. . (1988). Measurement of Longitudinal Dispersion Coefficients for Gas Flowing Through Porous Media. *SPE*, 5–9.

Nogueira, M., & Mamora, D. D. (2005). Effect of Flue-Gas Impurities on the Process of Injection and Storage of CO2 in Depleted Gas Reservoirs. *Journal of Energy Resources Technology*, *130*(1), 013301. https://doi.org/10.1115/1.2825174

Oldenburg, C. M. (2003). Carbon Sequestration in natural Gas Reservoirs: Enhanced Gas Recovery and natural Gas Storage. *TOUGH Symposium 2003*, 1–8.

Oldenburg, C M, Benson, K., & M, P. S. (n.d.). Process Modeling of CO2 Injection into Natural Gas Reservoir for Carbon Sequestration and Enhanced Gas Recovery. *Energy*, 726–730.

Oldenburg, Curtis M., & Benson, S. M. (2002). CO2 Injection for Enhanced Gas Production and Carbon Sequestration. *SPE International Petroleum Conference and Exhibition in Mexico*. https://doi.org/10.2118/74367-MS

Olson, E. (2011). Particle Shape Factors and Their Use in Image Analysis-Part 1: Theory. *Journal of GXP Compliance*, *15*(3), 85–96. Retrieved from http://www.ivtnetwork.com/sites/default/files/ImageAnalysis_01.pdf

Partovi, M., Mosalanezhad, M., Lotfi, S., Barati-Harooni, A., Najafi-Marghmaleki, A., & Mohammadi, A. H. (2017). On the estimation of CO2-brine interfacial tension. *Journal of Molecular Liquids*, *243*, 265–272. https://doi.org/10.1016/j.molliq.2017.08.027

Patel, M. J., May, E. F., & Johns, M. L. (2016). High-fidelity reservoir simulations of enhanced gas recovery with supercritical CO2. *Energy*, *IN PRESS*, 548–559. https://doi.org/10.1016/j.energy.2016.04.120

Pereira, Lu??s M C, Chapoy, A., Burgass, R., Oliveira, M. B., Coutinho, J. A. P., & Tohidi, B. (2016). Study of the impact of high temperatures and pressures on the equilibrium densities and interfacial tension of the carbon dioxide/water system. *Journal of Chemical Thermodynamics*, *93*, 404–415. https://doi.org/10.1016/j.jct.2015.05.005

Pereira, Luís M.C., Chapoy, A., Burgass, R., & Tohidi, B. (2017). Interfacial tension of CO2+ brine systems: Experiments and predictive modelling. *Advances in Water Resources*, *103*, 64–75. https://doi.org/10.1016/j.advwatres.2017.02.015

Perkins, T. ., & Johnston, O. . (1963). A Review of Diffusion and Dispersion in Porous Media. *Society of Petroleum Engineers Journal*, *3*(01), 70–84. https://doi.org/10.2118/480-PA

Pooladi-Darvish, M., Hong, H., Theys, S., Stocker, R., Bachu, S., & Dashtgard, S. (2008). CO2 injection for enhanced gas recovery and geological storage of CO2 in the Long Coulee Glauconite F Pool, Alberta. *Proceedings - SPE Annual Technical Conference and Exhibition*, *4*, 2271–2281. https://doi.org/10.2118/115789-MS

Rashid, S., Harimi, B., & Hamidpour, E. (2017). Prediction of CO2-Brine interfacial tension using a rigorous approach. *Journal of Natural Gas Science and Engineering*, *45*, 108–117. https://doi.org/10.1016/j.jngse.2017.05.002

Ren, Q. Y., Chen, G. J., Yan, W., & Guo, T. M. (2000). Interfacial tension of (CO2 + CH4) + water from 298 K to 373 K and pressures up to 30 MPa. *Journal of Chemical and Engineering Data*, *45*(4), 610–612. https://doi.org/10.1021/je990301s

Riaz, A., & Cinar, Y. (2014). Carbon dioxide sequestration in saline formations: Part I-Review of the modeling of solubility trapping. *Journal of Petroleum Science and Engineering*, *124*, 367–380. https://doi.org/10.1016/j.petrol.2014.07.024

Riis, F., & Halland, E. (2014). CO2 storage atlas of the Norwegian Continental shelf: Methods used to evaluate capacity and maturity of the CO2 storage potential. *Energy Procedia*, *63*(1876), 5258–5265. https://doi.org/10.1016/j.egypro.2014.11.557

Rochelle, C. a., & Moore, Y. a. (2002). *The solubility of supercritical CO2 into pure water and synthetic Utsira porewater. Indman.Sintef.No*. Retrieved from http://www.indman.sintef.no/project/IK23430000 SACS/other_reports/BGS_WA3_CO2_ solubility_expts.pdf

Sanguinito, S., Goodman, A. L., & Sams, J. I. (2018). CO2-SCREEN tool: Application to the oriskany sandstone to estimate prospective CO2storage resource. *International Journal of Greenhouse Gas Control*, *75*(June), 180–188. https://doi.org/10.1016/j.ijggc.2018.05.022

Schulze-Makuch, D. (2005). Longitudinal dispersivity data and implications for scaling behavior. *Ground Water*, *43*(3), 443–456. https://doi.org/10.1111/j.1745-6584.2005.0051.x

Shabani, B., & Vilcáez, J. (2017). Prediction of CO2-CH4-H2S-N2gas mixtures solubility in brine using a non-iterative fugacity-activity model relevant to CO2-MEOR. *Journal of Petroleum Science and Engineering*, *150*(December 2016), 162–179. https://doi.org/10.1016/j.petrol.2016.12.012

Shtepani, E. (2006). CO2 sequestration in depleted gas/condensate reservoirs. *Proceedings - SPE Annual Technical Conference and Exhibition*.

Sidiq, H., & Amin, R. (2009). Mathematical model for calculating the dispersion coefficient of super critical CO2 from the results of laboratory experiments on enhanced gas recovery. *Journal of Natural Gas Science and Engineering*, *1*(6), 177–182. https://doi.org/10.1016/j.jngse.2009.11.001

Sidiq, H., Amin, R., der Steen, E. Van, & Kennaird, T. (2011a). Super critical CO2-methane relative permeability investigation. *Journal of Petroleum Science and Engineering*, *78*(3–4), 654–663. https://doi.org/10.1016/j.petrol.2011.08.018

Sidiq, H., Amin, R., der Steen, E. Van, & Kennaird, T. (2011b). Super critical CO2-methane relative permeability investigation. *Journal of Petroleum Science and Engineering*, *78*(3–4), 654–663. https://doi.org/10.1016/j.petrol.2011.08.018

Sidiq, H. H., & Amin, R. (2010). SPE 137884 Supercritical CO2 / Methane Relative Permeability Investigation, (November), 10–12.

Sim, S. S. K., Brunelle, P., Canada, Q., Systems, F., Turta, A. T., & Singhal, A. K. (2008). SPE 113468 Enhanced Gas Recovery and CO 2 Sequestration by Injection of Exhaust Gases from Combustion of Bitumen. *Changes*, (1), 1–10.

Sim, S., Turta, A. T., Singhal, A., & Hawkins, B. F. (2009a). Enhanced Gas Recovery: Effect of Reservoir Heterogeneity on Gas-Gas Displacement. *Candian International Petroleum Conference*, (June), 1–14. https://doi.org/10.2118/2009-023

Sim, S., Turta, A. T., Singhal, A. K., & Hawkins, B. F. (2009b). Enhanced gas recovery: Factors affecting gas-gas displacement efficiency. *Journal of Canadian Petroleum Technology*, *48*(8), 49–55. https://doi.org/10.2118/09-08-49

Sminchak, J. R., Babarinde, O., & Gupta, N. (2017). Integrated Analysis of Geomechanical Factors for Geologic CO2Storage in the Midwestern United States. *Energy Procedia*, *114*(November 2016), 3267–3272. https://doi.org/10.1016/j.egypro.2017.03.1458

Stukan, M., Abdallah, W., & East, S. M. (2012). Interfacial Tension (IFT) and Surface Alteration Interplay. *Spe*, (November), 11–14. https://doi.org/10.2118/161279-ms

Sun, Q., Tian, H., Li, Z., Guo, X., Liu, A., & Yang, L. (2016). Solubility of CO2 in water and NaCl solution in equilibrium with hydrate. Part I: Experimental measurement. *Fluid Phase Equilibria*, *409*, 131–135. https://doi.org/10.1016/j.fluid.2015.09.033

Tensiometer, S., Pojman, J. a, Whitmore, C., Liria, M., Liveri, T., Lombardo, R., … Zoltowski, B. (2006). Evidence for the Existence of an Effective Interfacial Tension between Miscible Fluids : Isobutyric Acid-Water and 1-Butanol-Water in a. *Society*, (3), 2569–2577. https://doi.org/10.1021/la052111n

Thusyanthan, N. I., & Madabushi, S. P. G. (2003). Scaling of Seepage Flow Velocity in Centrifuge Models. *Engineering*, *326*(March).

Turta, A. T., Sim, S. S. K., Singhal, A. K., & Hawkins, B. F. (2007). Basic Investigations on

Enhanced Gas Recovery by Gas-Gas Displacement.

Valle, L. M., Rodríguez, R., Grima, C., & Martínez, C. (2018). Effects of supercritical CO2 injection on sandstone wettability and capillary trapping. *International Journal of Greenhouse Gas Control*, *78*(September), 341–348. https://doi.org/10.1016/j.ijggc.2018.09.005

Vanderburgt, M., Cantle, J., & Boutkan, V. (1992). Carbon dioxide disposal from coal-based IGCC's in depleted gas fields. *Energy Conversion and Management*, *33*(5–8), 603–610. https://doi.org/10.1016/0196-8904(92)90062-2

Werth, S., Lishchuk, S., Horsch, M., & Hasse, H. (2013). Interfacial Tension.

Yadali Jamaloei, B., Asghari, K., & Kharrat, R. (2011). Pore-scale flow characterization of low-interfacial tension flow through mixed-wet porous media with different pore geometries. *Experimental Thermal and Fluid Science*, *35*(1), 253–264. https://doi.org/10.1016/j.expthermflusci.2010.09.009

Yahaya, A. A., Akpan, E. U., Enyi, G. C., Nasr, G. G., & Abbas, J. (2018). Experimental investigation of methane-water and methane-brine IFT measurements using pendant drop (rising bubble) method Journal of Engineering Technology. *Journal of Engineering Technology*, *6*(1), 394–407.

Yan, W., Huang, S., & Stenby, E. H. (2011). Measurement and modeling of CO2 solubility in NaCl brine and CO2-saturated NaCl brine density. *International Journal of Greenhouse Gas Control*, *5*(6), 1460–1477. https://doi.org/10.1016/j.ijggc.2011.08.004

Yasuda, K., Mori, Y. H., & Ohmura, R. (2015). Interfacial tension measurements in water-methane system at temperatures from 278.15 K to 298.15 K and pressures up to 10 MPa. *Fluid Phase Equilibria*, *413*, 170–175. https://doi.org/10.1016/j.fluid.2015.10.006

Yu, D., Jackson, K., & Harmon, T. C. (1999). Dispersion and diffusion in porous media under supercritical conditions. *Chemical Engineering Science*, *54*(3), 357–367. https://doi.org/10.1016/S0009-2509(98)00271-1

Zatsepina, O. Y., & Pooladi-Darvish, M. (2012). Storage of CO2 as hydrate in depleted gas reservoirs. *SPE Reservoir Evaluation & Engineering*, *15*(1), 98–108. https://doi.org/10.2118/137313-pa

Zhang, D., & Song, J. (2013). Mechanisms for geological carbon sequestration. *Procedia IUTAM*, *10*, 319–327. https://doi.org/10.1016/j.piutam.2014.01.027

Zhang, L., Li, X., Ren, B., Cui, G., Zhang, Y., Ren, S., … Zhang, H. (2016). CO2 storage potential and trapping mechanisms in the H-59 block of Jilin oilfield China. *International Journal of Greenhouse Gas Control*, *49*, 267–280. https://doi.org/10.1016/j.ijggc.2016.03.013

Zhang, X., Yang, S., Li, G., Li, W., & Chen, H. (2011). Compressibility factor of gas with high content of CO 2 in Changshen gas reservoir. *Proceedings - 2011 International Conference on Computational and Information Sciences, ICCIS 2011*, 542–545. https://doi.org/10.1109/ICCIS.2011.111

Zhang, Yi, Liu, S., Song, Y., Zhao, J., Tang, L., Xing, W., … Zhan, Y. (2014). Experimental investigation of CO2-CH4 displacement and dispersion in sand pack for enhanced gas recovery. *Energy Procedia*, *61*, 393–397. https://doi.org/10.1016/j.egypro.2014.11.1133

Zhang, Yuan, Lashgari, H. R., Sepehrnoori, K., & Di, Y. (2017). Effect of capillary pressure and salinity on CO2 solubility in brine aquifers. *International Journal of Greenhouse Gas Control*, *57*, 26–33. https://doi.org/10.1016/j.ijggc.2016.12.012

Ziabakhsh-Ganji, Z., & Kooi, H. (2012). An Equation of State for thermodynamic equilibrium of gas mixtures and brines to allow simulation of the effects of impurities in subsurface CO2 storage. *International Journal of Greenhouse Gas Control*, 2007–2008. https://doi.org/10.1016/j.bjps.2007.11.077

APPENDICES

Appendix A: Journals and Conferences
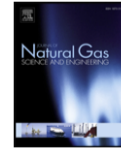
Experimental investigation on the impact of connate water salinity on dispersion coefficient in consolidated rocks cores during Enhanced Gas Recovery by CO_2 injection

Muhammad Kabir Abba[a,*], Athari Al-Othaibi[a], Abubakar Jibrin Abbas[a], Ghasem Ghavami Nasr[a], Abdulkadir Mukhtar[b]

[a] *Department of Petroleum and Gas Engineering, University of Salford Manchester, M4 5WT, United Kingdom*
[b] *Department of Chemical Engineering, Federal University of Technology, PMB 65, Minna, Nigeria*

ABSTRACT

Connate water salinity is a vital property of the reservoir and its influence on the displacement efficiency cannot be overemphasised. Despite the numerous analytical literature on the dispersion behaviour of CO_2 in CH_4 at different parametric conditions, studies have so far been limited to systematic effects of the process while parameters such as connate water salinity of the reservoir has not been given much attention and this could redefine the CO_2-CH_4 interactions in the reservoir. This study aims to experimentally determine the effect of connate water salinity on the dispersion coefficient in consolidated porous media under reservoir conditions. A laboratory core flooding experiment depicting the detailed process of the CO_2-CH_4 displacement using Grey Berea sandstone core sample at a temperature of 50 °C and at a pressure of 1300 psig was carried out to determine the optimum injection rate, from 0.2 to 0.5 ml/min, for the experimentation based on dispersion coefficients and methane recovery in the horizontal orientation. This was established to be 0.3 ml/min. At the same conditions, the effects of connate water saturation of 10% and a salinity of 0 (distilled water), 5, and 10% wt. with a CO_2 injection rate of 0.3 ml/min on the dispersion coefficients was investigated. The results from the core flooding process indicated that the dispersion coefficient decreases with increasing salinity, hence the higher the density of the immobile phase (connate water) the lower the dispersion of CO_2 into CH_4. This is a significant finding given that the inclusion of the connate water and its salinity have an effect on the mixing of the gases in the core sample and should be given importance and included during simulation studies for field scale applications of Enhanced Gas Recovery (EGR). This is the first experimental investigation into the relationship between the connate water salinity and the dispersion coefficient in consolidated porous media.

1. Introduction

As natural gas continues to gain widespread usage as a source of cleaner and efficient fossil fuel, and greenhouse gas emission is attracting environmental consequences, the need for a viable method to enhance and curtail these phenomena, respectively, is paramount (Al-abri et al., 2009; Al-Abri et al., 2012; Al-Abri, 2011; Benson et al., 2005; Benson and Cole, 2008; Oldenburg and Benson, 2002). The technique of injecting CO_2 into deep saline aquifers and oil and gas reservoirs have the potential for alternative methods for reducing CO_2 emissions (Vilcáez, 2015). Studies (Allen et al., 2017; Bennaceur, 2013; Riis and Halland, 2014; Sanguinito et al., 2018; Sminchak et al., 2017) have shown that deep saline aquifers have the advantage of more storage capacity as a result of different storage mechanisms over oil and gas reservoirs. However, incentives in the form of additional hydrocarbon resources (through Enhanced Oil/Gas Recovery techniques) come from using oil and gas reservoirs as storage sites which will, invariably, offset some of the cost of the sequestration process (Kalra and Wu, 2014). Thus, Enhanced Gas Recovery (EGR) is deemed one of the potential methods for simultaneously storing anthropogenic CO_2 emissions and improving additional natural gas recovery from depleted gas fields, provided that the gas miscibility in situ (mixing) can be reduced. This can be achieved by a better understanding of the mechanisms of displacement and the factors that affect them which will provide vital information for further studies aimed at a wider and robust field scale application and establish the economic viability of the process.

The adoption of EGR technique has not been generally well received. This is because of the excessive mixing of the injected carbon dioxide and in-situ natural gas during the flooding process (Al-abri et al., 2009; Honari et al., 2016, 2015; 2013; Hughes et al., 2012; Khan et al., 2013; Oldenburg and Benson, 2002; Shtepani, 2006; Sidiq et al., 2011a; Sim et al., 2008; Zhang et al., 2014). This mixing contaminates the recovered natural gas and reduces its market value by reducing its calorific value and also, incurs additional cost in the sweetening processes (Oldenburg and Benson, 2002; Sim et al. 2008, 2009). This necessitated an in-depth study to unearth ways to minimise this undesirable mixing phenomenon as these two gases are miscible in all ramifications. Mixing can only be minimised if the mechanics and dynamics of the process are understood. To do this, the interplay between different factors that influence the mixing of the injected CO_2 and the nascent CH_4 have to be investigated which will showcase the economic viability of the EGR technology. These factors stem from variations of the physical properties of the fluids, containing reservoir formations and operation conditions such as pressure, temperature, and flowrates.

Many authors (Al-abri et al., 2009; Honari et al., 2016, 2015; 2013; Hughes et al., 2012; Sidiq et al., 2011b; Sidiq and Amin, 2009) have carried out extensive researches on the sensitivity of factors, such as reservoir heterogeneity, pressure, temperature, injection rates, on the mixing between CO_2 and CH_4 to ascertain the influence of these investigated parameters on the gas-gas mixing during EGR. However, limited technical literature are available on the impact of connate water saturation and salinity on CO_2-CH_4 system displacements (Sidiq and Amin, 2009). were the only authors prior to (Honari et al., 2016) to consider connate water saturation when determining the dispersion coefficient of CO_2 in CH_4 in a carbon dioxide-methane systems (Sidiq and Amin, 2009). determined the dispersion coefficient using a new model developed in their work and validated it with experimental data. However, the study was limited to the analysis of the experimental dispersion coefficients to validate the developed model and no comparative analysis was presented between saturated and dry core samples to ascertain the effects of connate water saturation on the displacement process.

A number of literature, as reported by Honari et al. (2016), are available which considered the dispersion in a binary system comprising of different gaseous components (N_2, O_2, H_2O) in the presence of immobile water. In this work, focus is on the experimental investigations in CO_2-CH_4 systems alone. Albeit not exclusively in a CO_2-CH_4 systems, Turta et al. (2007) conducted a series gas-gas displacement tests on Berea cores at a temperature of 70 °C and a pressure of 6.2 MPa using Nitrogen and CO_2 as injection fluids. The tests were conducted both in the presence of connate water and without connate water (dry cores) to investigate the effects of connate water on the recovery efficiency. The tests on consolidated cores showed that for pure nitrogen and pure CO_2, used as the displacing fluids, the recovery was comparable. In the case where a mixture of CO_2 and nitrogen were used to displace the natural gas, it was observed that there were delays in CO_2 breakthrough, associated with a period when only a mixture of methane and nitrogen was produced. This can be attributed to the solubility of CO_2 in connate water which is considerably higher than that of nitrogen. This invariably leads to a higher gas recovery due to a longer resident period, given the fact that a 20% nitrogen contamination in marketable CH_4 tolerable in the produced stream, as opposed to only 2% contamination level for the case of CO_2. They concluded that when using CO_2 as a displacing fluid, recovery was higher in the presence of connate water saturation than in its absence invariably due to the dissolution of CO_2 in the formation brine.

The first ever experimental measurement of dispersion as function of water saturation for supercritical gases in a CH_4-CO_2 system was carried out by Honari et al. (2016). They systematically measured fluid dispersion in various rock cores (sandstones and carbonates), both dry and at irreducible water saturations, at reservoir conditions. They found out that irreducible water increases dispersivity by a factor of up to 7.3.

Irreducible water occupied smaller pores creating narrower pores and more tortuous flow paths giving rise to more dispersion/mixing between the injected CO_2 and the in-situ CH_4. Sim et al. (2009a,b) however, inferred that the presence of irreducible water in the reservoir tends to minimise its heterogeneity and as such minimises excessive mixing as shown in their work where they used a sand pack with various degrees of permeability distributions and also a N_2, CH_4, CO_2 binary systems.

These studies, however limited, have touched on the impact of connate water saturation on the displacement efficiency in EGR by CO_2 injection. They have attributed higher dispersion coefficients to the presence of connate water. Conversely, the effect of the salinity/concentration variation of the connate water on the recovery efficiency and or dispersion coefficient was not accounted for. In this paper, the effect of connate water salinity on the dispersion coefficient was investigated experimentally in a consolidated sandstone core sample during CH_4 displacement by supercritical CO_2. Investigating this salinity phenomenon will help reservoir engineers better characterise gas systems for better representation in the adoption of EGR by CO_2 and subsequent sequestration in natural gas reservoirs.

1.1. Theory and concept of enhanced gas recovery

Dispersion is the irreversible mixing that occurs during miscible displacements (Adepoju et al., 2013), it occurs as a result of two simultaneous mechanisms; molecular diffusion and mechanical dispersion (advection) (Perkins and Johnston, 1963). When a miscible fluid displaces another miscible fluid in a porous medium, the displaced fluid tends to mix with the displacing fluid. The efficiency of local displacement in miscible flooding is grossly affected by the mixing taking place within the rock matrix. This mixing is a result of the interaction between these two fluids in contact. A transition or mixing zone develops at the displacement front where the concentration of the displacing fluid decreases from one to zero (Fig. 1). It has been reported (Ekwere, 2007) that several experiments show that the mixing zone propagates longitudinally as displacement process progresses. The macroscopic mixing (dispersion) observed through porous media is used to quantify the mixing taking place (Jha et al., 2013). This can be, to an extent, analysed using empirical evaluation and laboratory experimentation as the concentration of injected CO_2 relative to the in-situ CH_4 in the produced effluent stream.

In order to minimise the cost of producing the recovered natural gas and maximise potential return during enhanced gas recovery, the degree to which injected CO_2 gas mixes with natural gas in situ needs to be well evaluated. Mixing has been found to be controlled by several factors including molecular diffusion/dispersion, pore geometry, turbulence, stagnant fraction of pore space, presence of an immobile fluid, viscous fingering, adsorption/desorption, and gravity segregation (Newberg and Foh, 1988). The viscosity ratio (Eq. (1)) is favourable in the case of supercritical CO_2 displacing CH_4 because CO_2 is more
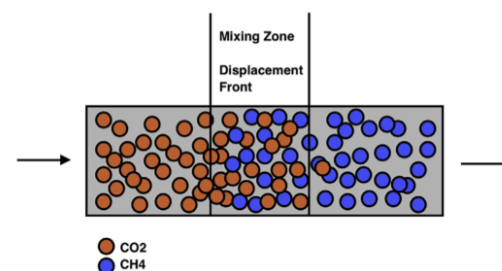
Fig. 1. Schematics of displacement front during CO2 injection displacing CH4.

viscous than CH_4 under reservoir conditions:

$$\frac{\mu CH_4}{\mu CO_2} < 1 \tag{1}$$

Gas transport in porous media occurs widely in numerous applications which include carbons sequestration, oil and gas exploitation, food processing industry etc. The importance of understanding the mechanisms of gas transport in porous media lies in allowing a number of models employed to optimise and evaluate the design and performance of the processes aforementioned.

1.2. Application of gas transport in porous medium in EGR

(Perkins and Johnston, 1963) defined the mixing phenomenon occurring in porous media as a diffusion-like process due to concentration and velocity gradient. The dispersion coefficient denotes the rate of mixing when two miscible fluids come in contact at the displacement front of a flooding process. It depends on the direction of the dispersion flux with respect to the main convective flux. The smallest value of this term occurs perpendicular to the main convective path/flux often called transverse dispersion, and the largest occurs for dispersion in the main convective flux called longitudinal dispersion. Transverse dispersion coefficient, K_t is more difficult to obtain experimentally and as result, very few data is available in literature besides those of (Perkins and Johnston, 1963).

Newberg and Foh (1988) used a single parameter diffusion-type equation based on the Advection-Dispersion equation (Coats et al., 2009, 1964; Perkins and Johnston, 1963) which was often used to describe the gas transport in porous media to correlate the numerical dispersivities with experimental results and the model is as shown in (Eq. (2)):

$$K_l \frac{\partial^2 C}{\partial x^2} - u \frac{\partial C}{\partial x} = \frac{\partial C}{\partial t} \tag{2}$$

Where, C is the CO_2 concentration at location x at time t, K_L is the coefficient of longitudinal dispersion, and u is the interstitial velocity.

This model was used to generate longitudinal dispersion coefficients and "scale of dispersion" (dispersion coefficient divided by velocity). It also describes the dispersion occurring during the displacement process in EGR.

Invariably (Eq. (2)), may be written in dimensionless form as follows (Mamora and Seo, 2002);

$$\frac{1}{P_e} \frac{\partial^2 C}{\partial x_D^2} - \frac{\partial C}{\partial x_D} = \frac{\partial C}{\partial t_D} \tag{3}$$

Where;

Parameter	Symbol	Expression
Peclet number	P_e	$\frac{uL}{K_l}$
Dimensionless time	t_D	$\frac{tu}{L}$
Dimensionless distance	x_D	$\frac{x}{L}$
Interstitial velociy	u	$\frac{Q}{\pi r^2 \phi}$

L is length of core.
Q is superficial velocity,.
ϕ is porosity.
K_l Longitudinal dispersion .

Since the carbon dioxide injection inlet is at $x = 0$,

then initial condition: $C = 0$ at $t_D = 0$,
boundary conditions: $C = 1$ at $x_D = 0$, $C \rightarrow 0$ as $x_D \rightarrow \infty$

The solution to (Eq. (3)) maybe shown as follows:

$$C = \frac{1}{2}\left\{ erfc\left(\frac{x_D - t_D}{2\sqrt{t_D/P_e}}\right) + e^{P_e x_D} erfc\left(\frac{x_D + t_D}{2\sqrt{t_D/P_e}}\right)\right\} \tag{4}$$

CO_2 concentrations profiles from EGR core flooding experimentation can be compared against those based on analytic solutions of (Eq. (3)) presented in (Eq. (4)) for several values of *Péclet* number, P_e (which is the ratio of advection to dispersion over the experimental length L) from which the corresponding dispersion coefficient can be evaluated.

(Perkins and Johnston, 1963) presented another definition of *Péclet* number termed medium *Péclet* number denoted by, P_{em}, which describes the dominant displacement regime during a dispersion process and expressed in (Eq. (5)) as:

$$P_{em} = \frac{u_m d}{D} \tag{5}$$

Where P_{em} is medium Péclet number, u_m is the mean interstitial velocity (m/s), D is the diffusion coefficient (m²/s), and d is the characteristic length scale of the porous medium. Generally, at $P_{em} < 0.1$, diffusion dominates the dispersion process and the ratio, is constant and equates to and conversely, at $P_{em} > 10$ advective mixing dominates the dispersion process and the ratio linearly proportional to P_{em}. And in this range of P_{em}, (Coats et al., 2009) correlated dispersion coefficient with diffusion shown in (Eq. (6)):

$$\frac{K_l}{D} = \frac{1}{\tau} + \alpha \frac{u_m^n}{D} \tag{6}$$

Where α is in m and is the dispersivity of the porous medium, n is an exponent. Which is and τ can range from for packed beds and can be as large as 13 for consolidated media as reported by (Honari et al., 2013) and literature therein. The parameter τ can be obtained empirically through several methods, but α and n can only be determined experimentally through core flooding (Hughes et al., 2012).

Furthermore, Takahashi and Iwasaki 1970, as reported by (Hughes et al., 2012) and (Liu et al., 2015), established a correlation between the molecular diffusion coefficient, temperature and pressure. This correlation was used by the authors to obtain accurate diffusivity using (Eq. (7)) at conditions relevant to enhanced gas recovery by CO_2 injection. The correlation is as follows:

$$D = \frac{(-4.3844 \times 10^{-13} p + 8.55440 \times 10^{-11}) T^{1.75}}{p} \tag{7}$$

where D (m²/s) is the molecular diffusion coefficient of CO_2 in CH_4 at temperature T (K) and pressure p (MPa). In the works of Takahashi and Iwasaki, the diffusion coefficients of CO_2 in CH_4 were measured at 298–348K and pressures of 5–15 MPa in a porous bronze plug which are well within the range of conditions applicable to EGR.

2. Experimental methodology

2.1. Materials used

Pure methane with a purity of 99.995% and research grade carbon dioxide with a purity of 99.999% were supplied by BOC UK a member of the Linde Group. The core sample was obtained from Kocurek Industries USA. The salts employed in this research were supplied by Fisher Scientific UK. The petrophysical properties of the core sample used are shown in Table 1. The porosity was evaluated experimentally using Helium Porosimetry technique.

2.2. Apparatus and procedure

2.2.1. Helium porosimetry

This method facilitates the determination of the grain volume of a core sample which is volume of the rock grains or solids alone. The pore

Table 1
Petrophysical properties of the core sample.

Core sample	Length (mm)	Diameter (mm)	Porosimetry Porosity (%)	Permeability (mD)
Grey Berea	76.27	25.22	20	217

volume was then determined from the difference between the grain volume obtained by this method and the bulk volume which is defined as the volume the sample occupies. The Bulk Volume is determined empirically and analytically by measuring the dimension of the core samples using a high accuracy Vernier caliper and using the cylinder volume determination formulation.

$$Pore\ Volume = Bulk\ Volume - Grain\ Volume \qquad (8)$$

Where, $Bulk\ Volume = \frac{\pi d^2}{4} \times L$, and d is the core diameter, and L is core length.

2.2.1.1. Procedure. The Helium gas supply was connected to the gas inlet port of the instrument and was set to 120 psig on the Helium gas bottle regulator. After a leak test, the system grain volume calibration was performed on the Porosimeter (Fig. 2). The matrix cup with reference discs was then connected to the instrument. The sample grain volume measurement was performed, and the obtained results were recorded in the provided application written in excel spreadsheet which evaluated the grain volume of each sample.

2.2.2. Core flooding equipment description

The core flooding equipment used is a branded system by CoreLab Oklahoma, USA. The equipment was modified to carryout gas-gas displacement processes by integrating an Agilent Gas Chromatograph 7890A for effluent analysis depicted in Fig. 3. The core flooding system was rated to 5000 psig confining pressure, 3500 psig pore pressure at room temperature. The inlet pressure into the core sample and outlet pressures on the other side of each core are measured with gauge pressure transducers. An integral part of the system is the SmartFlood software and computer data-acquisition-and-control system hardware which provides on-screen display of all measured values (pressures, temperatures, volumes etc.), automatic logging of test data to a computer data file. The core sample is held within a rubber sleeve inside a Hassler-type core holder by radial confining pressure, which simulates reservoir overburden pressures. The simulated pore pressure was applied through a ISCO model 500D, two-barrel metering pump system with a flow rate range adjustable from 0 to 200 ml/min and a maximum pressure rating of 4000 psig. The overburden (confining) pressure
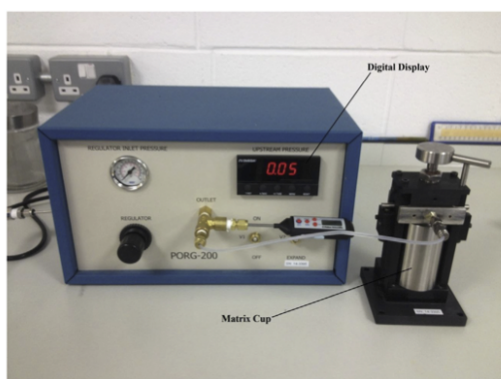
Fig. 2. PORG-200 porosimeter.

pump is a hydraulic pump Model S-216-JN-150 pump, with pressure output of up to 10,000 psig and will provide the desired overburden in the system. The back pressure is regulated with CoreLab dome-loaded type back-pressure regulator which controls the back pressure to a reference pressure supplied to its dome. It is rated for a maximum working pressure of 5000 psig. Floating-piston accumulators are provided as part of the system and are rated for 5000 psig pressure and 350 °F (177 °C) temperature. The accumulators provide for injecting fluids without allowing the fluid to come in contact with the metering pump. 2.5-inch-dial pressure gauges are used to monitor the Overburden Pressure and the BPR Dome Pressure. The pressure range on these gauges is 15,000-psig full scale. Rosemount transducer provided with the system measure differential pressure across the core holder. The effluent flowrate and produced volume was measured by *Bronkhorst* mass flow controllers/meters and records the effluent rates on the logging worksheet of the SmartFlood software. The picture and schematic of the equipment are presented in Figs. 3 and 4.

2.2.2.1. Procedure

2.2.2.1.1. Salt preparation and core sample saturation. The NaCl salt was measured and dissolved in distilled water contained in a round bottom flask with a magnetic stirrer to prepare the desired brine concentrations of 5 and 10 wt%. The core sample was saturated with 10% of its pore volume (determined from Helium porosimetry) with the brine of the concentrations as aforementioned using a vacuum technique. Initial dry runs were first carried out to ascertain repeatability of the set up and method. Then wet runs were performed subsequently, first using distilled water to establish a datum for the salinity variation experiments and then using the prepared concentrations of brine.

2.2.2.1.2. Core flooding. The core sample was wrapped in foil paper to avoid the permeation of the supercritical gases through the sleeve and into the annulus of the core holder. A layer of cling film was first placed between the core sample and the foil paper to prevent the foil paper from sticking to the core sample when subjected to high temperatures and pressures. The core sample was then placed inside the *Viton* sleeve and installed on the distribution plugs of the core holder and secured with clamps on both sides and inserted into the core holder. A heat jacket was placed around the core holder and the temperature ramping was set and the hydraulic pump was initiated to pump the hydraulic oil into the annulus of the core holder to provide the overburden pressure necessary for the experiment in lieu of the simulated reservoir depth pressure. A pressure of 2200 psig was set as the overburden pressure. The simultaneous hydraulic oil pumping and heating was done to avoid high temperature ramping with uncontrolled pressure rise. When the core holder temperature reached 50 °C, the temperature ramping was stopped, and the temperature was kept constant. Hydraulic oil leaks were checked for on both sides of the core holder to ensure that the clamping of the core sample and set up integrities were not compromised.

As a safety precaution, all the valves were shut off. V1 was opened to provide access to the accumulator. D1, depicted in the schematics in Fig. 4, was opened to purge pumps A and B to give room for filling the accumulator A, ACC-A, with the CH_4 gas from the bottle. When there was no increment in the level of the distilled water in the reservoir, D1 was shut off and then V1 was shut off too. The back pressure reference pressure was set to 1300 psig using the N_2 gas bottle. The N_2 gas was used to set the dome pressure of the back pressure regulator as opposed to the hydraulic oil because of the compressibility of the gas which provided a smoother flow of the gas and avoided pressure build-up within the core flooding and the reference pressure was kept constant. V2 was then opened to saturate the system with CH_4. Pumps A&B were engaged to compress the gas in the system to provide the desired system pressure. V2 was then shut off.

The same filling procedure was carried out with accumulator B, ACC-B. V4 was then opened and then the logging commenced and also

208

Fig. 3. A perspective depiction of the core flooding setup and the gas chromatogragh.
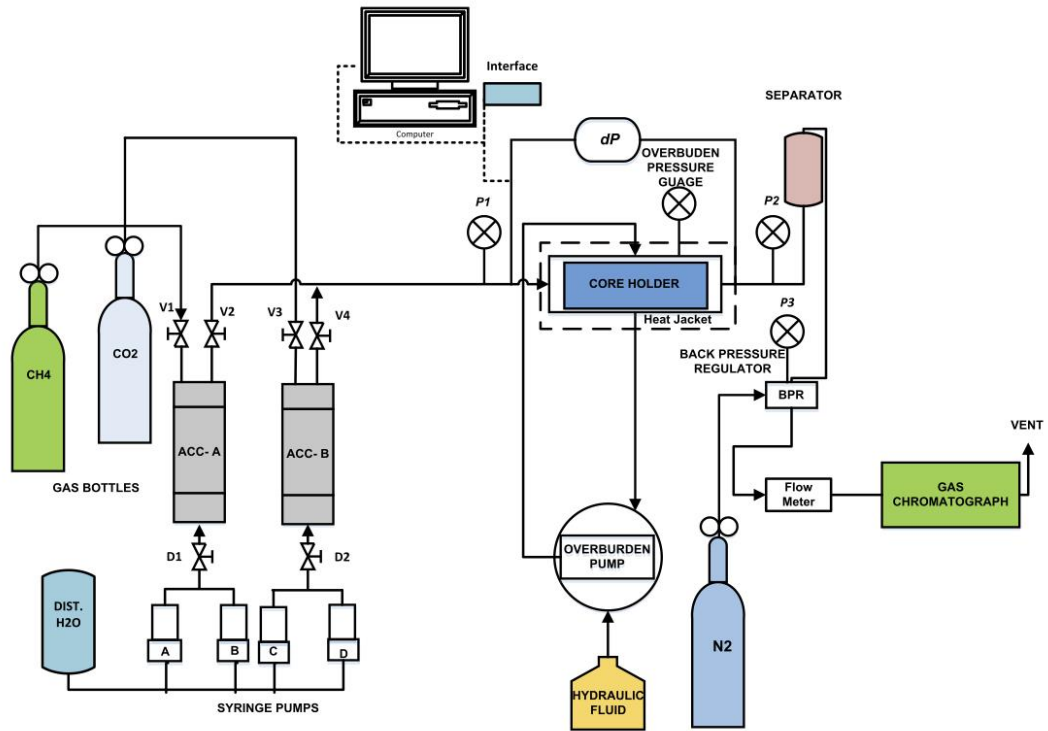
Fig. 4. Schematics of core flooding set up.

209

the GC sequence as run. The items logged were differential pressure, dP, production rate, each time stamp was recorded which corresponded with the injection times of the GC, whose method sequentially runs for five (5) minutes to sample the effluent every 5 min. The flowrate was measured with the flow meters. The overburden pressure was carefully monitored and was kept more than 500 psig above the pore pressures to avoid the rupturing of the vitton sleeve, given that the pumps deliver a constant flowrate and the pressures rapidly build to maintain the desired flowrate.

Each experimental run came to an end when there were insignificant volumes of CH_4 in the effluent analysis from the GC.

3. Results and discussion

3.1. Optimum injection rate determination

In order to carry out the investigation on the salinity effects on dispersion coefficient, an optimum injection rate for this case was determined. Here, an experimental screening was carried out based on the dispersion coefficient and the CH_4 recovery efficiency to evaluate the optimum injection rate from a range of experimental values – 0.2–0.5 ml/min adopted from literature (Liu et al., 2015). This is to ascertain the best case to evaluate the effects of the connate water salinity during flooding and to minimise other systematic effects emanating from the variation in interstitial velocity within the pore matrix. This systematics, as shown in literature cited within this work, have their various effects on dispersion coefficient and the rock dispersivity.

3.1.1. Dispersion coefficients and dispersivity

A number of displacement runs were carried out to check for consistency and repeatability of the experimental set-up using the same core sample under dry conditions. The evaluated K_L for the test runs are shown in Table 2. When the results became consistent by adjusting the experimental methodology and set-up, the different flowrates were then employed to determine the optimum injection rate from the range of interest. The concentration profiles were used to evaluate the rate of mixing of the injected CO_2 and the nascent CH_4 using (Eq. (3)) as aforementioned and adopting the longitudinal dispersion coefficient K_L as the fitting parameter. The values of the dispersion coefficients for different injection rates are shown in Table 3. The fitted graph of the different injection rates is shown in Fig. 7. The L was adjusted in the regression to provide a better fit as advised by (Hughes et al., 2012) and (Liu et al., 2015) given that the interstitial velocity was held constant as assumed in the 1D advection dispersion equation (Eq. (2)). Least square regression method was employed in the curve fitting technique. As expected, the higher injection rates showed early breakthrough of the CO_2 which is in agreement with the works of (Liu et al., 2015). This also shows that the higher the injection rate the higher the dispersion coefficient as seen in Fig. 5 which showcases the relationship between the two parameters.

Furthermore, the P_{em} was evaluated using (Eq. (5)), in that the

characteristic length scale of mixing, d, was evaluated by measuring the mean grain diameter of the core sample using a novel experimental method which will be presented in a subsequent paper. This value was found to be 94 μm. This was then used to determine the dominant mechanism of displacement i.e. the value of the *Peclet* number which was 0.018 meaning that diffusion is the dominant displacement mechanism in the experimental run.

The dispersivity was also evaluated using the relation in (Eq. (6)) where the ratio k/D was plotted against the ratio u/D which is a straight, shown in Fig. 6, and the gradient/slope represented the parameter. The value of the dispersivity was 0.0006m which is well within the range obtained by (Hughes et al., 2012) for consolidated porous media.

3.1.2. Optimum CH_4 recovery efficiency

To determine the percentage recovery of the CH_4, the original gas in place OGIP was determined using (Eq. (9)). The porosity obtained from the He porosimetry, the Gas formation volume factor was calculated at the experimental conditions with the compressibility factor, Z, obtained numerically from the models in works of (Shabani and Vilcáez, 2017; Ziabakhsh-Ganji and Kooi, 2012) which provided a better presentation of the parameter.

$$G = \frac{v_b \phi (1 - S_w)}{B_g} \tag{9}$$

The value of the OGIP was then used to calculate the CH_4 percentage recovery using the production rates obtained from the mass flow meters of the core flooding set-up. CH_4 production recovery, expressed as pore volumes produced, was evaluated and plotted as a function of time which as shown in Fig. 8.

Fig. 8 is a representation of the results of the CH_4 production recovery efficiency obtained from the core flooding experiments using different injection rates at the same reservoir conditions. Each run has a characteristic peculiarity and trend. For the experimental run at 0.2 ml/min, the recovery was substantial but the resident time for the displacement was longer and hence a stream of CH_4 laced or contaminated by the CO_2 was recovered. In that, there was substantial mixing between the displaced and displacing gases given the nature of the miscibility between them albeit having lower dispersion coefficient. This is not conceivably an economic derivative as more CH_4 will be produced which will be grossly contaminated by the injected CO_2 thereby undermining the sequestration idea.

Consequently, the experimental run at 0.3 ml/min showcases a different scenario with the highest recovery trend in all the experimental runs. There was a substantial CH_4 recovery and good sweep efficiency compared to the runs of 0.4 ml/min and 0.5 ml/min which show a very poor trend in terms of CH_4 recovery and sweep efficiency as a result of higher interstitial velocity. High interstitial velocities tend to increase the turbulence of the flow profile and agitate the molecules of the gas species which in turn facilitates the interaction between the displacing and displaced fluids.

With the results from the dispersion coefficient determination and CH_4 recovery efficiency, it is apparent that the best and optimum injection rate for CO_2 for this experiment is the 0.3 ml/min. Thus, this flow rate will be adopted in the main experiment to investigate the effect of connate water salinity on dispersion.

3.2. Connate water salinity investigation

Having determined the optimum CO_2 injection rate, the next step was to investigate the effect of connate water salinity on dispersion coefficient using the obtained injection rate. The connate water saturation was set to 10% to establish an immobile phase at the operating conditions based on the size and pore geometry of the core sample. This was done by saturating the core sample with 10% of its pore volume

Table 2
Dispersion coefficient determination for test runs.

Runs	Q (ml/min)	u (10^{-5} m/s)	Pressure (psig)	Temperature (°C)	K_L (10^{-8} m²/s)
Run 1	0.25	3.45	1300	50	1.989
Run 2	0.25	3.45	1300	50	4.125
Run 3	0.25	3.45	1300	50	8.732
Run 4	0.25	3.45	1300	50	2.681
Run 5	0.25	3.45	1300	50	2.849
Run 6	0.25	3.45	1300	50	2.206
Run 7	0.25	3.45	1300	50	2.848
Run 8	0.25	3.45	1300	50	2.452

210

Table 3
Dispersion coefficient determination for different injection rates.

Q (ml/min)	Pressure (psig)	Temperature (°C)	u (10^{-5} m/s)	K_L (10^{-8} m²/s)	D (10^{-8} m²/s)
0.2	1300	50	3.31	1.41	22.56
0.3	1300	50	5.01	2.69	22.56
0.4	1300	50	6.66	3.01	22.56
0.5	1300	50	8.33	3.85	22.56
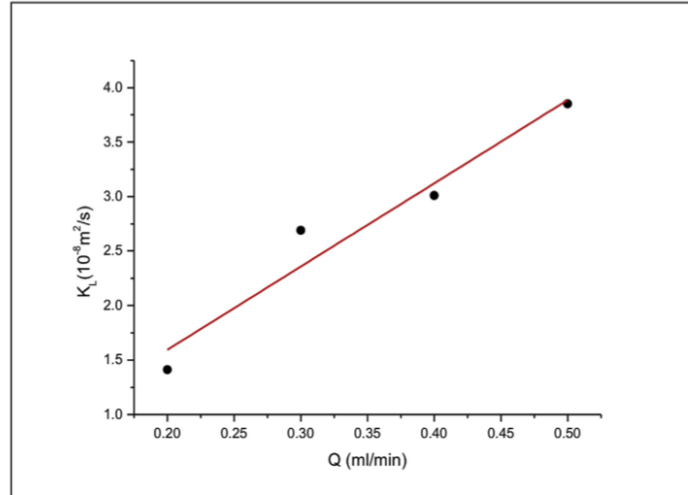
Fig. 5. Variation of Dispersion coefficient with injection rate.
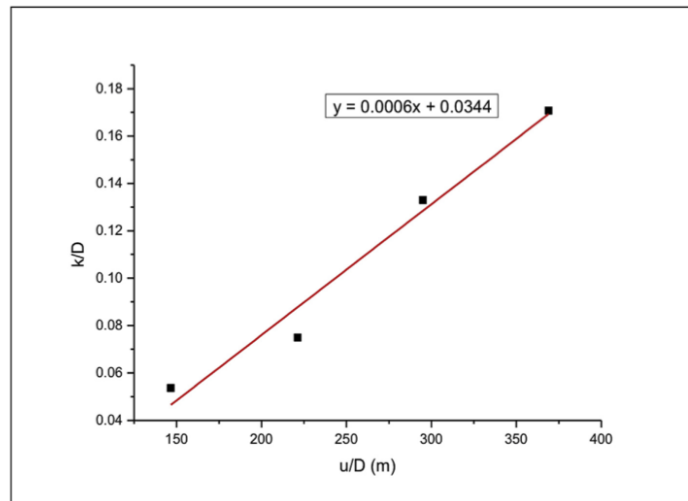
Fig. 6. Dispersity of the core sample at test conditions.

with distilled water, brine (5 wt%), and brine (10 wt%) under vacuum for effective distribution throughout the pore matrix of the core sample.

The dispersion coefficient of each saturation and salinity will be highlighted to evaluate the effect of the both parameters on the mixing during EGR.

3.2.1. Dispersion coefficient measurement

Table 4 shows the results obtained from curve fitting the
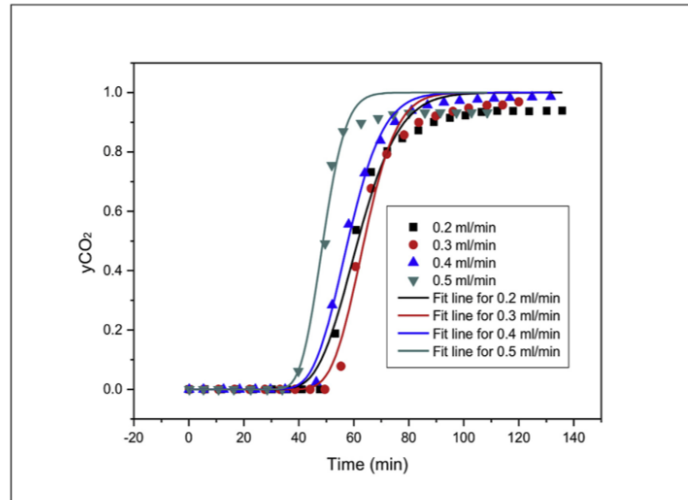
Fig. 7. Fitted concentration profiles of different experimental runs.
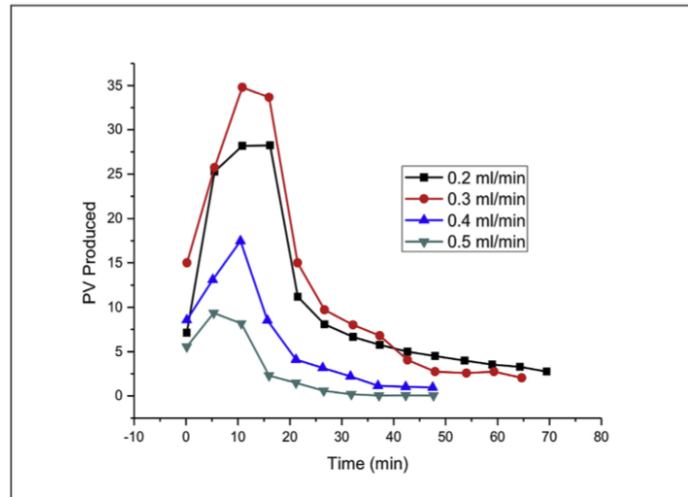
Fig. 8. CH_4 recovery as a function of time.

Table 4
Dispersion coefficient as a function of salinity.

Run	S_{wi} (%)	Salinity (wt %)	Pressure (psig)	Temperature (°C)	K_L (10^{-8} m²/s)
1	10	10	1300	50	0.44
2	10	5	1300	50	0.59
3	10	0	1300	50	3.61
4	0	0	1300	50	2.82

experimental data obtained from core flooding at different salinities but at the same operation conditions.

The results are consistent with the finding of (Abba et al., 2017) who carried out the investigation at a temperature of 40 °C and a pressure of 1300 psig. They explained the trend observed was as a result of reduction in the tortuous flow paths of the porous medium with connate water inclusion in the experimental run. However, when distilled water was used, the distribution of the water in the pore matrix did not completely seal off smaller pores but instead reduced the pore throats resulting in narrower flow paths and hence higher interstitial velocities. Here, the dispersion coefficient was highest, which was attributed that the low density of the connate water, compared to the brines, was responsible for higher dispersion coefficient observed.

The fitted curves of the concentration profiles are shown in Fig. 9. Early breakthrough of CO_2 was apparent in the runs with saturations of
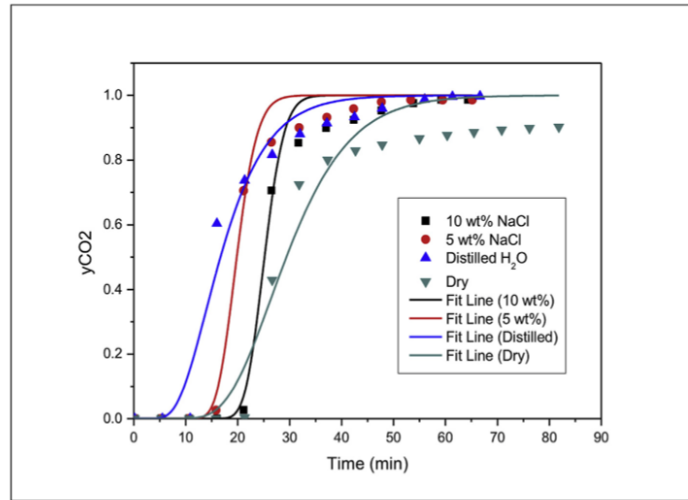
Fig. 9. Concentration profiles of different variants of salinities and air at test conditions.
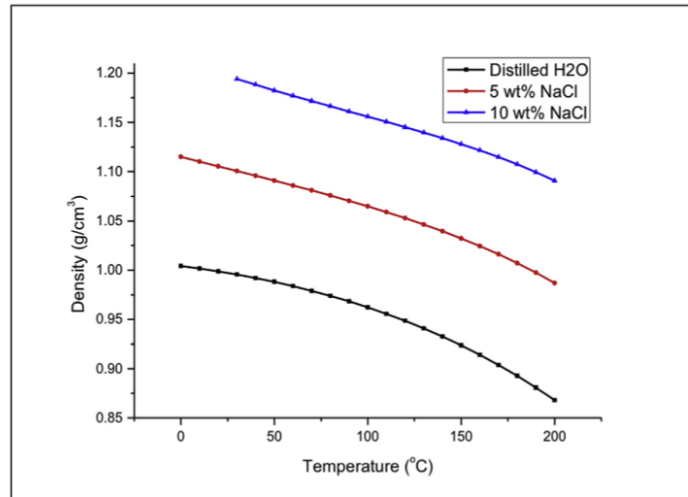
Fig. 10. Connate water densities as functions of temperature at 1400 psig (Generated from PVTsim 20).

Table 5
Brine concentrations with corresponding densities.

Salinity (wt%)	Temperature (^{o}C)	Pressure (psig)	Density (g/cm^3)
10	50	1300	1.18245
5	50	1300	1.09095
0	50	1300	0.98796

10% by volumes, given that the pore volume of the core sample was reduced by 10% due to the inclusion of connate water.

There was meagre fitting of the analytical solution to the experimental data at the tail end of the concentration profiles and this was as

a result of the entry and exit effects of the displacing supercritical CO_2 which was pointed out by (Honari et al., 2013; Hughes et al., 2012) and reiterated by (Liu et al., 2015). Details of this tailing effect are presented in (Liu et al., 2015).

The densities of the different connate water salinities were simulated and shown in Fig. 10 using PVTsim 20. This was carried out to highlight the interplay between the formation water salinities and the dispersion coefficient. This relationship between the connate water salinity and the dispersion coefficient is first shown in this body of work to the knowledge of this research.

From the simulation results, the densities were extracted at the desired conditions and tabulated below in Table 5.

Properties tabulated in Table 6 clearly show the observed

Table 6
Fluid densities with corresponding dispersion coefficients.

Run	Salinity (wt%)	Density (g/cm^3)	K_L (10^{-8} m^2/s)
1	10	1.18245	0.44
2	5	1.09095	0.59
3	0	0.98796	3.61

relationship between connate water densities and the longitudinal dispersion coefficients. The postulate that as the density of the connate water in the pore spaces of the core sample increases, the dispersion coefficient decreases is shown graphically in Fig. 11:

Albeit the good fit of the data in the graph, the standard error in the fit-line was within 1% of the average of the experimental data. The graph is mainly for representation and not aimed at describing a model to relate these two properties as there is no data, to the knowledge of this research, found in literature to back up this finding. However, this is a new data in the description of the CO_2 dispersion in CH_4 in consolidated porous media at conditions relevant to EGR.

The time it will take for the injected CO_2 to pass through the core sample will grossly be reduced since the tortuosity is reduced by the inclusion of connate in the core sample given the homogeneous nature of the core sample. This can explain what was observed in the experimental runs with higher density connate water as shown in Fig. 12. The pressure drop across the core sample during the run with 10%wt connate water was considerably higher in comparison with the other concentrations. Due to the high density of 10 wt% connate water (1.18245 g/cm^3), the capillary forces within the narrower pores in the core sample were overcome and the connate water occupied those pores thereby sealing some of the flow paths within the pore network. This reduces the flow channels, significantly, through which the injected CO_2 will flow to displace the nascent CH_4 which will eventually lead to higher pressure build-up in the core sample as the CO_2 transverses the now less tortuous and more constricted core matrix. With this higher pressure drop (ΔP), a lower permeability is evident according to Darcy relationship between permeability (k) and ΔP which states that permeability is inversely proportional to the differential pressure across a core sample as shown in (Eq. (10)). The injected CO_2 permeability decreased with increase in the density of the connate water.

$$k = \frac{q\mu L}{A\Delta P} \tag{10}$$

Where k is the permeability (md), q is flowrate (cm^3/s), μ is fluid viscosity (cp), A is cross sectional area of core (cm^2), and ΔP is differential pressure across the core sample (atm).

However, the experimental run with distilled water showed a higher differential pressure, invariably lower permeability, compared to that of the 5 wt%. This can be as result of the reason given by (Abba et al., 2017) that due to the lower density of the distilled water compared to that of the brine, the capillary forces within the pore matrix were not overcome by the density of the distilled water. Therefore, the distilled water did not entirely block or seal off the narrower flow paths, as in the case of the 10 wt% connate water, of the core sample as suggested by (Honari et al., 2016). Instead, it made it narrower and that decreased the permeability of the core sample and this phenomenon also explains the high dispersion coefficient observed with the Distilled water experimental run as shown in Table 4. This clearly shows the influence of connate water salinity on the dispersion coefficient, invariably the mixing of the gases during EGR. For 5 wt % brine, the low ΔP and high permeability translated to the sealing off narrower and smaller pore spaces, some of whose capillary forces superseded the density of the brine in question. Therefore, more flow channels were available for flow without impending restrictions as seen in the case of the 10 wt% brine experiment. Thus, the flow behaviour was close to that of the dry run were there was no inclusion of connate water. In higher salinity connate water environment, a lower mixing is expected because of the more homogenous flow paths as discussed earlier. This finding will be vital in the accurate depiction of EGR during simulation studies for field scale applications of the technique.

4. Conclusion

The optimum flow conditions for the connate water salinity effect on dispersion coefficient were successfully evaluated through systematic and comparative experimental. These were based on the CH_4 recovery and favourable dispersion coefficient of each investigated injection rate. Optimum flow conditions obtained were used to carry out the connate water salinity investigation. From the results, it can be inferred that an increase in the brine density, as a result of increasing its
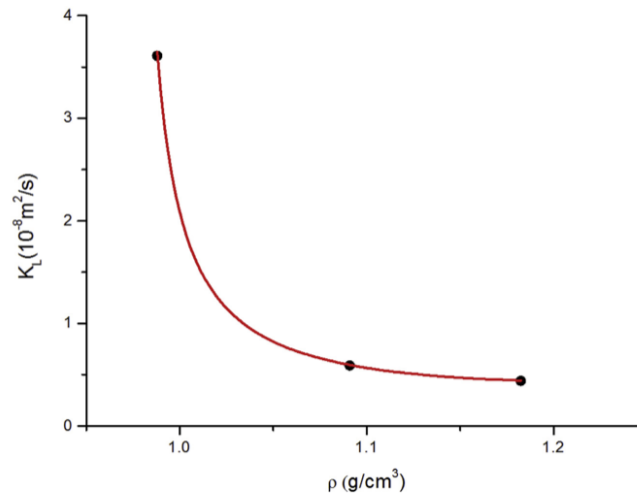
Fig. 11. Dispersion Coefficient as a function of connate water density.
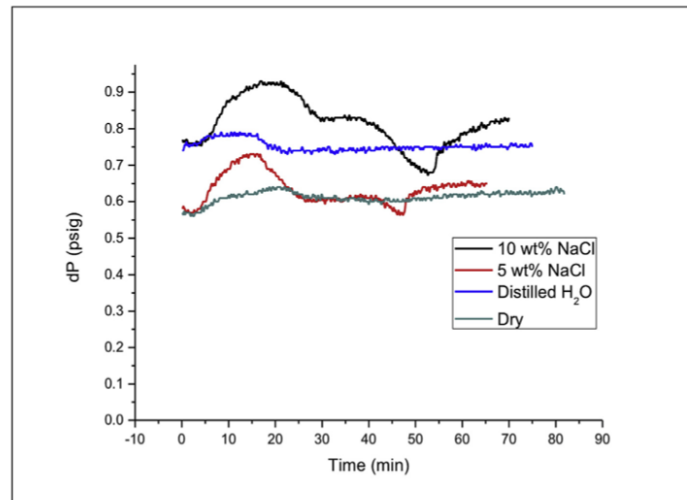
Fig. 12. Differential pressure of the experimental runs as a function of time.

concentration, increased the dispersion coefficient. The density of the connate water plays a significant role in the flow behaviour of the injected CO_2 in a way that it dictates the flow channels and matrix of the reservoir rock through which the displacement process develops. As seen with the experimental run using the 10 wt% brine with a density of $1.18245\,g/cm^3$, the dispersion coefficient was 8 times less than that of the distilled water with density of $0.98796\,g/cm^3$. This will have a major effect on the contamination of the produced natural gas from the reservoir through EGR. Thus, inclusion of connate water salinity in simulation studies for EGR field application could provide significant understanding of realistic displacement process in sandstones reservoirs.

Acknowledgement

Nomenclature

B_g	Gas formation volume factor, cm^3/scm^3
C	CO_2 mole fraction
D	Diffusion coefficient, m^2/s
d	Characteristic length scale, m
G	Original Gas in place, cm^3
k	Permeability, md
K_L	Longitudinal dispersion, m^2/s
L	Core sample length, mm
L_{exp}	Experimental length, m
μ	Viscosity, cP
P	Pressure, psig
P_e	Peclet number
P_{em}	Medium Peclet number
Q	Flowrate, ml/min
R	Radius of core sample, mm
S_w	Connate water saturation

T	Temperature, ^oC
t	Time, min
t_D	Dimensionless time
u	interstitial velocity, m/s
x	Distance from the upstream of the core face, m
x_D	Dimensionless distance
ϕ	Core porosity

References

Abba, M.K., Abbas, A.J., Nasr, G.G., 2017. Enhanced gas recovery by CO2 injection and sequestration: effect of connate water salinity on displacement efficiency. SPE Abu Dhabi Int. Pet. Exhib. Conf. https://doi.org/10.2118/188930-MS.

Adepoju, O.O., Lake, L.W., Johns, R.T., Energy, E.M.S., 2013. SPE 166390 Anisotropic Dispersion and Upscaling for Miscible Displacement. pp. 421–432.

Al-abri, A., Sidiq, H., Amin, R., 2009. Enhanced natural gas and condensate recovery by injection of pure SCCO2, pure CH4 and their Mixture: experimental investigation. In: SPE Annu. Tech. Conf. Exhib. New Orleans, Lousiana, USA, 4-7 Oct. 1–13.

Al-Abri, A., Sidiq, H., Amin, R., 2012. Mobility ratio, relative permeability and sweep efficiency of supercritical CO2 and methane injection to enhance natural gas and condensate recovery: corefloooding experimentation. J. Nat. Gas Sci. Eng. 9, 166–171. https://doi.org/10.1016/j.jngse.2012.05.011.

Al-Abri, A.S., 2011. Enhanced Gas Condensate Recovery by CO 2 Injection.

Allen, R., Nilsen, H.M., Andersen, O., Lie, K.A., 2017. Categorization of Norwegian continental shelf formations in terms of geological CO2Storage potentials. Energy Procedia 114, 4583–4594. https://doi.org/10.1016/j.egypro.2017.03.1579.

Bennaceur, K., 2013. CO2Capture and sequestration. Futur. Energy Improv. Sustain. Clean Options our Planet 583–611. https://doi.org/10.1016/B978-0-08-099424-6.00026-0.

Benson, S., Cook, P., Anderson, J., Bachu, S., Nimir, H.B., Basu, B., Bradshaw, J., Deguchi, G., 2005. Underground Geological Storage. Ipcc, pp. 195–276.

Benson, S.M., Cole, D.R., 2008. CO2 sequestration in deep sedimentary formations. Elements 4, 325–331. https://doi.org/10.2113/gselements.4.5.325.

Coats, K.H., Smith, B.D., van Genuchten, M.T., Wierenga, P.J., 1964. Dead-end pore volume and dispersion in porous media. Soil Sci. Soc. Am. J. 4, 73–84. https://doi.org/10.2118/647-PA.

Coats, K.H., Whitson, C.H., Thomas, K., 2009. Modeling conformance as dispersion. SPE Reservoir Eval. Eng. 12, 33–47. https://doi.org/10.2118/90390-PA.

Ekwere, P.J., 2007. Petrophysics 1049.

Honari, A., Bijeljic, B., Johns, M.L., May, E.F., 2015. Enhanced gas recovery with {CO2} sequestration: the effect of medium heterogeneity on the dispersion of supercritical CO2–CH4. Int. J. Greenh. Gas Control 39, 39–50. https://doi.org/10.1016/j.ijggc.2015.04.014.

Honari, A., Hughes, T.J., Fridjonsson, E.O., Johns, M.L., May, E.F., 2013. Dispersion of supercritical CO2 and CH4 in consolidated porous media for enhanced gas recovery simulations. Int. J. Greenh. Gas Control 19, 234–242. https://doi.org/10.1016/j.ijggc.2013.08.016.

Honari, A., Zecca, M., Vogt, S.J., Iglauer, S., Bijeljic, B., Johns, M.L., May, E.F., 2016. The

impact of residual water on CH4-CO2 dispersion in consolidated rock cores. Int. J. Greenh. Gas Control 50, 100–111. https://doi.org/10.1016/j.ijggc.2016.04.004.

Hughes, T.J., Honari, A., Graham, B.F., Chauhan, A.S., Johns, M.L., May, E.F., 2012. CO2 sequestration for enhanced gas recovery: new measurements of supercritical CO2–CH4 dispersion in porous media and a review of recent research. Int. J. Greenh. Gas Control 9, 457–468. https://doi.org/10.1016/j.ijggc.2012.05.011.

Jha, R.K., Bryant, S.L., Lake, L.W., John, A., 2013. Investigation of pore-scale (local) mixing. SPE/DOE Symp. Improv. Oil Recover. https://doi.org/10.2118/99782-MS.

Kalra, S., Wu, X., 2014. CO2 injection for enhanced gas recovery. SPE West. North Am. Rocky Mt 16–18.

Khan, C., Amin, R., Madden, G., 2013. Carbon dioxide injection for enhanced gas recovery and storage (reservoir simulation). Egypt. J. Pet. 22, 225–240. https://doi.org/10.1016/j.ejpe.2013.06.002.

Liu, S., Zhang, Y., Xing, W., Jian, W., Liu, Z., Li, T., Song, Y., 2015. Laboratory experiment of CO2-CH4 displacement and dispersion in sandpacks in enhanced gas recovery. J. Nat. Gas Sci. Eng. 26, 1585–1594. https://doi.org/10.1016/j.jngse.2015.04.021.

Mamora, D.D., Seo, J.G., 2002. Enhanced recovery by carbon dioxide sequestration in depleted gas reservoirs. SPE Annu. Tech. Conf. Exhib. 1–9.

Newberg, M., Foh, S., 1988. Measurement of longitudinal dispersion coefficients for gas flowing through porous media. SPE 5–9.

Oldenburg, C.M., Benson, S.M., 2002. CO2 injection for enhanced gas production and carbon sequestration. SPE Int. Pet. Conf. Exhib. Mex. https://doi.org/10.2118/74367-MS.

Perkins, T., Johnston, O., 1963. A review of diffusion and dispersion in porous media. Soc. Petrol. Eng. J. 3, 70–84. https://doi.org/10.2118/480-PA.

Riis, F., Halland, E., 2014. CO2 storage atlas of the Norwegian Continental shelf: methods used to evaluate capacity and maturity of the CO2 storage potential. Energy Procedia 63, 5258–5265. https://doi.org/10.1016/j.egypro.2014.11.557.

Sanguinito, S., Goodman, A.L., Sams, J.I., 2018. CO2-SCREEN tool: application to the oriskany sandstone to estimate prospective CO2storage resource. Int. J. Greenh. Gas Control 75, 180–188. https://doi.org/10.1016/j.ijggc.2018.05.022.

Shabani, B., Vilcáez, J., 2017. Prediction of CO2-CH4-H2S-N2gas mixtures solubility in brine using a non-iterative fugacity-activity model relevant to CO2-MEOR. J. Petrol. Sci. Eng. 150, 162–179. https://doi.org/10.1016/j.petrol.2016.12.012.

Shtepani, E., 2006. CO2 sequestration in depleted gas/condensate reservoirs. In: Proc. - SPE Annu. Tech. Conf. Exhib..

Sidiq, H., Amin, R., 2009. Mathematical model for calculating the dispersion coefficient of super critical CO2 from the results of laboratory experiments on enhanced gas recovery. J. Nat. Gas Sci. Eng. 1, 177–182. https://doi.org/10.1016/j.jngse.2009.11.001.

Sidiq, H., Amin, R., der Steen, E. Van, Kennaird, T., 2011a. Super critical CO2-methane relative permeability investigation. J. Petrol. Sci. Eng. 78, 654–663. https://doi.org/10.1016/j.petrol.2011.08.018.

Sidiq, H., Amin, R., der Steen, E. Van, Kennaird, T., 2011b. Super critical CO2-methane relative permeability investigation. J. Petrol. Sci. Eng. 78, 654–663. https://doi.org/10.1016/j.petrol.2011.08.018.

Sim, S., Turta, A.T., Singhal, A., Hawkins, B.F., 2009a. Enhanced gas recovery: effect of reservoir heterogeneity on gas-gas displacement. Candian Int. Pet. Conf. 1–14. https://doi.org/10.2118/2009-023.

Sim, S., Turta, A.T., Singhal, A.K., Hawkins, B.F., 2009b. Enhanced gas recovery: factors affecting gas-gas displacement efficiency. J. Can. Pet. Technol. 48, 49–55. https://doi.org/10.2118/09-08-49.

Sim, S.S.K., Brunelle, P., Canada, Q., Systems, F., Turta, A.T., Singhal, A.K., 2008. SPE 113468 enhanced gas recovery and CO 2 sequestration by injection of exhaust gases from combustion of bitumen. Changes 1–10.

Sminchak, J.R., Babarinde, O., Gupta, N., 2017. Integrated analysis of geomechanical factors for geologic CO2Storage in the midwestern United States. Energy Procedia 114, 3267–3272. https://doi.org/10.1016/j.egypro.2017.03.1458.

Turta, A.T., Sim, S.S.K., Singhal, A.K., Hawkins, B.F., 2007. Basic Investigations on Enhanced Gas Recovery by Gas-Gas Displacement.

Vilcáez, J., 2015. Numerical modeling and simulation of microbial methanogenesis in geological CO2storage sites. J. Petrol. Sci. Eng. 135, 583–595. https://doi.org/10.1016/j.petrol.2015.10.015.

Zhang, Y., Liu, S., Song, Y., Zhao, J., Tang, L., Xing, W., Jian, W., Liu, Z., Zhan, Y., 2014. Experimental investigation of CO2-CH4 displacement and dispersion in sand pack for enhanced gas recovery. Energy Procedia 61, 393–397. https://doi.org/10.1016/j.egypro.2014.11.1133.

Ziabakhsh-Ganji, Z., Kooi, H., 2012. An Equation of State for thermodynamic equilibrium of gas mixtures and brines to allow simulation of the effects of impurities in subsurface CO2storage. Int. J. Greenh. Gas Control 11, 21–34. https://doi.org/10.1016/j.ijggc.2012.07.025.

SPE-188930-MS

Enhanced Gas Recovery by CO2 Injection and Sequestration: Effect of Connate Water Salinity on Displacement Efficiency

M. K. Abba, A. J. Abbas, and G. G. Nasr, The University of Salford

Abstract

As natural gas continues to gain widespread usage as a source of cleaner and efficient fossil fuel, while greenhouse gas emission is attracting environmental consequences, the need for a viable method to enhance gas recovery and curtail greenhouse gas emissions, is paramount. The technique of injecting CO_2 for Enhanced Gas Recovery (EGR) is deemed one of the efficient methods for simultaneously storing CO_2 emissions and improving additional natural gas recovery from depleted gas fields, provided that the gas mixing in situ can be reduced. This can be achieved by an understanding of the mechanisms of displacement and the factors that affect them. This provides vital information for further studies aimed at a robust field scale application to establish the economic viability of the process. Connate water saturation and salinities are vital properties of the reservoir and their influence on the displacement efficiency cannot be overemphasised. This experimental study determines the effect of connate water salinity, in sandstone sample, on the displacement efficiency during EGR. This study presents the first novel experimental measurement of dispersion of CO_2 in CH_4 as a function of salinity in consolidated porous media. A laboratory experiment depicting the detailed process of the CO_2-CH_4 displacement in sandstone core samples at a temperature a temperature of 40°C and at a pressure of 1,300 psig, was carried in the investigation, at a CO_2 injection rate of 0.25 ml/min to evaluate the displacement efficiency. The findings indicated that salinity of the connate water tends to decrease the dispersion of CO_2 in CH_4 at the stated conditions. This can be attributed to the increase in density of the connate water with increase in salinity, which occupies smaller pore channels within the porous medium thereby making the core sample more homogeneous. Also, grain diameter measurements were carried out from Scanning Electron Microscopy (SEM) images of the porous media using image analysis to establish the characteristic length scale of mixing of the medium.

Introduction

The growing energy demand to cater for the growing world population has forced the exploitation of alternative sources of energy, using newer or otherwise unexploited technologies. Natural gas is considered one of the most abundant, cleanest, and cheapest sources of fossil fuels and is gaining more attention globally (Benson et al. 2005; Al-Abri et al. 2012). These features of natural gas have placed it at the forefront in

the race to obtain not only an efficient source of energy but also an environmentally friendly one. As time progresses, production of natural gas from the reservoirs can be interrupted and the reservoir abandoned. These reservoirs are termed depleted reservoirs. Depleted reservoirs are abandoned for a variety of reasons; common amongst which is the non-economic production rate, other reasons could be as a result of water invasion and also formation subsidence (Kalra & Wu 2014). These depleted reservoirs, however, are not devoid of residual hydrocarbons in-situ and the need for further production and recovery to cater for the growing energy demand merits employment of enhanced recovery techniques, especially when CH_4 is displaced and CO_2 is stored.

The services of these depleted gas reservoirs maybe "re-enlisted" for anthropogenic CO_2 geological storage. The concept of enhanced gas recovery by CO_2 injection utilises the availability of residual CH_4 in the reservoir and the storage volume of the depleted gas reservoirs to produce CH_4, and at the same time store the injected CO_2. This technique serves as a simultaneous phenomenon, as large volumes of CO_2 will be sequestered along with substantial recovery of CH_4 from the depleted reservoirs. This concept is gaining attention globally due to the growing concern about climate change and greenhouse gas emissions (Honari et al. 2015), hence call for further research in the miscibility of the two components.

The adoption of EGR generally has not been well received. This is because of the excessive mixing between the injected carbon dioxide and in-situ natural gas during the flooding process (Oldenburg & Benson 2002; Shtepani 2006; Turta et al. 2007; Sim et al. 2008; Al-abri et al. 2009; S. Sim et al. 2009; Sidiq et al. 2011; Hughes et al. 2012; Honari et al. 2013; Khan et al. 2013; Zhang et al. 2014; Honari et al. 2015; Patel et al. 2016; Honari et al. 2016). This mixing contaminates the recovered natural gas and reduces its calorific value and thus its market value, which will, in turn, incur more cost in the sweetening processes to maintain the natural gas purity after the process (Oldenburg & Benson 2002; Sim et al. 2008; S. S. K. Sim et al. 2009).

The problem with EGR by CO_2 injection is in the nature of the gas-gas displacement mechanism in-situ. The efficiency of this displacement process is affected by the mixing of the displacing fluid (CO_2) and the displaced fluid (CH_4), given the complete miscibility of these two gases at conditions relevant to EGR process (Hughes et al. 2012) albeit their density and viscosity contrasts at those conditions. This major challenge has not only limited the EGR project to a few field trials (Honari et al. 2015; Pooladi- Darvish et al. 2008), but has also made the process largely unprofitable because the contamination of the natural gas asset as a result of the mixing phenomenon which is poorly understood (Patel et al. 2016). Thus, finding a suitable approach to reducing the mixing extent could be valuable at varying connate water concentration.

Several authors, cited within the body of this study, investigated the effects of key factors including temperature, pressure, injection rate, reservoir heterogeneity, gas compositions, and gas-gas interfacial tension which affect the displacement of CH_4 by supercritical CO_2 for enhanced gas recovery. Among all these authors, only Honari et al., (2016) considered connate water in their investigation, which they assessed the effect of connate water on the dispersion coefficient. They however used a pulse displacement technique and did not account for the salinity of the connate water. This study however focuses on the sensitivity of displacement efficiency to the salinity of the connate water during enhanced gas recovery by CO_2 injection.

Dispersion and Diffusion Coefficients

The mixing phenomenon occurring in porous media is a diffusion-like process due to concentration and velocity gradient. The dispersion coefficient denotes the rate of mixing when two miscible fluids come in contact at the displacement front of a flooding process. It depends on the direction of the dispersion flux with respect to the main convective flux. The smallest value of this term occurs perpendicular to the main convective path (flux) often called transverse dispersion, and the largest occurs for dispersion in the main convective flux called longitudinal dispersion. Transverse dispersion coefficient, K_t, is more difficult to

obtain experimentally and as result, very few data is available in literature besides those of (Perkins, T.K. Johnston 1963).

Newberg & Foh (1988) used a single parameter diffusion-type equation (Eqn. 1) to correlate the numerical dispersivities with experimental results. This model was used to generate longitudinal dispersion coefficients and "scale of dispersion" (dispersion coefficient divided by velocity). It also describes the dispersion occurring during the displacement process in EGR, when CO_2 displaces the nascent CH_4 which this study will capitalise on.

$$K_l \frac{\partial^2 C}{\partial x^2} - u \frac{\partial C}{\partial x} = \frac{\partial C}{\partial t} \qquad (1)$$

Where, C is the CO_2 concentration at location x at time t, K (m²/s) is the coefficient of longitudinal dispersion, and u is the interstitial velocity (m/s). It is based on the assumption that the dispersion coefficient and interstitial velocity are independent on the concentration of CO_2 C (Liu et al, 2015).

Invariably, (Eqn. 1) may be written in dimensionless form as follows (Mamora & Seo 2002);

$$\frac{1}{P_e} \frac{\partial^2 C}{\partial x_D^2} - \frac{\partial C}{\partial x_D} = \frac{\partial C}{\partial t_D} \qquad (2)$$

Where;

$P_e = \dfrac{uL}{K_l}$, Peclet number (ratio of convection to dispersion), L is length of core

$t_D = \dfrac{tu}{Lexp}$, dimensionless time

$x_D = \dfrac{x}{Lexp}$, dimensionless distance, and

u, interstitial velociy, $= \dfrac{Q}{\pi r^2 \phi}$, Q is superficial velocity, ϕ is porosity

K_l, Longitudinal dispersion

Given that CO_2 injection at inlet is at $x = 0$,

then initial condition: $C = 0$ at $t_D = 0$,

boundary conditions: $C = 1$ at $x_D = 0$, $C \rightarrow 0$ as $x_D \rightarrow \infty$

The solution to (Eqn. 1.2) maybe shown as follows:

$$C = \frac{1}{2} \left\{ \text{erfc} \left(\frac{x_D - t_D}{2\sqrt{t_D/P_e}} \right) + e^{P_e x_D} \text{erfc} \left(\frac{x_D + t_D}{2\sqrt{t_D/P_e}} \right) \right\} \qquad (3)$$

The CO_2 concentrations profiles from EGR core flooding experimentations can be fitted with the analytical solution to the 1-D Advection Dispersion equation (eqn.3) in terms of the *Péclet* number to evaluate the corresponding dispersion coefficient. The appropriate dispersion coefficient for the experiment is the value which provides the best agreement between the experimental data and the analytical solution.

Perkins, T.K. Johnston (1963) presented another definition of *Péclet* number termed medium Péclet number denoted by, P_{em}, which describes the dominant displacement regime during a dispersion process and expressed as:

$$P_{em} = \frac{ud}{D} \qquad (4)$$

Where P_{em} is medium Péclet number, u is the mean interstitial velocity (m/s), D is the diffusion coefficient (m²/s), and d is the characteristic length scale of the porous medium, which is defined as the medium grain

diameter of the sand pack but it is poorly defined in consolidated medium (Hughes et al. 2012). Generally, at P_{em} <0.1, diffusion dominates the dispersion process, and at P_{em}>10 advective mixing dominates the dispersion process. Assumption in the mean grain diameter of consolidated samples gives rise to poor depiction of the quantity, given that measuring the mean grain diameter for consolidated media is tedious. This work will employ the use of image analysis as a method of mean grain diameter determination for a better representation of the parameter.

Takahashi and Iwasaki (1970), reported by Hughes et al. (2012) and Liu et al. (2015), established a correlation between the diffusion coefficient, temperature and pressure. This correlation was used by the authors to obtain accurate diffusivity using Eqn. (5) at conditions relevant to enhanced gas recovery by CO_2 injection. The correlation is as follows:

$$D = \frac{(-4.3844 \times 10^{-13}p + 8.55440 \times 10^{-11})T^{1.75}}{p} \tag{5}$$

where D (m²/s) is the molecular diffusion coefficient of CO_2 in CH_4 at temperature T (K) and pressure p (MPa). In the works of Takahashi and Iwasaki (1970), the diffusion coefficients of CO_2 in CH_4 were measured at 298 to 348 K and pressures of 5-15 MPa in a porous bronze plug. Determination of the dominant displacement mechanism in EGR is possible using Equations 4 and 5. This will help better understand the mixing phenomenon during EGR.

Description and application of equipment and processes

High purity CH_4 with a minimum purity of 0.995 and industrial grade CO_2 with a minimum purity of 0.99 were used for the study. Table 1 shows the dimensions and petrophysical properties of the *Berea* sandstone core sample used in this work. General purpose grade sodium chloride salt was used to prepare the brine to conduct the experiment.

Table 1—Dimensions and petrophysical sroperties of the core sample

Core sample	Length (mm)	Diameter (mm)	Porosity (%)	Permeability (md)	Weight (g)	Mean grain diameter (μm)
Grey Berea	76.27	25.22	20.3	217	80.12	94.66

The set-up of the experiment consists of two individual components; the branded core flooding system and the Gas chromatograph. The branded flooding system, configured for two phase liquid displacements under unsteady state or steady-state conditions and single-phase gas steady-state experiments, was reconfigured to accommodate gas flooding and was used in this study to carry out the core flooding experiment. The *GC*, located downstream of the flooding system, was used to obtain the concentration profile from analyses of the effluents of the flooding procedure. A schematic of the outline of the set-up is shown in Figure 6.

The branded core flooding system is rated to 5,000 psig confining pressure and 3,750 psig pore pressure. The injection system of the equipment is made up of a pair of dual ISCO two-barrel metering pump system for constant flow for pulseless transition and to maintain an accurate flow rate. It has flow rate range of 0-200 ml/min a maximum pressure rating of 3,750 psig. The pumps are attached to a pair of stainless steel floating piston accumulators which are also rated for 5,000 psig pressure and temperature of 177°C. They are designed for injection of the fluids of interest. The overburden confining pressure was realised using a hydraulic pump with a maximum pressure output of 10,000 psig.

The inlet, outlet, overburden, back pressures in the flooding system are measured with gauge pressure transducers with an accuracy of 0.1% and pressure range of 0-5000 psig. A *Rosemount* Static DP transmitter with an accuracy of 0.0055% is also available to measure the differential pressures across the core holder.

The Hassler-type core holder was employed to house the core sample. This is an integral part of the branded core flooding system. The core sample is held within the core holder by a *Viton* rubber sleeve. A core holder heat jacket to simulate the required temperature was also employed with an accuracy of 0.1%. Dome type back pressure regulator integrated into the flooding system ensured the confinement of the desired pressures within the core holder. Located downstream of the back-pressure regular is the mass flow controllers to measure the effluents volume produced which are analysed by the GC system in place.

Procedure

The core sample was wrapped cling film and also in foil paper and inserted into a heat shrink to minimise the permeation of the gases through sleeve into the annulus of the core holder. It was then loaded into the core holder and secured with clamps. Hydraulic oil was then pumped into the annulus of core holder to provide the desired confining pressure which was kept 500 psig above the pore pressures to avoid rupturing of the core sleeve. The heat jacket was then installed on the core holder and the temperature ramping was observed. The back pressure was engaged and CH_4 was slowly injected into the core sample from the accumulator using the metering pump. CO_2 is then injected into the core sample at a constant rate of 0.25 ml/min. When the methane concentration was insignificant, the run came to an end. At each injection time of the GC, the time was noted and also the effluent composition which is then used to report the concentration profile.

Presentation of data and results

Five sets of breakthrough times were measured at pressure of 1,300 psig and a temperature of 40°C as shown in Table 2. Three runs were done with dry core samples, one run was done on core samples with initial saturations of 10% distilled water, and the last one was done with initial brine saturation of 10 % (brine salinity 20 wt%).

Table 2—Core flooding experimental results

Run 1		Run 2		Run 3		Run 4		Run 5	
Dry		Dry		Dry		10% Distil		10% Brine (20 wt%)	
Time (min)	CO2 (%)	Time (min)	CO2 (%)	Time (min)	CO2 (%)	Time (min)	CO2 (%)	Time (min)	CO2 (%)
0.17	0	0.15	0	0.17	0	0.15	0	0.17	0
5.95	0	5.82	0	5.49	0	5.33	0	5.33	0
12.5	0	11.82	0	10.83	0	12.65	0	10.82	0
17.75	0	17.49	0	16.67	0	18.49	0	16.33	0
23.58	0	23.48	0	22.17	0	24.16	0	22.49	0
29.3	0	30.32	0	27.66	0	29.66	0	28.49	0
34.88	0	35.82	0	33.17	0	34.98	0	33.99	0
41.33	0	41.15	0	38.66	0	46.32	0.0245	39.82	0.0618
46.85	0	47.65	0	44.17	0	52.15	0.2839	49.55	0.4912
52.7	0.1275	53.32	0.1876	49.51	0	58.16	0.5559	51.99	0.7553
59.48	0.5107	60.82	0.5368	55.32	0.0778	63.99	0.7285	56.16	0.8689
65.48	0.7271	66.32	0.7318	60.67	0.4136	69.66	0.8389	62.66	0.8968
71.18	0.8203	72.15	0.8026	66.32	0.6769	74.99	0.9019	68.88	0.9135
77.18	0.8705	77.65	0.8457	71.99	0.7922	80.99	0.9389	74.33	0.9259
83.87	0.9062	83.48	0.8728	78.32	0.8573	86.82	0.9572	80.16	0.9309
89.65	0.9903	89.15	0.9009	83.67	0.8995	92.82	0.9676	85.82	0.9321
95.58	0.9887	94.98	0.9144	89.83	0.9208	98.48	0.9731	91.49	0.9328
101.88	0.987	100.65	0.9234	96.12	0.9364	104.98	0.9774	97.33	0.9325
108.08	0.9924	106.49	0.9345	101.83	0.9473	110.98	0.9804	102.82	0.9327
113.85	0.9936	112.15	0.9383	108.47	0.9568	116.82	0.9824	108.49	0.9331
		117.98	0.938	114.16	0.9583	124.83	0.9848		
		123.82	0.937	119.99	0.9688	131.66	0.9863		
		130.15	0.9382						
		135.82	0.9392						

Helium *Porosimetry* was used to determine the porosity of the core sample and was obtained as 0.203. Mean grain dimeter was measured from SEM image (Figure 5) of the core sample and then analysed using image analysis and shown to be 94.66 μm as reported in Table 1.

The longitudinal dispersion coefficient was obtained by curve fitting experimental data with Eqn.3 which is the dimensionless solution of Eqn.1. This was achieved by least square regression with the longitudinal dispersion coefficient (K_L) as the fitting parameter and the length (L_{exp}) was adjusted in the regression to minimise the tubing effect as suggested by Hughes et al (2012) given that the interstitial velocity was kept constant. The concentration profiles for with fitted eqn.3 for Runs 1 through 5 are shown in Figures 1 through 5 respectively. The diffusion coefficient was obtained from eqn. 4 using the experimental conditions of 1,300 (8.96 Pa) psig and 40°C (313.15 K). Value of which was used to determine the medium *Peclet* number, P_{em}, to identify the dominant displacement mechanism of the core flooding experiment. This was obtained as 0.018, using Eqn.4.
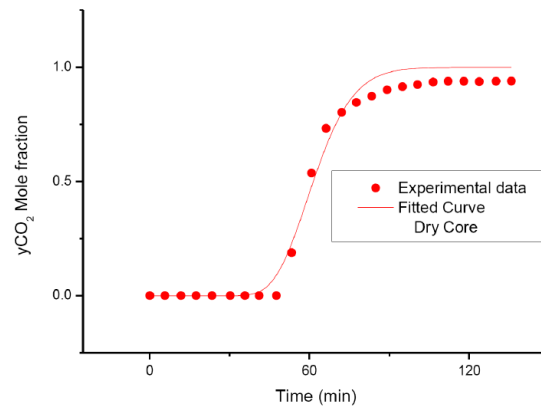
Figure 1—CO$_2$ Concentration profile for Run 1 at 1,300 psig and 40oC on dry core sample
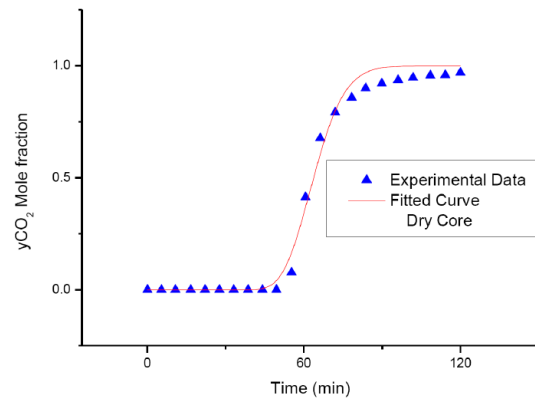
Figure 2—CO$_2$ Concentration profile for Run 2 at 1,300 psig and 40°C on dry core sample
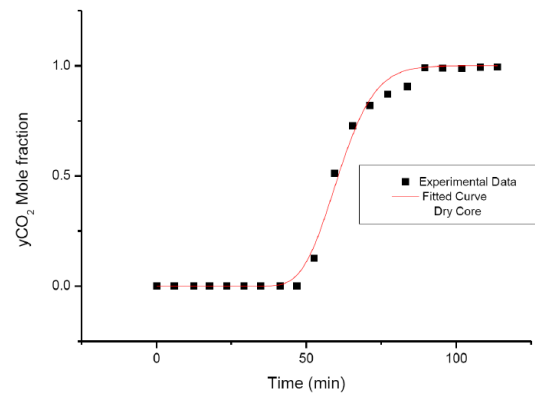
Figure 3—CO$_2$ Concentration profile for Run 3 at 1,300 psig and 40°C on dry core sample
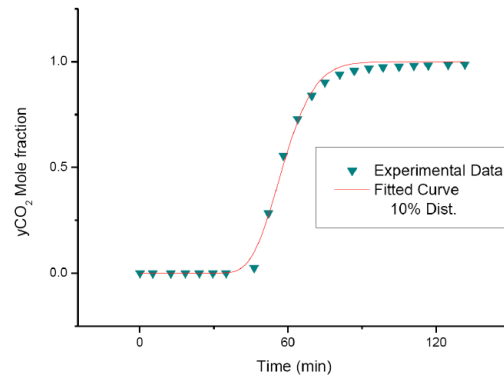
Figure 4—CO$_2$ Concentration profile for Run 4 at 1,300 psig and 40°C on 10% Swi distilled water
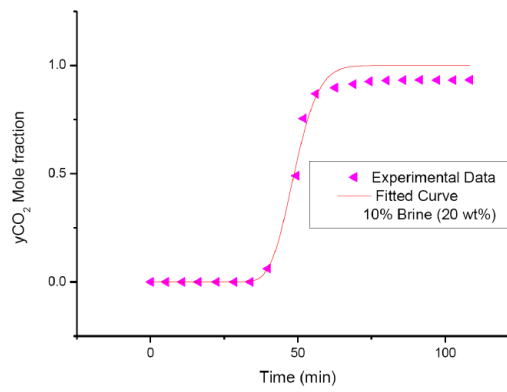
Figure 5—CO$_2$ Concentration profile for Run 5 at 1,300 psig and 40°C on 10% Swi Brine (20 wt%)
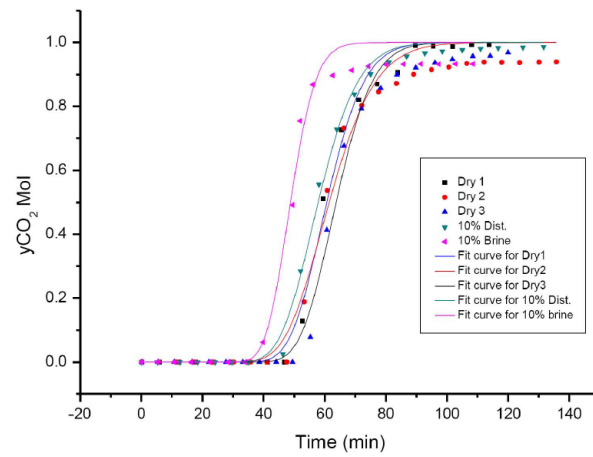
Figure 6—CO$_2$ Concentration profiles of all the runs at 1,300 psig and 40°C

224
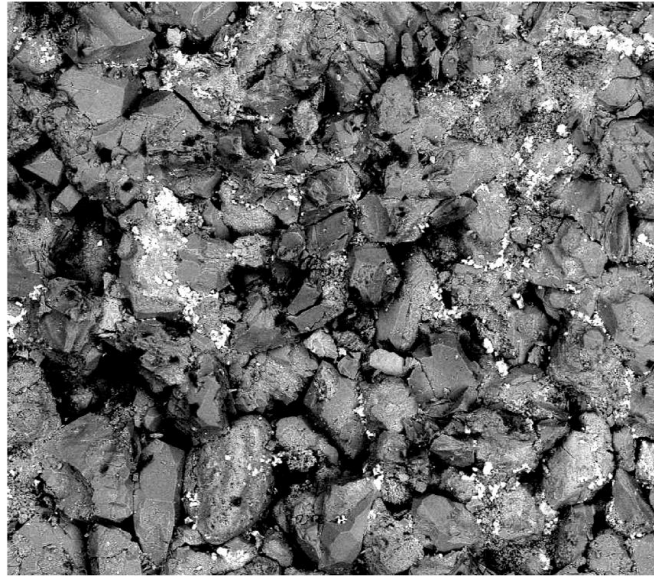
Figure 7—SEM image of a section of Grey Berea at 500 μm
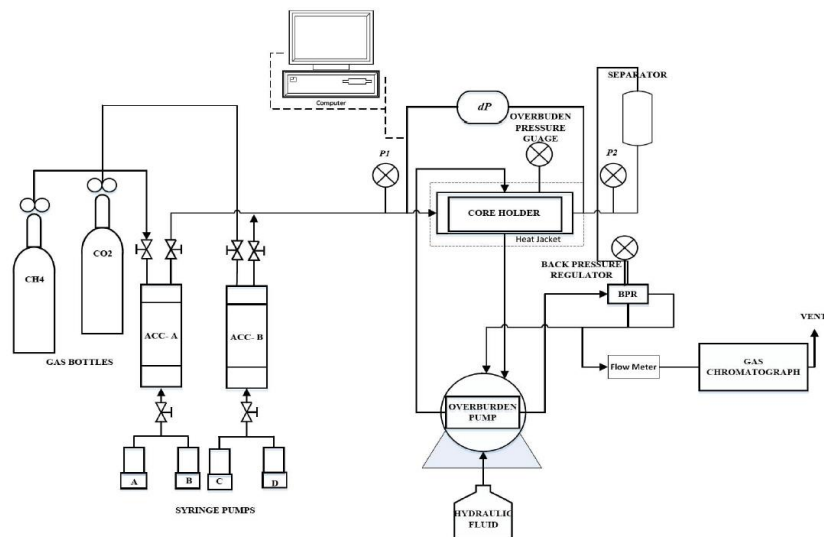
Figure 8—Schematics of core flooding set-up

Table 3 shows the summary of the breakthrough times of each of the five runs and their corresponding dispersion coefficients. There is significant closeness between breakthrough times of the dry core runs. These runs were made so as to obtain the optimum operational conditions for the experiment, and to establish a benchmark or reference to which subsequent parametric sensitivity analyses can be based on to ascertain

the effect of the investigation. As seen in Tables 2 and 3, the CO_2 breakthrough was realised almost at the same time for runs 1, 2, and 3 (dry cores). Invariably, earlier breakthrough was observed during the 4th run with 10% initial distilled water saturation. This can be attributed to the reduction in pore volume of the core sample which in effect reduces the volume of the nascent CH_4. Conversely, (in Tables 2 and 3) in run 5 at $Swi = 0.1$ with 20 wt% brine, there was an even earlier breakthrough of CO_2 than run 4 at $Swi = 0.1$ with distilled water. The breakthrough profile for all the runs is shown in figure 1. This showed that there was more reduction in the pore volume of the core sample as a result of high density saline water occupying more spaces within the pore matrix of the core sample. The dispersion coefficient, however, increases appreciably when Run 4 was compared to the dry core values. Honari et al. (2016) stated that this increase in dispersion is a result of connate water occupying smaller rock pores and constricting the flow paths, making them narrower, which eventually increases the dispersion and or mixing between the injected CO_2 and displaced CH_4. Additionally, run 5 thus showed a deviant trend in that it significantly showed a decrease in dispersion coefficient during the displacement process. This can be explained by the experiment carried out by Cui et al. (2016) that showed that with increase in formation temperature, the formation salinity will intensify formation damage as a result of salt precipitation. In this case, the salt precipitates will plug the smaller narrower pores making the core sample even more homogeneous with less tortuous flow paths. Therefore, less mixing/dispersion.

Table 3—Summary of experimental parameters

Runs	Swi	Flow rate (mL/min)	interstitial velocity (cm/s)	Temperature (°C)	Pressure (psig)	BT (min)	KL, 10^{-3} cm²/s	D, 10^{-1} cm²/s
Run 1	0.0	0.25	0.041	40	1300	52.70	1.16	
Run 2	0.0	0.25	0.041	40	1300	53.32	1.18	
Run 3	0.0	0.25	0.041	40	1300	55.32	1.14	2.12
Run 4	0.1	0.25	0.041	40	1300	46.32	1.46	
Run 5	0.1	0.25	0.041	40	1300	39.82	0.72	

Conclusion

Displacement experiments were carried out to investigate the effect of salinity on the displacement efficiency of CH_4 by CO_2 at conditions relevant to EGR. The results show that there was low dispersion coefficient in experimental run where there was high salinity initial water saturation compared to the significant increase in dispersion coefficient in the case of distilled water saturated core in relation to dry core runs. In all the runs, the diffusion was the dominant displacement mechanism. Future work will investigate the salinity effect on displacement during enhanced gas recovery at different operational conditions.

Acknowledgement

Nomenclature

C = CO_2 mole fraction
D = Diffusion coefficient, mm²/s
d = medium characteristic length scale, m
K_L = longitudinal dispersion, mm²/s
L = core sample length, mm
L_{exp} = experimental length as suggested by Hughes et al, m

P = Pressure, psig
P_e = Peclet number
P_{em} = medium Peclet number
Q = flowrate, ml/min
r = radius of core sample, mm
T = Temperature, °C
t = time, min
t_D = dimensionless time, defined in *eqn 3*
u = interstitial velocity, mm²/s
x = distance from the upstream of the core face, m
x_D = dimensionless distance, defined in *eqn 3*
ϕ = core porosity

References

Al-Abri, A., Hiwa S. & Robert A., 2009. Experimental investigation of the velocity-dependent relative permeability and sweep efficiency of supercritical CO2 injection into gas condensate reservoirs. *Journal of Natural Gas Science and Engineering*, **1**(4-5), pp.158-164. Available at: http://dx.doi.org/10.1016/jjngse.2009.10.002.

Al-abri, A., Sidiq H. & Amin R., 2009. Enhanced Natural Gas and Condensate Recovery by Injection of Pure SCCO2, Pure CH4 and Their Mixtures: Experimental Investigation. SPE Annual Technical Conference and Exhibition, New Orleans, Lousiana, USA, 4-7 October, pp.1-13.

Al-Abri, A., Sidiq H. & Amin R., 2012. Mobility ratio, relative permeability and sweep efficiency of supercritical CO2 and methane injection to enhance natural gas and condensate recovery: Coreflooding experimentation. *Journal of Natural Gas Science and Engineering*, **9**, pp.166-171. Available at: http://dx.doi.org/10.1016/jjngse.2012.05.011.

Amin, R. et al., 2010. Gas-gas experimental interfacial tension measurement. *Fluid Phase Equilibria*, **295**(2), pp.230-236.

Benson, S. et al., 2005. Underground geological storage. *Ipcc*, pp.195-276.

Cui, G. et al., 2016. Formation water evaporation induced salt precipitation and its effect on gas production in high temperature natural gas reservoirs. *Petroleum Exploration and Development*, **43**(5), pp.815-824. Available at: http://dx.doi.org/10.1016/S1876-3804(16)30097-0.

Honari, A. et al., 2013. Dispersion of supercritical CO2 and CH4 in consolidated porous media for enhanced gas recovery simulations. *International Journal of Greenhouse Gas Control*, **19**, pp.234-242. Available at: http://dx.doi.org/10.1016/j.ijggc.2013.08.016.

Honari, A. et al., 2015. Enhanced gas recovery with {CO2} sequestration: The effect of medium heterogeneity on the dispersion of supercritical CO2-CH4. *International Journal of Greenhouse Gas Control*, **39**(0), pp.39-50. Available at: http://www.sciencedirect.com/science/article/pii/S1750583615001577.

Honari, A. et al., 2016. The impact of residual water on CH4-CO2 dispersion in consolidated rock cores. *International Journal of Greenhouse Gas Control*, **50**, pp. 100-111. Available at: http://dx.doi.org/10.1016Zj.ijggc.2016.04.004.

Hughes, T.J. et al., 2012. CO2 sequestration for enhanced gas recovery: New measurements of supercritical CO2-CH4 dispersion in porous media and a review of recent research. *International Journal of Greenhouse Gas Control*, **9**, pp.457-468. Available at: http://dx.doi.org/10.1016/jijggc.2012.05.011.

Kalra, S. & Wu X., 2014. CO2 injection for Enhanced Gas Recovery. *SPE Western North American and Rocky Mountain …*, (April), pp.16-18. Available at: https://www.onepetro.org/conference-paper/SPE-169578-MS.

Khan, C., Amin R. & Madden G., 2013. Carbon dioxide injection for enhanced gas recovery and storage (reservoir simulation). *Egyptian Journal of Petroleum*, **22**(2), pp.225-240. Available at: http://www.sciencedirect.com/science/article/pii/S1110062113000500.

Liu, S. et al., 2015. Laboratory experiment of CO2-CH4 displacement and dispersion in sandpacks in enhanced gas recovery. *Journal of Natural Gas Science and Engineering*, **26**, pp.1585-1594. Available at: http://dx.doi.org/10.1016/jjngse.2015.04.021.

Mamora, D.D. & Seo J.G., 2002. Enhanced Recovery by Carbon Dioxide Sequestration in Depleted Gas Reservoirs. SPE Annual Technical Conference and Exhibition, pp.1-9.

Newberg, M.. & Foh S., 1988. Measurement of Longitudinal Dispersion Coefficients for Gas Flowing Through Porous Media. *SPE*, pp.5-9.

Nogueira, M. & Mamora D.D., 2005. Effect of Flue-Gas Impurities on the Process of Injection and Storage of CO2 in Depleted Gas Reservoirs. *Journal of Energy Resources Technology*, **130**(1), p.13301.

Oldenburg, C.M. & Benson S.M., 2002. CO2 Injection for Enhanced Gas Production and Carbon Sequestration. SPE International Petroleum Conference and Exhibition in Mexico. Available at: http://www.onepetro.org/doi/10.2118/74367-MS.

Patel, M.J., May E.F. & Johns M.L., 2016. High-fidelity reservoir simulations of enhanced gas recovery with supercritical CO2. *Energy, IN PRESS*, pp.548-559. Available at: http://dx.doi.org/10.1016/j.energy.2016.04.120.

Perkins, T.K. Johnston, O.C., 1963. A Review of Diffusion and Dispersion in Porous Media. *Society of Petroleum Engineers Journal*, **3**(1), pp.70-84.

Pooladi-Darvish, M. et al., 2008. CO2 injection for enhanced gas recovery and geological storage of CO2 in the Long Coulee Glauconite F Pool, Alberta. Proceedings - SPE Annual Technical Conference and Exhibition, **4**, pp.2271-2281. Available at: http://www.scopus.com/scopus/inward/record.url?eid=2-s2.0-58849157975&partnerID=40.

Shtepani, E., 2006. CO2 sequestration in depleted gas/condensate reservoirs. Proceedings - SPE Annual Technical Conference and Exhibition.

Sidiq, H. et al., 2011. Super critical CO2-methane relative permeability investigation. *Journal of Petroleum Science and Engineering*, **78**(3-4), pp.654-663.

Sidiq, H. & Amin R., 2009. Mathematical model for calculating the dispersion coefficient of super critical CO2 from the results of laboratory experiments on enhanced gas recovery. *Journal of Natural Gas Science and Engineering*, **1**(6), pp.177-182. Available at: http://dx.doi.org/10.1016/j.jngse.2009.11.001.

Sim, S. et al., 2009. Enhanced Gas Recovery: Effect of Reservoir Heterogeneity on Gas-Gas Displacement. Candian International Petroleum Conference, (June), pp.1-14.

Sim, S.S.K. et al., 2009. Enhanced gas recovery: Factors affecting gas-gas displacement efficiency. *Journal of Canadian Petroleum Technology*, **48**(8), pp.49-55.

Sim, S.S.K. et al., 2008. SPE 113468 Enhanced Gas Recovery and CO 2 Sequestration by Injection of Exhaust Gases from Combustion of Bitumen. *Changes*, (1), pp.1-10.

Turta, A.T. et al., 2007. Basic Investigations on Enhanced Gas Recovery by Gas-Gas Displacement.

Zhang, Y. et al., 2014. Experimental investigation of CO2-CH4 displacement and dispersion in sand pack for enhanced gas recovery. *Energy Procedia*, **61**, pp.393-397. Available at: http://dx.doi.org/10.1016/j.egypro.2014.11.1133.

Th CO2 P03

Effects Of Gravity On Flow Behaviour Of Supercritical CO2 During Enhanced Gas Recovery (EGR) By CO2 Injection And Sequestration

M. Abba[1]*, A. Abbas[1], B. Saidu[1], G. Nasr[1], A. Al-Otaibi[1]
[1]University Of Salford

Summary

A core flooding experiment was carried out to simulate an Enhanced Gas Recovery (EGR) process to inject supercritical Carbon Dioxide (SCO2) into a core sample saturated with methane (CH4). This was done to investigate the flow behaviour of the injected SCO2 at the flow conditions when the injection orientation was switched from horizontal to vertical during the CH4 displacement. From the results, it was found that gravity has significant effects on the flow behaviour of SCO2 at lower flowrates; more pronounced is the seemingly lower permeability in the horizontal orientation compared with the vertical orientation. So the choice of the injection pattern or direction during EGR by SCO2 injection for the purpose of additional recovery of CH4 and subsequent sequestration of the injected CO2 should be made in conjunction with the determination of optimum injection rate for efficient injectivity.

Introduction

CO₂ underground storage for the purpose of reduction of anthropogenic greenhouse gas (GHG) emissions is gaining attention globally (Ganjdanesh & Hosseini 2017; Raza *et al*. 2017). These underground storage sites can be in the form of oil and gas reservoirs or deep saline aquifers. To effectively store the undesirable CO₂ underground, some economic incentives add additional shock-value to the process as a whole. These incentives come in the form of economies of scale derivable from the additional recovery of oil and gas resources from the CO₂ storage sites. Pre-existing techniques in the oil and gas industry, termed Enhanced Oil/Gas Recovery (EOR/EGR), are in place to produced additional oil and gas trapped in the reservoir after primary production of the hydrocarbon (HC) resource. These techniques have the potential to be promising methods of CO₂ storage and sequestration (Kalra & Wu 2014). Natural gas reservoirs have the potential to safely store this anthropogenic CO₂. There are a number of reasons, presented by (Kalra & Wu 2014), why the choice of natural gas reservoirs as best potential sequestration site (Raza *et al*. 2017). One of the reasons is its proven integrity in that they have stored natural gas for a million of years. Hence, the problems of leakages and contamination of adjacent fresh water aquifers for domestic use is solved. This calls for the development and optimisation of techniques to efficiently carryout these simultaneous advantages of storing and sequestering large volumes of CO₂ and at the same time recover additional HC resources.

Exploring this opportunity to its fullest, however, requires the investigation of the interplay between the gas species at underground/reservoir conditions. CO₂ injectivity is an area in CO₂ sequestration which is still under investigation. Injectivty is the sustainable flow capacity of CO₂ from the injection well i.e. the transmissivity or how fast can CO₂ be injected through the well. CO₂ reaches its critical point at a pressure of 73.7 bar (1070 psi) and temperature of 31°C (87.8°F). Gas reservoirs, however, are well above these critical conditions of CO₂ and CO₂ will be in its supercritical state and will exhibit certain behaviour which deviates from a normal gas and will have an influence on the injectivity. This work focuses on the flow behaviour of supercritical CO₂ at reservoir conditions in relation to its injection orientation to assess the effects of gravity. This is vital as it will provide reservoir engineers with tools to better characterise the transport of injected supercritical CO₂ in the reservoir for enhanced gas recovery and sequestration.

Methodology and Theory

This work employed an experimental approach where a laboratory core flooding process was carried out to simulate the displacement of natural gas (CH₄) by supercritical CO₂ during EGR at 1300 psig pressure, 50°C temperature, and flowrate was varied from 0.2-0.5 ml/min. These conditions are chosen in accordance with the works of (Abba *et al*. 2017). The core flooding was carried out using a *Bandera Grey* sandstone core sample, 10 md permeability, in horizontal and vertical orientations. The results from both experiments were compared and analysed to evaluate the extent of the effect of gravity on the flow behaviour which may have an influence on the injectivity of the CO₂ in terms of efficient displacement. The governing transport equation that best describes the specie transport for EGR is the 1- D Advection Dispersion equation as described by (Perkins, T.K. Johnston 1963; Coats *et al*. 1964; Newberg & Foh 1988; Coats *et al*. 2009) and is given by:

$$K_l \frac{\partial^2 c}{\partial x^2} - u \frac{\partial c}{\partial x} = \frac{\partial c}{\partial t} \qquad\qquad 1$$

Where, C is the CO₂ concentration at location x at time t, K_l is the coefficient of longitudinal dispersion, and u is the interstitial velocity. Furthermore, D'Arcy equation, after Henry D'Arcy (1856), will be used to relate the pressure differential with time to simplify the flow behavioural depiction. The model is valid in for low injection rate, in our case, given that the inertial effect may not be significant to render the Darcy law assumption invalid (Mijic *et al*. 2014). It can adequately describe the flow in the experiment. Darcy equation is described as:

$$Q = \frac{kA\partial P}{\mu L} \qquad 2$$

Where Q is the flow rate (cm^3), k is permeability (md), P is pressure (atm), μ is viscosity (cp), A is cross sectional area (cm^2), and L is length of sample (cm).

The procedure followed a core flooding set up suited for gas-gas displacement process where the CO_2 was injected at a constant flowrate of 0.2-0.5 ml/min into the core sample from the accumulator. This was to displace the CH_4 earlier saturated in the core sample at a pressure of 1300 psig and a temperature of 50°C. The effluents rates were measured by flow meters and their composition were measured with a gas chromatograph until the volumes of the CH_4 were insignificant where the experiment came to an end. The sample procedure was used in both vertical and horizontal orientations.

Results and Discussion

Having carried out the experiment at varying flowrates and at different orientations to investigate the effect of gravity on the flow behaviour of supercritical CO_2, the results were presented in such way to observe the difference in the differential pressures (dP) during the flooding process against time for each of the investigated flowrates. From the results obtained, *Figure 1* to *Figure 4*, the dP during the displacement process of the CH_4 by CO_2 varies significantly with increase in injection rates as the orientation of the core sample was changed from horizontal to vertical. The most notable deviations were from the low injection rates of 0.2 and 0.3 ml/min (*Figure 1* and **Figure 2** respectively). The horizontal dP from these runs were higher, meaning that the permeability was lower, according to Darcy Law, in the horizontal orientation. Gravity is most influential at these flow rates and at this orientation and hence affects the flow behaviour of the supercritical CO_2 during EGR. However, *Figure 3* and *Figure 4* have almost similar trend in dP fluctuations and magnitude, i.e. the various supercritical CO_2 permeabilities to the core sample of the higher flow rates are not grossly affected by the orientation of the injection. Hence, gravity has the most effects on flow behaviour of the supercritical CO_2 at lower injection rates.
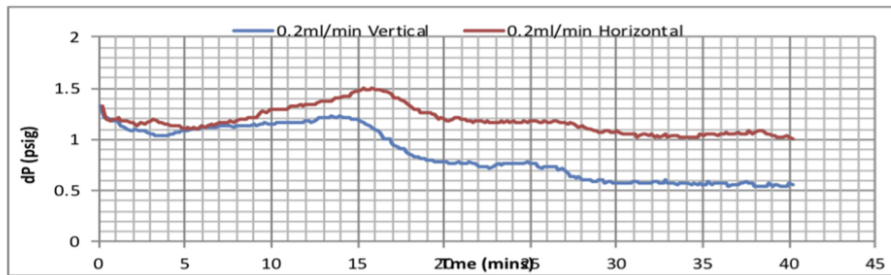
Figure 1 *Differential pressure as a function of time in vertical and horizontal orientations for 0.2 ml/min.*
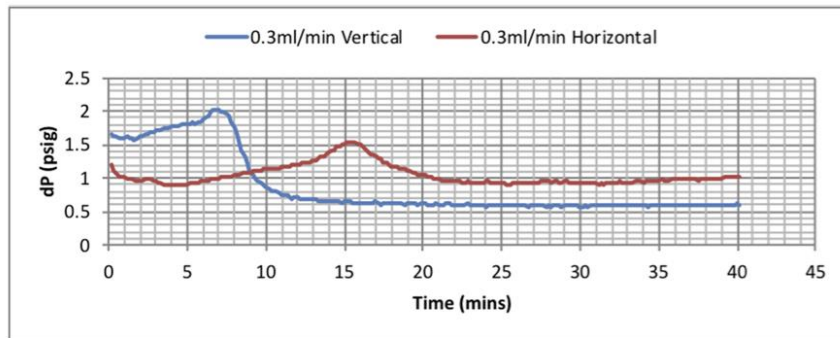
Figure 2 *Differential pressure as a function of time in vertical and horizontal orientations for 0.3 ml/min.*
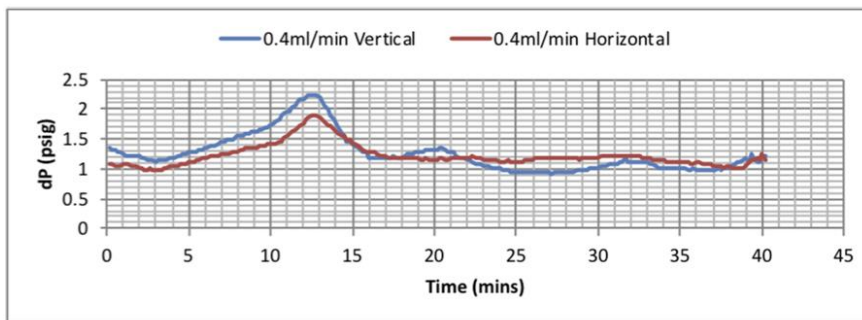
Figure 3 *Differential pressure as a function of time in vertical and horizontal orientations for 0.4 ml/min.*
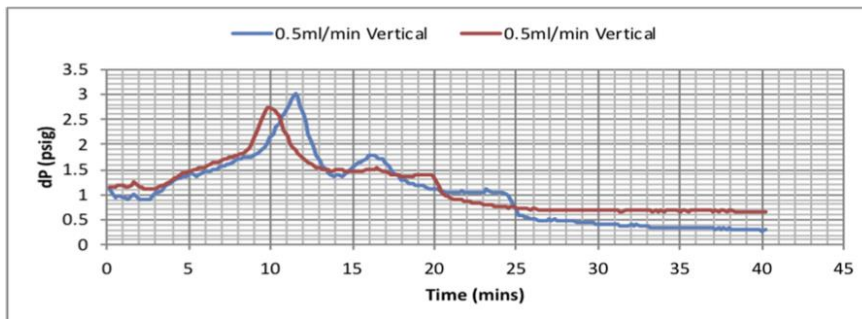
Figure 4 *Differential pressure as a function of time in vertical and horizontal orientations for 0.5 ml/min.*

Conclusion

The investigation of the gravity effects on the flow behaviour of supercritical CO_2 was successfully carried out. Gravity is more dominant at lower injection rates as presented. CO_2 permeability at these supercritical conditions is higher in the vertical orientation compared to the horizontal direction. Therefore, CO_2 injectivity may significantly be affected by the orientation of the injection into the displacing reservoir. Optimum CO_2 injection rate determination is vital in order to adequately and

efficiently displace the nascent CH_4 with good sweep efficiency and minimise contamination of the recovered CH_4 with less injected fluid resident time.

Acknowledgement

References

Abba, M.K., Abbas, A.J. & Nasr, G.G., 2017. Enhanced Gas Recovery by CO_2 Injection and Sequestration: Effect of Connate Water Salinity on Displacement Efficiency. *SPE Abu Dhabi International Petroleum Exhibition & Conference*. Available at: http://www.onepetro.org/doi/10.2118/188930-MS.

Coats, K.H. *et al*., 1964. Dead-End Pore Volume and Dispersion in Porous Media. *Soil Science Society of America Journal*, 4(01), pp.73–84. Available at: https://www.soils.org/publications/sssaj/abstracts/40/4/473.

Coats, K.H., Whitson, C.H. & Thomas, K., 2009. Modeling Conformance as Dispersion. *SPE Reservoir Evaluation & Engineering*, 12(01), pp.33–47. Available at: https://www.onepetro.org/journal-paper/SPE-90390-PA.

Ganjdanesh, R. & Hosseini, S.A., 2017. Geologic Carbon Storage Capacity Estimation Using Enhanced Analytical Simulation Tool (EASiTool). *Energy Procedia*, 114(November 2016), pp.4690–4696. Available at: http://dx.doi.org/10.1016/j.egypro.2017.03.1601.

Kalra, S. & Wu, X., 2014. CO_2 injection for Enhanced Gas Recovery. *SPE Western North American and Rocky Mountain ...*, (April), pp.16–18. Available at: https://www.onepetro.org/conference-paper/SPE-169578-MS.

Mijic, A., LaForce, T.C. & Muggeridge, A., 2014. CO_2 injectivity in saline aquifers: the impact of non darcy flow, phase misciibility and gas compressibility. *Water Resources Research*, WR014893(May), pp.4163–4185.

Newberg, M.. & Foh, S.., 1988. Measurement of Longitudinal Dispersion Coefficients for Gas Flowing Through Porous Media. *SPE*, pp.5–9.

Perkins, T.K. Johnston, O.C., 1963. A Review of Diffusion and Dispersion in Porous Media. *Society of Petroleum Engineers Journal*, 3(01), pp.70–84.

Raza, A. *et al*., 2017. Preliminary assessment of CO2injectivity in carbonate storage sites. *Petroleum*, 3(1), pp.144–154. Available at: http://dx.doi.org/10.1016/j.petlm.2016.11.008.

Appendix B: Gas chromatography method and sequence

The method and sequence adopted for this experiment is shown below as extracted from the Agilent Gas Chromatograph 7890A.

```
                        Method Information

       Method: C:\CHEM32\7890_EGR - COPY\7890-0192.M
     Modified: 2/10/2017 at 3:10:50 PM

   EGR Analysis



                        Run Time Checklist

         Pre-Run Cmd/Macro:  off

          Data Acquisition:  on

   Standard Data Analysis:  on

 Customized Data Analysis:  off

            Save GLP Data:  off

       Post-Run Cmd/Macro:  off


     Save Method with Data:  on



                   Injection Source and Location

     Injection Source:   GC Valve

     Injection Location: Valve 1

=======================================================================
                        Agilent 7890A
=======================================================================

Oven
Equilibration Time                          3 min
Max Temperature                             350 degrees C
Slow Fan                                    Disabled
Oven Program                                On
    130 °C for 5 min
Run Time                                    5 min
Cryo                                        Off

Sample Overlap
Sample overlap is not enabled

Front PP Inlet He
```

```
Heater                                          On     150 °C
Pressure                                        On     79.008 psi
Total Flow                                      On     35 mL/min
Septum Purge Flow                               On     3 mL/min


Thermal Aux 1 (Unknown)
Heater                                          On
Temperature Program                             On
     135 °C for 0 min
Run Time                                        5 min


Thermal Aux 2 (Unknown)
Heater                                          On
Temperature Program                             On
     135 °C for 0 min
Run Time                                        5 min


Column #1
350 °C: 30 m x 320 µm x 0 µm
In: Front PP Inlet He
Out: Front Detector TCD


(Initial)                                       130 °C
Pressure                                        79.008 psi
Flow                                            32 mL/min
Average Velocity                                206.55 cm/sec
Holdup Time                                     0.24207 min
Flow Program                                    On
     32 mL/min for 0 min
Run Time                                        5 min


Front Detector TCD
Heater                                          On     150 °C
Reference Flow                                  On     45 mL/min
Makeup Flow                                     On     2 mL/min
Const Col + Makeup                              Off
Negative Polarity                               Off
Filament                                        On


Valve 1
Gas Sampling Valve
GSV Loop Volume                                 1 mL
Load Time                                       0.05 min
Inject Time                                     0.05 min


Valve 2
Other                                           On


Valve 3
Other                                           Off


Signals
Signal #1: Front Signal                         Save On
                                                20 Hz


Signal #2: None


Signal #3: None
```

235

Appendix C: Scanning Electron Microscopy (SEM) Images

Buff Berea at different magnification
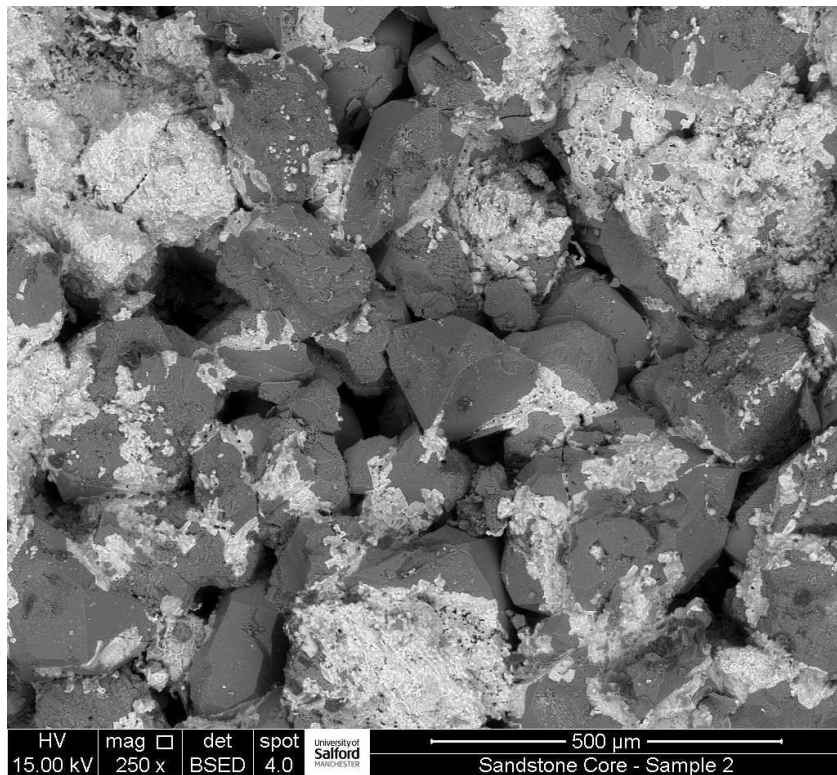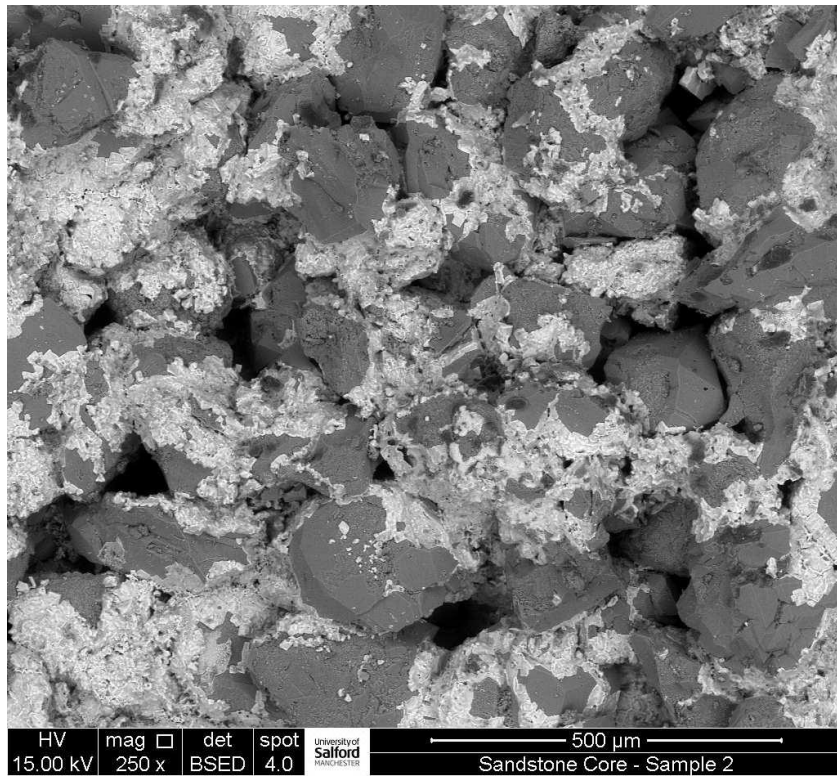
Bandera Grey at different magnification
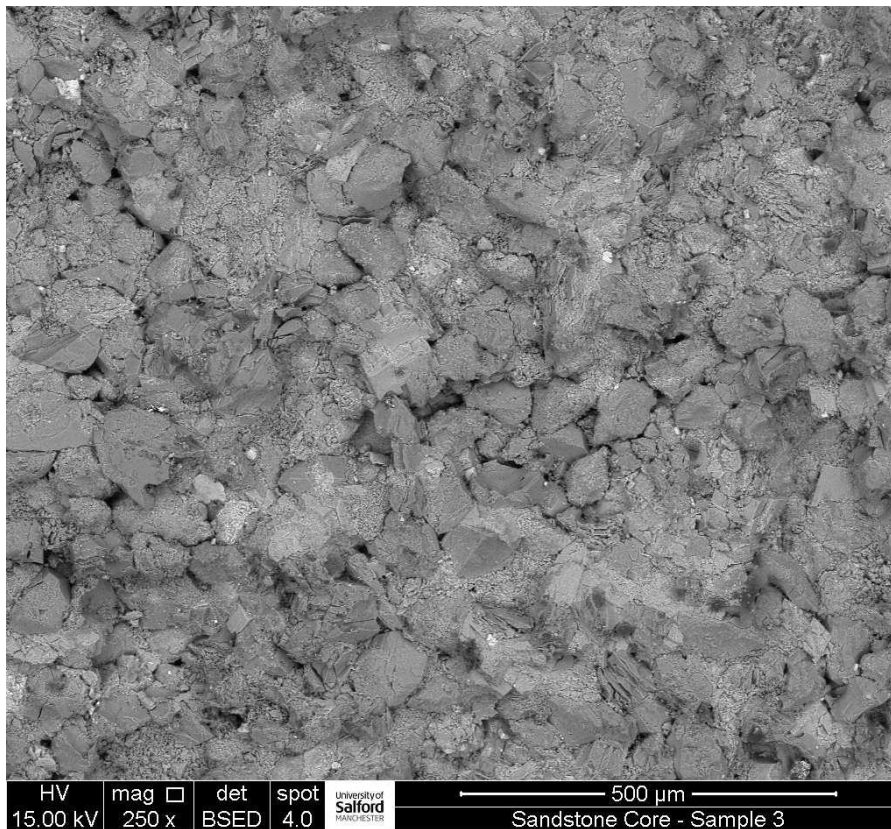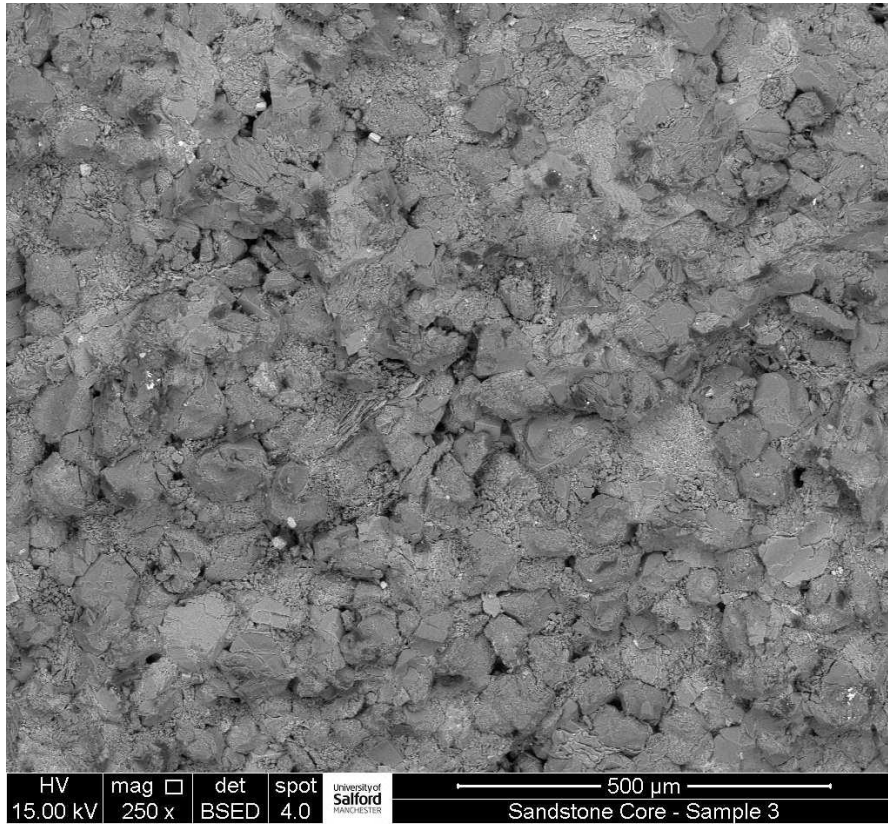
Grey Berea at different magnification
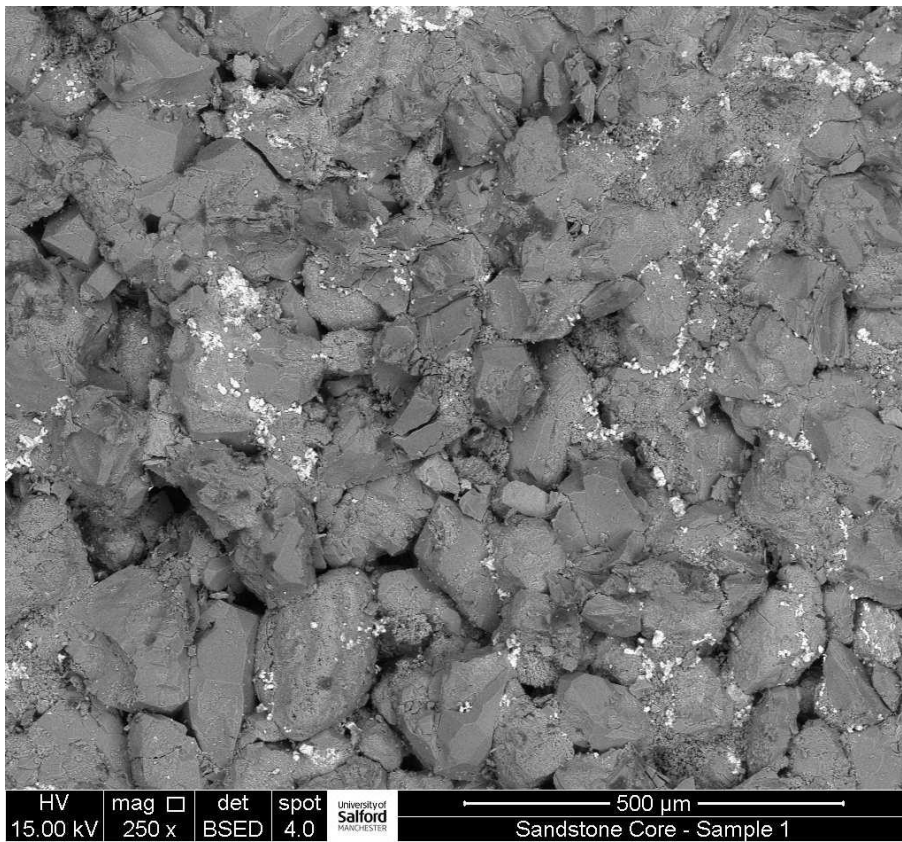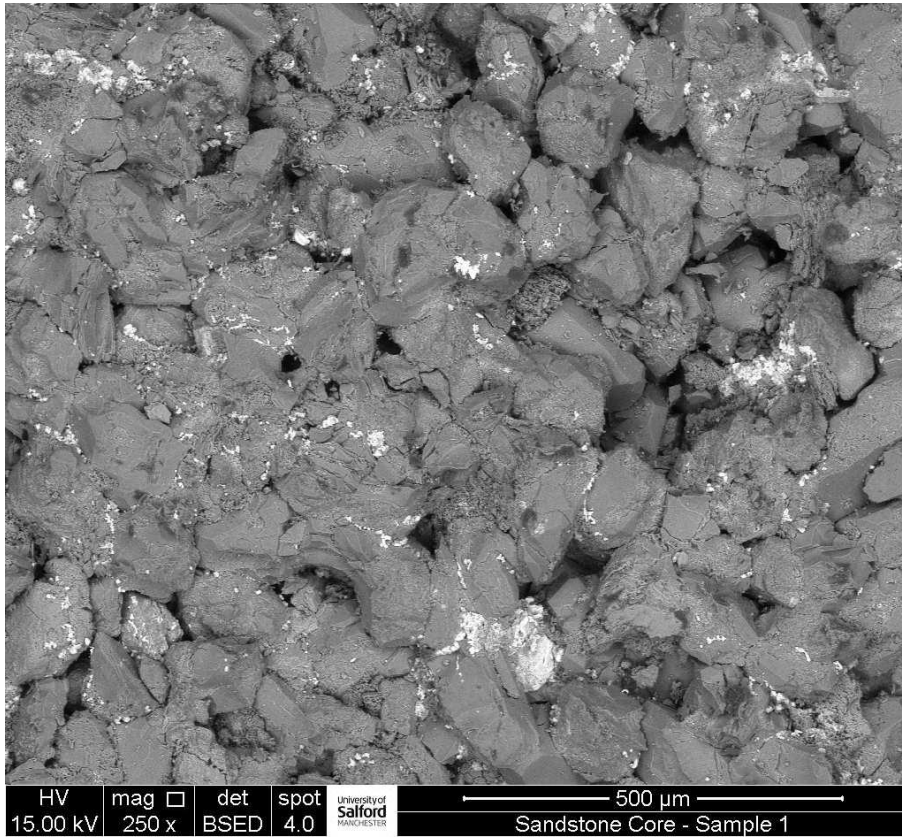
Appendix D: Bubbles from IFT measurements

Methane and brine bubbles
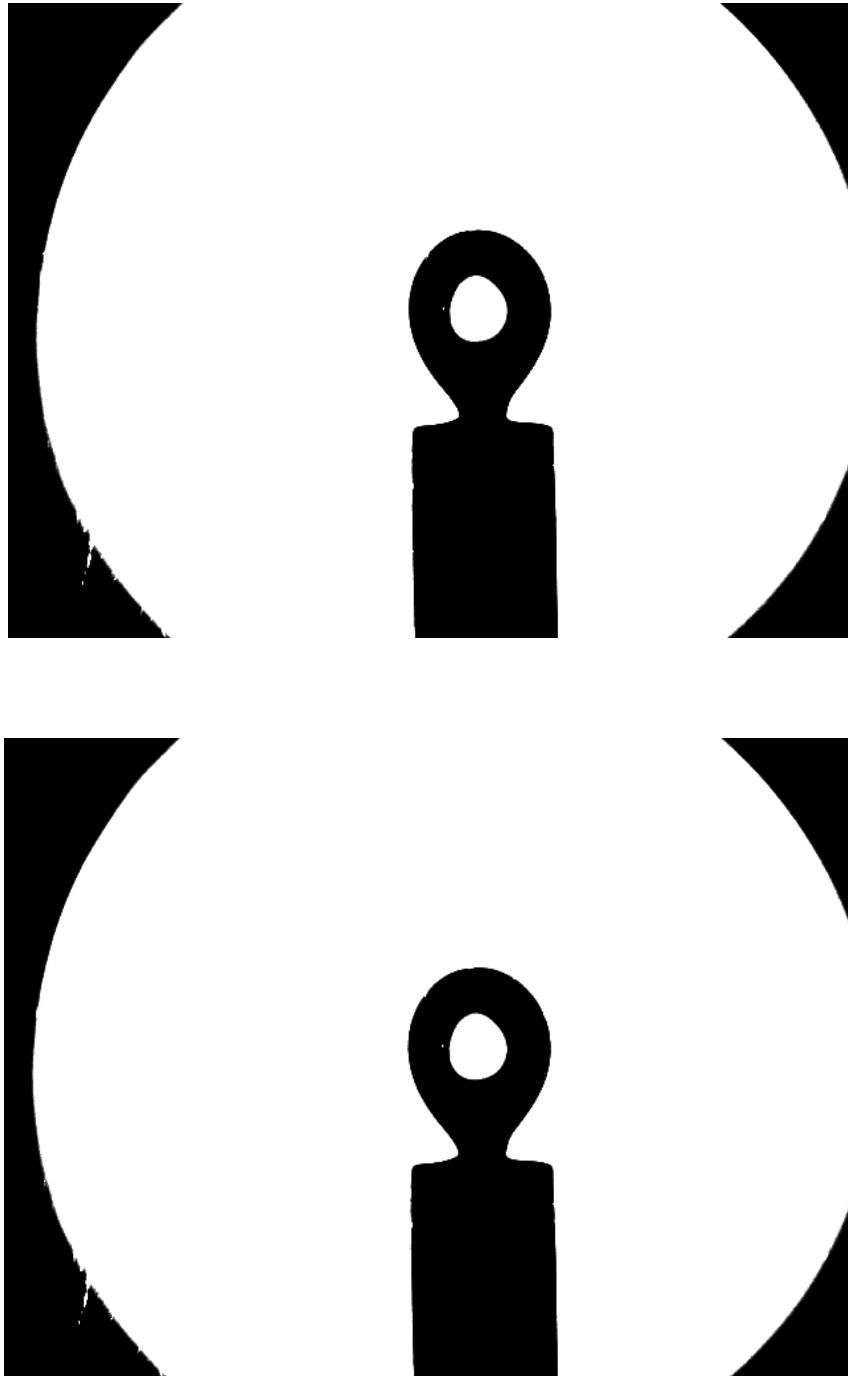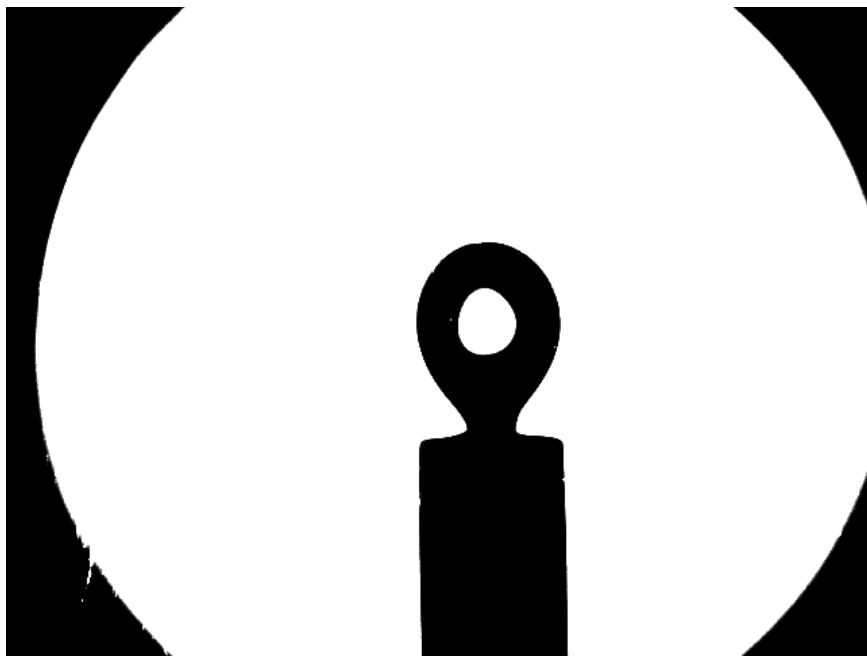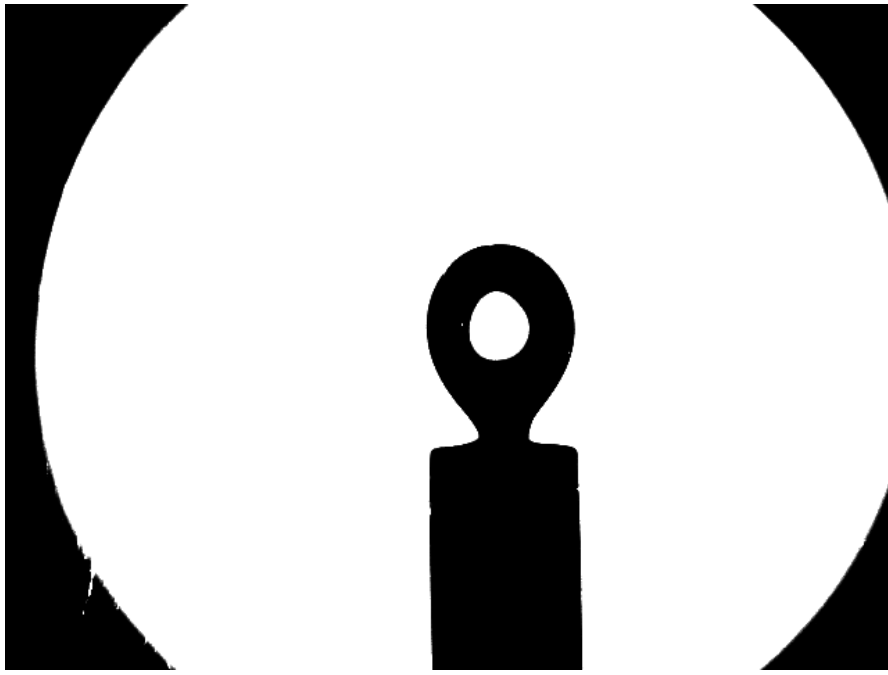
Carbon Dioxide and Brine
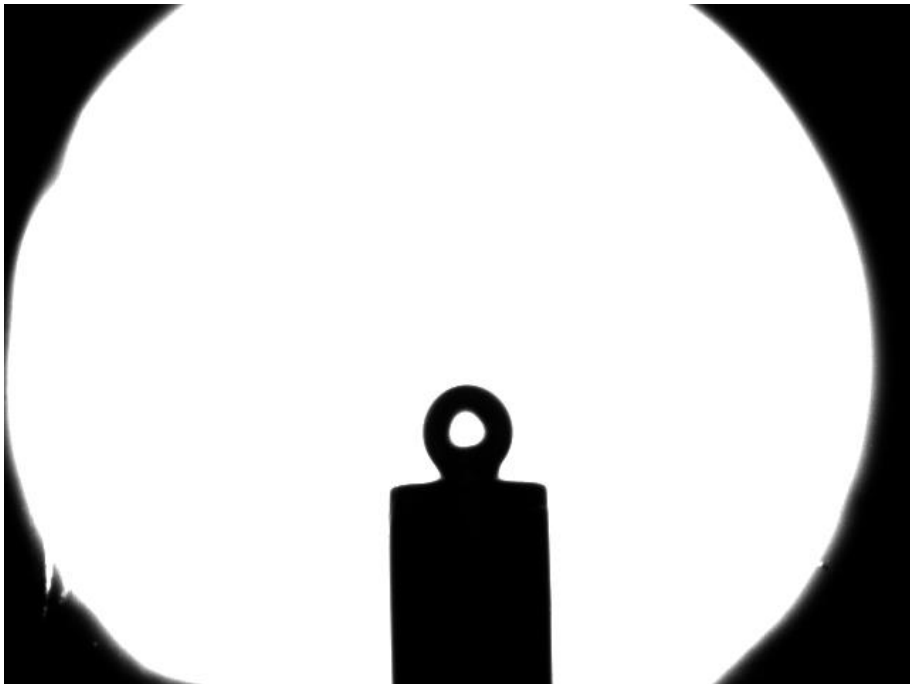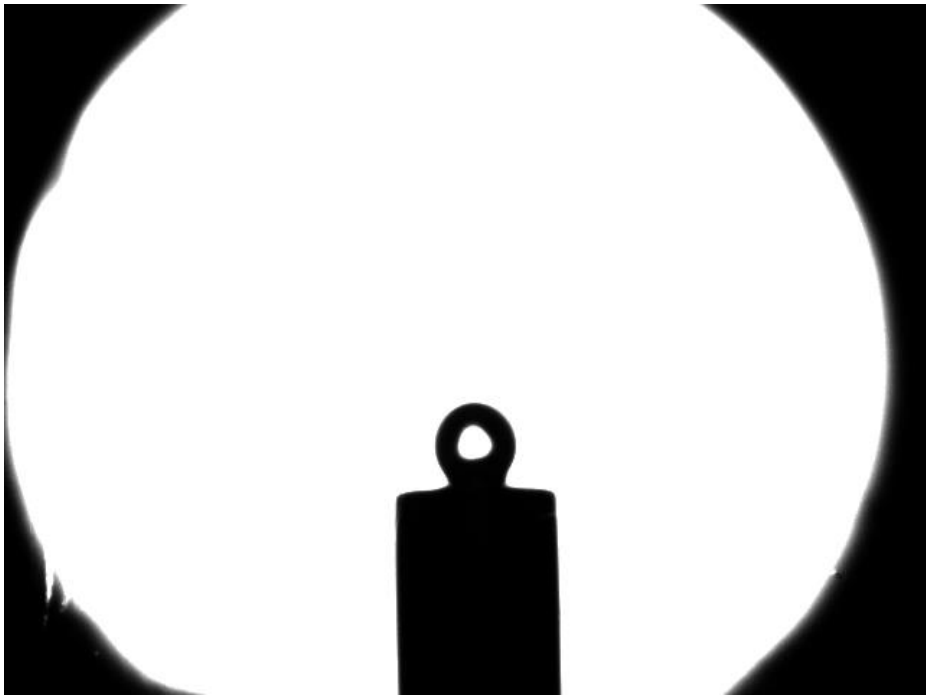
Appendix E: MATLAB program for *z* factor determination

```matlab
% Compressibility modelling
% Input parameters for constants evaluation
      w = 0.228;
      R = 8.3145;
      Tc = 304.5;
      Pc = 73;
      d1 = 1+(sqrt (2))
      d2 = 1-(sqrt (2))

  P = input ('Enter Pressure in bar > ');
  T = input ('Enter Temperature in Kelvin > ');


      alt = (1+(0.37646+1.4522*w - 0.26992*w^2) *(1 - sqrt(T/Tc)) ^2)

% Where the variables are defined as

      a = 0.46724*((R^2*Tc^2)/(Pc)) *alt
      b = 0.07780*((R*Tc)/Pc)

% and also:

      A = (a*P/(R*T) ^2)
      B = (b*P/R*T)

% solve for z in the model ('z^3 -(1-B) *z^2 + (A-2*B-3*B^2) *z-(')
      z = roots ([1 (-(1-B)) (A-2*B-3*B^2) (-(A*B -B^2-B^3))])

% when the cubic root is evaluated - the highest values and lowest of
the cube root are inputted

      zh = input ('Enter zh >')
      zl = input ('Enter zl >')

% These are used to solve for the next expression for Gibbs energy
model

      J = ((zl-B)/(zh-B))- (A/(B*(d2-d1)))
      K = ((zl +d1*B)/ (zl + d2*B) *((zh +d2*B)/(zh+d1*B)))

% Gibbs energy model is given by
Gibbs = (zh - zl) + log (K)*log (J)


% If Gh - Gl/RT = +, Zl is used
% if Gh - Gl/RT = -, Zh is used


OUTPUT
          d1 = 2.4142
          d2 = -0.4142


          alt = 1.0001
```

243

```
a = 4.1032e+04
b = 2.6982


A = 0.5816
B = 9.7512e+03


z =
   1.0e+04 *

   -2.3542
    0.9352
    0.4039


zh = 0.9752
zl = 0.4039


J = 1.0001

K = 0.9998

Gibbs = 0.5713
```

Appendix F: Solution to dimensionless advection dispersion equation

Solution process

a. The PDE is converted into ODE employing Laplace Transforms
b. Evaluate the solution for the converted ODE
c. The ODE solution is then inverted to obtain the PDE solution

$$\frac{\partial C}{\partial t_D} = \frac{1}{P_e}\frac{\partial^2 C}{\partial x_D^2} - \frac{\partial C}{\partial x_D} \tag{1}$$

Thus

$$\frac{\partial C}{\partial t_D} - \frac{1}{P_e}\frac{\partial^2 C}{\partial x_D^2} + \frac{\partial C}{\partial x_D} = 0 \tag{2}$$

The boundary conditions

$$C = 0 \; at \; t_D = 0, 0 < x_D < \infty \tag{3}$$

$$C = 1 \; at \; x_D = 0, t_D > 0 \tag{4}$$

$$C \to 0 \; at \; x_D \to \infty, t_D > 0 \tag{5}$$

Using C_T to represent C in the Laplace Transforms;

$$C_T = L\,[C] = \int_0^\infty e^{-st} C \; dt \tag{6}$$

The transformed equation is thus

$$[s\,C_T - C(0)] + \frac{\partial C_T}{\partial x_D} - \frac{1}{Pe}\frac{\partial^2 C_T}{\partial x_D^2} = 0 \tag{7}$$

Applying the boundary conditions

$$C_T = (A)e^{mx_D} \tag{8}$$

$$\frac{dC_T}{dx_D} = (Am)e^{mx_D} \tag{9}$$

$$\frac{d^2 C_T}{dx_D^2} = (Am^2)e^{mx_D} \tag{10}$$

Substituting equations (8) (9) (10) into (7)

245

$$m^2 - Pe\,m - Pe = 0 \qquad (11)$$

Transform boundary conditions

$$C_T = \frac{1}{s} \ at \ x_D = 0 \qquad (12)$$

$$C_T \ \to 0 \ as \ x_D \ \to \ \infty$$

From

$$m = \frac{Pe \ \pm \ \sqrt{Pe^2 + 4\,Pe}}{2s} \qquad (13)$$

Substitute Eq. (13) into (8)

$$C_T = A\,e^{\left[\frac{Pe \ \pm \ \sqrt{Pe^2 + 4\,Pe\,s}}{2} \ x_D \right]} \qquad (14)$$

Where, $\sqrt{Pe^2 + 4\,Pe\,s} \ > Pe$

Using the negative root to satisfy of Eq. (12) conditions

$$C_T = A\,e^{\left[\frac{Pe \ - \ \sqrt{Pe^2 + 4\,Pe\,s}}{2} \ x_D \right]} \qquad (15)$$

$$A = \frac{1}{s} \qquad (16)$$

Since,

$$C_T = \frac{1}{s} \ at \ x_D = 0$$

Therefore,

$$C_T = \frac{1}{s}\,e^{\left[\frac{Pe \ \pm \ \sqrt{Pe^2 + 4\,Pe\,s}}{2} \ x_D \right]} \qquad (17)$$

To invert Eq. (17), a shifted Laplace variable is defined as follows

Let

$$G = s + \frac{Pe}{4} \qquad (18)$$

Where G is the defined shifted Laplace transform variable

Substituting the Eq into Eq. (17)

$$C_T = \cfrac{1}{P - \cfrac{Pe}{4}} e\left(\cfrac{Pe\, x_D}{2}\right) e(-x_D\sqrt{Pe\, G}) \qquad (19)$$

Comparing Eq with a table of Laplace transforms

$$f(G) = \cfrac{e^{-qx}}{G - \alpha} \qquad (20)$$

$$q = \sqrt{\cfrac{G}{k}} \qquad (21)$$

$$\alpha = \cfrac{Pe}{4} \qquad (22)$$

$$x = x_D \qquad (23)$$

$$k = \cfrac{1}{Pe} \qquad (24)$$

$$C = \cfrac{1}{2} e\left(\cfrac{Pe\, t}{4}\right)\left\{ erfc\left[\cfrac{x_D - t}{2\sqrt{\cfrac{t}{Pe}}}\right] + e(Pex_D)\, erfc\left[\cfrac{x_D + t}{2\sqrt{\cfrac{t}{Pe}}}\right] \right\} = F(td) \qquad (25)$$

To obtain $F(td)$ we use the shifting property of the Laplace transform

$$L^{-1}\left[f\left(s + \cfrac{Pe}{4}\right)\right] = L^{-1}\left[f\left(s - \left(\cfrac{-Pe}{4}\right)\right)\right] = L^{-1}[f(s - a)] \qquad (26)$$

Where

$$a = \cfrac{-Pe}{4} \qquad (27)$$

So,

$$L^{-1}\left[f\left(s + \cfrac{Pe}{4}\right)\right] = e\left(\cfrac{Pe}{4}t\right) F(t) = F(t_D) \qquad (29)$$

And combining Eq. (29) and Eq. (25) yields,

$$C = \cfrac{1}{2}\left\{ erfc\left[\cfrac{x_D - t_D}{2\sqrt{\cfrac{t_D}{Pe}}}\right] + e(Pex_D)\, erfc\left[\cfrac{x_D + t_D}{2\sqrt{\cfrac{t_D}{Pe}}}\right] \right\} \qquad (30)$$

Appendix G: Grain diameter Tables

Table 1: Grain diameter results from ImageJ for Grey Berea

	Area (µm²)	Mean (µm²)	Min	Max	Diameter (µm)
1	10307.76	124.865	0	255	114.5537
2	28332.78	118.391	0	255	189.9204
3	13530.29	149.204	0	255	131.2443
4	7779.648	135.292	0	255	99.5192
5	5880.85	101.211	0	255	86.52607
6	10296.91	110.625	0	255	114.4934
7	24269.35	110.66	0	255	175.7746
8	5479.389	131.178	0	228	83.52048
9	15128	110.689	0	255	138.777
10	11508.07	128.184	0	255	121.0398
11	9065.405	141.936	0	255	107.4287
12	2511.839	151.245	0	255	56.54872
13	2397.911	113.856	0	255	55.25142
14	1231.506	117.67	0	179	39.59544
15	4139.38	87.546	0	255	72.59297
16	12047.88	113.327	0	255	123.846
17	960.249	116.059	0	233	34.96382
18	2237.869	139.644	0	255	53.37578
19	3694.519	104.935	0	255	68.58132
20	6694.62	111.243	0	255	92.31874
21	9841.2	126.114	0	255	111.9311
22	2799.371	70.417	0	251	59.69764
23	4089.198	143.104	0	255	72.1516
24	1863.535	157.782	0	255	48.70748
25	2937.712	68.095	0	233	61.15494
26	9689.296	117.637	0	255	111.0639
27	13543.86	102.444	0	255	131.3101

	Area (µm^2)	Mean (µm^2)	Min	Max	Diameter (µm)
1	3157.196	108.252	0	255	63.39831
2	2765.808	126.833	0	255	59.33869
3	1483.154	143.142	0	255	43.45303
4	1604.004	159.895	0	255	45.18868
5	6146.851	200.176	0	255	88.46129
6	3960.571	129.879	0	255	71.00776
7	1028.595	118.993	0	255	36.18671
8	4125.366	139.402	0	255	72.46998
9	2481.537	134.089	0	255	56.2066
10	1856.689	156.089	0	255	48.61793
11	2526.855	96.051	0	255	56.7175
12	4078.674	132.113	0	255	72.0587
13	1251.068	92.82	0	255	39.90868
14	4663.696	89.535	0	255	77.05344
15	2704.01	137.3	0	255	58.67202
16	1518.86	133.779	0	255	43.97297
17	1340.332	143.28	0	255	41.3079
18	1774.292	96.57	0	255	47.5269
19	2752.075	142.235	0	255	59.19119
20	3861.694	121.388	0	255	70.11579
21	2934.723	124.355	0	255	61.12382
22	1165.924	106.68	0	255	38.52672
23	3205.261	154.275	0	255	63.87907

Table 3: Grain diameter results from ImageJ for Buff Berea

	Area (µm^2)	Mean (µm^2)	Min	Max	Diameter (µm)
1	36747.89	93.713	0	255	216.2933
2	34129.03	106.624	0	255	208.4437
3	34486.08	117.548	0	255	209.5313
4	13739.78	94.302	0	255	132.2564
5	23464.05	108.175	0	255	172.8337
6	22447.82	94.352	0	252	169.0495
7	23806	112.691	1	255	174.0885
8	12347.26	102.811	0	255	125.3754
9	32470.09	124.123	10	255	203.3146
10	44674.53	121.736	1	255	238.4827
11	9026.642	106.824	0	255	107.1988
12	30715.03	89.207	0	251	197.7436
13	33390.2	104.154	0	255	206.1752
14	17770.39	129.661	0	255	150.4095
15	19603.73	132.639	0	255	157.9779
16	8118.896	87.502	0	244	101.6659
17	14485.47	100.695	7	255	135.798
18	12436.52	79.782	0	213	125.8277
19	21836.7	116.677	12	255	166.7326
20	9349.365	117.766	0	255	109.0983
21	23063.05	94.168	0	255	171.3505

Appendix H: Permeability measurement

Grey Berea permeability results

Parameters	Run 1	Run 2	Run 3	Run 4	Run 5
Q (cm³/s)	5.00	10.00	18.33	41.67	63.33
Δp (atm)	1.60	1.80	2.30	3.00	4.30
K (mD)	192.78	342.73	491.66	856.89	908.59

Buff Berea permeability results

Parameters	Run 1	Run 2	Run 3	Run 4	Run 5	Run 6
Q (cm³/s)	41.67	86.67	115	126.67	148.33	170
Δp (atm)	1.80	3.00	3.00	2.80	3.00	3.00
K (mD)	1430.29	1785.00	2368.55	2795.19	3055.09	3501.34

Bandera Grey permeability results

Parameters	Run 1	Run 2	Run 3	Run 4
Q (cm³/s)	0.42	0.65	0.75	0.92
Δp (atm)	5.60	6.50	7.48	8.31
k (mD)	14.59	16.18	16.20	16.82

Appendix H: Sample GC Chromatograph

```
Data File C:\CHEM32\1\DATA\EGR 2018-04-04 14-23-24\001F0401.D
Sample Name: EGR Effluents
   ===================================================================
Acq. Operator   : SYSTEM                       Seq. Line :   4
Acq. Instrument : 7890A                         Location : Vial 1
Injection Date  : 4/4/2018 2:39:40 PM              Inj :    1
                                            Inj Volume : 1000 µl
Sequence File   : C:\Chem32\1\DATA\EGR 2018-04-04 14-23-24\EGR.S
Method          : C:\CHEM32\1\DATA\EGR 2018-04-04 14-23-24\EGR.M (Sequence Method)
Last changed    : 4/4/2018 2:23:24 PM by SYSTEM
Method Info     : EGR Analysis


   ===================================================================
```
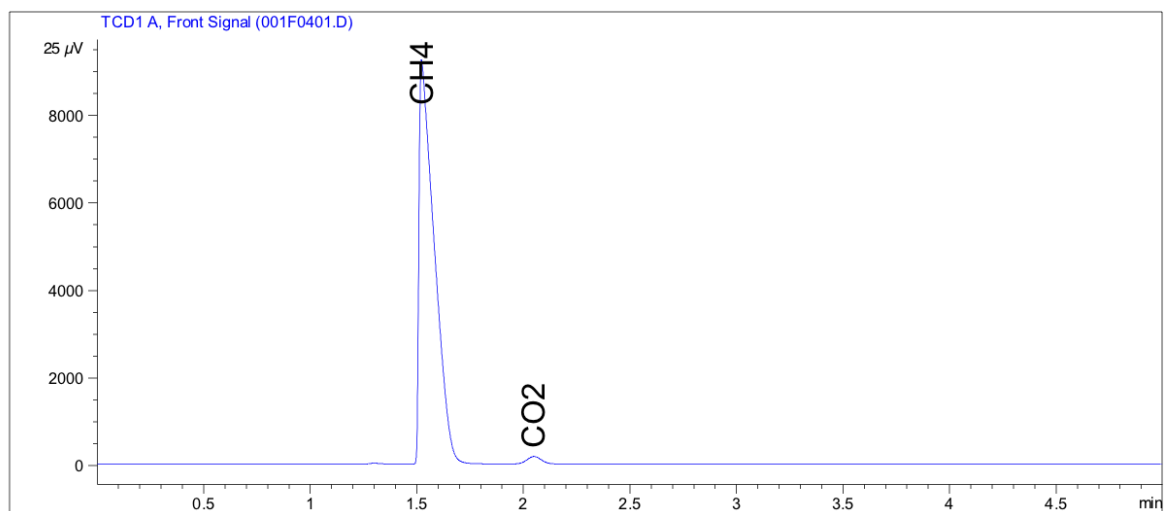


```
   ===================================================================
                         Area Percent Report
   ===================================================================

Sorted By           :        Signal
Calib. Data Modified :        9/20/2017 7:35:39 PM
Multiplier          :        1.0000
Dilution            :        1.0000
Sample Amount:      :        1.00000 [ng/ul]   (not used in calc.)
Do not use Multiplier & Dilution Factor with ISTDs


Signal 1: TCD1 A, Front Signal

Peak RetTime  Type   Width     Area       Area      Name
  #   [min]          [min]  [25 µV*s]      %
----|-------|------|-------|----------|--------|--------------------
   1   1.243         0.0000    0.00000  0.00000 N2
   2   1.523 BB S    0.0735 4.58179e4 98.28848 CH4
   3   1.877         0.0000    0.00000  0.00000 CO2*
   4   2.050 BB      0.0731  797.83923  1.71152 CO2
   5   3.879         0.0000    0.00000  0.00000 Air

Totals :                      4.66158e4
```